SETCOR
Conferences & Events

Nanotech MEET Tunisia 2014 International Conference Proceeding

www.setcor.org/conferences/NANOTECH-MEET-Tunisia-2014

Wireless Sensors Networks For Medical Monitoring

Jihed KHASKHOUSSI
Laboratory EμE, Faculty of Sciences
Monastir, Tunisia
Jihed.khaskhoussi@tunisietelecom.tn

Ridha OUNI
College of Computer and
Information Sciences (CCIS)
University of King Saud (UKS)
Saudi Arabia
rouni@ksu.edu.sa

Abdellatif MTIBAA
Laboratory EμE, Faculty of Sciences
Monastir, Tunisia
Abdellatif.mtibaa@enim.rnu.tn

***Abstract*— While there are many areas where Wireless Sensors Networks (WSNs) can be deployed to offer fast and low cost solutions for the monitoring, few real deployments could be found due to energy constraint. Medicine is one of the areas where we can deploy the WSN to monitor vital parameters like temperature, Electrocardiogram, blood pressure and oxygen saturation to allow urgent intervention.**

The WSN for telemedicine is composed of many devices (nodes) scattered on the patient body as bracelets. These devices are equipped by physical sensors responsible for measuring a specifics metrics. They collaborate together to send data to one or multiple sinks (doctors and medical staff) for diagnostic and intervention if necessary. In this paper, we analyze the behavior of a medical WSN where all nodes (or patient) are mobile. We simulate multiple transmission scenarios to describe urgent situations where we deploy the Multi Point Relay protocol as a solution to ensure the full network functions when the nodes are in move.

***Keywords*— Medical network, MPR, WSN.**

I. INTRODUCTION

In the upcoming years, wireless communication will be embedded in everyday objects, such as clothes, gadgets, toys, home appliances, food carts to cars, bridges, roads, farm lands, buildings, animals and people. The integration of a wireless module is not just enabling a way to communicate but it is a means to make objects smarter and granting those new abilities. Wireless Sensor Networks will enable a wide range of new applications and usages like building automation, consumer electronics, industrial automation and personal health care (e.g. body sensor networks). This computing will help improving the quality of life and change the way individuals perceive the world.

Recently, the WSN-based telemedicine is considered as a new paradigm for supporting remote clinical health care. It allows facilitating preliminary and periodically health diagnostics through a data base history of the patients. This paradigm was successfully employed in several pilot studies and commercial applications. In telemedicine, the WSN is composed of many devices (nodes) scattered on the patient body as bracelets. These devices are equipped by physical sensors responsible for measuring target metrics. They collaborate together to send data to one or multiple sinks (doctors and medical staff) for diagnostic and intervention if necessary.

The aim of this study is to perform a simulation for large scale wireless sensor networks working on medical diagnosis. The main issue in this environment focuses on the density of nodes and how to ensure their connectivity despite their mobility within different radio ranges. Our approach helps medical staff to diagnose diseases in an automated way. In this context, each patient is equipped by a set of sensors. Each sensor is connected to a transducer dedicated to measure health parameters.

This paper is organized as follows. Section 2 briefly discusses works related to medical monitoring. Section 3 draws our context and introduces our evaluation. Sections 4 and 5 describe the simulation processes and analyze the results respectively. Finally, section 6 concludes the paper and draws some future works.

II. RELATED WORKS

In [1], authors discuss how wireless technologies, reducing the healthcare cost, can be used for medical applications and how well they perform in a healthcare/hospital environment. This work considers low-rate Wireless Personal Area Network (WPAN) technology as specified in the IEEE 802.15.4 standard and evaluates its suitability to the medical environment. They focus on scalability issues and multi-

disciplinary of communicating devices in a patient's hospital room.

In [2], authors present the design, implementation and demonstration of a smart medication system, which employs the wireless sensors network (WSN) technologies. The primary functions of the system include the medication reminder and tracking for the patients with chronic diseases. The system can be easily deployed in a nursing home which accommodates many elderly people. Also [3] presents and demonstrates a wireless heart disease monitoring hardware/software systems based on ad hoc interconnection of tiny ECG sensors, called medical ad hoc sensor networks (MASN).

Many researchers[4,7] have relied in simulation to validate their ideas and methods due to the difficulty of deploying real systems (i.e., deploying tens or hundreds of sensor nodes in the physical environment, program them, excite them, and monitor their behavior and state as the algorithm implementing the research idea unfolds). While many authors [8,10,11,12] present the experimental implementation with real equipments for monitoring.

III. PROPOSED MODEL

Applications for wireless telemedicine were presented as a low bit rate applications delay sensitive with low cost and robust topology. Researches outline always the mobility fact of patients which needs a self-organized network. While the protocols for the self-organization process presented for the wireless sensors networks still limited face mobility, some protocols source dependents like the Multipoint Relay MPR [3, 5, 6, 9] appears promoted.

In this paper, we aim to evaluate the performance of mobile medical wireless sensors networks used to monitor the multiple healthcare patient parameters. Each patient presenting an emergency case should have the necessary treatment at time. The delay is very sensitive especially for heart diseases. Sometimes, patients need many doctors, therefore network should be able to send message for many destinations including the sink node where data are stored. So, doctors can react and even give a treatment with specific device like injecting sugar dose in patient body by vibration.

While one packet is transmitted each time, problems of collision and access delay are avoided but the problem persist at emergencies cases (many patients needs care). In this paper, we will analyze the behavior of the network shown on the figure 1. where all nodes (patients) are moving.

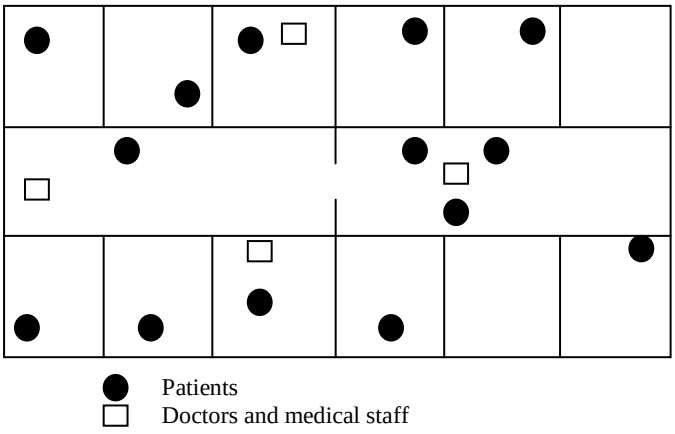

Fig.1. Medical WSN-based network.

IV. SIMULATION

The simulation is a very important step to improve the ability and the efficiency of our proposal to monitor vital parameters in telemedicine environment. However, if the network to be analyzed is yet to be deployed and to be made operational, simulation modeling is used. It is the most important method for network performance analysis. CASTALIA is one of the best tools capable of modeling and evaluating new protocols for wireless sensors networks.

In this work, the network topology includes 40 patients sensing nodes with three sensors for each one, 5 nodes for doctors and one sink node. Nodes exchange HELLO messages to complete the neighbor's tables. Each node will calculate their own relays with the Multipoint Relays protocol (MPR) presented in the literature as a technique to reduce the number of redundant retransmission in the wireless sensors networks by electing a special node set to cover the network based on 2-hop neighbors' knowledge. Several rules and algorithms are proposed for this calculation. In this paper, we resort to the greedy MPR set computation described in the algorithm below.

MPR Algorithm

1. Start with an empty multipoint relays set.
2. Add nodes which are the only neighbour of some nodes in the 2-hop neighbours.
3. If still there will be some two-hop nodes which are not yet covered, so computes the one-hop nodes degrees and chooses the maximum one.
4. Repeat step 3 until all two-hop neighbourhoods are covered.

The simulation study was carried out to evaluate the performance of the network based on the metrics media access delay and packet delivery ratio with the parameters of table 1.

TABLE I
SIMULATION PARAMETERS

Parameter	Value
field_x	200
field_y	200
field_z	0
numNodes	40
TxOutputPower	0
constantDataPayload	20,100,1000,2400
packetHeaderOverhead	5
startupDelay	0
speed	0.2
maxNetFrameSize	2500
maxMACFrameSize	2500
maxPhyFrameSize	2500

For primitive network we did not have to write application in Castalia because the standard simulator contains an application called "ThroughputTest" which provides the exact functionality we need to simulate. All we have to do was to configure the application (i.e. the number of packets, the interval of packet sending, transmission power etc.). While we wrote a new application to support the behaviour of the MPR organized network. In the new application, only relays nodes can forward the received packet. We have also written a new mobility management module for Castalia 3.2 based on the "Random Waypoint" mobility model to describe the movements of patients and doctors.

V. RESULTS

A. *Media Access Delay*

Media access delay parameter represents the total queuing and contention delay of the data frames transmitted by all the 802.15.4 MAC levels. This delay is defined as the duration from when the frame is inserted into the transmission queue until when it is sent to the physical layer. The queuing delay includes the data packets arrival time from higher layer and frame creation time.

Figure 2 shows the media access delay for (a) a primitive network where all nodes are equal in terms of operating mode and (b) an organized networks based on the MPR protocol. These curves illustrate the enhancement of the self-organization on the media access delay.

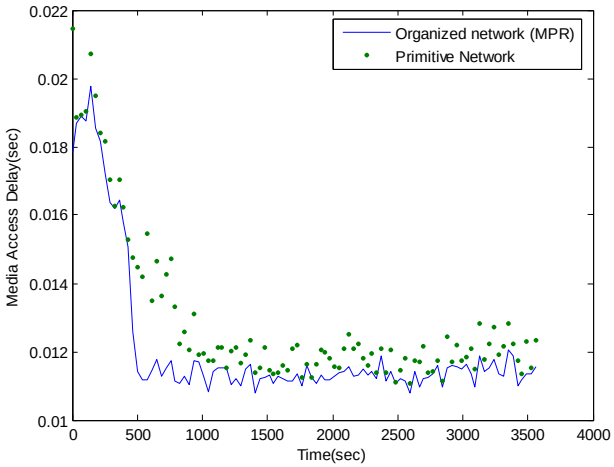

Fig. 2. Media access delay for primitive and organized networks.

B. *Packet Reception rate (PRR)*

Packet Delivery Ratio (PDR) or Packet Reception Rate (PRR) is the ratio between the number of packets transmitted by a traffic source and the number of packets received by a traffic sink. It measures the loss rate as seen by transport protocols and as such, it characterizes both the correctness and efficiency of WSN routing protocols where high packet delivery ratio is desired in any network. The basics reasons of packets reception/non-reception are:

1) Received with NO interference,
2) Received despite interference,
3) Failed with NO interference – when the bits error rate (BER) is too high,
4) Failed with interference,
5) Failed, below sensitivity of the receiver.

As many sensors are scattered on the body of the patient, we generate different size packets to support multiservice functionalities.

Two scenarios were simulated depending on the number of sources (patients) and the number of sinks (doctors or medical staff).

Scenario 1: many sources for one sink.

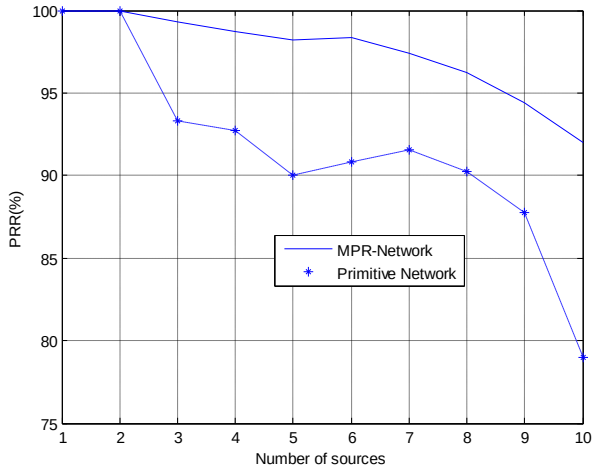

Fig.3. Effect of the number of transmitters on the PRR.

Figure 3 shows the PRRs of the primitive and the MPR-organized networks. The MPR-network is better when the number of sources traffics increases.

Scenario 2: many sources and many sinks.

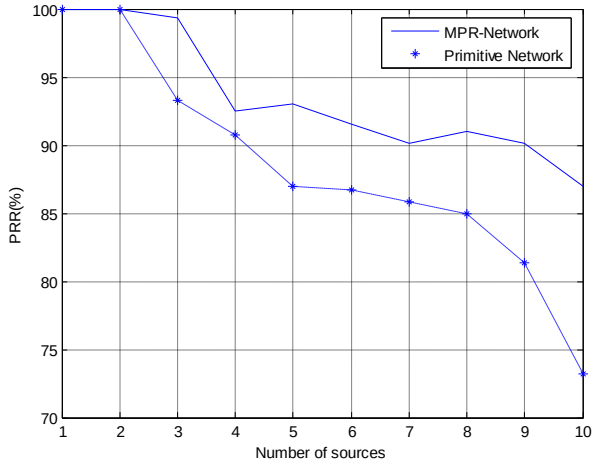

Fig. 4. Average PRR face multiple sources and destination.

The figure 4 depicts the average PRR of the sinks nodes. MPR-network shows better performance than primitive network. Also, many sources and destinations presents the worst delivery ratio compared to one destination.

VI. CONCLUSION

In this paper, the performance of the MPR protocol for medical network was analyzed using Castalia simulator. We have simulate the media access delay time and the packet reception rate by varying the number of traffic sources and sinks in a full mobile network to describe possible scenarios of emergencies cases. Results show that the MPR protocol enhances the behaviour of the medical network but it still inefficient for the emergencies. Simulation proof that routing protocol is strongly needed. Also, security aspect should not be avoided in the multi-uses devices environments to grant patients privacies and protect data from unwanted actions of unauthorized users.

ACKNOWLEDGMENT

The authors would like to thank the Research Center at the College of Computer and Information Sciences- King Saud University, for its support in funding this research.

REFERENCES

[1] Crisostomo, S., Barros, J. and Bettstetter, C., “Flooding the network: Multipoint relays versus network coding”, ICCSC, 2008, pp.119-124.

[2] Dessart, N., Fouchal, H., Hunel, P. and Rabat, C.,” Imulation of Large Scale WSN for Medical Care”, ISCC, 2010, pp.1115-1120.

[3] FURTADO, H. and Trobec, R., ” Applications of wireless sensors in medecine”, MIPRO, 2011, pp.257-261.

[4] Geoffrey, G.M. and Ivars G.F.,” Traffic Models for Medical Wireless Sensor Networks”, IEEE COMMUNICATIONS LETTERS, VOL.11, NO.1, pp.13-15, Jan. 2007.

[5] Jie, W., Wei, L. and Fei, D.,” Extended Multipoint relays to determine connected dominating sets in MANET’s”, IEEE transaction on computer, VOL. 55, NO. 3, pp.334-347, March 2006.

[6] Rajiv, M.,” On self-stabilization of multipoint relays for connected dominating set in ad hoc networks”, TENCON, 2009, pp.1-6.

[7] Xiaoyu, S., ” Modeling and Simulation of WSN Routing Protocols, Communication Software and Networks”, ICCSN, 2011, pp.586-590.

[8] XIONG, S., WANG, L., WANG, X. and ZHAN, Y.,” Application of Wireless Sensor Networks to Remote Medical Treatment System”, ITIME, 2009, pp.96-99.

[9] Yongsheng, F., Xinyu W., Wei, S. and Shanping, L., ” Connectivity based greedy algorithm with multipoint relaying for mobile ad hoc networks”, MSN, 2008, pp.72-76.

[10] Hu, M. J., Laura, C. and Yang X.,” Robust medical ad hoc sensor networks (MASN) with wavelet-based ECG data mining”, Ad Hoc Networks, Vol. 11, NO.7, pp. 986–1012, Sep. 2008.

[11] Wei-Chih, H., Chi-Wei, K., Wen-Wei, C., Jhe-Jhao, C., Yi-Ting, H., Yi-Chung, L., Tung-Jung, S. and Yao-Joe, Y.,” A WSN Smart Medication System”, Procedia Engineering, VOL.5, pp.588-591, 2010.

[12] Fei, H., Laura, C., and Yang, X.,” Error-resistant RFID-assisted wireless sensor networks for cardiac telehealthcare”, Wireless Communications & Mobile Computing, VOL.9, NO.1, pp.85-101, Jan.2009.

Synthesis and characterizations of sol-gel Ag-doped ZnO nanostructured thin films for optoelectronic applications

T. Touam [1], F. Boudjouan [2], A. Chelouche [2], M. Dehimi [1], D. Djouadi [2], J. Solard [3], A. Fischer [3], A. Boudrioua [3]

[1]Laboratoire des Semi-conducteurs, Université Badji Mokhtar-Annaba, Annaba 23000, Algérie
[2]Laboratoire de Génie de l'Environnement, Université de Bejaia, Bejaia 06000, Algérie
[3]Laboratoire de Physique des Lasers, Université Paris 13, Villetaneuse 93430, France

ABSTRACT

Pure and silver-doped zinc oxide (SZO) thin films were prepared on glass substrates by sol-gel dip-coating method. The influence of Ag doping percentage (1, 2, 3, 4 and 5 at.%) on the microstructure, surface morphology, optical transmittance and electrical resistivity of ZnO thin films were systematically investigated by means of X-Ray Diffraction (XRD), Scanning Electronic Microscopy (SEM), Atomic Force Microscopy (AFM), UV-visible spectrophotometer and four points probe technique. The XRD patterns of the undoped and Ag-doped ZnO thin films have shown that the preferential growth is strongly affected by Ag-doping and crystallinity of the films was enhanced with increasing silver contents. SEM micrographs and AFM images have revealed that the grain size and surface roughness tend to decrease with increasing silver concentration. The maximum optical transmissions in the visible region were observed higher than 80% and Ag-doped ZnO thin films show better transparency than the undoped ones. The electrical measurement have revealed that the resistivity of the thin films decrease with increasing Ag doping amounts, suggesting that a sol-gel SZO thin film has low resistivity. The optical and electrical results demonstrate that the ZnO thin films doped with 4 at.% Ag can be well adapted for optoelectronic applications.

Keywords

Ag-doped ZnO, sol-gel thin film, atomic force microscopy, UV-visible transmittance, electrical properties, optoelectronic applications.

1. INTRODUCTION

Over the few decades, Zinc oxide (ZnO) has attracted considerable attention due to its unique properties such as non-toxicity, low material costs, chemical stability, high electron mobility, wide and direct band gap (E_g = 3.37 eV at 300 K), large exciton binding energy (60 meV) and high transparency in the visible and near infrared spectral region [1]. Since all these properties, ZnO thin films have found applications in a lot of fields including solar cells, surface acoustic wave devices, gas sensors and optoelectronics [2–4]. Synthesis parameters, deposition conditions and doping can tune the properties of ZnO thin films. Doping ZnO by appropriate elements can lead to a significant improvement of its optical, magnetic and electrical properties without any change in the crystalline structure [5]. Among dopants, silver is one of the most promising to enhance optoelectronic ZnO properties. A variety of techniques have been employed to prepare pure and Ag-doped ZnO thin films such as pulsed laser deposition [6], sputtering techniques [7, 8], spray pyrolysis [9], vapor–liquid–solid mechanism [10] and sol-gel methods [11, 12]. Among these techniques, the sol-gel method has attracted much attention owing to its distinctive advantages including low cost, simplicity, controllability of compositions, large area film fabrication and the possibility to easily incorporate dopants for required technological applications. Although some results have been reported on the effect of Ag-doping on physical properties of ZnO thin films, there are still some inconsistency between them [7, 11] and further study is needed. Moreover, in the majority of works dealing with electrical properties, authors have been mostly interested by the p-type conductivity and to the best of our knowledge the effect of Ag contents on resistivity of the SZO thin films prepared by sol-gel process has not been reported. The present paper is devoted to the study of the Ag-doping on structural, morphological, optical and electrical properties of ZnO nano-structured thin films prepared by sol-gel dip-coating method.

2. EXPERIMENTS

Pure and Ag-doped ZnO thin films were prepared by the sol-gel process. As a starting material, zinc acetate dihydrate ($Zn(CH_3COO)_2\ 2H_2O$)(Sigma-Aldrich) was dissolved in a mixture of absolute ethanol (EtOH, 100%, BioChem) and monoethanolamine (MEA) (Sigma-Aldrich) yielding to a precursor concentration of 0.75 mol L^{-1}. MEA acts, at the same time, as a base and a complexing agent and the MEA to zinc acetate molar ratio was set to 1. For doped films, silver nitrate ($AgNO_3$) was added to the mixture with an atomic percentage fixed at 1, 2, 3, 4 and 5 at.% Ag. The resulting ZnO and SZO sol were stirred at 50 °C for 1 h, and then aged at room temperature for 36 h to get a clear and transparent homogeneous ZnO and SZO aqueous solutions. The commercial glass substrates (Esco Optics) were cleaned with detergent, rinsed in flowing deionized water and immersed in 4 M nitric acid for one hour. Rinsing with acetone and isopropanol, drying with nitrogen and in an oven at 100 °C for 30 min complete the procedure. The substrates were dipped in the prepared sols and then withdrawn at a constant dip-coating speed of 15 mm/min (KSV NIMA Dip Coater). The prepared films were preheated at 200 °C for 10 min after each coating. This procedure was repeated twelve times to increase the thickness. The films were subsequently heated up to 500 °C for 1 h in order to obtain crystallized ZnO.

The crystal structure and orientation of undoped and Ag-doped ZnO thin films were investigated by X-ray diffraction (XRD) with a PANalytical X´Pert diffractometer , operating at 40 kV and 30 mA using Cu $K\alpha_1$ radiation (λ= 1.54056 Å) at a grazing incidence angle ω equal to 0.54°. Scanning Electronic

Microscopy (SEM) characterizations were carried out by means of a Raith PIONEER System. Surface morphology of the thin films was analyzed from the images collected in contact mode by Atomic Force Microscopy (AFM, Nanosurf easyScan 2). The optical transmittance measurements were performed with a Safas UVmc2 UV-Visible spectrophotometer and the optical bandgap energy was calculated. The four-point probe method was employed for electrical meaurements. The thickness of the all samples was estimated from surface profile analysis by a Veeco Dektak 150 Surface.

3. RESULTS and discussions:

Figure 1. illustrates the diffraction patterns of the pure, 1, 2, 3, 4 and 5 at.% Ag-doped 12-layer ZnO samples. The diffracted peaks have been identified using standard ZnO cards indicating that all the deposited films have a polycrystalline wurtzite hexagonal structure, and no other crystallized phases are observed. This means Ag-incorporation does not change the crystal structure. The results show that all the pure ZnO thin films have (101) as the preferred orientation. The intensity of the (002) peak of Ag-doped samples indicate that all the SZO thin films exhibit preferential orientation growth along (002) direction, that is, perpendicular to the substrate surface. We have to note the broadening of the diffracted peaks, which is usually a result of a smaller crystallite size and lattice. It is clearly seen that the peak intensities of the Ag-doped ZnO thin films increase when the silver content were increased from 1 to 5 at.%. This feature demonstrates that the crystallinity of the samples is enhanced when Ag concentration was increased [13].

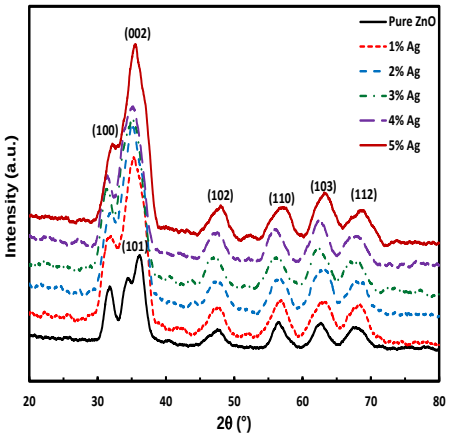

Figure 1. XRD patterns of the pure, 1, 2, 3, 4 and 5 at.% Ag doped ZnO thin films.

Figure 2. displays high-magnification scanning electronic micrographs of the undoped and SZO thin films on glass substrates. The films show uniform and dense morphology overall the surface consisted of spherical aggregate grains in the 50-90 nm range around which and on which much finer nanoparticles can be observed, with a mean diameter around 15-25 nm. It is clear from these micrographs that the surface morphology of SZO films were slightly modified with doping. It can be seen that grain size seems to be sensitive to the Ag content as finer particles and aggregate grains are observed. Our finding seems to be in agreement with reported results by Thongsuriwong et al. [14], where it was demonstrated from their AFM images that the grain size of the Ag-doped ZnO thin films slightly decreased with increasing Ag concentration.

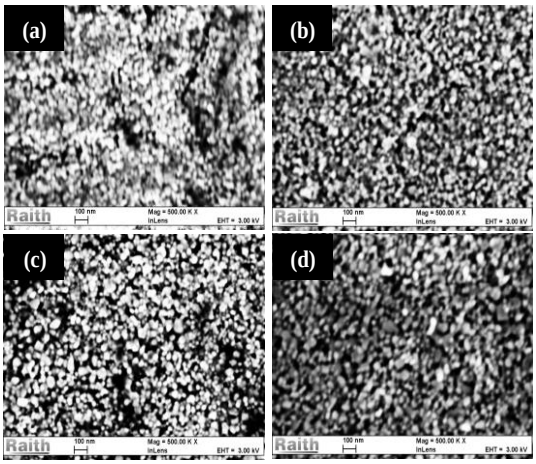

Figure 2. SEM micrographs of Ag-doped ZnO thin films: (a) 0 at.% Ag, (b) 2 at.% Ag, (c) 4 at.% Ag and (d) 5 at.% Ag.

The three-dimensional AFM images of the undoped and Ag-doped ZnO thin films are shown in Figure 3. It is clearly seen that all the samples have uniform and dense ZnO grains. Furthermore, the grains have columnar shapes which grow preferentially along the c-axis orientation. This observation is in good agreement with the results of XRD and SEM analyses. The films exhibit different surface roughness which seems to be dependent on the Ag-doping. The root mean squared roughness (R_{rms}) was also calculated and found to be as 19.57, 18.87, 17.76, 12.64, 10.52 and 15.44 nm for 0, 1, 2, 3, 4 and 5 at.% Ag-doped ZnO thin films, respectively. Undoped ZnO thin film has the largest surface roughness, but when Ag-doping concentration is increased, the surface roughness decreases gradually reaching its minimum value at 4 at.% silver contents, then slightly increase when the Ag concentration is increased to 5 at.%. It is possibly connected with the decrease of ZnO grain as revealed by SEM micrographs.

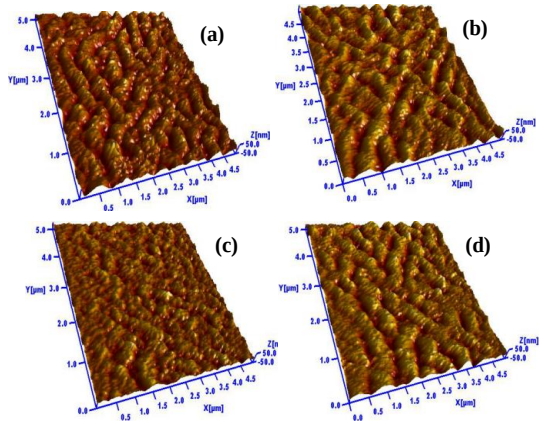

Figure 3. AFM images of Ag-doped ZnO thin films: (a) 0 at.% Ag, (b) 2 at.% Ag, (c) 4at.% Ag and (d) 5 at.% Ag.

Figure 4. shows the UV-Vis-NIR transmittance spectra of Ag-doped ZnO thin films for various Ag-doping concentrations. The maximum optical transmissions in the visible region were observed higher than 80% and SZO films show better transparency than the undoped ZnO. This result seems to be in good agreement with the calculated values of the root mean squared roughness (R_{rms}). From the magnification of absorption edge region shown by inset Figure 4, it is found that by increasing silver contents up to 4 at.% , the absorption edge shift toward

shorter wavelengths indicating an increase in the bandgap. However, at 5 at.% doping, opposite behavior is observed by a slight shift to a longer wavelength region.

Direct optical bandgap of undoped and Ag-doped ZnO thin films has been calculated using the technique based on the derivative of the transmittance against energy. This method has been well described by Wang *et al.* [15], and was successfully used previously for the analysis of the bandgaps. Bandgap values of 3.204, 3.212, 3.221, 3.229, 3.238 and 3.221 eV were obtained for pure ZnO, 1 at.%, 2 at.%, 3at.%., 4 at.%. and 5 at.%. of Ag, respectively. It is shown that the band gap increases as the Ag contents increases but then slightly decreases when the Ag concentration is increased to 5 at.%. Several reports indicated controversial results concerning the energy gap (E_g) change of Ag-doped ZnO thin films. For example, Xue et al. [7] have investigated the influence of Ag-doping on the optical properties of ZnO films prepared by rf magnetron sputtering technique. It was demonstrated that the optical band edge shifted to a shorter wavelength first as Ag is incorporated, and then to a longer wavelength with the increasing of Ag-doping concentration. While, Sahu [8] has studied the effect of Ag-doping on the structural, optical and electrical properties of ZnO thin films prepared by simultaneous rf magnetron sputtering of ZnO and dc magnetron sputtering of Ag on glass substrate. It was found that the absorption edge shifted slightly to a longer wavelength and the band gap narrowed with increasing Ag content. Our finding seems to be in very good agreement with the work of Xue *et al.* [7]. According to our obtained results, the increment in the band gap may be attributed to the quantum size effect as indicated by the work of Marotti *et al.* [16], where it was suggest-ed that the band gap and the absorption edge of nano-structured materials shift due to quantum size effects.

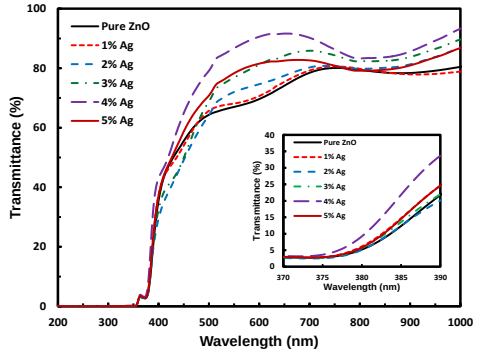

Figure 4. Transmittance spectra of pure and Ag-doped ZnO thin films. The inset shows the magnification of absorption edge region.

The electrical resistivity was measured at room temperature by four-probe method. The thickness of the all thin films was determined from surface profile analysis. Thickness values of 450, 412, 382, 372, 371 and 382 nm were obtained for pure ZnO, 1 at.%, 2 at.%, 3at.%., 4 at.%. and 5 at.%. of silver, respectively. Figure 5. depicts the variation of resistivity of Ag doped ZnO films with doping concentration. The resistivity of undoped ZnO is about 4.56 10^{-4} Ωcm, while it is reduced with increasing Ag concentration and a lowest value of 9.6 10^{-3} Ωcm is obtained at Ag-doping concentration of 5 at.%. This decrease in the resistivity with increase in Ag concentration can be attributed to increase in carrier concentration and also due to increase in mobility.

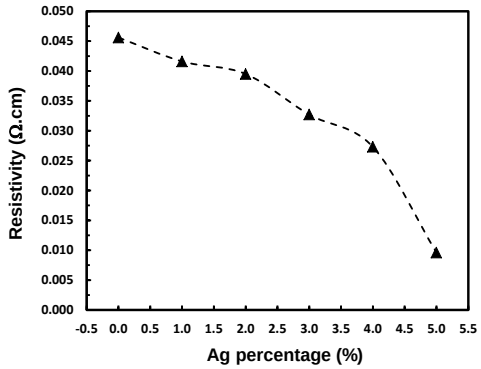

Figure 5. Electrical resistivity of undoped and Ag-doped ZnO thin films.

4. CONCLUSION

In this work, transparent and conductive Ag-doped ZnO thin films have been successfully prepared by sol-gel dip-coating method. Structural, morphological, optical and electrical properties of the thin films as a function of silver concentration have been investigated using X-ray diffraction, scanning electronic microscopy, atomic force microscopy, UV-visible spectrophotometer and four points probe technique. XRD spectra have shown that undoped thin film exhibit (101) orientation while Ag-doped ones have a preferred crystalline structure in (002) direction perpendicular to the substrates. SEM micrographs and AFM images have revealed that grain sizes and surface roughness decrease with increasing silver concentration. The UV-visible transmittance results show that SZO thin films exhibit better transparency than undoped ZnO thin films with highly transparency in the visible region. A change in the optical bandgap of ZnO thin films is also revealed. The electrical measurement have shown that the resistivity of the thin films decrease with increasing Ag doping amounts between 0 and 5 at.%. The obtained results have demonstrated that the ZnO thin films doped with 4 at.% Ag have suitable properties of high transmittance and low resistivity for application in optoelectronics devices.

5. REFERENCES

[1] Hass, M., Weller, H. and Henglein, A. 1988. Photochemistry and radiation chemistry of colloidal semiconductors. 23. Electron storage on ZnO particles and size quantization. *J. Phys. Chem.* 92, 2 (Jan. 1988), 482-487. DOI= http://pubs.acs.org/doi/abs/10.1021/j100313a047.

[2] Major, S. and Chopra, K. L. 1988. Indium-doped zinc oxide films as transparent electrodes for solar cells, *Sol. Eenerg. Mat. Sol. C.* 17, 5 (Aug. 1988), 319-327. DOI= http://ac.els-cdn.com/0165163388900147.

[3] Shishiyanu, S. T., Shishiyanu, T. S. and Lupan, O. I. 2005. Sensing characteristics of Tin-doped ZnO thin films as NO_2 gas sensor, *Sensor. Actuat. B-Chem.* 107, 1 (May 2005) 379-386. DOI=http://ac.els-cdn.com/S0925400504007233.

[4] Kim, H. S., Lugo, F., Pearton, S. J., Norton, D. P., Wang, Y. L. and Ren, F. 2008. Phosphorus Doped ZnO light emitting diodes fabricated via pulsed laser deposition. *Appl. Phys. Lett.* 92, 11 (Mar. 2008), 112108-112110. DOI= http://dx.doi.org/+10.1063/1.2900711.

[5] Znaidi, L., Touam, T., Vrel, D., Souded, N., Ben Yahia, S., Brinza, O., Fischer and A., Boudrioua, A. 2013. AZO thin films by sol-gel process for integrated optics. *Coat.* 3, 3 (Jul. 2013), 126-139. DOI= http://www.mdpi.com/2079-6412/3/3/126.

[6] Myers, M. A., Lee, J. H., Bi, Z. and Wang, H. 2012. High quality p-type Ag-doped ZnO thin films achieved under elevated growth temperatures. *J. Phys. Condens. Matter.* 24, 14 (Apr. 2012), 145802-145808. DOI= http://iopscience.iop.org/0953-8984/24/14/145802.

[7] Xue, H., Xu, X.L., Chen, Y., Zhang, G.H. and Ma S.Y. 2008. Influence of Ag-doping on the optical properties of ZnO films, *Appl. Surf. Sci.* 255, 5 (Dec. 2008), 1806-1810. DOI= http://iopscience.iop.org/0953-8984/24/14/145802.

[8] Sahu, D.R. 2007. Studies on the properties of sputter-deposited Ag-doped ZnO films. *Microelectron. J.* 8, 12 (Dec. 2007), 1252-1256. DOI= http://dx.doi.org/10.1016/j.mejo.2007.09.025.

[9] Liu, K., Yang, B., Yan, H., Fu, Z., Wen, M., Chen, Y., Zuo, J. 2009. Effect of Ag doping on the photoluminescence properties of ZnO films. *J. Lumin.* 129, 9 (Sep. 2009), 969-972. DOI= http://dx.doi.org/10.1016/j.jlumin.2009.04.021.

[10] Song, Y-W, Kim, K., Ahn, J. P., Jang G-E. and Lee, S. Y. 2009. Physically processed Ag-doped ZnO nanowires for all-ZnO p–n diodes. *Nanotechnology.* 20, 27 (Jul. 2009), 275606-275610. DOI= http://iopscience.iop.org/09574484/20/27/275606.

[11] Xian, F., Miao, K., Bai, X., Ji, Y., Chen, F. and Li, X. 2013. Characteraction of Ag-doped ZnO thin film synthesized by sol-gel method and its using in thin film solar cells. *Optik* 124, 21 (Nov. 2013), 4876-4879. DOI= http://dx.doi.org/10.1016/j.ijleo.2013.02.034.

[12] Chelouche, A., Djouadi, D., Merzouk, H. and Aksas, A. 2013. Influence of Ag doping on structural and optical properties of ZnO thin films synthesized by the sol-gel technique. *Appl. Phys. A*, Published online: 24 October 2013, DOI= http://link.springer.com/ 10.1007/s00339-013-8029-0.

[13] Li, J.-C., Cao, Q. and Hou, X.-Y. 2013. Effects of Ag-induced acceptor defects on the band gap tuning and conductivity. *J. Appl. Phys*. 113, 20 (May 2013), 203518-1-203518-7. DOI= http://dx.doi.org/10.1063/1.4807932.

[14] Thongsuriwong, K., Amornpitoksuk, P. and Suwanboon, S. 2012. Photocatalytic and antibacterial activities of Ag-doped ZnO thin films prepared by a sol-gel dip-coating method. *J. Sol-Gel Sci. Technol.* 62, 3 (Jun. 2012), 304-312. DOI= http://link.springer.com/ 0.1007/s10971-012-2725-7.

[15] Wang, M., Kim, E. J., Kim, S., Chung, J. S., Yoo, I., Shin, E. W., Hahn, S. H. and Park, C. 2008. Optical and structural properties of sol-gel prepared Mg ZnO alloy thin films. *Thin Solid Films* 516, 6 (Jan. 2008), 1124-1129. DOI= http://dx.doi.org/10.1016/j.tsf.2007.05.039.

[16] Marotti, R. E., Giorgi, P., Machado, G. and Dalchiele, E. A. 2009. Crystallite size dependence of band gap energy for electrodeposited ZnO grown at different temperatures. *Sol. Energ. Mat. Sol. C.* 90, 15 (Sep. 2006), 2356-2361. DOI= http://dx.doi.org/10.1016/j.solmat.2006.03.008.

Structural, morphological, optical and waveguiding properties of sol-gel nano-structured TiO_2 thin films

M. Atoui [1], T. Touam [1], I. Hadjoub [1], A. Chelouche [2], B. Boudine [3], A. Fischer [4], A. Boudrioua [4], A. Doghmane [1]

[1]Laboratoire des Semi-conducteurs, Université Badji Mokhtar-Annaba, Annaba 23000, Algérie
[2]Laboratoire de Génie de l'Environnement, Université de Bejaia, Bejaia 06000, Algérie
[3]Laboratoire de Cristallographie, Université Constantine 1, Constantine 25000, Algérie
[4]Laboratoire de Physique des Lasers, Université Paris 13, Villetaneuse 93430, France

ABSTRACT

Anatase nanocrystalline TiO_2 thin films were prepared by a sol-gel dip-coating process. Structural, morphological, and optical properties of the synthesized films were investigated by X-ray Diffraction (XRD), Raman Spectroscopy (RS), Scanning Electron Microscopy (SEM), Atomic Force Microscopy (AFM), and UV-visible Spectrophotometry. Waveguiding properties such as propagating modes, and optical loss were measured by M-lines Spectroscopy (MLS). The results indicate that all the TiO_2 films annealed at 500°C exhibit XRD patterns and Raman spectra consistent with an anatase phase. SEM micrographs and AFM images have revealed that film morphology and surface roughness depend on withdrawal speed and heat treatment temperature. The UV-visible transmittance results show that all the films were transparent with an average transmittance of more than 70 % in the visible region. With increasing dip-coating speed, the absorption edge shifts toward longer wavelengths, indicating a decrease in the band gap energy of the films. The results have also demonstrated from MLS measurements that the TiO_2 thin film slab waveguides deposited at withdrawal speed of 2 cm/min were better confined and exhibit lower optical losses.

Keywords

Sol-gel, TiO_2 thin film, micro-Raman spectroscopy, optical properties, UV-visible transmittance, m-lines spectroscopy, waveguiding applications.

1. INTRODUCTION

Titanium dioxide (TiO_2) has attracted extensive attentions during last decades as an extremely promising material due to its unique chemical, electrical and optical properties. TiO_2 thin films have been widely used in many application oriented fields like integrated optics [1] and micro-nano photonics [2]. A variety of physical and chemical techniques have been employed to prepare TiO_2 thin films, including reactive RF magnetron sputtering [3], plasma enhanced chemical vapor deposition (PECVD) [4], and sol-gel method [5]. Among them, the sol-gel route is still one of the most widely used process as it is particularly a low cost and versatile technique to produce at low temperature polycrystalline thin films of many compositions with excellent homogeneity on any types of substrates. Several investigations have been reported on the preparation of TiO_2 thin films by sol-gel method using many types of Ti-precursors, solvents and catalytic agents [6, 7]. These studies have indicated that different properties of TiO_2 thin films are strongly affected by film preparation procedures. In this paper, amorphous and anatase nano-structured TiO_2 thin films have been prepared on glass substrate by sol-gel dip-coating method using titanium tetraisopropoxide, ethanol, and hydrochloric acid as Ti-precursor, solvent, and catalyst, respectively. The effect of process parameters and fabrication conditions on structural, morphological, optical and waveguiding properties of the TiO_2 thin films is investigated.

2. EXPERIMENTAL

TiO_2 thin films were prepared by the sol-gel process according to the following procedure: titanium tetraisopropoxide diluted in absolute ethanol was mixed with deionized water, ethanol and hydrochloric acid mixture with a controlled hydrolysis ratio (h = [H2O]/[TTIP] = 1.5) and for 0.9 molar final titanium concentration. Prior to deposition of film, glass substrates were ultrasonically cleaned in deionized water, ethanol and acetone for 15 min, respectively. Then, substrates were dried in an oven at 100 °C for 1 hr. Finally, substrates were dipped in the freshly prepared sol and then withdrawn at a constant dip-coating speed (*V*) of 1, 2 and 3cm/min, respectively. These thin films were dried in an oven at 80 °C for 15 min to evaporate the solvent and further heated in ambient atmosphere at 300 and 500°C for 1 hour, at a heating rate of 5°C / min.

The prepared nano-structured thin films were characterized for the crystalline structure by X-ray Diffraction (XRD) with a PANalytical X´Pert diffractometer , operating at 40 kV and 30 mA using Cu $K\alpha_1$ radiation at a grazing incidence (ω= 0.54°). Raman spectra of the all samples were recorded at room temperature with a Bruker Optik GmbH Raman microscope-spectrometer SENTERRA using a 100x MPLN Olympus objective with 532 nm excitation. Scanning Electronic Microscopy (SEM) characterizations were carried out by means of a Raith PIONEER System. Surface morphology of the thin films was analyzed from the images collected in contact mode by Atomic Force Microscopy (AFM, Nanosurf easyScan 2) operated at room temperature. The optical transmittance spectra were recorded at room temperature by a Safas UVmc2 UV-Visible spectrophotometer and the optical band gap energy was calculated. Optical waveguiding characterizations of the thin films have been carried out by M-lines spectroscopy (Metricon system model 2010). The thickness of the TiO_2 thin films was estimated from surface profile analysis by a KLA - Tencor Alpha-Step IQ Surface Profiler.

3. RESULTS and discussions:

Figure 1. and inset show XRD patterns of the one layer TiO_2 thin films deposited at a dip-coating speed of 1, 2 and 3 cm/min and

annealed 1h at 300° and 500°C, respectively. As seen from inset of Figure 1, all TiO_2 thin films heated at 300°C were amorphous. The films heated at 500°C clearly indicate the anatase phase of TiO_2 since the reflection is perfectly matching with the (1 0 1) peak given in the JCPDS data file for anatase TiO_2 [PDF-04-0477]. The diffraction peaks are broad, which indicates small crystal sizes. It is also found that the crystallization of the TiO_2 thin films was evidently improved as the dipping rate increases. The full width at half maximum (FWHM) of the (101) diffraction peak decreases when the withdrawal speed increases, demonstrating that the crystalline quality of the film gets better as the thickness increases [8].

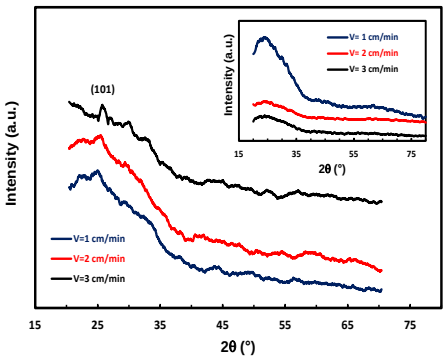

Figure 1. XRD patterns of TiO_2 thin films deposited at different dip-coating speed and annealed 1h at 500°C. The inset show XRD patterns of TiO_2 thin films annealed 1h at 300°C.

Figure 2. illustrates room temperature recorded Raman spectra of one-layered samples dip-coated at the speed ranging from 1 to 3 cm/min. The anatase TiO_2 phase could be identified by the Raman bands at 142 and 391 cm^{-1}, respectively [9].

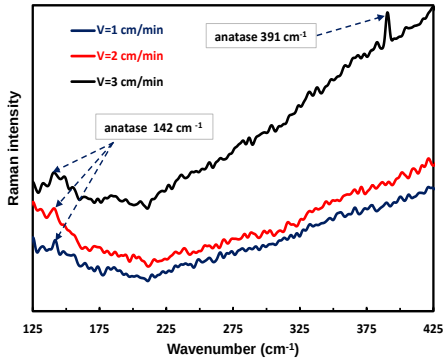

Figure 2. Room temperature Raman spectra of TiO_2 thin films deposited at different dip-coating speed and annealed 1h at 500°C.

The AFM images of a surface of 2x2 mm^2 for the all samples are depicted in Figure 3. The root mean squared roughness (R_{rms}) values were measured at 0.60, 0.63 and 0.66 nm, for amorphous films, and at 0.98, 1.18 and 1.36 nm for the crystallized ones, dip-coated at the speed of 1, 2 and 3 cm/min, respectively. The roughness of the amorphous films is extremely small and does not seem to be significantly affected by withdrawal speed. Crystallized thin films exhibit a smooth surface with a slightly greater roughness [10] and are in good agreement with the results revealed by SEM micrographs (not shown).

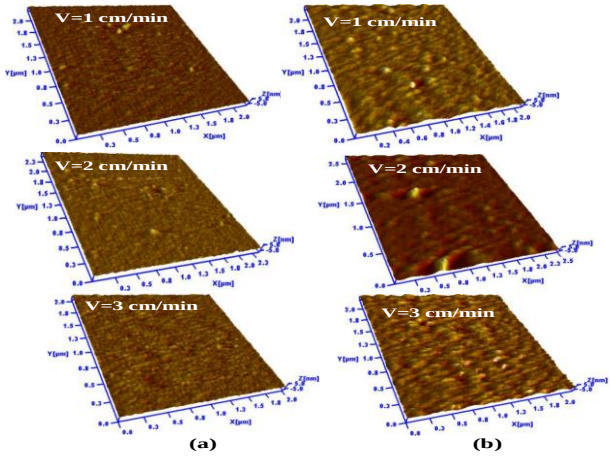

Figure 3. AFM images of TiO_2 thin films deposited at different dip-coating speed and annealed 1h at: (a) T=300°C, (b) T= 500°C.

Figure 4. shows the transmittance spectra in the interval 200-900 nm for the films deposited at withdrawal speed of 1, 2 and 3 cm/min and annealed 1 hour at 500°C. The films were transparent with an average optical transmittance of more than 70% in the visible region and present a sharp absorption edge in the UV region at wavelength ranging from 300 to 400 nm. With increasing dip-coated speed, the absorption edge and maximum transmittance peak position shift toward longer wavelengths, indicating a decrease in the band gap of the films (inset Figure 4). It is related to the increase in the thickness of the films and the size of the grain. The allowed direct bandgap of the films were determined by computing the derivative of the transmittance against energy [11]. Bandgap values of 3.76, 3.73 and 3.71 eV were obtained for the TiO_2 films withdrawn at 1, 2 and 3 cm/min and annealed 1h at 500°C, respectively, in good agreement with literature data for nano-structured TiO_2 thin films [12].

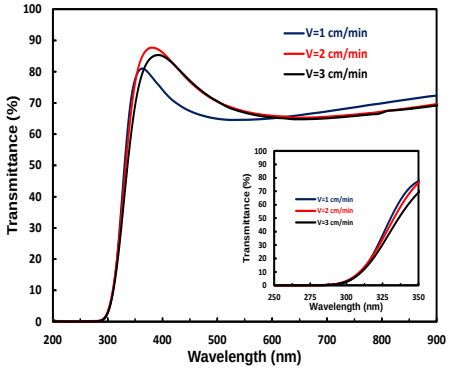

Figure 4. UV-Vis-NIR transmittance spectra of the TiO_2 thin films deposited at different withdrawal speed and annealed 1h at 500 °C. The inset shows the magnification of absorption edge region.

Refractive index and waveguiding properties of the thin films at a 632.8 nm wavelength have been carried out by Metricon system model 2010 prism coupler. This apparatus uses the M-lines spectroscopy method which is based on the prism coupling technique [13]. Figure 5. shows the schematic of a prism coupling setup, where *T* is the film thickness and *n* is the film refractive index.

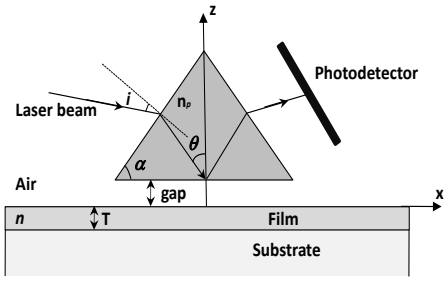

Figure 5. Schematic of the prism coupling setup.

A laser beam strikes the base of a high refractive index prism and is reflected onto a photodetector. The film to be measured is brought into contact with the prism base so that an air gap separate the sample and the prism. The angle of incidence, *i*, of the laser beam can be varied by means of a rotary table upon which the prism, film, and photodetector are mounted. At certain value of *i*, called mode angles, the light tunnel from the base of the prism across the air gap and into the film and enter into optical propagation modes, causing a sharp drop in the intensity of light striking the photodetector. The reflected intensity is measured versus the angle of incidence. From the measured incident angle, the mode effective index n_{eff} can be calculated using the following formula [14]:

$$n_{eff} = \cos\alpha \sin i + \sin\alpha \sqrt{n_p^2 - \sin^2 i} \qquad (1)$$

where α is the prism angle and n_p is the refractive index of the prism. Figure 6. displays typical transverse electric (TE) guided mode spectra of the TiO_2 thin films deposited at withdrawal speed of 1, 2 and 3 cm/min and annealed one hour at 500°C.The results show that all of our TiO_2 thin films support only one guided mode (fundamental transverse electric mode: TE_0). Since all of our slab waveguides are monomode, to compute the refractive indices, the measured value of the effective indices and that of thickness estimated from surface profile analysis are used through the theoretical approach of MLS based on a step-index profile model, i.e. the refractive index is constant with respect to film thickness. The thickness was measured to be about of 55, 73 and 106 nm, and the computed refractive indices are found to be: n = 2.0328, 2.0457 and 2.0603 for the crystallized films deposited at withdrawal speed of 1, 2 and 3 cm/min, respectively.

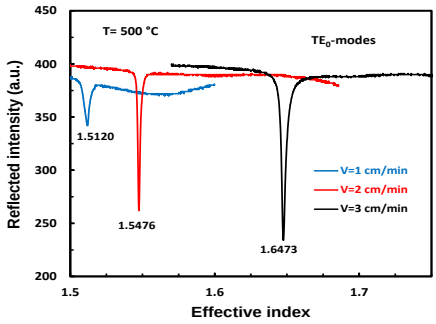

Figure 6. Typical TE guided mode spectra of the the TiO_2 thin films dip-coated at different speed and annealed 1h at 500 °C. The effective indices of the modes are shown next to the corresponding dips.

The sharpness of the reflectivity dips and the full width at half maximum (FWHM) of the mode spectra indicate that the guided mode of the TiO_2 thin film prepared at a rate of 2 cm/min is better confined and will exhibits lower propagation loss compared to other ones. Loss measurements were achieved using the same M-line apparatus by measuring the intensity of scattering from the waveguide as a function of distance with a multimode optical fiber. If we assume the waveguide to be uniform over the measured area, the losses can be determined by fitting an exponential function.

$$f(L) = A\exp(-\alpha L / 4.34) \qquad (2)$$

where L is the distance from a chosen zero-point, A the intensity at the zero-point, and α is the optical attenuation in decibels par centimeter (dB/cm). Figures 7. shows the scattering intensity at 632.8nm wavelength as a function of distance for the crystallized sol-gel TiO_2 films and a fitting curves with α = 1.2 dB/cm for the layer dip-coated at the speed of 2 cm/min. The scattering loss measurement results seem to be in agreement with the surface morphology of films as the optical losses strongly depend on the surface roughness of the material, and are rather consistent with the obtained FWHM of the mode spectra already discussed.

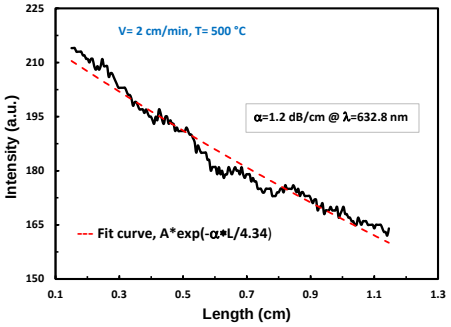

Figure 7. Scattering intensity as a function of distance L for the crystallized sol-gel TiO_2 thin film with a fitted exponential function (red dotted line): V= 2 cm/min, α = 1.2 dB/cm.

4. CONCLUSION

In this work, we have successfully synthesized nano-structured TiO_2 thin films by a sol-gel dip-coating method. The effects of dip-coating speed and heat treatment temperature on the structural, morphological, optical and waveguiding properties of the prepared films were investigated. The results indicate that all the films annealed at 500°C exhibit XRD patterns, Raman spectra and IR data consistent with an anatase phase. SEM micrographs and AFM images have shown that all the thin films heated at 500°C are crystallized with homogeneous and smooth surface. The UV-visible transmittance results show that all the films were transparent with an average transmittance of more than 70 % in the visible region. The bandgap energy (E_g) of the TiO_2 films annealed at 500°C has been observed to decrease from 3.76 to 3.71. M-lines spectroscopy characterizations have revealed that TiO_2 thin films withdrawn at the speed of 2 cm/min exhibits better light confinement and demonstrates lower optical loss.

5. REFERENCES

[1] Montagna, M., Moser, E., Visintain, F., Ferrari, M., Zampedri, L., Martucci, A , Guglielmi, M. and Ivanda, M. 2003. Nucleation of titania nanocrystals in silica titania waveguides. *J. Sol-Gel Sci. Technol.*, 26, 1 (Jan. 2003), 241-244. DOI= http://link.springer.com/10.1023/A:1020755200573.

[2] Wijnhoven, J. E. G. J., and Vos, W. L. 1998. Preparation of photonic crystals made of air spheres in titania. *Science*, 281, 5376 (Aug. 1998), 802-804. DOI= http://www.sciencemag.org/10.1126/science.281.5378.802.

[3] Sung, Y.M. and Kim, H.J. 2007. Sputter deposition and surface treatment of TiO_2 films for dye-sensitized solar cells using reactive RF plasma. *Thin Solid Films* 515, 12 (Apr. 2007), pp.4996-4999. DOI= http://dx.doi.org/10.1016/j.tsf.2006.10.079.

[4] Kubala, N. G. and Wolden, C. A. 2010. Self-limiting growth of anatase TiO_2: A comparison of two deposition techniques. *Thin Solid Films* 518, 23 (Sep. 2010), 6733-6737. DOI= http://dx.doi.org/10.1016/j.tsf.2010.05.128.

[5] Touam, T., Znaidi, L., Vrel, D., Hadjoub, I., Kuznetsova, I. N., Brinza, O., Fischer, A. and Boudrioua, A. 2014. Low optical loss nano-strctured TiO_2 planar waveguides by sol gel route for photonic crystal applications. *Opt. Quant. Electron.* 46, 1 (Jan. 2014), 23-37. DOI= http://link.springer.com/ 10.1007/s11082-013-9692-2.

[6] Nishide, T., Sato, M., Hara, H. 2000. Crystal structure and optical property of TiO_2 gels and films prepared from Ti-edta complexes as titania precursors. *J. Mater. Sci.* 35, 2 (Jan. 2000), 465-469. DOI= http://link.springer.com/ 10.1023/A:1004731804075.

[7] Senthil, T. S. and Kang, M. 2013. Transparent thin film dye sensitized solar cells prepared by sol-gel method. *Bull. Korean Chem. Soc.* 34, 4 (Apr. 2013), 1188-1194. DOI= http://dx.doi.org/10.5012/bkcs.2013.34.4.1188.

[8] Su, C., Hong, B.-Y and Tseng, C.-M. 2004. Sol-gel preparation and photocatalysis of titanium dioxide. *Catal. Today* 96, 3 (Oct. 2004), 19-1263. DOI= http://dx.doi.org/10.1016/j.cattod.2004.06.132.

[9] Zhang, W. F., He, Y. L., Zhang, M. S., Yin, Z. and Chen, Q. 2000). Raman scattering study on anatase TiO_2 nanocrystals. *J. Phys. D: Appl. Phys.* 33, 8 (Apr. 2000), 912-916. DOI= http://iopscience.iop.org/0022-3727/33/8/305.

[10] Mechiakh, R., Ben Sedrine, N., Ben Naceur, J. and Chtourou, R. 2011. Elaboration and characterization of nanocrystalline TiO_2 thin films prepared by sol-gel dip-coating. *Surf. Coat. Technol.* 206, 2–3 (Oct. 2011), 243-249. DOI= http://dx.doi.org/10.1016/j.surfcoat.2011.06.053.

[11] Wang, M., Kim, E. J., Kim, S., Chung, J. S., Yoo, I., Shin, E. W., Hahn, S. H. and Park, C. 2008. Optical and structural properties of sol-gel prepared Mg ZnO alloy thin films. *Thin Solid Films* 516, 6 (Jan. 2008), 1124-1129. DOI= http://dx.doi.org/10.1016/j.tsf.2007.05.039.

[12] Habibi, M.H., Talebian, N. and Choi, J.H. 2007. The effect of annealing on photocatalytic properties of nanostructured titanium dioxide thin films. *Dyes Pigments* 73, 1, 103-110. DOI= http://dx.doi.org/10.1016/j.dyepig.2005.10.016.

[13] Tien, P. K. 1971. Light waves in thin films and integrated optics. *Appl. Opt.* 10, 11, 2395-2413. DOI= http://dx.doi.org/10.1364/AO.10.002395.

[14] Ulrich, R. and Torge, R. 1973. Measurement of thin film parameters with a prism coupler. *Appl. Opt.* 12, 12, 2901-2908. DOI= http://dx.doi.org/10.1364/AO.12.002901.

Nano-Sized Zero Valent Iron and Covalent Organic Polymer Composites for Azo Dye Remediation

Paul Douglas Mines[1,2,a], Jeehye Byun[2,b], Y. Hwang[1], H. Patel[2], H. Andersen[1], and Cafer T. Yavuz[2,c,*]

[1]Department of Environmental Engineering, Technical University of Denmark, Miljøvej, B113, DK-2800, Kongens Lyngby, Denmark

[2]Graduate School of EEWS, Korea Advanced Institute of Science and Technology, 291 Daehak-ro, Yuseong-gu, Daejeon 305-701, Korea

[a]padm@env.dtu.dk, [b]jhbyun@kaist.ac.kr, [c]yavuz@kaist.ac.kr

Keywords: nZVI, covalent organic polymer, azo dyes, naphthol blue black, groundwater contaminant, dye decolorization.

Abstract. Having superior reductive properties and large surface areas, nanosized zero valent iron (nZVI) is ideal for the degradation of chemicals such as azo dyes and trichloroethylene (TCE). However, immobilization of nZVI is a key parameter in its effectiveness as a chemical degradation agent. In this study, the effect of various covalent organic polymers (COPs) as effective supporting materials for nZVI for optimal pollutant degradation was assessed. These COPs demonstrate promising results for the ability to adsorb and remove carbon dioxide, yielding the notion that they are capable of groundwater contaminant removal. Composites of nZVI impregnated within COPs of high surface areas exhibit effective ability to degrade azo dyes, up to 95%, over a 30-minute reaction period. Dye decolorization results were designated a precursor for effectiveness of pollutant decontamination; pollutants ranging in chlorinated organics, heavy metals, and various other groundwater contaminants.

Introduction

Zero valent iron is commonly used in a variety of treatment technologies (e.g. permeable reactive barriers), though recently a heavier focus has been placed on nano-sized zero valent iron (nZVI). Having superior reductive properties and large surface areas, nZVI is ideal for the degradation of chemicals such as azo dyes and halogenated organic compounds, among others [1]. However, stabilization and immobilization of nZVI is a key parameter in its effectiveness as a chemical degradation agent for both *in-situ* and *ex-situ* applications. Most importantly, this inhibits unwanted iron oxidation from the environment and prevents particle agglomeration; but also still allows for contaminant diffusion into the composite matrix, leading to removal and degradation. In this study, the effect of various covalent organic polymers (COPs) as effective supporting materials for nZVI for optimal pollutant removal was assessed. These COPs demonstrate promising results for the ability to adsorb and remove carbon dioxide [2], yielding the notion that they are capable of adsorbing water contaminants as well. Composites of nZVI impregnated within COPs of high surface areas exhibit effective ability to decolorize azo dyes, specifically naphthol blue black, up to 96%, over a 30-minute reaction period; comparable to azo dye decolorization rates seen using pure nZVI alone [3].

Materials and Methods

Synthesization of COPs employed methods explicitly stated in previous literature, and closely related to those methods for polymers not mentioned in said literature [2,4]. Substituting COPs in place of alginate beads, impregnation and reduction of nZVI into polymers was achieved using a previous method targeting groundwater remediation [5]. In this study, five COPs, each with different core/linker groups, were utilized for synthesis.

The reactivity of COP-nZVI composites was determined by azo dye degradation via UV-Vis spectrometry. Naphthol blue black was applied as the representative azo dye in this study, and the

peak absorbance of 618 nm was monitored over a 30-minute period. Initial dye concentration was 60µM with a peak absorbance (λ_{max}=618nm) of 3.14±0.07.

Results and Conclusions

Using transmission electron microscopy (TEM), dimensional extrapolation of composite widths were on average approximately 6 nm, with extremes at 2.5 nm and 24 nm. Composite lengths exhibited much more variance, and although the average was approximately 110 nm, many lengths were observed as low as 50-70 nm and as high as 260-280 nm ranges. However, individual composite strands exhibited a tendency to coalesce into porous masses with diameters as large as 10 µm. This phenomenon makes these composites ideal for use in a sand filtration column for water treatment applications.

BET surface areas of the composites were as small as 5.9 m^2/g using COP61, and as large as 332 m^2/g using COP19. Using water miscible COPs, dye removal rates were as high as 95% and 96% in COPs 1 and 19, respectively. Removal efficiency was determined to be a function of the BET surface area, as well as individual properties of the core/linker molecular make-up of each COP, specifically their wettability in aqueous solution. The dye adsorption into the COP matrix and subsequent degradation by impregnated nZVI combines to form a synergistic effect. This translates well for treatment of many groundwater pollutants, including halogenated organics (e.g. TCE), due to the similar chemical reduction mechanism involved.

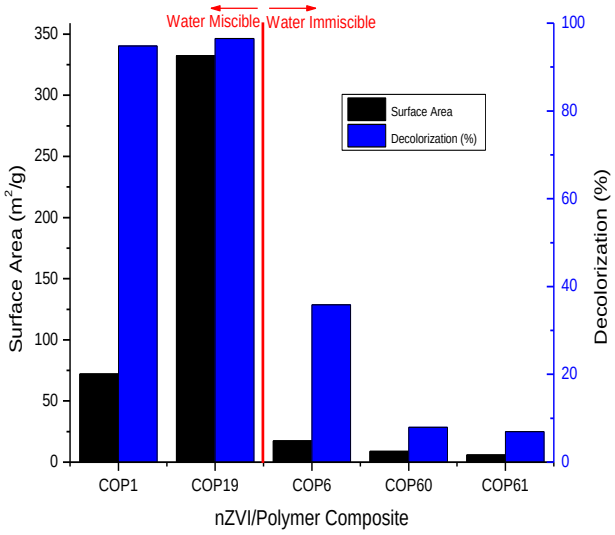

Figure 1: Relationship of composite surface area with decolorization of naphthol blue black ability, in terms of removal percentage, organized by water miscibility.

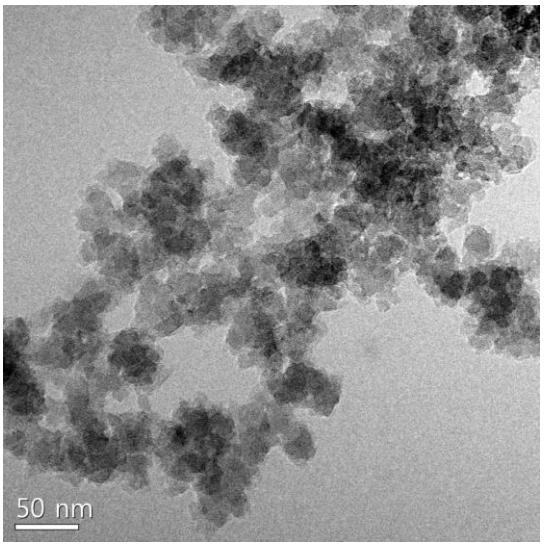

Figure 2: TEM image of the COP19/nZVI composite at a 50 nm resolution scale. Impregnation of iron is observed in the dark inner areas of the polymer matrix

References

[1] R.A. Crane, T.B. Scott, Journal of Hazardous Materials 211–212 (2012) 112-125.

[2] H.A. Patel, F. Karadas, A. Canlier, J. Park, E. Deniz, Y. Jung, M. Atilhan, C.T. Yavuz, Journal of Materials Chemistry 22 (2012) 8431-8437.

[3] S. Nam, P.G. Tratnyek, Water Research 34 (2000) 1837-1845.

[4] H.A. Patel, F. Karadas, J. Byun, J. Park, E. Deniz, A. Canlier, Y. Jung, M. Atilhan, C.T. Yavuz, Advanced Functional Materials 23 (2013) 2270-2276.

[5] H. Kim, H.-J. Hong, J. Jung, S.-H. Kim, J.-W. Yang, Journal of Hazardous Materials 176 (2010) 1038-1043.

Theoretical Study of the Optical Properties of $Si_{1-x}Ge_x$ alloy and, Si/Ge and Ge/Si core/shell Nanoparticles

H. Jdidi and A. Chehaidar

ABSTRACT

The scattering and absorption properties of light by individual silicon-germanium spherical nanoparticles are analyzed theoretically in the framework of Lorenz-Mie formalism. We have examined homogeneous $Si_{1-x}Ge_x$ alloy, as well as Si/Ge and Ge/Si core/shell nanoparticles, addressing the influence of particle-diameter and Ge composition on their scattering and absorption efficiencies. Our simulation clearly shows that the Ge composition provides and additional degree of freedom to tailor the optical response of these nanostructures. The optical properties of $Si_{1-x}Ge_x$ alloy nanoparticles are found to evolve smoothly from those of pure Si to those of pure Ge nanoparticles by increasing *x*, as expected. The Si/Ge and Ge/Si core/shell nanoparticles show a completely different behavior from that of the alloy nanoparticles as regards the scattering and absorption of light. The former shows a Ge-like behavior irrespective of the Ge-shell thickness, while the later shows a Si-like behavior for shell thickness strictly greater than the nanoparticle mid-radius, and Ge-like one elsewhere.

Keywords

Optical properties, silicon-germanium, nanoparticle, Mie theory.

1. INTRODUCTION

Semiconductor nanostructures have received significant attention in recent years due to their size-tunable electronic and optical properties. Particular interest is devoted to silicon and germanium based nanoparticles as potential candidates for new optoelectronic, photovoltaic and bioimaging/sensing devices [1-3] due to their exceptional ability to emit or absorb light, from ultraviolet to infrared.

The occurrence of morphology-dependent optical resonances in nanostructures, so-called Mie resonances [4], has paved the way for intensive basic researches. These aim at an efficient control of light-matter interaction at the nanoscale dimensions, and therefore, a better design of performant light-scattering and/or -absorption based devices. Silicon nanoparticles have practically monopolized these fundamental investigations, although there is a growing interest for synthesis, functionalization and characterization of pure Ge as well as Si-Ge alloy and core/shell nanoparticles [5-7].

The present wok is devoted to a detailed theoretical analysis of the optical properties of silicon-germanium based spherical nanoparticles. Using the analytical Lorenz-Mie theory, we computed the absorption and the scattering efficiencies of light by homogenous $Si_{1-x}Ge_x$ alloy as well as Si/Ge and Ge/Si core/shell nanoparticles. A particular attention is devoted to the influence of nanoparticle diameter and alloy composition on their scattering and absorption cross-sections.

2. THEORETICAL APPROACH

The problem consists in a single dielectric sphere of radius *R* placed in vacuum and illuminated by a plane wave propagating in the *z* direction, as illustrated schematically in Fig. 1. The optical response of the nanoparticle is characterized by two dimensionless quantities so-called scattering efficiency Q_{sca} and absorption efficiency Q_{abs}.

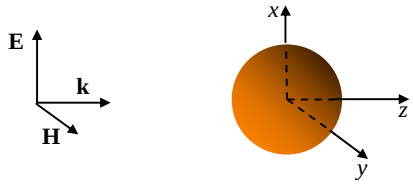

Figure. 1

The problem consists on the resolution of the Helmholtz equations for the electric **E** and the magnetic **H** fields of the electromagnetic wave of wavevector **k**:

$$\begin{cases} \Delta\mathbf{E} + k^2\mathbf{E} = \mathbf{0} \\ \Delta\mathbf{H} + k^2\mathbf{H} = \mathbf{0} \end{cases} \quad (1)$$

In our problem, three electromagnetic fields are required: the incident $\{\mathbf{E}_{inc},\mathbf{H}_{inc}\}$ and scattered $\{\mathbf{E}_{sca},\mathbf{H}_{sca}\}$ fields in the surrounding medium, and the internal $\{\mathbf{E}_{int},\mathbf{H}_{int}\}$ field inside the particle. In the case of core/shell particle, the internal field is divided into a field $\{\mathbf{E}_{int},\mathbf{H}_{int}\}$ in the core and a field $\{\mathbf{E}_{int},\mathbf{H}_{int}\}$ in the shell. These electromagnetic fields must satisfy the boundary conditions requiring continuity of the tangential components of the electric fields as well as the magnetic fields at the core/shell and the shell/air interfaces.

In the framework of Lorenz-Mie theory, rigorous solutions to the Helmholtz equations [Eqs. (1)] can be obtained via expansion of the electromagnetic fields in vector spherical harmonics **M** and **N** [10]. For the scattered fields, in particular, we write:

$$\begin{cases} \mathbf{E}_{sca} = \sum_{n=1}^{\infty} i^n \frac{2n+1}{n(n+1)} E_0 \left(i a_n \mathbf{N}_{e1n}^{(3)} - b_n \mathbf{M}_{o1n}^{(3)} \right) \\ \mathbf{H}_{sca} = \frac{k}{\omega\mu_0} \sum_{n=1}^{\infty} i^n \frac{2n+1}{n(n+1)} E_0 \left(i b_n \mathbf{N}_{o1n}^{(3)} + a_n \mathbf{M}_{e1n}^{(3)} \right) \end{cases} \quad (2)$$

with E_0 the incident field amplitude, and *k* the wavenumber in the surrounding medium; the superscript (3) is appended to vector spherical harmonics for which the radial dependence of the generating functions is specified by the spherical Bessel function $h_n^{(1)}$. For the expansion coefficients a_n and b_n, we have found:

$$\begin{cases} a_n = \frac{\psi_n(y)(\widetilde{D}_n y + m_2 n) - m_2 y \psi_{n-1}(y)}{\xi_n(y)(\widetilde{D}_n y + m_2 n) - m_2 y \xi_{n-1}(y)} \\ b_n = \frac{\psi_n(y)(\widetilde{G}_n m_2 y + n) - y \psi_{n-1}(y)}{\xi_n(y)(\widetilde{G}_n m_2 y + n) - y \xi_{n-1}(y)} \end{cases} \quad (3)$$

where:

$$\begin{cases} \tilde{D}_n = \frac{\mathrm{D_n(m_2y)\psi_n(m_2y)-A_n\chi_n'(m_2y)}}{\mathrm{\psi_n(m_2y)-A_n\chi_n(m_2y)}} \\ \tilde{G}_n = \frac{\mathrm{D_n(m_2y)\psi_n(m_2y)-B_n\chi_n'(m_2y)}}{\mathrm{\psi_n(m_2y)-B_n\chi_n(m_2y)}} \\ \mathrm{A_n} = \frac{\mathrm{m_2\psi_n(m_2x)D_n(m_1x)-m_1\psi_n(m_2x)D_n(m_2x)}}{\mathrm{m_2\chi_n(m_2x)D_n(m_1x)-m_1\chi_n'(m_2x)}} \\ \mathrm{B_n} = \frac{\mathrm{m_2\psi_n(m_2x)D_n(m_2x)-m_1\psi_n(m_2x)D_n(m_1x)}}{\mathrm{m_2\chi_n'(m_2x)-m_1\chi_n(m_2x)D_n(m_1x)}} \end{cases} \quad (4)$$

with $x = ka$ and $y = kb$ are the so-called size parameters of the core and the shell, respectively; $m_1 = N_1/N$ and $m_2 = N_2/N$ are the complex refractive indices of the core and the shell, respectively, relative to the host medium (N); $\Psi_n(z) = z\, j_n(z)$, $\chi_n(z) = -zy_n(z)$ and $\xi_n(\mathrm{z}) = \mathrm{z}\, h_n^{(1)}(z)$ are the spherical Ricatti-Bessel functions; and $\mathrm{D_n(z) = \Psi_n'(z)/\psi_n(z)}$ is the logarithmic derivative.

For a homogeneous sphere one may find the expressions of the scattered fields from the above equations. Indeed, just take $m_2 = m_1 = m$, then $\mathrm{A_n = B_n = 0}$, and consequently the coefficients (3) reduce to those of a simple homogeneous sphere of radius b.

The efficiency of a nanoparticle to scatter and to absorb incident light can be expressed by the scattering efficiency Q_{sca} and absorption efficiency Q_{abs}. For both homogeneous sphere and core/shell sphere, these efficiencies can be expressed in terms of the scattering coefficients $\{a_n,b_n\}$ as follows:

$$\begin{cases} Q_{sca} = \frac{\sigma_{sca}}{\mathrm{G}} = \frac{2}{R^2k^2}\sum_{\mathrm{n=1}}^{\infty}(2\mathrm{n}+1)(|\mathrm{a_n}|^2 + |\mathrm{b_n}|^2) \\ Q_{abs} = \frac{\sigma_{abs}}{\mathrm{G}} = \frac{2}{R^2k^2}\sum_{\mathrm{n=1}}^{\infty}(2\mathrm{n}+1)\,\Re\mathrm{e}(\mathrm{a_n}+\mathrm{b_n}) - Q_{sca} \end{cases} \quad (5)$$

where $G = \pi b^2$ is the geometrical cross-section of the sphere, σ_{sca} and σ_{abs} are the scattering and absorption cross-sections, respectively.

3. RESULTS and discussions:

The formalism described above is used to compute optical response of single homogeneous $Si_{1-x}Ge_x$ alloy and Si/Ge and Ge/Si core/shell nanoparticles in air. Effects such as strain as well as quantum confinement that may affect the optical properties have been neglected. We thus used the complex refractive indices of crystalline $Si_{1-x}Ge_x$ bulk compounds [8,9]. The spherical Bessel functions and Ricatti-Bessel functions are computed numerically following exactly the strategy adopted by Bohren and Hufman [4].

3.1. $Si_{1-x}Ge_x$ alloy nanoparticle:

The scattering and absorption efficiencies of a single $Si_{1-x}Ge_x$ alloy nanoparticle are plotted in two-dimensional color maps as a function of the particle diameter D, the vacuum wavelength λ and for different alloy compositions x; the results are shown in Fig. 2. Our calculations are given for λ in the 200-1500 nm range, and for particle diameters in the 5 - 500 nm range. Given the exciton Bohr radii in bulk silicon and germanium (4.7 and 17.7 nm, respectively), quantum confinement effects are expected to play a significant role when the diameters of nanoparticles are close to these characteristic length scales. Even if these effects have been neglected in our calculations, our results allow us to understand the influence of the nanoparticle morphology even below this limit.

First of all, we notice that our calculations reproduce very well the computed scattering efficiencies of a single Si nanosphere in air,

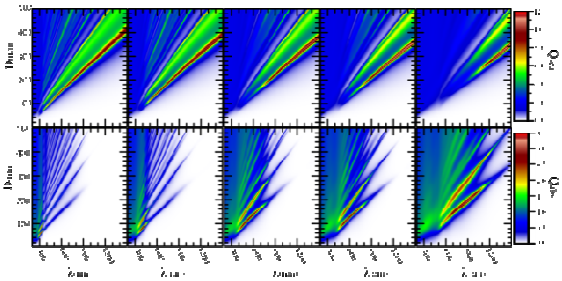

Figure. 2

reported recently Spinelli et *al*. [10]. From the Q_{sca} and Q_{abs} color maps shown in Fig. 2, we deduce that the scattering and absorption of light by $Si_{1-x}Ge_x$ alloy nanoparticles manifest themselves in the considered spectral range only for diameters greater than 40 nm and 20 nm, respectively. These particle-size thresholds are found to be insensitive to the alloy composition x. On the other hand, above the size threshold, the nanoparticle scatters light in a finite spectral range which cuts at a wavelength that redshifts quasi-linearly with increasing the nanoparticle size. This wavelength cutoff is found to be nearly insensitive to the alloy composition x. The absorption spectral range of $Si_{1-x}Ge_x$ alloy nanoparticles is also finite, and its extent depends on the particle size as well as the alloy composition x; but, it can never go beyond the spectral range where the extinction coefficient (κ) of the nanoparticle material is non-zero.

A detailed observation of Q_{abs} and Q_{sca} color maps highlights a characteristic wavelength, which we will call wavelength threshold, from which appear strong optical resonances distributed on a complex branched structure. The resonances apparent above this wavelength threshold are the so-called Mie resonances. On each branch, λ grows almost linearly with increasing the particle size; a red shift of the Mie resonances is thus observed as the particle size increases, as expected for geometrical resonances in a cavity. Figure 2 shows that the wavelength threshold, shown as white vertical line, is redshifted with increasing composition x of germanium. More quantitatively, it shifts from about 380 nm in pure Si to about 620 nm in pure Ge nanoparticles. Referring to the extinction coefficient curves of bulk $Si_{1-x}Ge_x$ crystals [9], we infer that the wavelength threshold is the wavelength where κ = 1.

Below the wavelength threshold (left of vertical white line in Fig. 2), the optical properties of the $Si_{1-x}Ge_x$ alloy nanoparticles are dominated by their intrinsic absorption due to direct electronic transitions from the valence bands to the conduction bands. These yield very short penetration depths in the nanoparticle and thus prevent the occurrence of Mie resonances. As a consequence, Mie resonances are practically absent and therefore the absorption efficiency seems almost uniform below the wavelength threshold. This region stretches towards the red when increasing the alloy composition x. This is consistent with the expansion towards the red of the high absorption region (κ > 1) of $Si_{1-x}Ge_x$ bulk crystals with increasing x. Above the wavelength threshold, the intrinsic absorption of the material is negligible and the optical properties of the alloy nanoparticles are dominated by Mie resonances. The corresponding resonance branches span a spectral range that intersects the large wavelength side to a wavelength at which the extinction coefficient κ vanishes. This wavelength cutoff is found to be independent on the nanoparticle size; it is thus intrinsic to the nanoparticle material. As a matter of fact, only two absorption branches are the most significant. They manifest themselves on a

limited nanoparticle-size range. The onset of this interval as well as its length evolve with the alloy composition *x*; the former shifts from 40 nm for pure Si to 100 nm for pure Ge; the later increases from 80 nm for $x = 0$ to 300 nm for $x = 1$.

As mentioned above, scattering resonances manifest themselves beyond the wavelength threshold, as are the absorption resonances. But the most significant ones appear actually further, just beyond the spectral range over which the absorption is more significant, and persist throughout the remaining spectral range. With increasing the alloy composition *x*, the onsets of these scattering resonance branches redshift, and simultaneously shift toward greater particle sizes. Accordingly, the silicon-germanium alloy nanoparticles scatter less efficiently UV-Vis light than the pure Si nanoparticles. It is quite the contrary as regards as absorption.

3.2. Si/Ge and Ge/Si core/shell nanoparticles:

The scattering and absorption efficiencies of single Si/Ge and Ge/Si core/shell nanoparticles in air are plotted in two-dimensional color maps as a function of the outer diameter *D*, the vacuum wavelength λ, and for different shell thickness fractions t_f $(= (b-a)/a)$. The results for t_f = 0.25, 0.5 and 0.75 are shown in Figs. 3 and 4, respectively. Results for pure silicon and pure germanium nanoparticles are also presented here for comparison.

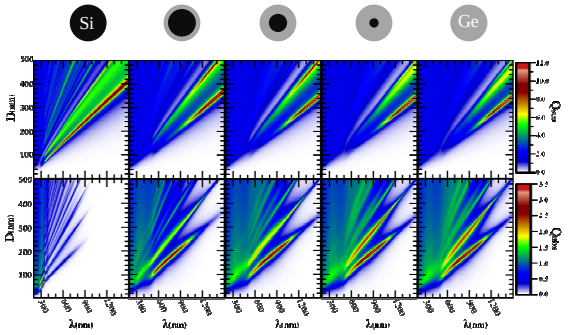

Figure. 3

The scattering and absorption of light by Si/Ge and Ge/Si nanoparticles manifest themselves in the considered spectral range for particle diameters greater than 40 nm and 20 nm, respectively, just as in the case of $Si_{1-x}Ge_x$ alloy nanoparticles.

The 2D maps are characterized by branches having relatively high absorption or scattering efficiencies. These branches correspond to (λ, *D*) couples satisfying the Mie resonance conditions.

It should be emphasized that the overall aspect of the color maps corresponding to Si/Ge core/shell nanoparticles is significantly different from that of pure silicon, even with an ultrathin shell. By cons, it is more like that of pure Ge nanoparticle. Two main branches dominate the scattering efficiency as well as the absorption efficiency maps of Si/Ge nanoparticles. The Mie resonances redshift by increasing the particle diameter, but are nearly insensitive to the variation of the shell thickness.

Contrary to the case of Si/Ge core/shell nanoparticle, the scattering as well as absorption efficiencies of Ge/Si core/shell nanoparticle depend on the shell thickness. The overall aspect of the corresponding 2D maps is getting closer and closer to that of pure Si nanoparticle by increasing the shell thickness. In the other sense, the overall aspect of Q_{sca} maps of Ge/Si nanoparticles tends

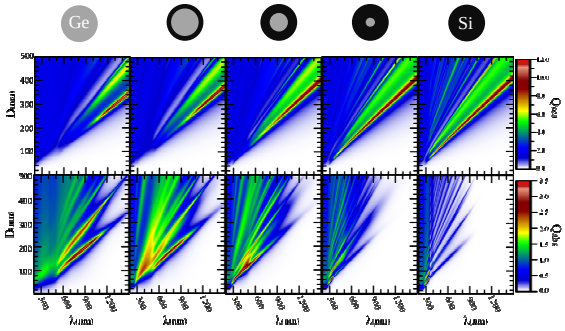

Figure. 4

toward that of pure Ge nanoparticle. This is not the case, however, for Q_{abs} maps; a neat difference persists even with an ultrathin shell. Absorption resonances manifest themselves beyond $\lambda = 300\ nm$ and, moreover, for nanoparticle diameters greater than 50 nm, whatever the shell thickness. It should be noted here that these two characteristic thresholds coincide with those of pure Si nanoparticle.

4. CONCLUSION

The present work has focused on the analysis by numerical modeling technique of the scattering and absorption efficiencies of light by single $Si_{1-x}Ge_x$ alloy, Si/Ge and Ge/Si core/shell spherical nanoparticles in air. Our simulation shows that Mie resonances occur in these nanoparticles and their characteristics depend on the size, the alloy composition and also the structure of the silicon-germanium nanoparticle. The optical properties of $Si_{1-x}Ge_x$ alloy nanoparticles evolve smoothly from those of pure Si to those of pure Ge nanoparticles by increasing *x*, as expected. The Si/Ge and Ge/Si core/shell nanoparticles show a completely different behavior from that of the alloy nanoparticles as regards the scattering and absorption of light. The former shows a Ge-like behavior irrespective of the Ge-shell thickness, while the later shows a Si-like behavior for shell thickness strictly greater than the nanoparticle mid-radius, and Ge-like one elsewhere. This preliminary analysis shows that enhancement of scattering and/or absorption of light by silicon-germanium nanoparticles can be tailored, depending on the intended application, by judiciously choosing the particle size, its germanium composition and also its structure. The optical properties of too small silicon-germanium nanoparticles, for which the quantum confinement occurs, should be reviewed.

5. REFERENCES

[1] Liu, C. –Y., Holman, Z. C., and Kortshagen, U. R. 2009. Hybrid solar cells from P3HT and silicon nanocrystals, *NanoLett.* 9 (2009) 449-452. doi: 10.1021/nl8034338

[2] Erogbogbo, F., Yong, K. –T., Roy, I., Hu, R., Law, W. –C., Zhao, W., Ding, H., Wu, F., Kumar, R., Swihart, M. T., and Prasad, P. N. 2011. In vivo targeted cancer imaging, sentinel lymph node mapping and multi-channel imaging with biocompatible silicon nanocrystals, *ACS Nano* 5 (2011), 413-423. doi: 10.1021/nn1018945

[3] Cosentino, S., Mirabella, S., Liu, P., Le, S. T., Miritello, M., Lee, S., Crupi, I., Nicotra, G., Spinella, C., Paine, D., Terrasi, A., Zaslavsky, A., Pacifici, D. 2013. *Role of Ge nanoclusters in the performance of photodetectors compatible with Si*

technology, *Thin Sol. Films* 548, (2013) 551-555. http://dx.doi.org/10.1016/j.tsf.2013.09.028

[4] Bohren, C. F. and Huffman, D. R. 1998. *Absorption and Scattering of Light by Small Particles* (John Wiley & Sons, Inc., New York, 1998).

[5] Holman, Z. C., and Kortshagen, U. R. 2012, Absolute absorption cross sections of ligand-free colloidal germanium nanocrystals, *Appl. Phys. Lett.* 100 (2012) 133108-133111. http://dx.doi.org/10.1063/1.3698091

[6] Pi, X. D., and Kortshangen, U. 2009. Nonthermal plasma synthesized freestanding silicon-germanium alloy nanocrystals, *Nanotech.* 20 (2009) 295602-295607. doi:10.1088/0957-4484/20/29/295602

[7] Erogbogbo, F., Liu, T., Ramadurai, N., Tuccarione, P., Lai, L., Swihart, M. T., and Prasad, P. N. 2011. Creating ligand-free silicon germanium alloy nanocrystal inks, *NanoLett.* 5 (2011) 7950-7959. doi: 10.1021/nn2023304

[8] Humlícek, J. 2000, In *Properties of Silicon, Germanium and SiGe:Carbon*, EMIS Datareviews Series Vol. 24, Ed. E. Kasper and K. Lyutovich (INSPEC London, UK, 2000).

[9] Kallel, H., Arbouet, A., Benassayag, G., Chehaidar, A., Potié, A., Salem, B., Baron, T., and Paillard, V. 2012. Tunable enhancement of light absorption and scattering in $S_{i1-x}G_{ex}$ nanowires, *Phys. Rev. B* 80 (2012), 085318-085325. http://dx.doi.org/10.1103/PhysRevB.86.085318

[10] Spinelli, P., Verschuuren, M. A., and Polman, A. 2012. Broadband omnidirectional antireflection coating based on subwavelength surface Mie resonators, *Nature Comm.* 3 (2012) 692-695. doi: 10.1038/ncomms1691

Calorimetric Study and optimization of crystallinity rate for the composite: isotactic polypropylene/micro-talc (iPP/µ-talc)

A. Makhlouf[(1)], D. Frihi[(1)], H. Satha[(1)], A. Layachi[(1)], S. Gherib[(1)] & R. Séguéla[(2)]
(1) :Silicates, Polymers and Nano- Composites laboratory (LSPN)

(2) : MATEIS Laboratory, Insa de Lyon, France

8 May 45 Guelma, University.

Abstract: The aim of our work is to show the importance of developing a new reinforcing filler of polyolefins namely isotactic polypropylene (iPP), widely used in our daily life and to optimize the crystallinity rate of the composites prepared at different filler rate depending on the cooling speed. The company Mutlitibase (France) has developed a talc filler of submicron size (intermediate between the nano-filler and conventional filler) to reinforce an organic matrix of polypropylene in order to solve the problem raised by the exfoliation during the incorporation of filler nanoscopic size in polyolefins (PE and iPP).

To demonstrate the efficiency of choice of this mineral filler (µ-talc) which will be compared to conventional fillers like (standard talc) and ($CaCO_3$), we have operated at a microscopic and structural characterization by different techniques : thermogravimetric analysis (TGA) , differential scanning calorimetry (DSC) , thermal deformation (HDT) , XRD , ...

Then the samples have been prepared by the isotactic polypropylene reinforced by micro-talc with a filler rate going from 3 % to 30% by mass. For comparative purposes we have studied other composites with standard talc and calcium carbonate as fillers.

As part of the optimization of crystallinity rate, DSC tests were carried out using a full factorial design (7^2 = 49 trials). The results were statistically processed by analysis of variance (ANOVA) to reach mathematical models which will be used for predicting the of crystallinity rate in function of the cooling speed and the filler rate. The contour graphs were used to determine the effect of each parameter on the response (the crystallinity rate).

This characterization study has allowed us to prove that the incorporation of this new filler of talc into the iPP matrix composite has improved the thermal behavior by distancing, for example, the degradation of the composites to the high temperatures, and that the crystallinity rate is inversely proportional to the cooling speed.

Key words: Polypropylene, composite, DSC, micro-talc, ANOVA**,** crystallinity rate

1. Introduction

Isotactic polypropylene (iPP) filled with black carbon, CaCO3 or glass fibers has been the subject of research and numerous publications, works on that reinforced with the talc are less important [1-8], but those on composites (iPP/µ- talc) are very rare. The role of fillers is multiple: it can be cheaply fill a volume, if the filler is much less expensive than the polymer [1,2,3], but also to modify the macroscopic properties. In this context, Composite materials produced by dispersing inorganic nano-fillers in polymeric compounds are recently emerged new materials [21]. With the development and application of surface treatment techniques and, particularly, techniques to obtain ultra-fine filler particles [12,13], the filling modification of polymeric compounds has developed from the simple reinforcement at the initial stage to a new stage of both reinforcement and toughening [9], and from enhancing only mechanical properties to the development of functional polymeric materials [14,15]. However, studies on the effect of the addition of the talc particles in the amorphous matrix of the polymeric products and, in particular, on properties and cellular structure of foam products [17,18], as well as on the corresponding extrusion equipment and conditions are scarce in literature [21,18]. These problems were investigated in the present study. The inclusion of these fillers in a matrix of isotactic polypropylene aims to acquire mechanical properties approaching those of nano-fillers [2,7,14] but with an intermediate size between the conventional and the nano-composites. This new filler called µ-talc (micro talc) has a shape factor four times more than that of the conventional talc and a specific surface area three times greater [2]. Recently, with the rapid development of computer technology and computational methods [21], many engineering problems have found satisfying numerical solution by computer using discrete numerical compotation method such as analysis of variance (ANOVA) surface plot [22,23,24], outline plot that we used to optimize the onset, offset, and the crystallinity rate of the composite studied.

2. Materials and experimental techniques

2.1. Materials: This study focuses on isotactic polypropylene (iPP) provided by Multibase company; molecular weight: Mw = 380 000. Fillers studied are

platelet of Talc with micron size. The filler rate varies from 03% to 30% by weight of µ-talc. For comparative purposes the pure polypropylene, 03% talc and 20% classic talc (larger size), and composites iPP reinforced with calcium carbonate and glass fibers, have also been studied.

Table 1: Geometric characteristics of the fillers

	µ-Talc	Industrial talc
Form factor	5.5	1.3
Specific surface area (m^2/g)	17	6.2

2.2 Characterization Techniques:

2.2.1. Thermogravimetric analysis (TGA)

Most of the physical, chemical or physico-chemical phenomena are characterized by variation of reactant samples mass when these samples were subjected to various environmental conditions, such as, for example, temperature change [10]. Thermogravimetry is thus based on a weighing of the sample mass. The thermobalance can carry a solid at determined temperatures by recording the mass variations acting in time. It has three variables, the mass (m), the time (t) and temperature (T). Usually, curves should be drawn either at constant temperature or by varying the temperature linearly over time (which is the case here). This technique should allow to determine precisely the filling rate of talc contained in the samples (iPP/µ-talc), the latter being required to calculate the crystallinity rate by DSC [2,4,19]. Indeed, these are the only components that remain after high temperature passage. Thermic degradation tests were performed on a Shimadzu DTG.60 apparatus in the temperature range (25–650) °C at a heating speed of 10 °C / min under nitrogen. The thermic degradation temperature of isotactic PP (TD) is determined from the minimum of the first derivative of the curve.

$$m=f(T) \qquad (1)$$

2.2.2. Differential scanning calorimetry DSC

DSC is a technique used to study the polymer transitions (glass transition, melting and crystallization) when these latters are heated or cooled from the molten state [11]. The experimental device used in this work is a thermic analysis machine: DSC (Differential Scanning Calorimetry) Type Setaram, LABSYS model evo, allows TGA and TGA/DTA or DSC simultaneous also measures of Cp on range of temperature of the ambient at 1600 ° C. The measurement of the specific heat capacity at constant pressure Cp depending on the temperature characteristic of the phase transformations affecting the sample, in particular, the fusion of the crystalline parts of a semi- crystalline polymer (or their cooling crystallization from the molten state) Cp (T) then has a peak associated to the exchanged enthalpy during the processing and for determining characteristic quantities of the microstructure : the crystallinity rate and the thickness of the crystalline lamellae. The crystallinity rate (Xc) is calculated as the ratio of the enthalpy of fusion of the studied material melting enthalpy of a pure crystalline sample. (Xc) is calculated by the following formula:

$$X_c = \frac{\Delta H_f}{\Delta H_f^0} \qquad (2)$$

Where: ΔH_f is the specific enthalpy of fusion of the polymer in question. And ΔH_f^0 enthalpy of fusion of 100 % crystalline polymer to the thermodynamic equilibrium temperature. When the polymer is charged, its fusion enthalpy must be corrected by a factor:

$\frac{1}{1-\emptyset}$ Where ¤ is the mass ratio of the filler.

2.2.3. X-ray diffraction at wide angles (WAXS)

The technique of X-rays diffraction at large angles (WAXS) is used to characterize different crystal parts present in the investigated polymers. Diffraction occurs when the Bragg condition on the angle of incidence θ of the X -rays beam is verified:

$$2 d_{hkl} \sin^{-} = n^{a} \qquad (3)$$

With λ the wavelength of the monochromatic beam (1.54 Å), n the order number of dhkl and spacing of reticular plans belonging to the same family. If we study the angular distribution of the reflected signal, we obtain a set of intensity maxima corresponding to different families of crystalline plans of the constituent system. From the peak position, can be inferred nature of the crystalline phase of the semi crystalline studied polymer. A spectrum of X -rays diffraction pattern consists of the superposition of a halo caused by the amorphous phase and peaks corresponding to the crystal plans (hkl).

2.2.4. Scanning electron microscopy "SEM"

The observations were performed using a JOEL 840 unit A LGS in topographic fashion on metallic surfaces. The acceleration voltage of the electrons most suitable was found to be 20 kV.

2.2.5. Planning experiments

The test parameters, the cooling speed and the filler rate (VR, M), are considered as input parameters; the various thermic transitions, (crystallinity rate, Onset, Offset, Cp,…), represent the output parameters. The tests have been performed according to the method of planning experiments.

Approach to planning experiments

This method allows us to organize and to run experiments in an optimal way in order to obtain mathematical models of simulation of the test process [21].The experiments were conducted based on central composite design (CCD) approach of experiments (DOE). CCD is a powerful diagnosing experimental tool to study the large number of factors

[21]. Experimental research strategy consists first to determine the number of tests needed. The number of tests is as a function of the basic factors (input function) and the number of levels of variation in these factors. Several papers have reported the application of CCD to optimize the process and properties of the composites. Suresha and Sridhara [22], Ruijun and Kokta [23], and Onal and Adanur [24] have successfully employed CCD approach to determine the optimum properties and process of composites. In our study we considered the influence of two basic factors: the cooling speed and the filler rate (V_R, M) on various functions (crystallinity rate, Onset, Offset and Cp). To determine the number of necessary tests we apply the following formula:

$$N=q^k \qquad (4)$$

Where: N: number of trials, q: number of levels of variations of the basic factors and k: number of basic factors. So we have: N = 72 = 49..... (5)

The tests have been numbered from 1 to 49. The levels of the two factors of test parameters are shown in Table 2.

Table 2: Levels of both factors test parameters

Levels	Cooling speed (V_R), (°C/min)	Filling rate (M),(%)
1	2	0
2	5	3
3	10	5
4	15	7
5	20	10
6	30	20
7	40	30

3. Results and discussion

3.1. Thermogravimetric analysis (TGA)

The above figure (Figure 1) shows the beneficial side of adding fillers of microtalc, by removing the degradation of composites (iPP/µ-talc) to the high temperatures and this is gradually done with the filling rate. It represents the actual rate of microtalc support incorporated in the matrix of isotactic polypropylene.

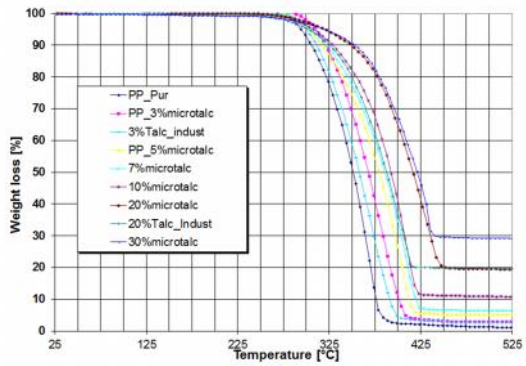

Figure 1: weight loss curves as a function of temperature for various composites compared to that of pure iPP.

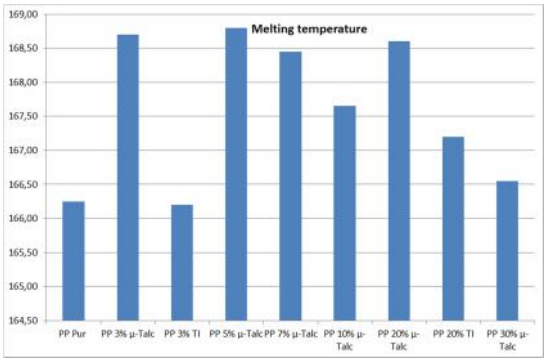

Figure 2: the variation of melting temperature of the composites according to the filler rate.

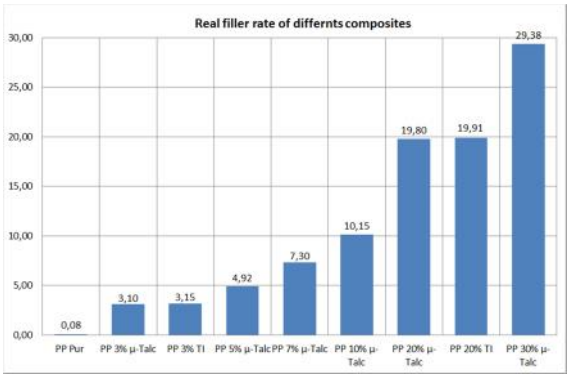

Figure 3: real filler rate of different composites

3.2. X-ray diffraction at wide angles (WAXS)

In order to see the different crystalline phases existing in the material and possibly the orientation of fillers and crystalline lamellae, diffraction tests were carried out on samples of cubic shape (2mm) of isotactic PP. No peak (reticular plan) is located for angles 16,1° and 21°corresponding to the (300) plan and (301) of the crystalline form β of iPP.

So, our studied composites are formed only with iPP in his α crystalline phase. (Zero percent β therefore or too low to be detected with this technique) which confirms the results of DSC [12,13;14]. We note that the three characteristics of reflection (110), (130) and (-131) of the crystalline phase α appear under the form of uniform rings; the only plan in this direction (X axis: thickness) which is oriented is the (040) plan. It is clear that all reflections are clearly oriented; it means that the injection gave rise to a strong texture in the direction of the injection and the width of the injection plate. In the thickness direction; the orientation is not really clear. In addition [2,20], we saw the presence of the reticular plan corresponding to the introduced filler (µ-talc) in the iPP matrix; this plan is not visible in the thickness direction, it means that the platelets of talc are (lying) in the plan of the plate and are parallel to the direction of injection. The increase of the weight fraction of reinforcement fillers gives only the decrease of diffracted intensity, linked to the X-rays absorption by the talc particles. Following these tests, it was confirmed (in addition to the SEM images) the existence of preferential orientation of the talc platelets which

are injected into the flat plate. Thus the plates are disposed alone to the thickness axis (⊥ X axis) [14].

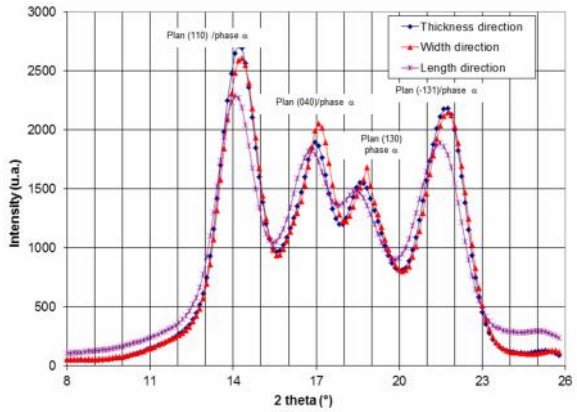

Figure 4: Diffractograms of diffraction determined in three directions for pure iPP

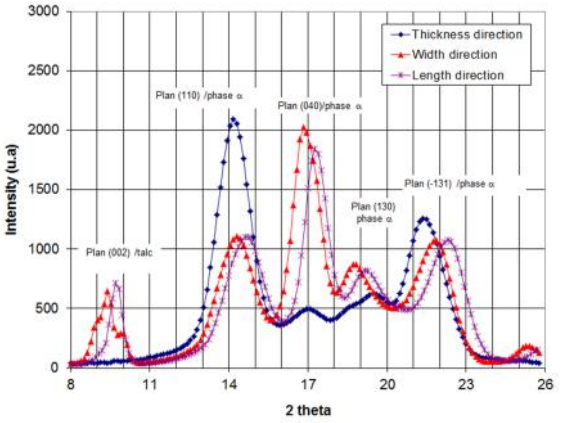

Figure 5: diffractograms of diffraction determined in three directions, (iPP / 7 % µ-talc).

The diffractogram in Figure 5 compared to that of (figure 4), shows the existence of the corresponding reticular plan in talc (002) at the angle 2θ = 9.5°. The peak amplitude and intensity of the (002) plan increases gradually as the percentage increase in mass (the effect of the form factor and specific area) which is visible on all of the diffraction patterns and the diffractograms corresponding [2,20].

3.3. Scanning electron microscopy "SEM"

As an example, we present a SEM image which was taken to the (µ - iPP/30 % µ-talc). It shows clearly that the µ - talc platelets have a fixed orientation. Following these images a micro- analysis E.D.S. has been made to check and quantify the presence location of the introduced filler.

Through SEM images, we uphold the good dispersion and orientation of renforcente fillers of the composite matrix (iPP / µ-talc)

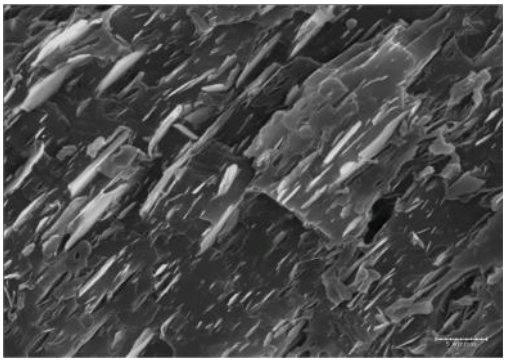

Figure 6: SEM image for (iPP/30 % µ-talc) (X2500)

3.2. Differential scanning calorimetry DSC

The results of DSC shows clearly that the cooling speed has a larger effect (heterogeneous nucleation) in the presence of micro talc (the case of iPP with 20 % microtalc in mass), because the crystallization rate goes from 71 % at 20°C/min to 82% at speed of 2°C/min.

Unlike the matrix (pure iPP), there is no visible effect of the cooling speed on the crystallization rate [4,19]. On all thermograms obtained (Figure 7) illustrates an example of thermogram for pure iPP , (iPP/10 % µ-talc) and (iPP/30 % µ-talc), we observe a single peak whose summit is between 165°C and 168°C and can be attributed to the alpha (α) crystalline form of isotactic polypropylene (iPP). No melting peak visible on the beta (β) crystalline form appears [2].

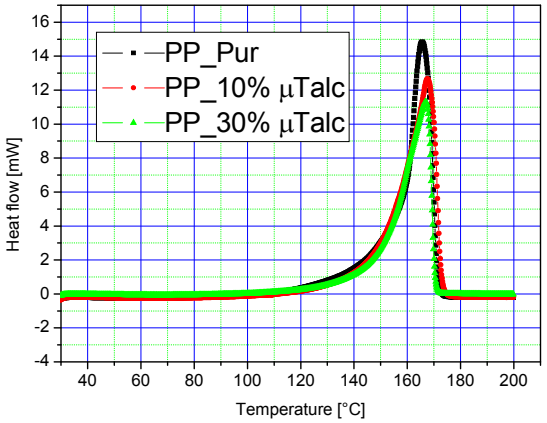

Figure 7: Example of isothermal DSC thermogram

In the presence of µ-talc, the crystallization occurs at higher temperature [4,6,10,11] that is to say to lower surfusions.

The temperature and the melting enthalpy, and the temperature and the crystallization enthalpy are determined from the curves of mass capacity at constant pressure as a function of temperature (isothermal DSC). Results of the studied composites are shown in table .3.

Table.3: Results of crystallinity rate, Onset and offset depending on the speed of cooling and filling rate (complete plan (N=72).

N°	V_R (°C/min)	M (%)	Heat flow (J/g)	Onset (°C)	Offset (°C)	X_C (%)
1	2	0	-81,37	129,86	122,72	74,03
2	2	3	-82,47	131,03	124,31	75,1
3	2	5	-83,9	132,3	125,42	76,4
4	2	7	-92,54	140,45	134,75	79,22
5	2	10	-93,33	140,9	134,93	80,6
6	2	20	-96,67	141,07	135,05	82,01
7	2	30	-98,83	142,21	136,3	83,2
8	5	0	-76,39	125,37	116,23	71,14
9	5	3	-81,2	128	118	73,78
10	5	5	-82,12	130,3	118,4	74,94
11	5	7	-87,35	132,04	118,96	78,33
12	5	10	-93,03	134,04	122,31	80,04
13	5	20	-96,25	140,52	136,33	81,17
14	5	30	-98,18	142,3	136,91	82,13
15	10	0	-71,78	121,59	108,91	70,3
16	10	3	-76,63	133,41	119,28	71,32
17	10	5	-80,2	133,86	120,02	71,89
18	10	7	-80,5	133,68	119,84	72,02
19	10	10	-80,79	133,64	119,68	73,77
20	10	20	-83,55	135,26	122,56	76,22
21	10	30	-91,65	135,13	122,76	79,19
22	15	0	-62,1	118,16	103,44	69,63
23	15	3	-68,2	133,03	119,41	70,01
24	15	5	-73,12	132,41	117,04	70,7
25	15	7	-73,97	132,48	118,07	70,91
26	15	10	-79,76	133,23	119,61	71,63
27	15	20	-80,68	134,16	120,77	73,27
28	15	30	-88,44	139,32	121,49	78,89
29	20	0	-60,98	126,35	122,75	69,14
30	20	3	-61,1	133,46	120,12	69,28
31	20	5	-63,34	132,21	119,35	69,81
32	20	7	-67,03	132,09	116,4	69,87
33	20	10	-70,1	135	120,82	70,15
34	20	20	-78,08	136,34	121,89	71,33
35	20	30	-85,8	137,1	122,82	77,91
36	30	0	-42,8	122,88	110,75	58,58
37	30	3	-47,3	133,41	120,01	63,7
38	30	5	-49,7	134,2	121,01	65,72
39	30	7	-57,7	134,61	121,23	66,66
40	30	10	-58,3	133,7	120,6	67,11
41	30	20	-61	134,76	121,13	69,19
42	30	30	-70,96	135,97	125,1	70,15
43	40	0	-41,5	120,11	106,18	57,13
44	40	3	-45,8	127,78	113,89	61,31
45	40	5	-46,6	133,33	121,32	62,2
46	40	7	-47,9	134,28	119,91	63,91
47	40	10	-48,5	134,66	121,01	64,05
48	40	20	-51,3	135,87	121,77	66,01
49	40	30	-59,9	138,55	125,82	68,17

A significant increase of the fraction mass fillers leads to a negligible increase, compared to the precision of measurements, of crystallinity rate. Indeed, for a percentage by mass with µ-talc giving from simple to doubled, the change of crystallinity rate is very weak.

3.3. Statistical Analysis

3.3.1. Optimizing of the crystallinity rate (Xc)

By applying the analysis of variance (ANOVA), we consider a confidence interval of 95% ($\alpha = 0.05$).

Table 4: Results of the analysis of variance for the crystallinity rate (Xc).

Source	Sum of Squares	df	Mean Square	F Value	p-value Prob > F
Model	1766.18	9	196.24	92.94	< 0.0001
A-V_R	103.86	1	103.86	49.19	< 0.0001
B-M	10.47	1	10.47	4.96	0.0318
AB	0.12	1	0.12	0.055	0.8155
A^2	9.95	1	9.95	4.71	0.0361
B^2	11.55	1	11.55	5.47	0.0246
A^2B	0.55	1	0.55	0.26	0.6129
AB^2	0.12	1	0.12	0.055	0.8155
A^3	0.29	1	0.29	0.14	0.7127
B^3	12.59	1	12.59	5.96	0.0192
Residual	82.34	39	2.11		
Cor Total	1848.52	48			

The results presented in Table 4 show that all the parameters with the interactions among themselves have a significant impact on the crystallinity rate , but the terms : ($V_R \times M$), ($V_R^2 \times M$), ($V_R \times M^2$), and (M^3) values as the probability P is greater than 0.05 . It was noted that the cooling speed (V_R) is the most influential factor because its contribution is 49.19 %.

Generalized model: The model describing the variation of the crystallinity rate as a function of all factors and interactions is defined as follows:

Crystallinity rate (Xc):

$$\mathbf{Xc} = 74.94984 - 0.5649\ \mathbf{V_R} + 0.86750 \times \mathbf{M} - 2.16564 \times 10^{-3}\ \mathbf{V_R} \times \mathbf{M} + 6.02281 \times 10^{-3} \times \mathbf{V_R^2} - 0.039787 \times \mathbf{M^2} + 7.68736 \times 10^{-5}\ \mathbf{V_R^2} \times \mathbf{M} - 4.84563 \times 10^{-5} \times \mathbf{V_R} \times \mathbf{M^2} - 5.78442 \times 10^{-5} \times \mathbf{V_R^3} + 7.64295 \times 10^{4} \times \mathbf{M^3} \quad (6).$$

Scale model

$$\mathbf{Xc} = 74.94984 - 0.5649\ \mathbf{V_R} + 0.86750 \times \mathbf{M} + 6.02281 \times 10^{-3} \times \mathbf{V_R^2} - 0.039787 \times \mathbf{M^2} - 5.78442 \times 10^{-5} \times \mathbf{V_R^3}.$$

R^2 = 90.9 %

V_R: Cooling speed (°C / min).

M: reinforcement rate (%).

Figure 8 below shows the influence area of system parameters, reinforcing rate (%) and cooling speed, on the crystallinity rate (Xc). The contour graphs allow to visualize the response surface (Xc), and also

to establish the response values and desirable operating conditions.

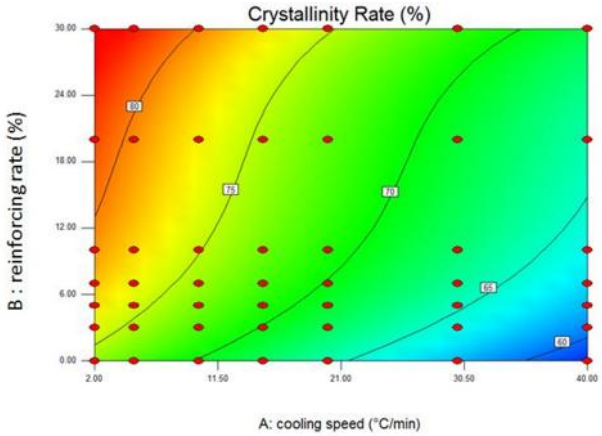

Figure 8: Contour plot of the crystallinity rate (Xc).

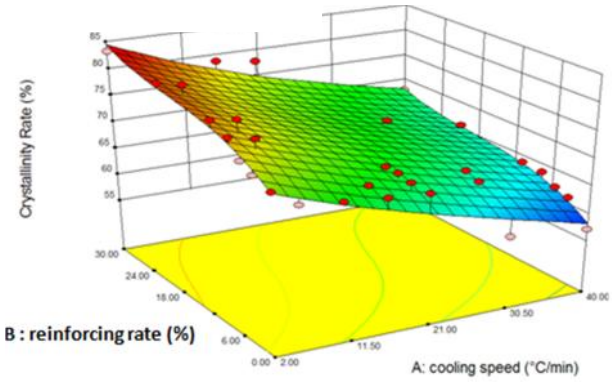

Figure 9: surface diagram of Xc according to V_R and M

The 3D presentation (Figure 9) shows that the slope of the cooling speed is greater than the relative rate of filler, which implies that this factor has a major influence on the crystallinity rate (Xc).

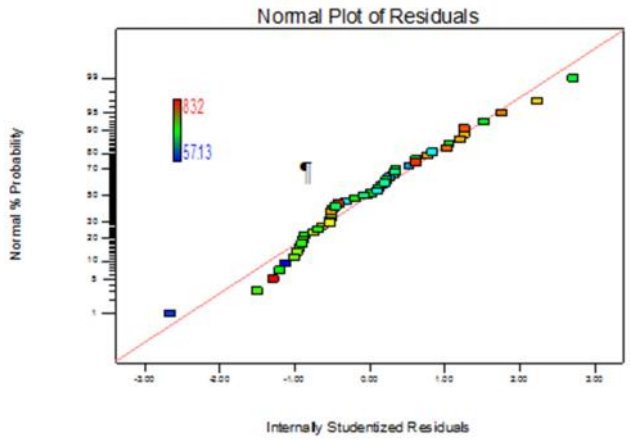

Figure 10: Normal plot of Residuals

The figure 10 revealed that the residuals fall on a straight line implying that the errors are distributed normally.

The figure 11 shows the residuals with respect to the forty nine experimental runs of Xc. The residuals do not show any obvious pattern and are distributed in both positive and negative directions. This implies that the model is adequate and there is no reason to suspect any violation of the independence or constant variance assumption

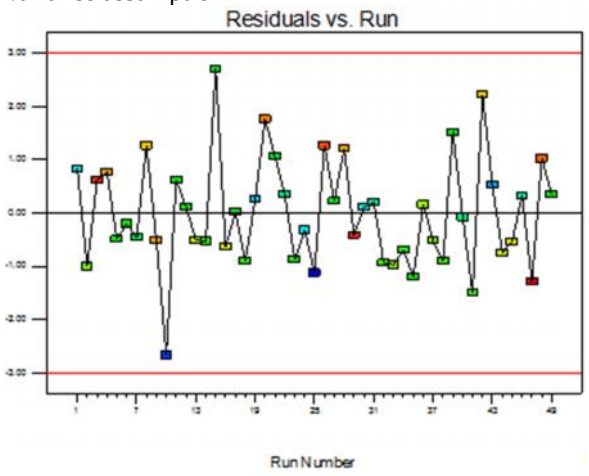

Figure 11: Residuals vs. Run

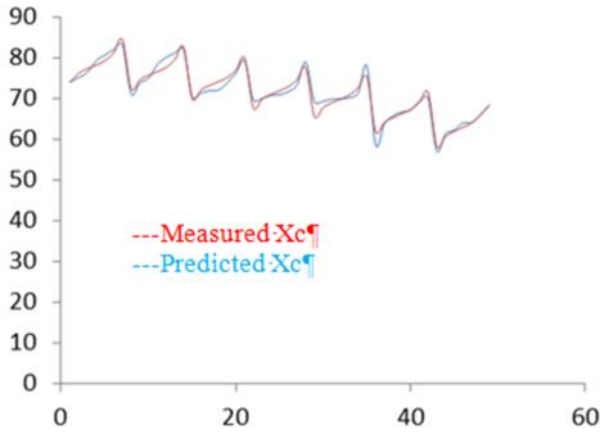

Figure 12: comparison between measured and predicted values for crystallinity rate (Xc).

4. Conclusion

In this paper, the application of variance (ANOVA) for the optimization of the crystallinity rate and micro structural characterization of iPP with different techniques have led to obtain mathematical models for the crystallinity rate. And the while investigating the influences of parameters (cooling speed reinforcement rate). Optimum values of parameters have been studied and computed. The foremost conclusions which can be drawn are as follows:

1 / TGA and tests allowed us to check the filling rate in µ-talc incorporated into the iPP matrix. It is also noted that the addition of fillers of microtalc increases the melting temperature of iPP to a level of less than 10 % load , which represents the degree of saturation of the polypropylene isotactic.

2 /From the DSC testing and WAXS , we can say that the talc relative to another filler such as glass fibers , increases the nucleation rate of the crystal phase α of the iPP. Furthermore, the crystallization occurring at lower surfusions, the effect of the

heterogeneous nucleation is more notable in the case of composite -filled with talc. It seems that the talc platelets more significantly reduce the interfacial energy and therefore would adsorb more easily the iPP on their surface. The free energy opposing the formation of a critical nucleus is thus to advantage lowered. In summary, we can say that the crystallization of iPP is favored by the presence of talc and this influence will be greater when the talc becomes finer.

3 / At low filler contents, the µ-talc technology leads to the same stiffness as a composite (iPP-CaCO3) heavily filled, so it reduces the weight and thereafter the price.

4 / The analysis of machining parameters using RSM
technique allows investigating the influence of each one on the cutting process progress outputs such as roughness and force components.

5 / Comparison of experimental and predicted values of the crystallinity rate components show that a good agreement has been achieved between them.

6 / The crystallinity rate is strongly influenced by the cooling speed.

7 / The best surface roughness was achieved at the lower feed rate and the highest cutting speed. ANOVA results show that the cooling speed and reinforcing rate, affect the crystallinity rate (Xc).

5. References:

[1] Karian HG (ed) (2003) Handbook of polypropylene and polypropylene composites, 2nd edn. Marcel Dekker, New York.

[2] D. Frihi, K. Masenelli-Varlot, G. Vigier, H. Satha ; Mixed percolating network and mechanical proprieties of PP / talc composites : effect of the talc particle size ; Journal of applied polymer science, volume 114, issue 5, december 2009.

[3] H. Naguib, C. B. Park, P. C. Lee, effect of talc content on the volume expansion ratio of PP foams, Journal of cellular Plastics Volume 39 (2003).

[4] Helson M. da Costa, Valéria D. Ramos, Marcia G. de Oliveira; degradation of polypropylene (PP) during multiple extrusions: thermal analysis, mechanical properties and analysis of variance; Polymer Testing, 26 (2007) 676-684.

[5] Guerrica-Echevarria G, Eguiazabal JI, Nazabal J. Effects of reprocessing conditions on the properties of unfilled and talc-filled polypropylene. Polym Degrad Stab. 1996;53:1-8.

[6] Bruno Rotzinger, talc-filled PP: a new concept to maintain long term heat stability; Polymer Degradation and Stability 91 (2006) 2884-2887.

[7] Woo Jin Choi, Sung Chul Kim; effects of talc orientation and non-isothermal crystallization rate on crystal orientation of polypropylene in injection-moulded polypropylene / ethylene-propylene rubber/talc blends; Polymer ,45 (2004) 2393–2401.

[8] Sarrionandia M, Lopez-Arraiza A, Aurrekoetxea J, Arostegui A. Structure and mechanical properties of a talc-filled polypropylene/ethylene-propylene-diene composite after reprocessing in the melt state. J Appl Polym Sci. 2009;114:1195-201.

[9] Oya A, Kurokawa Y, Yasuda H. Factors controlling mechanical properties of clay mineral/propylene nanocomposites. J Mater Sci, 2000, 35: 1045—1050

[10] Qiao J, Guo M, Wang L, Liu D, Zhang X, Yu L, Song W, Liu Y. Recent advances in polyolefin technology. *Polym Chem*, 2011, 2: 1611–1623

[11] Huang Y, Chen G, Yao Z, Li H, Wu Y. Non-isothermal crystallization behavior of polypropylene with nucleating agents and nano-calcium carbonate. *Eur Polym J*, 2005, 41: 2753–2760

[12] Ma J S, Qi Z N, Hu Y L. Synthesis and characterization of polypro-pylene/clay nanocomposites. J Appl Polym Sci, 2001, 82: 3611— 3617

[13] L. Százdi, A. Pozsgay, B. Pukánszky, Factors and processes influencing the reinforcing effect of layered silicates in polymer nanocomposites, European Polymer Journal, 43 (2007) 345-359.

[14] I. Hejazi, F. Sharif, H. Garmabi, Effect of material and processing parameters on mechanical properties of Polypropylene/Ethylene-Propylene-Diene-Monomer/clay nanocomposites, Materials and Design, 32 (2011) 3803-3809.

[15] J.K. Mishra, K.J. Hwang, C.S. Ha, Preparation, mechanical and rheological properties of a thermoplastic polyolefin (TPO)/organoclay nanocomposite with reference to the effect of maleic anhydride modified polypropylene as a compatibilizer, Polymer, 46 (2005) 1995-2002.

[16] S. Zhu, J. Chen, Y. Zuo, H. Li, Y. Cao, Montmorillonite/polypropylene nanocomposites: Mechanical properties, crystallization and rheological behaviours, Applied Clay Science, 52 (2011) 171-178.

[17] S. Sinha Ray, M. Okamoto, Polymer/layered silicate nanocomposites: A review from preparation to processing, Progress in Polymer Science (Oxford), 28 (2003) 1539-1641.

[18] L.M. Wang, Preparation and characterization of polypropylene/clay nanocomposites, in, 2011, pp. 1584-1587.

[19] Da Costa HM, Ramos VD, De Oliveira MG. Degradation of polypropylene (PP) during multiple

extrusions: Thermal analysis, mechanical properties and analysis of variance. Polym Test. 2007;26:676-84.

[20] Somani RH, Hsiao BS, Nogales A, Fruitwala H, Srinivas S, Tsou AH. Structure development during shear flow induced crystallization of i-PP: In situ wide-angle X-ray diffraction study. Macromolecules. 2001;34:5902-9.

[21] P.Kiran Kumar, N.V. Raghavendra, B.K. Sridhara. Optimization of infrared radiation cure process parameters for glass fiber reinforced polymer composites. Materials end design 32 (2011) 1129-1137.

[22] Suresha S. Sridhara BK. Effect of addition on graphite particulates on the wear behavior in aluminium-silicon carbide-graphite composites. Prog Polym Sci 1996; 21: 593-650.

[23] Gu Ruijun, Kokta Bohuslav V. Maximization of mechanical properties of bitch-polypropylene composites with additives by statistical design. J Thermoplast Compos 2010; 23: 239-63.

[24] Onal L, Adanur S. Optimization of compression molding process in laminated woven composites. J Reinf Plast Compos 2005; 24: 775-80.

Effect of Co-Solvent on Structural and Morphological Properties of ZnO Aerogel Prepared by a Modified Sol-Gel Process

M.Meddouri[1], D.Djouadi[1]*, A. Chelouche[1], T. Touam [2], A. Chergui[3]

[1]Laboratoire de Génie de l'Environnement (LGE), Université de Bejaia, 06000, Bejaia, Algérie

[2]Laboratoire des Semi-conducteurs, Université Badji Mokhtar, BP 12 Annaba 23000, Algérie.

[3]Département de Physique, Faculté des Sciences, Université de Sétif, , Algérie

*e-mail :djameldjouadi@hotmail.fr

ABSTRACT

Nanocrystalline zinc oxide (ZnO) aerogel powders were synthesized by the modified sol-gel process. Ethanol, acetone and methanol were used as supercritical drying fluids. Effects of co-solvent on morphological and structural properties were investigated. The as prepared powders were characterized using X-ray diffraction (XRD), Scanning electron microscopy (SEM) and Fourier transform infrared (FTIR). The XRD results show that drying in solvents mixture affects the crystalline quality and acts as a compression agent by exerting stress on the lattice parameters. SEM images show that co-solvent plays a key role in controlling ZnO nucleation and favors the particles agglomeration with increasing the pressure and the temperature. The EDAX analysis shows that the obtained ZnO powder with ethanol and acetone as co-solvent is pure with different stoichiometries (an excess of oxygen (O) with ethanol and zinc (Zn) atoms with acetone). However, when methanol is used as supercritical drying fluid, the obtained powder contains an excess of carbon (C) atoms. The FTIR spectrum reveals the presence of solvent traces in the powder obtained by drying in methanol.

Keywords

ZnO aerogel, sol-gel,co-solvent, supercritical drying, morphology.

1. INTRODUCTION

ZnO is an important material with a wide and direct band gap (3.37 eV) and a large exciton binding energy (60 meV) [1]. Due to these properties, ZnO powder is used in different technological applications [2-4]. It is demonstrated that crystallites sizes, morphology and consequently physical and chemical properties of ZnO powder are strongly affected by the preparation methods [5-7]. Zinc oxide powder has been synthesized by different methods and process [8-10]. Several morphologies were obtained using sol-gel process [11-13]. The sol gel modified process has been only used by El-Mir et al. [14] to prepare ZnO aerogel powder using methanol and ethanol as solvent and co-solvant respectively. To our knowledge, the effect of other co-solvants has not been investigated. In this work, ZnO aerogel has been synthesized by dissolving zinc acetate dehydrate in the methanol followed by supercritical drying in different co-solvents (methanol, acetone and ethanol). The aim of this work is to study the effect of the solvents mixture on the structure and the morphology of ZnO aerogel obtained by the used process.

2. EXPERIMENTAL PROCEDURES

ZnO solution was prepared by dissolving zinc acetate in methanol under continuous stirring. The solution was then diluted and dried under supercritical conditions of the used dilution co-solvent. After cooling a white powder was recuperated and analyzed without any heating or chemistry treatments. The crystalline structure of the as-prepared aerogel powders were investigated by X-ray diffraction (XRD), scanning electron (SEM) and infrared (FTIR) spectroscopies.

3. RESULTS and discussions:

The XRD spectra of aerogel powders obtained by supercritical drying in different co-solvents are shown in Figure 1. The diffraction peaks positions indicate that ZnO aerogel has a crystalline hexagonal wurtzite structure.

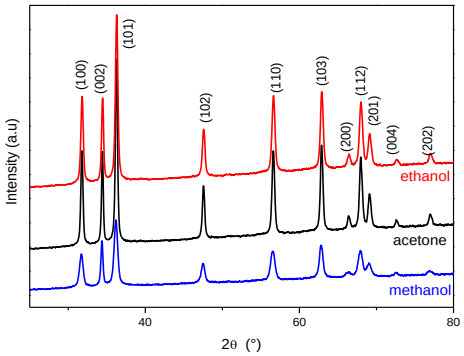

Figure.1: XRD patterns of ZnO aerogel nanopowders obtained by drying in supercritical conditions of different solvents

The values of crystallites size D and lattice parameters (a and c) are presented the table.

co-solvent / parameter	Ethanol (243 °C, 63 bars)	Acetone (236°C ,48 Bars)	Methanol (240 °C, 79 Bars)
a (Å)	3.2480	3.2490	3.2590
c (Å)	5.1970	5.1990	5.2113
D(nm)	26	29	17

Table. 1: Crystallites size *D* and lattice parameters (*a* and *c*) of the ZnO aerogels

The results indicate that critical pressure of solvent is a parameter which affects the crystalline lattice parameters and the particles size only when solvents mixture is used in the supercritical drying process. The dilution solvent acts as a compression agent by exerting stress on the structure and decreases its lattice parameters. As result, one can note that the supercritical drying process in a co-solvent (ethanol, acetone), which differs from the dissolution one (methanol), decreases the lattice parameters and thus causes a stress on the unit cell.

SEM images and EDAX patterns of ZnO aerogel powders obtained by critical drying in different solvents are shown in figure 2. The comparison result between the images shows that the solvent plays an important role in the rate of particles agglomeration and the grains size. Particles agglomeration is observed when a co-solvent is used.

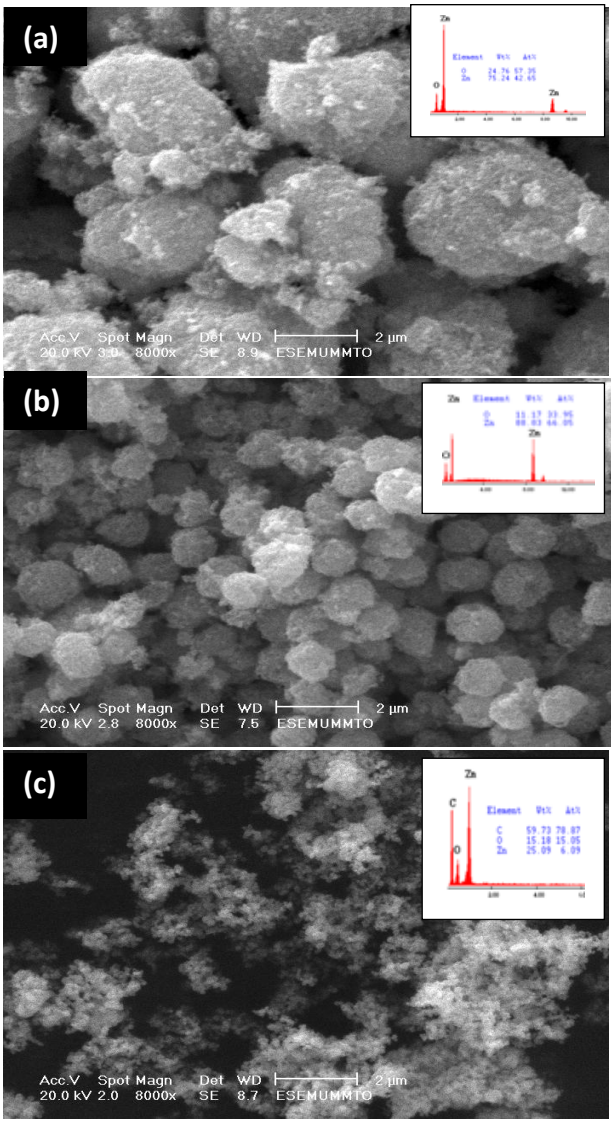

Figure.2: SEM micrographs of ZnO aerogel nanopowders synthesized using different co-solvents: (a) ethanol, (b) acetone, (c) methanol

The aerogel obtained by supercritical drying in ethanol has the biggest grains size and the very prominent agglomeration effect as compared to those obtained in acetone and methanol. This result suggests that ethanol leads to the most agglomeration rate. The aerogel obtained by drying in methanol has the littlest grains size. The result indicates that using solvents mixture in the drying process favors the ZnO particles agglomeration rate. In solvents mixture ZnO nanoparticles agglomerate to form micro-torus (or micro-disks with hole in the center) with an external diameter of about 2µm (for ethanol) and 1µm (for acetone). This obtained morphology (micro-tori) could be due to the critical drying conditions in co-solvent [11]. Li et al. [15] reported that the origin of these morphologies is due to the manner of particles agglomeration. The grains size is directly related to the critical pressure of the co-solvent: grains size increases when critical pressure increases. ZnO aerogel particles obtained by critical drying in ethanol have the littlest crystallites size and the biggest grains size. For those obtained in methanol alone, the crystallites size is the biggest and the grains size is the smallest. One can note the ZnO powder obtained in methanol has the lower particles agglomeration rate. The methanol, as others organic solvents, has a better dispersing ability compared the solvents mixture. This result indicates that supercritical drying parameters of the used co-solvent, in particularly the pressure, favor the small crystallites agglomeration and lead to obtain grains with size directly related to the critical pressure value. In the other hand, we can suggest that using solvents mixture in the drying process plays a key role in controlling the ZnO nucleation. The nucleation rate in solvents mixture is faster than in methanol alone. The reaction time in co-solvent is lower and the crystallites lead, after their formation, to agglomerate together during the increasing of pressure and temperature. In the other hand, we can note that small ZnO particles (obtained in ethanol and acetone) easily agglomerate to form micro-tori shape grains than the big ones (obtained in methanol). This result indicates that supercritical drying process in solvents mixture favors the agglomeration of ZnO particles.

The EDAX patterns show the presence only of zinc and oxygen atoms in the aerogels obtained by drying in co-solvent and hence indicate the purity of ZnO nanopowder. The ZnO particles obtained by supercritical drying in ethanol mixture contain 57.35 % of oxygen atoms and 42.65% of zinc atoms. This aerogel is relatively rich on O atoms. The excess O atoms can be located on the surface of the crystallites. The ZnO aerogel obtained by drying in acetone as co-solvent contains 33.95 % of oxygen atoms and 66.05 % of Zn atoms, and this one is rich on Zn atoms. The excess Zn atoms can be located on the crystallite surface. ZnO particles obtained by drying in methanol contain 78.97 %, 15.05 and 6.09 % of C, O and Zn atoms respectively. The low grains density observed in this aerogel is probably due to the presence of carbonyl groups in the product. It has been reported that carbonyl groups (C=O) affect the ZnO crystals growth [16]. This result indicates that the esterification chemical reaction realized during the drying process in methanol alone is not completely achieved after reaching the critical conditions comparatively to those in which a co-solvent is used.

Chemical bonding that appeared in ZnO aerogel obtained by supercritical drying in different organic solvents was examined using FTIR spectroscopy. The elaborated ZnO aerogels FTIR spectra are presented in figure 3. The scanned region is ranged from 250 cm^{-1} to 4000 cm^{-1}. For all ZnO aerogels obtained by drying in solvent (methanol) and solvents mixture (methanol-

ethanol, methanol-acetone), we observe the same peaks located at 3440, 1600, 1420, 890 and 480 cm^{-1}. The large peak at 3440 cm^{-1} is attributed O-H stretching vibration. The band located at 1600 cm-1 is attributed to H-O-H bending vibration. These two peaks are assigned to the presence of small amount of water in the as-prepared ZnO aerogel. The large bands located at 460-520 cm^{-1} is ascribed to Zn-O stretching vibration [17]. The absorption bands appeared at 1420 and 890 cm^{-1} can be ascribed to C-H bending modes. These bands are more intense in the powder obtained by drying in methanol. This result can be explained by the C atoms present in this powder as shown by the EDAX measurements. We can also note the absence of acetates stretching indicating the complete formation of ZnO particles.

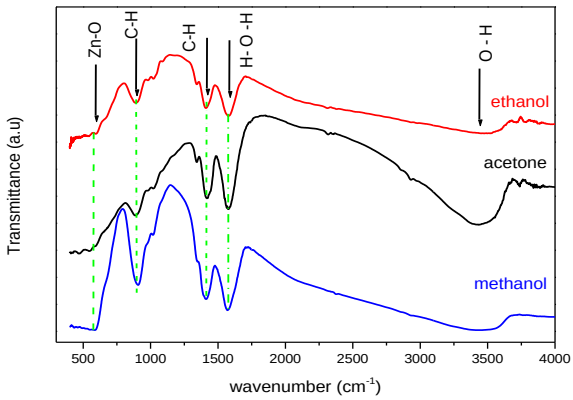

Figure. 3: FTIR spectra of ZnO aerogel nanopowders synthesized in different supercritical drying solvents

4. CONCLUSION

ZnO aerogel nanopowders with high crystalline quality were obtained by dissolving zinc acetate dehydrate in methanol followed by critical drying in solvent (methanol) and co-solvents (acetone and ethanol). The products were characterized without heating treatments. The synthesized aerogels have a well-defined polycrystalline hexagonal wurtzite structure of ZnO. Drying in methanol alone leads to obtain the best crystalline texture of the aerogel. The critical pressure of co-solvent exerts compression on the lattice and decreases its parameters. The EDAX spectra show the absence of C atoms in ZnO aerogel obtained by drying in co-solvent. ZnO aerogel powders obtained by drying in ethanol and acetone contain respectively more O and Zn atoms. With co-solvent as critical fluid in drying process, the obtained crystallites are the littlest and the grains are the biggest. The co-solvent plays a key role in controlling the crystallites agglomeration during the supercritical drying process. The ZnO aerogel obtained by drying in methanol alone contains traces of solvent which is due to the non-achievement of the esterification reaction during the process and, in the other hand, using a co-solvent accelerates the chemical reaction and leads to the formation of pure ZnO aerogels without any contaminations.

5. REFERENCES

[1] Norton D. P., Heo Y. W, Ivill M. P., Pearton S. J., Chosholm M. F., Steiner T.2004. ZnO: growth, doping & processing, *Mater. Today*, 7 (6) (2004),34-40 .

[2] Xiao H., Sun M., Li C., Yang D., Han B., He S.2008. Formation and evolution of oxygen vacancies in ZnO white paint during proton exposure, *J.Nucl. Instrum. Methods* B 266 (2008) 3275–3280.

[3] Yan X., Itoh T., Dai S., Ozaki Y., Fang Y.2013. Cu, Mn doping effect to optical behavior and electronic structure of ZnO ceramic, *J. Phys.Chem. Solids*, 74 (8) (2013) 1127-1130.

[4] Li J-L., Chen G-H., Yuan C-L.2013. Microstructure and electrical properties of rare earth doped ZnO-based varistor ceramics, *Ceram. Int.*, 39(3) (2013) 2231-2237.

[5] Li Z., Huang X., Liu J., Li Y., Li G.2008. Morphology control and transition of ZnO nanorod arrays by a simple hydrothermal method, *Mat. Lett.* 62 (2008) 1503–1506

[6] Kim J.Y., Cho J. W., Kim S. H.2011. The characteristic of the ZnO nanowire morphology grown by the hydrothermal method on various surface-treated seed layers, *Mater. Lett.* 65 (2011) 1161–1164.

[7] Tao Y., Fu M., Zhao A., He D., Wang Y.2010. The effect of seed layer on morphology of ZnO nanorod arrays grown by hydrothermal method, *J. Alloy. Compd*. 489 (2010) 99–102.

[8] Bacsa R., Kihn Y., Verelst M., Dexpert J., Bacsa W., Serp P.2007. Large scale synthesis of zinc oxide nanorods by homogeneous chemical vapor deposition, *Surf. Coat. Technol*. 201 (2007) 9200–9204.

[9] Ozcan S., Can M.M., Ceylan A.2010. Single step synthesis of nanocrystalline ZnO via wet-milling, *Mater. Lett.* 64 (2010) 2447–2449.

[10] Dev A., Kar S., Chakrabarti S., Chaudhuri S.2006. Optical and field emission properties of ZnO nanorod arrays synthesized on zinc foils by the solvothermal route, *Nanotechnology* 17, (2006)1533- 1540.

[11] Djouadi D., Aksas A., Chelouche A.2010. Élaboration et Caractérisations structurale et optique des Nanocristallites toriques de ZnO. *Ann. Chim-Sci. Mat* (35) (2010) 255–260.

[12] Zak A.K, Majid W.H.A., Darroudi M., Yousefi, R.2011. Synthesis and characterization of ZnO nanoparticles prepared in gelatin media, *Mater. Lett.* 65 (2011) 70–73.

[13] Angwafor N. G. N., Riler D. J.2008. Synthesis of ZnOnanorod/nanotube arrays formed by hydrothermal growth at a constant zinc ion concentration, *Phys. Status Solidi A*, 205 (2008) 2351–2354.

[14] El Mir L., El Ghoul J., Alaya S., Ben Salem M., Barthou C., von Bardeleben H.J.2008. Synthesis and luminescence properties of vanadium-doped nanosized zinc oxide aerogel, *Physica B*, 403, (2008) 1770-1774.

[15] Li G-R., Lu X-H., Zhao W-X.,Su C-Y., Tong Y-X.2008. Controllable Electrochemical Synthesis of Ce4+-Doped ZnO, Nanostructures from Nanotubes to Nanorods and Nanocages, *Growth design*, 8 (2008) 1276-1281.

[16] Ma J., Jiang C.., Xiong Y., Xu G.2006. Solvent-induced growth of ZnO microcrystals, *Powder Technol*. 167 (2006) 49–53.

[17] Foo K.L.,. Kashif M, Hashim U.,Liu W.-W. 2014. Effect of different solvents on the structural and optical properties of zinc oxide thin films for optoelectronic applications, *Ceram. Int.* 40 (1) (2014) 753–761.

Stabilization of Negative Bias Illumination Stress Induced Instability on Electrical Characteristics of Amorphous Oxide Thin Film Transistor Integrated with Plasmonic Filter

Seongpil Chang[1], Yun Seon Do[2], Jong-Woo Kim[1], Tanyoung Kim[1], Byung-Hyun Choi[3], Kyung Cheol Choi[2] and Byeong-Kwon Ju[1,*]

[1] Department of Electrical Engineering, Korea University, Seoul 136-713, Republic of Korea

[2] Department of Electrical Engineering, KAIST, Daejeon 305-701, Republic of Korea

[3] Electronic Materials and Module Team, Korea Institute of Ceramic Engineering and Technology, Seoul 153-801, Republic of Korea

Fax: +82-2-3290-3791,

E-mail: csp715@korea.ac.kr, missddo@kaist.ac.kr, clo8327@korea.ac.kr, tanyong@korea.ac.kr, bhchoi@kicet.re.kr, bkju@korea.ac.kr

*Corresponding author is Byeong-Kwon Ju

Abstract To realize the transparent electronics, oxide semiconducting materials ensure negative bias illumination stress (NBIS) stability. This work represents oxide-TFTs integrated with plasmonic filters for improving NBIS stability. Two species of plasmonic filters with different cut-off wavelengths are fabricated by simple evaporation process and patterned by laser interference lithography technique. a-IGZO TFT with PF-R exhibited less ΔV_{th} of ~0.3 V than ~2.2 V of a-IGZO TFT without PF after 3000s. Finally, incident light into oxide-TFTs filtered selectively thereby NBIS stability is improved through integrating PFs**.**

Keywords: Amorphous oxide-semiconductor, Negative-bias-illumination stress, Plasmonic filter, Stability, Transparent electronics

Reference for publisher use only

Biographical notes: 100 words for each authors. 150-200 for corresponding author

1 Introduction

Recently, research interests in amorphous oxide semiconductors (AOSs) as promising electronic materials have increased considerable. AOSs show superior characteristics necessary for electronic devices: high electron mobility, uniform surface due to its amorphous structure, and high transparency in the visible range.[1, 2] In particular, amorphous indium-gallium-zinc-oxide (a-IGZO) shows a mobility over 10 $cm^2\ V^{-1}\ s^{-1}$, which is large enough for operating standard displays such as organic light-emitting diodes (OLEDs) and liquid crystal displays (LCDs) with a fast driving scheme.[1]

Although a-IGZO has been regarded as a promising material for future electronics, the stability of TFTs has to be ensured for more practical use. OLEDs, for example, undergo negative gate bias stress during most of the driving time and transparent devices are exposed to ambient light unavoidably. The stability resulting from electrical stress under light illumination is important since it can deteriorate the switching performances of a-IGZO-based TFTs. It was found that the positive bias illumination stress is insignificant compared to the negative bias illumination stress (NBIS).[3] NBIS has been explained by photo-induced carriers and the state transition,[3-6] but the exact mechanism is under debate. In addition, previous reports to improve the stability from NBIS are still insufficient from a device viewpoint.

With this point of view, we suggest a novel AOS-device that has possible applications in transparent electronics, by integrating a-IGZO-TFTs and PFs.[7-8] A study on NBIS of the suggested a-IGZO-TFTs combined with PFs was performed. Unlike previous work with white or a monochromatic light source, the photosensitivity of a-IGZO-TFTs was investigated with the selectively controlled spectral range of the illumination by the PFs. The suggested TFTs showed extremely improved stability even under a NBIS environment. In addition, compared to the prior AOS TFTs which were equipped with equipped with metal shielding layer to block the light, [9] our suggestion provides not only the spectral selectivity from the light source but also reduces in the loss of transparency. We expect that the photosensitivity subdivided into spectral ranges will provide a practical guideline for designing structures or a fabrication process of transparent devices and enlarge the usage of AOS TFTs.

2 Results and Discussion

Figure 1(a) represents the schematic illustration of the suggested TFT integrated with the plasmonic filter. The a-IGZO TFTs with W/L = 40 μm/20 μm were fabricated with a bottom-gate configuration and operated on n-type depletion mode. The electrical properties of the fabricated a-IGZO TFTs were estimated as followings: the saturation mobility (μ_{SAT}) of ~11.9 $cm^2V^{-1}s^{-1}$; the threshold voltage (V_{th}) of -4.74 V; the on/off current ratio ($I_{on/off}$) of 1.39×10^7; the subthreshold gate swing (SS) of 0.39 $Vdec^{-1}$ as expected in Fig. 1(b). PFs were attached on the opposite side of the substrate. Since the attached filter contributes to screen the lights with shorter wavelength than λ_{max} of each filter, the transparent TFTs appeared different colors

The negative shift behavior of V_{th} can be explained by the following mechanisms: i) photo-accerlated state-creation from [Vo] to [Vo^{2+}],[6] ii) the hole trapping model, [7] and iii) the oxygen photo-desorption model.[5] We excluded the oxygen desorption effect on account of the passivation on the channel back surface. Other models deal with the

variable carrier concentration due to the state transition or photo-created holes that originate from the external light energy. The PF of the suggested device acts as a low-cut filter that blocks the light in the spectral range below λ_{max}. Therefore, the different stability characteristics between the reference and the TFTs integrated with PFs can be simply interpreted by the amount of the variation of photosensitive carriers.

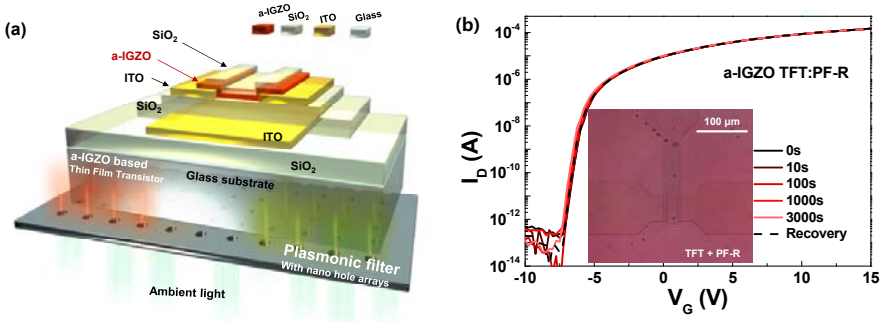

Figure 1. (a) The schematic illustration of the a-IGZO TFT integrated with the plasmonic filter (PF). (b) Stabilized transfer characteristics of a-IGZO TFT by integrating the plasmonic filter. (Inset shows the microscope image of a-IGZO TFT with red plasmonic filter.)

The external light excites electrons from the ground state [V_O] (~2.5 eV from the conduction band) to the [V_O^{2+}] state (~0.4 eV from the conduction band), releasing delocalized free electrons in the conduction band.[10] In addition, the excited photo-induced electrons from the [V_O] state to the conduction band can be generated.[6] These carriers survive without direct recombination with excess holes that are trapped in the stable [V_O^{2+}] state under NBIS.[4] The released free electrons and [V_O^{2+}] itself lead to the negative shift of V_{th}.

.

Since the transmission range of nanohole-based PFs is easily tuned via the periodicity of the nanohole arrays, the stability of a-IGZO TFTs with integrated PFs showed potential for more practical use. This is especially true for transparent electronics, components such as the black matrix or color filters can possibly be replaced by PFs to enhance transmission.

3 Conclusions

In conclusion, we studied photo-insensitive a-IGZO TFTs integrated with PFs. Since the spectral response of PFs is easily controlled, the stability of a-IGZO under NBIS is investigated at different wavelength ranges with a white light source. The PFs block out the light at higher energy, which excites photo-created electrons into the conduction band. In addition, the number of carriers from the state transition of the oxygen defects was restrained by reduced light transmission in the pass band. These results suggest a higher possibility for application to practical devices as well as provide an understandable explanation of the NBIS effect on a-IGZO devices. We believe these results will lead to advances in transparent electronics by giving a realistic guideline to design and fabrication of the AOS-based devices.

Acknowledgements

This work was supported by the National Research Foundation of Korea (NRF) grants funded by the Korea government (MSIP) (CAFDC/Byeong-Kwon Ju and Kyung Cheol Choi/No. 2007-0056090) and (No. 2011-0016621).

References

1 T. Kamiya, and H. Hosono, (2010) 'Present status of amorphous In–Ga–Zn–O thin-film transistors', NPG Asia Mater. Vol.2, p.15.

2 E. Fortunato, P. Barquinha, and R. Martins, (2012) 'Oxide Semiconductor Thin-Film Transistors: A Review of Recent Advances', Adv. Mater. Vol.24, p.2945.

3 J. H. Jeon, J. Kim, and M. K. Ryu, (2011) 'Instability of an Amorphous Indium Gallium Zinc Oxide TFT under Bias and Light Illumination', J. Kor. Phys. Soc. Vol.58, p.158.

4 J. S. Park, T. S. Kim, K. S. Son, J. S. Jung, K. H. Lee, J. Y. Kwon, B. Koo, and S. Lee, (2010) 'Influence of Illumination on the Negative-Bias Stability of Transparent Hafnium–Indium–Zinc Oxide Thin-Film Transistors', IEEE Elec. Dev. Lett. Vol.31, p.440.

5 K.-H. Lee, J. S. Jung, K. S. Son, J. S. Park, T. S. Kim, R. Choi, J. K. Jeong, J.-Y. Kwon, B. Koo, and S. Lee, (2009) 'The effect of moisture on the photon-enhanced negative bias thermal instability in Ga–In–Zn–O thin film transistors', Appl. Phys. Lett. Vol.95, p.232106.

6 H. Oh, S. M. Yoon, M. K. Ryu, C. S. Hwang, S. Yang, and S. H. K. Park, (2010) 'Photon-accelerated negative bias instability involving subgap states creation in amorphous In–Ga–Zn–O thin film transistor', Appl. Phys. Lett. Vol.97, p.183502.

7 Q. Chen, D. Chitnis, K. Walls, T. D. Drysdale, S. Collins, and D. R. S. Cumming, (2012) 'CMOS photodetectors integrated with plasmonic color filters', IEEE Photonic Tech. Lett. Vol.24, p.197.

8 Y. S. Do, J. H. Park, B. Y. Hwang, S. M. Lee, B. K. Ju, and K. C. Choi, (2013) 'Plasmonic Color Filter and its Fabrication for Large-Area Applications', Adv. Opt. Mater. Vol.1, p.133.

9 S. Jeon, S.-E. Ahn, I. Song, C. J. Kim, U.-I. Chung, E. Lee, I. Yoo, A. Nathan, S. Lee, J. Robertson and K. Kim, (2012), 'Gated three-terminal device architecture to eliminate persistent photoconductivity in oxide semiconductor photosensor arrays', Nat. Mater. Vol.11, p.301.

10 B. Ryu, H.-K. Noh, E.-A. Choi, K. J. Chang, (2010) 'O-vacancy as the origin of negative bias illumination stress instability in amorphous In–Ga–Zn–O thin film transistors', Appl. Phys. Lett. Vol.97, p.022108.

Hydrogen produced by steam reforming for use steel

M. Kahalerras, M. T. Abedghars, Z. Zarour, S. Boulekroune.
Welding and NDT Research center (CSC) / Unit for Applied Steel and Metals. URASM /CSC-Annaba, BP 196 Annaba -23000.
Mail: Kahalerrasmounir@yahoo.com

ABSTRACT
The world is facing of a double problem of Management of energy resources and environmental impacts. This is the result of the using of massive of fossil fuels since the beginning of the industrial era, which generates a huge costs and a major pollution. The conventional method of steelmaking requires the use of blast furnaces with ancillary facilities which are expensive and have a significant impact on the environment.
Now, the installations of hydrogen producing by steam reforming are incorporated in many chemical factories (production of synthesis gas) and steel factories (gas reducer of iron-oxides) [3] [4]. In steel, the direct reduction of hydrogen is advantageous in metallurgical, environmental and economic domains [1] [5]. The substitution of coke by hydrogen allows to remove two major polluters (the coking and agglomeration), and save a lot on the cost per ton of steel [2]. The objective of this work is the production of hydrogen for use in the steel industry as reducing gas iron oxides. This production is clean and less cost.

CH_4 (Natural gas) + H_2O (Steam) = CO + $3H_2$ (1)

We used a control installation of vaporeformage, consisting of a four reformer tubes with catalysts based on nickel oxide, and a heat exchanger. The principle was to produce a mixture of reducing gas (72% H_2 and 16% CO) from a natural gas (83% CH_4) and water vapor. The S/C ratio equal to 1.4 at 730 ° C gave us very good results both for the production of hydrogen as for the performance of the reduction of iron oxides, shown above.

Keywords
Natural gas, hydrogen, reforming, gas reducing, sponge iron.

1. INTRODUCTION
Hydrogen does not exist in nature in the Free State, it is in the combined state, especially in water and hydrocarbons, it must therefore occur. Hydrogen is not an energy source in its own right because it requires energy for its production: it is an energy vector, and it will do so only ecological just if the energy used to produce is environmentally friendly.
In this work, we approach the hydrogen only in the case where the energy value related to its physicochemical properties. In this folder, we treat production for use in the steel industry.
Algeria has large reserves of iron ore. It is the fifth largest producer in the world of natural gas, but absent in the classification of consumer countries. Thus the alternative reforming of natural gas – direct reduction - melting sponge iron, we have emerged as an interessant solution for the recovery of iron ore of Gara Djebilet and natural gas (source of hydrogen production by the principle of steam reforming). Our studies and researches were focused on developing a process for converting natural gas into reducing gas (make hydrogen), and more particularly to determine the operating conditions of reforming to define the optimal settings for a good production and quality of hydrogen.

2. EXPERIMENTAL METHODS

2.1 Raw materials
For the tests of hydrogen production, we used natural gas Algerian whose properties are given in table n°1 and deionizer water.

Table n°1: Properties of Algerian natural gas

Natural gas GL1K	Composition (%)
Helium (%)	0.18
Nitrogen (%)	5.71
Methane (%)	83.06
Ethane (%)	6.91
Propane (%)	2.36
Butane (%)	0.25
Pentane (%)	0.26
Carbon dioxide (%)	0.14
H_2S (mg/Nm^3)	1.86
Calorific value (kWh/m^3)	≈ 11.3
Density	0.6
Water content (ppm)	< 80

Source: Laboratory of Skikda refinery

Natural gas consists mainly of methane and therefore has a ratio H/C close to 4, the oil has a ratio H/C close to 2 and for coal, the ratio is lower than 1. Natural gas is the most interesting source for hydrogen production. Table n°1 takes us to the conclusion that natural gas is in the standards of density, it is rich in methane and poor in heavy hydrocarbons. Its content of sulfur and helium are relatively large. The reaction between the water vapor and natural gas at 1000°C cannot be carried out without a catalytic contribution.
Despite its low reactivity, methane remains the most economical raw material for the hydrogen and carbon monoxide production. Although methane reforming in presence of water vapor is the process that has prevailed for more than 80 years [3], it has the disadvantage of its high endothermicity. The catalyst used in our tests is based on nickel. This type of catalyst in ring-shaped of reaching consists of nickel oxide deposited on the alumina-refractory used of catalyst support. The reduction of nickel oxide in

elemental nickel, will take place when the reaction temperature will be ensured by the water vapor.

2. 2 Equipment

The reforming test was conducted in a pilot plant (Figure 3). The converting furnace is equipped with only one burner (heating from the bottom with ascending gaseous flow), ensure a sufficient temperature of the reforming of natural gas in admixture with steam, and four (O4) tubes catalysts wherein is the nickel catalyst.

The steam produced by the boiler is introduced the first to heat the catalyst tubes. Natural gas and water vapor must be in a steam / carbon ratio defined for it can provide a reducing gas with maximum hydrogen avoiding cracking of methane and the formation of solid carbon in the form of soot [3]. This installation includes:

- Vertical furnace
- Four tubes catalysts (catalyst: 80% Al_2O_3 and 12% Ni)
- Boiler (for steam production)
- Desulfurization system (to remove sulfur from natural gas)
- A main burner

The Temperature and proportions of hydrogen of gas mixture obtained (called "reducing gas") at the exit of the reforming condition the metallization ratio or the degree of reduction in the reduction furnace. The reaction of the conversion of methane in the presence of water steamer and a nickel catalyst in the form of Raschig ring takes place under a pressure equal 02 bars and a temperature between 800°C to 950°C according to reaction:

$CH_4 + H_2O \rightarrow CO + 3H_2$ + 206 Kj. mol^{-1} (1)

The principle of operation of the reforming equipment is shown in Figure 1. The operating conditions are:

- Inlet temperature of process gas mixture: 600 °C
- Reformed gas temperature at outlet: 780 °C
- Number of catalyst tubes(04)
  Tube length: 06 m
  Tube diameter: 0.15 m
- Catalyst volume: 1.40 m3
- Pressure: 02 bars
- Ratio: S/C: 1,5

Reformed gas: 70% H_2, 16% CO, 2% CO_2, 8% H_2O, 1% CH_4, 3% N_2.

3. EXPERIMENTAL RESULTS

The research work focuses specifically on the direct reduction for enhance Algerian natural gas. The method used to obtain a synthesis gas for the specific reduction of iron oxides is the treatment of methane to water steam. Chain: Reformer-Direct reduction furnace- Electric arc-furnace to slag resistance; we has emerged as an interesting alternative for the recovery of iron ore in Gara Djebilet and natural gas.

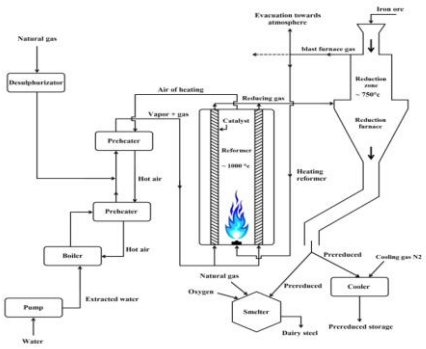

Figure1: diagram of Installation for producing hydrogen

The temperature is the first energy source for the conduct of the reforming reaction.

Effectively and as shown in Figure 2, the temperature affects on all components of the reformed gas if we use a ratio S /C = 1,5.

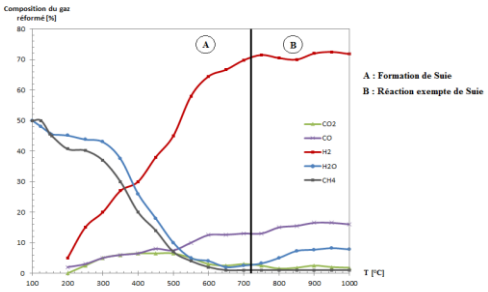

Figure.2: effect of temperature on the reforming reaction
With S / C = 1, 5. $[CH_4 + H_2O \rightarrow 3H_2 + CO]$ (1)

For a working temperature of 900 °C and an S / C between 1, 4 to 2, 2 we have:
- A significant amount of CO from 0% to 20%,
- An amount of H_2 produced stable.
- A lack of carbon soot. These results are given in table n° 4.

Table.1: Quality of reformed gas with S/C =1, 5 and a temperature equal 900 °C.

Elements in the product gas		% weight
Hydrogen	(H_2)	70%
Carbon monoxide	(CO)	16 %
Carbon dioxide	(CO_2)	2 %
Water	(H_2O)	8%
Methane	(CH_4)	1%
Nitrogen	(N_2)	3%

The reduction of iron oxides by the gas mixture that we obtained by steam reforming and with its hydrogen content and carbon monoxide are respectively 70% and 16%, gave a sponge iron with a rate of metallization 92.

Table 2: Composition of the sponge iron (scrap synthetic) obtained from these tests:

Elements	Fe^t	FeO	Tm	C	O_2	S
(%)	78 ,12	72,73	93,10	2,38	1,31	0,01

The figure 3 shows that the hydrogen reduction is considerably better than that achieved by carbon monoxide. This is explained by a better diffusion of a gas is much easier that its density is lower, the hydrogen diffuses four times faster in a solid than carbon oxide, which is a great advantage for the kinetics of reduction by H_2.

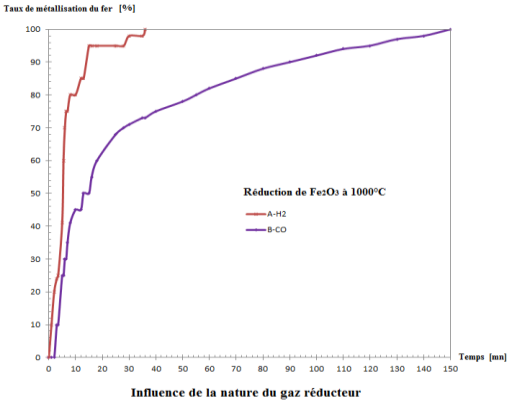

Figure 3: Reduction of the hematite by the pure hydrogen and the pure monoxide Carbon.

4. CONCLUSION

The result of our research has shown that obtaining a reducing gas rich in hydrogen can be realized by reducing the vapor/carbon. The increase in temperature of the gas product (70% H_2) at the bottom of the reduction furnace allows us to obtain a high quality of pre-reduced.

The operating conditions that were used for our tests are: (t °C= 900 °C, P= 2 bars, ratio S /C = 1,4), allowed us to obtain a synthesis gas composed of 70% hydrogen, 16% carbon monoxide, from 2% carbon dioxide, from 8% water vapor,1% methane and 3% nitrogen.

Reducing gas in this well-defined proportion (hydrogen content and carbon monoxide), is ideal for the reduction reaction of iron oxides. The sponge iron obtained has a metallization 92.

The production of steel from the reforming process-reduction has several advantages:

- Costs of investing, operating and maintenance are much lower (coal, coke).
- Decreased implementation thousand coke / ton of pig iron.
- Simple and clean technology.
- Natural-Gas abundant and cheap.
- Protection of the environment, the risk of contamination of the air and soil are minimal, there is no emission of toxic fumes (complete elimination of two major polluters: the coke oven and blast furnace).

These tests were used to prove in general that it is technically possible to obtain from natural gas and iron ore Gara -Djebilet sponge iron with satisfactory physicochemical characteristics, which can be easily replaced and meet the global market scrap. As regards the economic aspect, it can not be enjoyed in a general way, it is related to several factors, firstly the strategy adopted by each country market and secondly, it is linked to prices of raw materials used to know ore, gas and electricity.

5. REFERENCES

[1] Astier (J.). – Reduction direct. [M 7 580]. Traité Matériaux métalliques.

[2] Astier (J.). – Usines sidérurgiques fondées sur la réduction directe. [M 7 110]. Traité Matériaux métalliques.

[3] Jenkins (J.H.) and Stephens (T.W.). – Kinetics of catalytic reforming. Hydrocarbon Processing (USA) Nov. 1980

[4] Jonchere (J.P.) et Baudouin (C.). – Production d'hydrogène à Grande échelle à partir des hydrocarbures. L'actualité Chimique, 20-25 déc. 2001.

[5] Raguin (J.). – Protection de l'environnement: Stratégie. M 7 150, M 7 151, traité Matériaux métalliques volume

PREPARATION AND IN VITRO EVALUATION OF ARTEMISININ-DIFFERENT CARRIERS FREEZE DRIED POWDERS

GAMAL OSMAN ELHASSAN[1], YUEN KAH HAY[2], WONG JIA WOEI[2], AKHTAR JAWED[1], REIAZ KHAN[1,] KHALID OMER ALFAROUQ[3] AND JIAUDDIN KHAN[4]

1. Unaizah College of Pharmacy,Qassim University,Qassim-KSA

2. School of Pharmaceutical Sciences, University Sains Malaysia, , Penang, Malaysia.

3. Minstry of Health Khartoum State, Khartoum –Sudan

4. Mangement and science University, Selangoor-Malaysia

ABSTRACT

Artemisinin (ART) is an oral antimalarial agent that is poorly soluble drug with low oral bioavailability. The present study describes the preparation of artemisinin freeze dried powder using different carriers (polyvinyl pyrolidone K-25 (PVP K-25), hydroxyl propyl cellulose (HPC) and dextrin) designed to increase the solubility of artemisinin. Artemisinin freeze dried powders were prepared by dissolving different carriers (PVP K-25, HPC and dextrin) in water followed by the addition of artemisinin at a ratio of 1:4. The resultant products were evaluated using the solubility and dissolution studies, differential scanning calorimeter (DSC) and scanning electron microscopic (SEM). These in vitro studies showed that the aqueous solubility of artemisinin has increased significantly for the preparation containing artemisinin-dextrin at a ratio of 1:4. Further, the effect of incorporation of different co-carriers (citric acid or mannitol) to artemisinin-dextrin freeze dried powder at different ratio was evaluated. There was a significant increase in the solubility and dissolution rate of artemisinin was obtained with the artemisinin-dextrin-citric acid freeze dried powder at a ratio of 1:3:1.

Keywords

Artemisinin,dextrin,solubility,PVP K25,freeze drying

1. INTRODUCTION

Artemisinin (ART) and its derivatives have been known since time immemorial as a potent antimalarial agent, due to their low toxicity and high efficacy against malarial parasites (Klayman, 1985). It is a fast acting blood schizonticide with short parasite clearance time, leading to rapid symptomatic relief of malarial infections (Qinghaosu, Antimalarial Coordinating Research Group, 1979). It is one of the few antimalarials that remain effective against multi drug-resistant strains of *Plasmodium falciparum* (World Health Organization, 1994).

The major draw back of this compound is the low aqueous solubility, resulting in poor and erratic absorption upon oral administration. This together with its short half life and high first pass metabolism might lead to incomplete clearance of parasites resulting in recrudescence (Titulaer et al., 1991).

To overcome the problem of poor solubility and dissolution, various approaches have been reported. One of these approaches is freeze drying (lyophilization) technique, which is used widely in the pharmaceutical industry. Tachibana and Nakuma (1965) were among the first to dissolve both the drug and the carrier in common solvent and then evaporate the solvent to produce a solid solution. Jaccard and Leyder (1985) employed freeze drying technique in making oral pharmaceutical preparation and found that the product have increased absorption and bioavailability with poorly water soluble drugs like spironlactone, nicerogline and trolendymein in comparison to their respective conventional formulations. Betageri and Makarla (1995) reported that lyophilized solid dispersions of glyburide-PEGs had the maximum effect on the rate and extent of dissolution of glyburide compared to their physical mixtures. The results clearly suggested that inclusion of a carrier together with suitable

lyophilization process can have a positive influence on poorly water-soluble drugs.

Van Eerdenbrugh et al. (2007) reported that, the dissolution rate and absorption properties from Loviride, sucrose co-freeze dried nano-powder were improved significantly. The use of freeze drying techniques to enhance the solubility, the dissolution rate and bioavailability of poorly water soluble drugs (nimesulide, nifeldipine, griseofulvin and loviride) has been demonstrated by Shoikri et al. (2009), Oshima et al. (2005), Iman & Mona (2007) and Van Eerdebrugh et al. (2007) respectively.

The aim of the present study to enhance the aqueous solubility and the dissolution rate of artemisinin using freeze drying technique

2. MATERIALS

Artemisinin was obtained from Kuming Pharmaceutical Corporation (Kuming, Germany). Dextrin, citric aid and mannitol were obtained from BDH Chemicals (Poole, England). All others chemical and reagents used were either analytical or HPLC grades.

2.1.1. PREPARATION OF ARTEMISININ-(DIFFERENT CARRIERS) FREEZE DRIED POWDERS

Freeze dried powders containing different proportions of artemisinin to Polyvinyl Pyrolidone (PVP K-25), hydroxyl propyl cellulose (HPC) and dextrin, were prepared using these ratios of drug to carrier of 1:4, 2:3, 3:2 and 4:1. They were prepared by first dissolving each carrier in distilled water followed by the addition of artemisinin with constant heating at 70 – 80°C and stirring. Dextrin is not soluble in most common solvent, but it is highly soluble in hot water.

Another set of experiment were done by adding co-carriers citric acid or mannitol into the artemisinin-dextrin mixture. They were prepared by dissolving dextrin with citric acid / mannitol in hot distilled water followed by addition of artemisinin with constant heating at 60°C - 80°C. Various ratios of ART : dextrin : citric acid/mannitol were prepared, the composition details are shown in Table 1.

All the above mixtures were prepared and freezed at -53°C for 24 hours before lyophilization. The frozen mixtures were transferred to the freeze dryer (Labocono freeze dryer, Labocono Corporation USA) under pressure 8-10 mm Hg and condensed at -75°C for a period of 24 hours. The lyophilized powders were stored in a dessicator at a room temperature prior to their characterization by SEM, DSC and solubility determination.

2.1.2. Determination of artemisinin solubility in the prepared freeze dried powders

The solubility of artemisinin in the above prepared freeze dried powders was determined. An excess amount of pure artemisinin and freeze dried powder were separately added into flasks containing 20 ml of distilled water. All the samples were shaken vigorously at 30°C for 24 hours, 5 ml samples were collected from each flask and filtered through a membrane filter (0.2 μm). The filtrate were then suitably diluted and treated prior to analysis by high performance liquid chromatography (HPLC) using ultra violet UV detector operated at a wave length 260nm. The chromatographic separation was performed using a Genesis C_{18} column (150 x 4.6 mm) (Genesis, UK). The mobile phase composed of a mixture of 0.01M disodium hydrogen phosphate adjusted to pH 6.5 and acetonitrile (75:25, v/v). The HPLC analysis was based on the method reported by Zhao & Zeng (1985).

2.1.3. Differential scanning calorimetry (DSC) studies

Thermal analysis using DSC has proven to be a useful tool in characterizing the freeze dried powders (Topaloğlu et al., 1999, Monkhouse and Lach, 1972). Differential scanning calorimetric studies were performed for all the freeze dried powders with TA instrument model 2010 differential scanning calorimeter (DE, USA). Each sample (10 mg of powder in aluminum pans) was scanned from 25 to 200°C at a rate of 10°C per minute, the data were analyzed using the Universal analysis software (TA instrument, USA).

2.1.4. Scanning electron microscopy (SEM) studies

The images of artemisinin and all the above freeze-dried powder were obtained by using a scanning electron microscope and the micrographs were taken at a magnification of 500X.

2.1.5. Dissolution study

The in vitro dissolution studies of pure artemisinin, freeze-dried product of artemisinin-dextrin-citric acid, artemisinin-dextrin-

mannitol and their corresponding physical mixture (PM) were evaluated using the paddle method of the USP 24 dissolution test-apparatus (Sotax AT7, Bassel, Switzerland).

The test was performed in 900 ml of distilled water as the dissolution medium under non-sink condition. The temperature was maintained at 25.0 ± 0.5 °C while the paddle rotation speed was set at 100 rpm. The temperature of 25°C was chosen because at a higher temperature artemisinin would recrystallize out when the samples are exposed to room temperature after collection. A weight of 250 mg of pure artemisinin was used for each vessel. An equivalent weight of 250 mg of artemisinin was also used for freeze-dried products of artemisinin-dextrin-citric acid or mannitol and their corresponding physical mixture.

All powders were sieved through a 300 μm laboratory test sieve (Endecotts Ltd., England) prior to the dissolution studies. Sample of 5 ml were withdrawn at various designated time intervals of 15, 30, 60, 90, 120, 180, 240, 300 and 360 minutes; using an automatic fraction collector (SDX Fractional Collector, Sadex, Malaysia). The samples were filtered through 0.2 μm syringe membrane filter (Whatman, UK). The initial portion of the filtrate was discarded and the subsequent portion collected was subjected to appropriate dilution with distilled water prior to analysis by the HPLC method. For each sample, the dissolution test was run in triplicate.

3. RESULT AND DISCUSSION

3.1.1. Preparation of artemisinin freeze dried powders in different carrier

The freeze drying process could be completed in 24 hours. After 24 hours, the freeze-dried powder residues appeared as a porous light and fluffy mass, except for the preparation containing HPC, which was very sticky in nature and difficult to be collected and processed and hence was excluded from further study.

*3.1.2.*Determination of artemisinin solubility

Fig (1) shows the solubility of artemisinin in the artemisinin-carrier freeze dried powders with different ratios of artemisinin to dextrin or PVP K-25. It can be observed that the solubility of artemisinin was influenced by the type and amount of carrier used. Dextrin was able to increase the solubility of artemisinin to a greater extent than PVP K-25 at all drug to carrier ratios used. The above results showed that not only the type of the carriers used was important, but also the amount used can influence the drug solubility (Corrigan, 1985). It is evident that at a ratio of 100 : 400 drug to carrier the solubility of artemisinin was optimum. The solubility of artemisinin in both carriers at a ratio of 100 : 400 is shown in Table 2.

*3.1.3.*DIFFERENTIAL SCANNING CALORIMETER (DSC) STUDIES

Fig 2 and 3 represent the DSC thermograms of pure artemisinin, PVP K-25, dextrin, physical mixture of artemisinin-PVP K-25 / artemisinin-dextrin and freeze dried product of artemisinin-PVP K-25 / artemisinin-dextrin respectively.

From Fig 2, it can be observed that the characteristic peak of artemisinin was clearly visible in the physical mixture and freeze dried product of artemisinin-PVP K-25 even in those powder with a high amount of PVP K-25 (1:4), indicating that there was no interaction between PVP K-25 and artemisinin. These results indicate that artemisinin was still in the crystalline form.

From the DSC thermograms in Fig 3, it can be observed that there was an endothermic peak at 157.7°C for artemisinin, while for dextrin, an endothermic peak was observed at 75°C-125°C indicating the presences of residual moisture in dextrin. In case of physical mixture of artemisinin-dextrin, the endothermic peak of artemisinin was intact with a negligible decrease in enthalpy of melting from 63.1 to 61.50J/g, indicating that there was no interaction between artemisinin and dextrin.

In case of freeze dried product of artemisinin-dextrin, it was observed that at a ratio of 1:4 and 2:3, the characteristic peak of artemisinin in the thermogram was absent. This indicates that artemisinin was no longer present in the crystalline form but was converted into the amorphous state (Mooter et al., 1998). The disappearance of the thermal features of the drug in the DSC thermogram indicated that the drug and the dextrin interacted with each others (Kumar & Mishra, 2005). Similar finding has been reported by Te Wierk et al. (1993) in the freeze drying of diazepam with amylodextrin.

While at ratios of 3:2 and 4:1 of artemisinin-dextrin, it can be observed that a small peak of artemisinin was recorded in the

DSC thermogram indicating the presence of artemisinin still in the crystalline form.

3.1.4. SCANNING ELECTRON MICROSCOPY (SEM) STUDIES

Fig 4 illustrated the SEM micrographs of artemisinin, PVP K-25, dextrin, their physical mixture and freeze dried product of artemisinin-PVP K-25 / dextrin. From the micrographs it can be noted that dextrin existed as small oval shaped particles. While in the physical mixture of artemisinin-dextrin the characteristic crystals of artemisinin were apparent. The freeze dried product of artemisinin-PVP K-25 also showed the characteristic of artemisinin crystals but were smaller in size. On the contrary, the freeze dried product of artemisinin-dextrin, appeared in the form of irregular particles in which the original morphology of both components were not visible at the ratio 1:4 and 2:3. But when the ratio of artemisinin to dextrin was increased (3:2) and (4:1), the characteristic crystals of artemisinin were clearly visible in Fig 5. Thus, based on the results obtained from the above mentioned, DSC, SEM and solubility studies, the artemisinin-dextrin freeze dried product at the ratio of 1:4 was selected for further investigation.

3.1.5. Study of effect of additional of cryprotectant

Molpeceres et al. (1996) and Ozaki and Hayashi, (1997) reported that for freeze dried products, addition of cryoprotectant was essential for the maintenance of the initial formulation characteristics. So, in the present study to enhance the solubility of the freeze dried artemisinin-dextrin powder, cryoprotectants were added.

Chacon et al. (1998) used mannitol and other cryoprotectants to enhance the stability of the freeze dried products of cyclosporine loaded poly (D, L lactide glycolide). Table 1 shows the formula used for the preparation of the freeze dried product of artemisinin-dextrin using different ratios of two cryoprotectant, mannitol or citric acid.

From Fig 6, it can be observed that both citric acid and mannitol at different ratios increased the solubility of artemisinin-dextrin freeze dried products. Each carrier was incorporated into the mixture of artemisinin-dextrin in water and then were freeze dried. The freeze dried powder containing citric acid was able to significantly increase the solubility of artemisinin more than the one with mannitol.

The increase in solubility was well supported by SEM and DSC studies as shown in Fig 7 and Fig 8 respectively. From Fig 5, it can be observed that the artemisinin freeze dried powder containing either citric acid (CA) or mannitol were present as irregular particles in which the original morphology of all components disappeared in the case of citric acid, tiny aggregate of amorphous small pieces of irregular size were present compared to mannitol. Therefore reduced particle size resulted in an increase in surface area responsible for enhancing the solubility of the drug (Ruan et al., 2005).

Fig (5) represent the DSC curves of pure artemisinin, dextrin, citric acid, mannitol and artemisinin-dextrin, freeze dried powder containing citric acid / mannitol at a ratio of 100 : 300 : 100. From the thermogram it is clear that the endothermic peaks at 154.7°C, 165°C and 156°C corresponding to the melting points of pure artemisinin, mannitol and citric acid respectively were observed. The DSC thermogram for the freeze dried products artemisinin-dextrin and artemisinin-dextrin-citric acid showed no characteristic endothermic peak. The disappearance of the specific peak of the drug indicates that the drug and the carrier interacted with each others (Kumar & Mishra, 2005). Whereas the DSC curves of the freeze dried product of artemisinin-dextrin-mannitol recorded a peak corresponding to artemisinin melting enthalpy. This indicates that artemisinin and the carrier did not interact with each other and artemisinin is still in its crystalline form.

4. DISSOLUTION

Fig 9 shows the dissolution profile of freeze dried powders of artemisinin-dextrin citric acid / mannitol and their physical mixtures at ratio of 100 : 300 : 100 and pure artemisinin. From the Figure it is evident that the dissolution of freeze dried powders was faster compared to either physical mixture or drug alone. From Fig 10, it can be observed that the freeze dried product of artemisinin-dextrin-citric acid prepared at 80°C displayed faster rates than freeze dried product prepared at 60°C and freeze dried product of artemisnin-dextrin-mannitol prepared at 60°C and 80°C. The above results were in line with findings reported by Corrigan (1985) that the physiochemical

characteristics of the drug are affected by the method of its preparation, the type and properties of the polymer used.

The high rate and the extent of dissolution from freeze dried powder of artemisinin-dextrin may be attributed to the hydrophillic effect of dextrin which can reduce both the hydrophobicity of artemisinin as well as interfacial tension between artemisinin and the dissolution medium, so the particle size is reduced to molecular size, thus faster dissolution rate can be achieved.

5. CONCLUSION

From the above results it can be concluded that freeze drying technique could be employed to prepare artemisnin-dextrin freeze dried product, which was capable of increasing the solubility and dissolution rate of artemisinin. Moreover, incorporating of citric acid into the mixture of artemisinin-dextrin lead to a further enhancement in the dissolution rate.

Table 1. Composition details of artemisinin : dextrin : citric acid/mannitol used for the preparation of freeze dried powder.

Ratio	Artemisinin (mg)	Dextrin (mg)	Citric Acid or Mannitol (mg)
1:3:1	100	300	100
1: 2.75 : 1.25	100	275	125
1: 3.25 : 0.75	100	325	75

Table 2.Solubility of plain artemisinin in pure artemisinin and artemisinin-carrier at a ratio of drug to carrier 1:4

Preparation	Solubility (µg/ml) Mean±SD, n=3
Pure artemisinin	10.50±0.03
Freeze dried of artemisinin - Dextrin	79.55±0.05
Freeze dried of artemisinin - PVP K-25	23.45±0.03

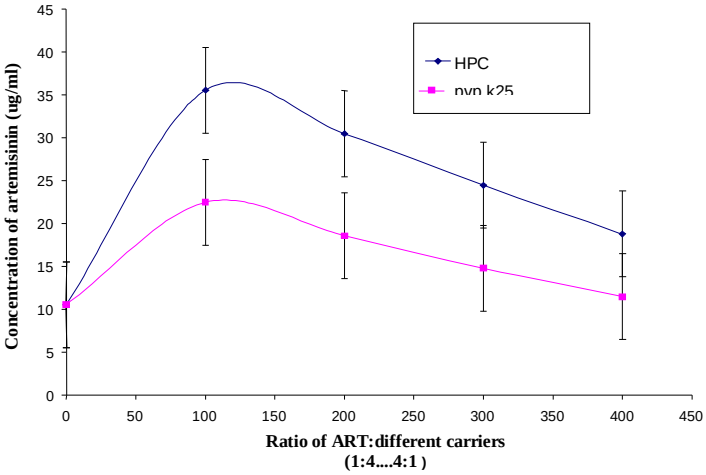

Figure1.Comparative solubility profiles of artemisinin in different carriers (HPC/PVP K- 25) prepared using water as a solvent

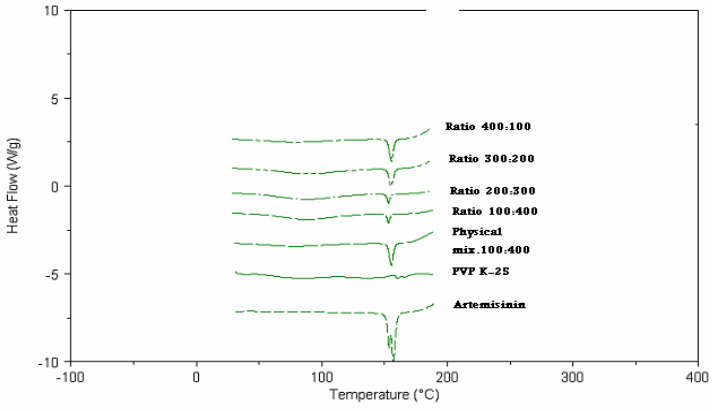

Figure.2 Thermograms of artemisinin and artemisinin-PVP K-25 at different ratio prepared using water as solvent

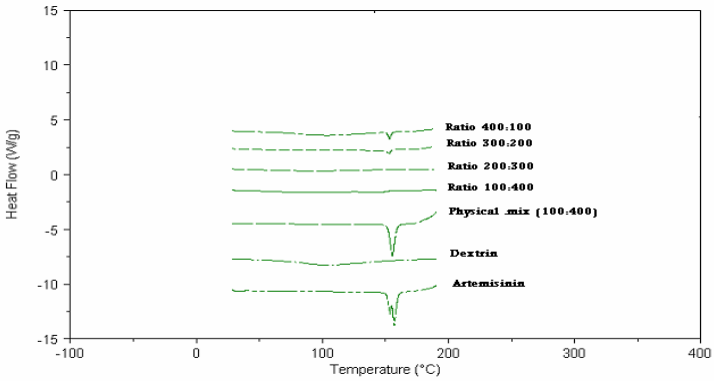

Figure.3Thermograms of artemisinin and artemisinin-dextrin at different ratios

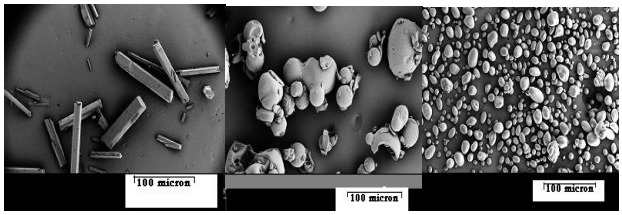

Artemisinin PVP K-25 Dextrin

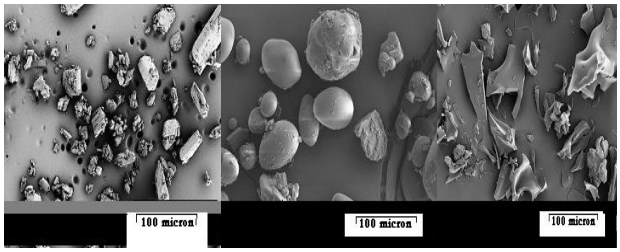

PM (ART-PVP K-25) PM (ART-Dextrin) ART-PVP K-25 FD

Figure.4 Micrographs of artemisinin, carriers, physical mixture (PM) of artemisinin-different carriers and freeze dried (FD) of product of artemisinin-PVP K-25 prepared

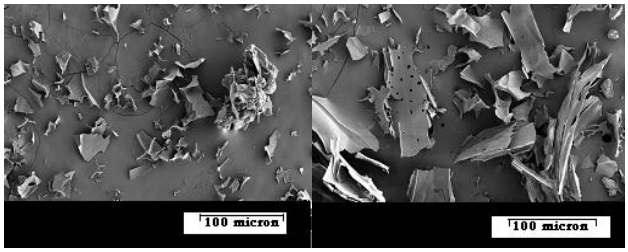

ART-Dextrin (1:4) FD ART-Dextrin (2:3)FD

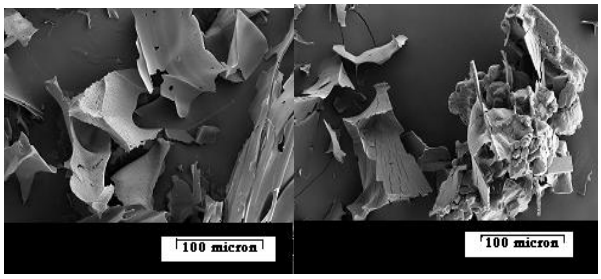

ART-Dextrin (3:2) FD ART-Dextrin (4:1) FD

gure.5 Micrographic of artemisinin- different freeze dire wder at different ratios

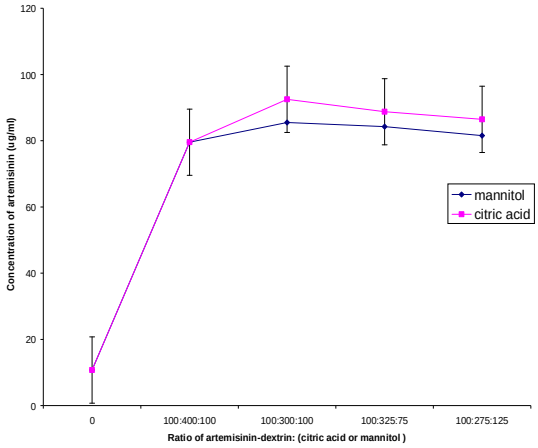

Figure.6 Artemisinin solubility in ART:dextrin:citric acid/mannitol freeze dried powder

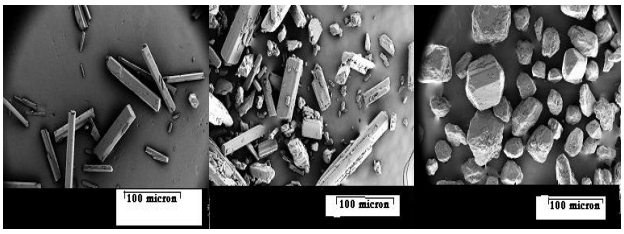

Artemisinin Mannitol Citric Acid

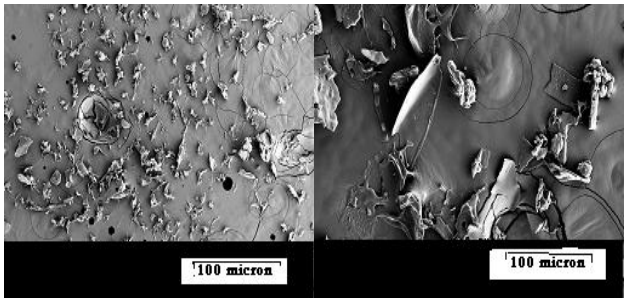

Artemisinin-Dextrin–CA (FD) Artemisinin-Dextrin-Mannitol (FD)

Figure.7 Micrographs of pure artemisinin, mannitol, citric acid and freeze dried product of artemisinin-dextrin-citric acid / mannitol

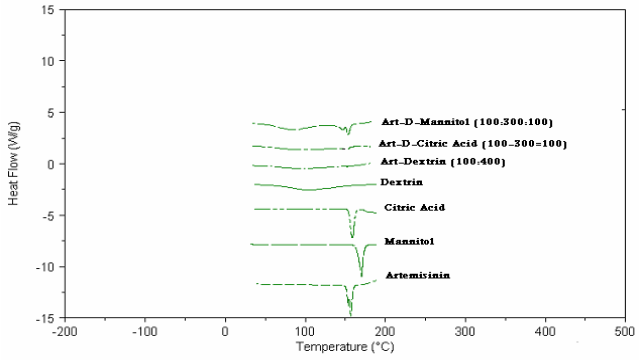

Figure. 8 Thermograms of artemisinin and artemisinin-dextrin (D)-mannitol / citric acid at ratio of 1:3:1

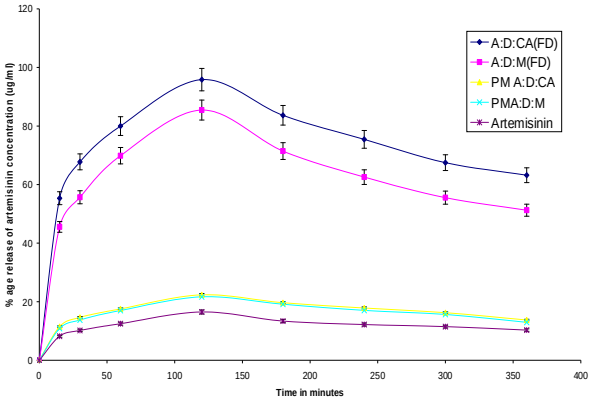

Figure.9 Compartive dissolution profile of artemisinin from freeze dried product and physical mixture (PM) of artemisinin-dextrin-citric acid / mannitol (A:D:CA/M) at ratio 1:3:1

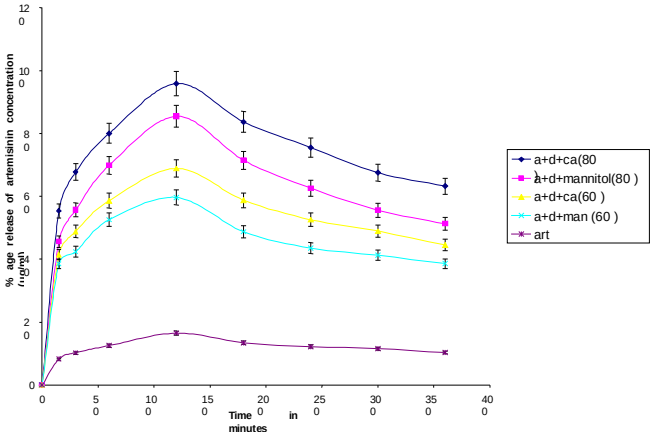

Figure.10 Comparative dissolution profile of artemisinin from pure artemisinin and in artemisinin-dextrin-citric acid / mannitol freeze dried product (A-D-CA/M) at ratio of 1:3:1 using water at 80°C and 60°C

6. REFERENCE

[1]Chacon, M., Malpeceres, J., Berges, L., Guzman, M. & Arbeturas, M.R., (1998). Stability and freeze drying of cyclosporine leaded poly (D, L Lactide-glycolide) carriers. *Eur J Pharm Sci* **8**, 99 – 107.

[2]Corrigan, O.I. (1985). Mechanism of fast release solid dispersion. *Drug Dev Ind Pharm* **11**, 697 – 724.

[3]Iman, S. A. and Mona, H.A. (2007). In vitro and in vivo evaluation of fast-disintegrating lyophilized dry emulsion tablet containing griseofulvin. *Eur J Pharm Sci* **32**(1), 58-68

[4]Jaccard, T.T. & Leyeder, J., (1985). Une Nouvelle Forme *Galerique* : Le Lyoc. *Ann Pharm* Fr (**43**)2 : 123–131.

[5]Klayman, D.L. (1985). Qinghasou (Artemisinin) : An antimalaria drug from China. *Science* **228**, 1049-1055.

[6]Kumar, S. G. V. & Mishra, D. N. (2005). Preparation and evaluation of solid dispersion of meloxicam with skimmed milk, *Yakugaku Zasshi* **126** (2), 93–97. The pharmaceutical society of Japan

[7]Molpeceres, J., Guzman, M., Bustamante, P. & Aberturas, M.R. (1996). Exothermic-endothermic heat of solution shift of cyclosporine A related to poloxamer 188 behavior in aqueous solution. *Int J Pharm* **130**, 75 – 81.

[8]Monkhouse, D.C. & Lach, J.L. (1972). Use of adsorbants in enhancing of drug dissolution II. *J Pharm Sci* **61**, 1435 – 1441.

[9]Mooter, V.G., Augustigins, P., Blatun, N. & Kinget, R. (1998). Physio-chemical characterization of solid dispersions of temazepam with polyethylene glycol 6000 and PVP K-30. *Int J Pharm* **164**, 67–80.

[10]Ohshima H., Miyagishima A., Kurita T., Makino Y., Lawa Y., Sonobe T. and Itai S. (2009). Freeze dried nifedipine-lipid nanoparticles with long term nano-dispersion stability after reconstitution. *Int J Pharm* **337** (1-2), 180-184.

[11]Ozaki, K. & Hayshi, M, (1998). The effect of glucose oligomers (maltodextrin) on freeze drying liposomes. *Chem Pharm Bull* **45**, 165 – 170.

[12]Qinghasou Antimalaria Coordinating Research Group (1979). Antimarial Studies on qinghasou. *Chin Med J* **92**, 811-816.

[13]Ruan, L.P., Yu, B.Y., Fu, G.M. & Zhu, D. (2005). Improving the solubility of ampelopsin by solid dispersions and inclusion complexes. *J Pharm Biomed Anal* **38**, 457 – 464.

[14]Shoukri A.R., Iman S.A. and Shamma R.N. (2009). In vitro and in vivo evaluation of nimesulide lyophilized orally disintegrating tablets. *Eur J Pharm Biopharm* **73**(1), 162-171.

[15]Tachibana, T. & Nakamura, A., (1965). A method for preparing an aqueous colloidal dispersion of organic materials by using water-soluble polymers : Dispersion of beta-carotene by polyvinyl pyrolidone. *Kolloid-Z Polym* **203**, 130–133.

[16]Te Wierik, G. H. P., Elssens, A. C., Besemer, A. C. & Lerk, C. F. (1993). Preparation, characterization and pharmaceutical application of linear Dextrins II. Complexation and dispersion of drug with amylodextrin by freeze-drying and kneading. *Pharm Res* **10**, 1280-1284.

[17]Topaloğlu, Y., Yenev, G. & Gönüllü, U. (1999). Inclusion of ketoprofen with skimmed milk by freeze drying. *IL Pharmaco* **54**, 648 – 652.

[18]Ttulaer, H.A.C., Zuidema, j. & Lugt, C. B. (1991). Formulation and pharmacokinetics of artemisinin and its derivatives. *Int J Pharm* **69**, 83-92.

[19]Van Eerdenburgh B., Froyen L., Martens J.A., Balton, N., Augustijin P., Brewster M. and Vanden Mooter G. (2007). Characterization and physicochemical properties and pharmaceutical performance of sucrose co-freeze-dried solid nanoparticulate powders the anti-HIV Loviride prepared by media milling. *Int J Pharm* **338** (1-2), 198-206.

[20]World Health Organization. (1994). The role of artemisinin and it's derivatives in the current treatment of malaria. Report of an informal consultation. Geneva. WHO/Mal/94.1067.

[21]Zhao, S.S. & Zeng, M.Y. (1985). High performance liquid chromatographic determination of artemisinin (qinghaosu). *Planta Medica* **(3).** 233-237

Enzymatic Degradability of Corn Starch Nanocomposites

I. Alemzadeh[*,1], M. Vossoughi[1,2] A. Heydari[1,3], H. Ostadi[1]

1 Department of Chemical and Petroleum Engineering, Sharif University of Technology, Azadi Avenue, Tehran, Iran

2 Institute for Biotechnology and Environment (IBE), Sharif University of Technology, Azadi Avenue, Tehran, Iran

3 Department of Chemical Engineering, University of Mohaghegh Ardabili, Daneshgah Avenue, Ardabil, Iran

ABSTRACT

Corn starch nanocomposites were placed in a solution containing alpha-amylase (EC 3.2.1.1) and the rates and extents of enzymatic degradation were measured according to weight reduction and reducing sugars production. Alpha-amylase enzyme was obtained from *Bacillus licheniformis*. According to central composite design (CCD), nine samples with different Na-Montmorillonite (Na-MMT) and glycerol contents were prepared using casting method and experiments were studied in three replications. Results were analyzed by response surface methodology (RSM).

By increasing glycerol content, the weight loss of the films in both water and enzyme solution increased. For each sample, the weight reduction in enzyme solution was significantly higher than results of water solubility which indicate the effect of enzyme degradation. Also, by increase in nanoparticle contents, resistance against enzyme solution will increase and weight loss will decrease. The result demonstrated that increase in enzymatic degradation is related to penetration of enzyme solution in the matrix of polymer.

Keywords

Corn starch, Nanocomposite, Enzymatic degradation, Water sensitivity, Alpha-amylase

1. INTRODUCTION

Biodegradability of biopolymers make them environmental friendly packaging materials [1]. One of the most investigated items in this category is starch, owing to its wide availability, good biodegradability as well as low cost. Starch films are very sensitive to water which limits their applications for packaging[2].

Enzymatic degradation could be used as an accelerated test method and as an alternative for biodegradability in soil. Alpha-amylase is one of the enzymes could be produced by some microorganisms. Enzymatic degradation, using α-amylase and/or amyloglucosidase is the reason to explain the biodegradability of starch based polymers. Starch is composed of two types of complex carbohydrate polymers of glucose, namely amylose (20–30%), a mostly linear α-D-(1,4)-glucan, and amylopectin (70–80%), a highly branched α-D-(1,4)-glucan which has α-D-(1,6) linkages at the branch point [3, 4]. Amylases are the class of glucosidase hydrolyzing enzymes that cleave the α-1,4 and/or α-1,6 glucosidic linkages in starch and other polysaccharides. Amyloglucosidase hydrolyses the last α-1,4 glucosidic linkages at the non-reducing end of amylose and amylopectin as well as the α-1,6 linkages in amylopectin, however the rate of hydrolysis of α-1,4 bonds is higher than of α-1,6 bonds. Some investigation on the enzymatic hydrolysis of starch blends by the abovementioned enzymes preformed in the literature. Effects of Na-MMT and SiO2 nanoparticles on hindering polyvinyl alcohol/starch hydrolysis by α-amylase and amyloglucosidase were reported [5, 6].

The object of current research is enzyme degradation of starch biopolymers plasticized with glycerol and reinforced using Na-MMT. The central composite design (CCD) at three levels combined with response surface methodology (RSM) has been applied in this investigation. The effects of Na-MMT and glycerol contents on enzyme degradation because of alpha-amylase (EC 3.2.1.1, 1,4-a-D-glucan glucanohydrolase) obtained from *Bacillus Licheniformis* were studied.

2. MATERIALS AND METHODS

2.1. Materials

Corn starch (11% moisture) was obtained from Glucosan (Ghazvin, Iran). Na-MMT Cloisite was purchased from Southern Clay Products (USA). Food grade glycerol as a plasticizer was prepared from Merck Company. Bacillus licheniformis BBRC 100053, the microorganism used in this study was obtained from Biochemical and Bioenvironmental Research Center, a Local Culture Collection at Sharif University of Technology.

2.2. Medium composition and culture condition

The culture was maintained on nutrient broth medium at 30°C for 2 days. According to our preliminary tests, the most appropriate medium for the growth and alpha-amylase production is composed of: corn starch 10 g/l, peptone 5 g/l, NaCl 1.5 g/l, CaCl2 0.1 g/l, yeast extract 3 g/l, KH2PO4 0.5 g/l and MgSO4.7H2O 0.5 g/l. After incubation of 72 h at 37°C under shaking condition (150 rpm), the culture was centrifuged (20 min, 4000 rpm) and the cell-free supernatants were used as a crude enzyme solution for enzymatic degradation tests.

2.3. Film preparation

The specified amount of Na-MMT (0, 2.5 and 5 %) was added to 99.5 g of distillated water under rigorous mixing for 20 min at 80°C. Then, the resulted aqueous suspension homogenized for 20 min at 80°C via sonication method to make a uniform solution. Then proper amount of glycerol (25, 30 and 35 %) with 5 g of pristine corn starch was added and mixed by stirrer for 10 min and sonicated for 20 min at room temperature. The final mixture placed in water bath (80 ±0.2°C) under mild stirring for 30 min. The gelatinized solution was gently mixed in order to release bubbles. The casting solution was poured into polystyrene petri dishes and placed on a flat surface in the laboratory (23 ± 2 °C, 52 ± 3 % RH). All samples were prepared three times and their average results were reported. After 36 hours, films were carefully separated and stored in poly ethylene bags. All films were prepared in triplicates. The prepared samples were designated with label such as G30C2.5, where G and C referred to glycerol and clay, respectively and the number 30 indicated 30% glycerol and 2.5 referred to 2.5% Na-MMT.

2.4. FTIR Test

Some samples before and after degradation were examined by FTIR spectroscopy in the form of KBr pellets were recorded using an ABB Bomem MB-100 FTIR spectrophotometer.

2.5. Enzyme degradation

Samples were cut into 2×2 cm square specimens and dried at 37 °C for 2 h, weighted, and immersed in the conical flasks containing 80 cc of crude enzyme solution in non sterile conditions. The 27 flasks related to nine samples with their replications simultaneously were placed in a shaking incubator (150 rpm and 37 °C). The doors of beacons were sealed to prevent solution evaporation, which causes overestimation in measuring the concentration of reducing sugars. At intervals, 1 cc of each flask was analyzed to determine the concentration of reducing sugars. In parallel, the samples were removed and rinsed with distilled water, and then samples were dried at 37 °C for 2 h to reach constant weight. The degree of enzymatic degradation (DED) was calculated using the following equation:

$$\text{DED}(\%)=\frac{\text{Weight of initial sample-Weight of sample at interval}}{\text{Weight of initial sample}}\times 100$$

Finally, samples were returned to their flasks and 1 cc of crude enzyme solution was added to all of the flasks. The enzymatic degradation studies were carried out for 24 h. Slope of produced glucose over time was considered and reported as enzymatic degradation rate of the samples.

In the next phase, the above mentioned experiments were carried out using distillated water to obtain the weight loss of the samples because of solubility in water. The percentage of weight loss in water was calculated as follows:

$$\text{Solubility}(\%)=\frac{\text{Weight of initial sample-Weight of sample at interval}}{\text{Weight of initial sample}}\times 100$$

The difference between enzymatic degradation and solubility could be considered as the neat enzyme role in degradation and weight loss of starch nanocomposites.

3. RESULTS AND DISCUSSIONS:

3.1 Enzymatic degradation

Effects of glycerol contents on weight loss of samples containing 2.5% Na-MMT were presented in Figure 1(a). By increasing in glycerol content, the weight loss of the films in both water and enzyme solution increased. For each sample, the weight losses in water and enzyme solution were significantly different. Figure 1(b) indicates the role of Na-MMT in reduction of weigh loss for samples containing 30% glycerol. By increase in nanoparticle contents, resistance against enzyme solution will increase and weight loss will decrease. Results of degradation of samples in enzyme solution and weight loss in water for 24 h are presented in Table 1.

Results are in good agreement with published results [5, 6]. Also, by incorporation of nanoparticles, the water solubility will decrease as reported for ZnO [8].

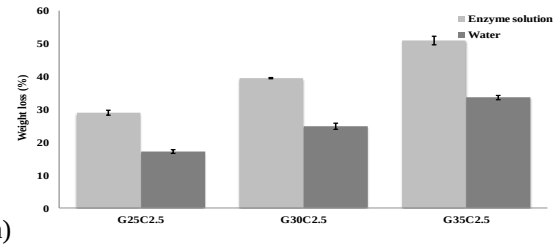

a)

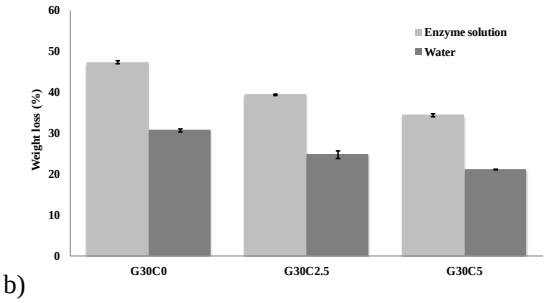

b)

Figure 1: Figure illustrating the weight loss of the samples in water and enzyme solution affected by a) glycerol content and b) Na-MMT content

Table 1: Table illustrating degradation of samples in Enzyme solution and weight loss in water.

Sample	Degradation in enzyme solution for 24 h (%)	Degradation in water for 24 h (%)	Degradation in enzyme solution- degradation in water (%)
G25C0	38.83±0.97 aA	23.79±0.86 aA	15.04±0.32 aA
G25C2.5	28.85±0.74 bA	19.08±0.87 bA	9.87±1.60 bA
G25C5	23.30±0.47 cA	17.67±1.12 bA	5.63±1.49 cA
G30C0	47.24±0.42 aB	30.72±0.69 aB	16.52±1.10 aB
G30C2.5	39.36±0.17 bB	24.79±0.75 bB	14.57±0.64 bB
G30C5	34.34±0.38 cB	21.06±0.43 cB	13.29±0.34 cB
G35C0	55.03±2.44 aC	35.43±0.81 aC	19.60±3.21 aC
G35C2.5	50.90±1.32 bC	32.62±1.25 bC	18.28±0.41 aC
G35C5	42.66±1.16 cC	26.28±0.79 cC	16.38±1.85 bC

*Means at same glycerol content, with the same lower case letter are not significantly different ($P > 0.05$).**Means at same nanoparticles content, with the same capital letter are not significantly different ($P > 0.05$).

3.2. FTIR Spectrum

The FTIR spectrums of pristine Na-Montmorillonite and some undegraded and partially degraded G25C5 samples are shown in Fig. 2.

Some typical absorbance bands of Na-MMT silicates occurred in the following bands: O-H symmetrical vibration around 3630 cm-1 in the crystal layer; the broad peak around 3430 cm-1 corresponding to the vibration of water absorbed by the crystal layer and Si-O vibration of strong absorption around 1008 cm-1.

For the starch nanocomposite, the broad band in the region of 3430 cm-1 is due to the O-H stretching vibration which is related to hydroxyl groups present on starch–glycerol films[9].

The shift of band 3630 cm-1 from the free OH group of pristine MMT surface, to a lower frequency, 3430 cm-1 indicates the interaction between starch and MMT, and similar finding was reported in Liu et al.'s work [10]. Therefore, it could be concluded that the casting of corn starch to nanocomposite included the formation of hydrogen bonds and ternary interactions in starch/glycerol/Na-MMT system.

After 24 h of biodegradation in enzyme solution for G25C5 sample, the intensity of the peaks at 1115 and 1040 cm-1 decreased which are related to glycosidic linkages of starch. These reductions could be explained because of the action of α-amylase in cleaving the glycosidic linkages [11]. In addition, the intensity of the peak around 3430 cm-1 decreased which means that by degradation of starch by enzymes, the amount of water and glycerol in the undegraded films will be diminished and also part of reduction in this peak is related to the leaching of glycerol [12].

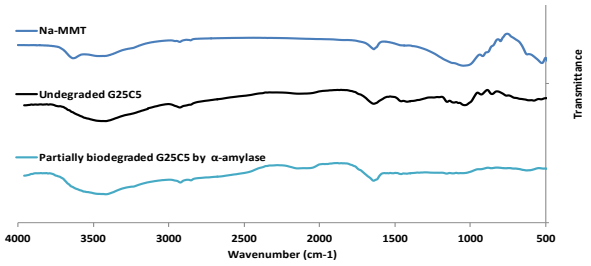

Figure 2: Figure illustrating the FTIR spectrums of Na-MMT and G25C5 before degradation and after partially degradation by alpha-amylase.

4. REFERENCES

[1]Avella, M., et al., *Biodegradable starch/clay nanocomposite films for food packaging applications.* Food Chemistry, 2005. 93(3): p. 467-474.

[2]Prachayawarakorn, J., et al., *Effect of jute and kapok fibers on properties of thermoplastic cassava starch composites.* Materials & Design, 2013. 47(0): p. 309-315.

[3]Saibene, D., et al., *Iodine-binding in granular starch: Different effects of moisture content for corn and potato starch.* Starch/Staerke, 2008. 60(3-4): p. 165-173.

[4]Hoover, R., *Composition, molecular structure, and physicochemical properties of tuber and root starches: A review.* Carbohydrate Polymers, 2001. 45(3): p. 253-267.

[5]Taghizadeh, M.T., Z. Abbasi, and Z. Nasrollahzade, *Study of enzymatic degradation and water absorption of nanocomposites starch/polyvinyl alcohol and sodium montmorillonite clay.* Journal of the Taiwan Institute of Chemical Engineers, 2012. 43(1): p. 120-124.

[6]Abbasi, Z., *Water resistance, weight loss and enzymatic degradation of blends starch/polyvinyl alcohol containing SiO2 nanoparticle.* Journal of the Taiwan Institute of Chemical Engineers, 2012. 43(2): p. 264-268.

[7]Miller, G.L., *Use of dinitrosalicylic acid reagent for determination of reducing sugar.* Analytical Chemistry, 1959. 31(3): p. 426-428.

[8]Nafchi, A.M., et al., *Antimicrobial, rheological, and physicochemical properties of sago starch films filled with nanorod-rich zinc oxide.* Journal of Food Engineering, 2012. 113(4): p. 511-519.

[9]Zhang, Y. and J.H. Han, *Plasticization of Pea Starch Films with Monosaccharides and Polyols.* Journal of Food Science, 2006. 71(6): p. E253-E261.

[10]Liu, H., et al., *Glycerol/starch/Na+-montmorillonite nanocomposites: A XRD, FTIR, DSC and 1H NMR study.* Carbohydrate Polymers, 2011. 83(4): p. 1591-1597.

[11]Azevedo, H.S., F.M. Gama, and R.L. Reis, *In Vitro Assessment of the Enzymatic Degradation of Several Starch Based Biomaterials.* Biomacromolecules, 2003. 4(6): p. 1703-1712.

[12]Torres, F.G., et al., *Biodegradability and mechanical properties of starch films from Andean crops.* International Journal of Biological Macromolecules, 2011. 48(4): p. 603-606.

Production of Pure Nano Iron by using Ball Milling Machine, Chemical Batch Reactor and K-M Micro Reactor

Mohamed Ahmed AbdelKawy[1], Ahmed El Shazly[2], Yehia El Shazly[3]

ABSTRACT

In this study, pure nano iron was formed by two techniques: top to down and bottom up technique .top to down including production of nano iron by using ball mill machine and bottom up including two methods batch and K-M micro reactor. Different techniques were used for investigation and characterization of the produced nano iron particles such as SEM, XRD, UV, TEM and PSD. The produced Nano particle using micro mixer showed better characteristics than those produced using batch reactor and ball mill in different aspects such as homogeneity of the produced particles, particle size distribution and size, as 10nm particle size were obtained. The results showed that 10 nm core diameter were obtained using Micro mixer as compared to 40 nm and 80 nm core diameter using ball mill and batch reactor respectively.

Keywords

Nano iron , batch reactor , ball milling , K-M Micro reactor

1. INTRODUCTION

Nanotechnology is the engineering and art of manipulating matter at the nanoscale (1–100 nm) For environmental applications, nanotechnology offers the potential of novel functional materials, processes and devices with unique activity toward recalcitrant contaminants, enhanced mobility in environmental media and desired application flexibility [1-8]. Many nano-based environmental technologies (e.g., sensors, sorbents, and reactants) are under very active research and development, and are expected to emerge as the next generation environmental technologies to improve or replace various conventional environmental technologies in the near future [1-8].

Iron nanoparticles technology represents perhaps one of the first generation nanoscale environmental technologies [4-6]. Over the last few years, various synthetic methods have been developed to produce iron nanoparticles [1-8], modify the nanoparticles surface properties [8], and enhance the efficiency for field delivery and reactions. Extensive laboratory studies have demonstrated that nanoscale iron particles are effective for the transformation of a wide array of common environmental contaminants such as chlorinated organic solvents, organochlorine pesticides, PCBs, organic dyes, various inorganic compounds and metal ions such as As(III), Pb(II), Cu(II), Ni(II) and Cr(VI). Several field tests have

demonstrated the promising prospective for in situ remediation [8]

Many research papers on applications of iron nanoparticles have been published over the last few years. While several types of iron nanoparticles are available on the market, information on the nanoparticles synthesis and properties is still limited in peer reviewed journals. Fundamental information on characterization methods has not been well documented. Quality control and insurance is rapidly becoming a major issue as nanoparticles are being used in more and more projects. Objective of this work is to produce nano iron by using different teqniches for getting high value of nano iron produced from each teqniches

2. EXPERIMENTAL METHODS

2.1 Top down method

2.1.1 Mixing by ball mill

In this method, commercial pure iron was milled by using planetary ball milling machine as shown in **Fig.1**, this mill consists of 4 jars, two of the them fill with iron mixed with ethanol to prevent oxidation of iron and other fill with sand for stability under high centrifugal force, two forces were affected in decreasing the size of this pure iron, one high impact force due action of balls and friction force due to centrifugal force , two different ball size using for milling 30 mm and 10 mm .after milling time , produced iron was dried under hot plate and then characterized.

2.2 Bottom up process

2.2.1 Mixing by batch reactor

For the synthesis of nanoscale Zero Valent Iron **(**nZVI) by using batch rector ; 4.83 g $FeCl_3.6H_2O$ was dissolved in a 4/1 (v/v) ethanol/water mixture (216 ml ethanol + 54 ml deionized water) and stirred well by using magnetic stirr[15] . On the other hand, 0.614 M sodium borohydride solution was prepared i.e., 6.30 g $NaBH_4$ was dissolved in 270 ml of deionized water [15]. The borohydride solution is poured in a burette and added drop by drop (1drop per 2 seconds) into iron chloride solution with pipe attached with valve. After the first drop of sodium borohydride solution, black solid particles immediately appeared and then the remaining sodium borohydride is added completely to accelerate the reduction reaction. The mixture was left for another 10 minutes of stirring after adding the whole borohydride solution[15]. Magnetic separation technique was used to separate the black iron nanoparticals from the liquid phase as shown in **Fig.2**. The solid particles were washed three times with 25 ml portions of absolute ethanol to remove all of the water. This washing process is probably the key step of synthesis since it prevents the rapid oxidation of zero valent iron nanoparticals [15].

The synthesized nanoparticles were finally dried in vacuum oven at 70 ºC overnight.

2.2.2 Mixing by K-M Mixer

For production of nanoiron by using K-M Mixer [16] as shown **Fig.3**, concentration of ferric chloride and sodium borohydride is the same like at batch reactor at constant flow rate 373 ml/h. The solid particles were washed three times with 25 ml portions of absolute ethanol to remove all of the water. This washing process is probably the key step of synthesis since it prevents the rapid oxidation of zero valent iron nanoparticals. The synthesized nanoparticals were finally dried in vacuum oven at 70 ºC overnight.

3. RESULTS and discussions:

Figure.1 shows Ball milling machine

Figure. 1

Figure.2 shows batch reactor

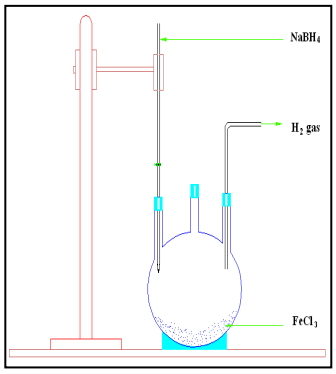

Figure. 2

Figure 3 shows K-M Micro reactor

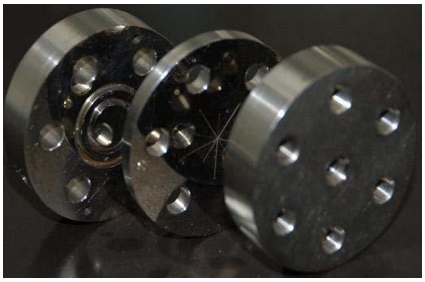

Figure.3

Figure .4 shows TEM images of nano iron after mixing in a-K-M Micro reactor ,b-ball milling and c-batch reactor

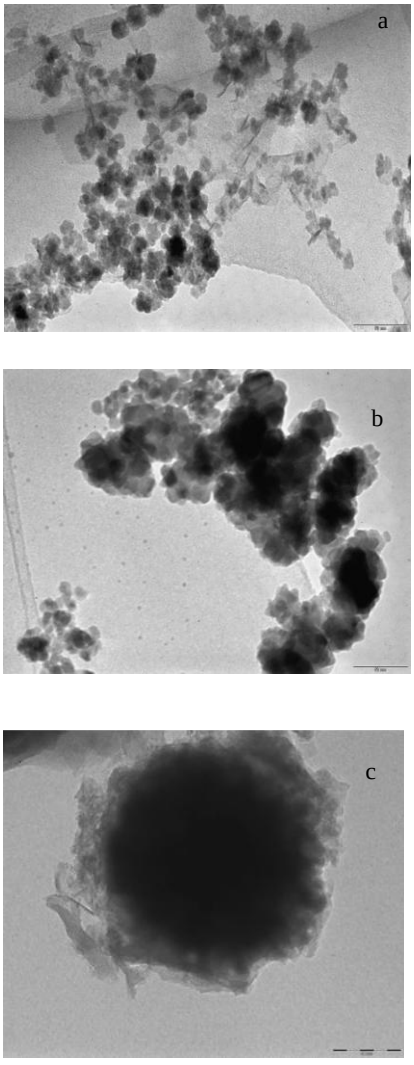

Figure. 4

TEM images shows very clear images of nano iron after different techniques, from this images

the size of nano iron after mixing in K-M Micro reactor is 10 nm(fig.3-a), after milling is 40nm (fog.3-b)and after batch reactor is 80 nm (fig-3-c)

So nano iron (10-20 nm) was synthesized in ethanol medium by borohydride reduction method under atmospheric conditions by using K-M micro mixer with compared with batch reactor and ball milling .K-M mico mixer gives many advantages like that short time of the reaction , decreasing of nano iron size and normal conditions. It was observed that iron nanoparticles are mainly in zero valent oxidation state and that no significant oxidation took place for days of storage under atmospheric conditions due steady black color of iron. The characterization of nano iron was performed using XRD, SEM, TEM, UV-Vis studies and indicated partial dispersion of the chainlike structure of iron nanoparticles. From the results of TEM, it was observed that iron nanoparticles without agglomeration. The iron nanoparticles tend to form chain like structures with a particle size in the range 10-20 nm. The nanoparticles have strong tendency to form microscale aggregates likely due to strong surface charges. By increasing sodium bothydried and flow rates, yield of nano iron will increase and average size decrease.

4. ACKNOWLEDGMENTS

The authors thank Prof.Kazuhiro Mae, Environmental Process Engineering Lab., and Dr. Satoshi Watanabe, Surface Control Lab., Chemical Engineering Department, Graduate School of Engineering, Kyoto University for recommendations, advices and supplies us K-M micro reactor for producing of nano iron.

5. REFERENCES

[1] Yuan-Pang Sun a, Xiao-qin Li , Jiasheng Cao , Wei-xian Zhang , H. Paul Wang (2006) '*Characterization of zero-valent iron nanoparticles*', Advances in Colloid and Interface Science 120 47–56

[2] R. Yuvakkumar, , V. Elango, V. Rajendran, N. Kannan (2011) ' *Preparation and characterization of zero valent iron nano particles'* , Digest Journal of Nanomaterials and Biostructures Vol. 6, No 4, 2011, p. 1771-1776

[3] H. Nagasawa, N. Aoki, K. Mae (2005) '*Design of a new micromixer for instant mixing based on the collision of micro segments'* ,Chem.Eng.Technol,28,No.3

[4] A. R. Rahmani, H.R. Ghaffari, M.T. Samadi '*A Comparative study on arsenic (III) removal from Aqueous Solution using nano and micro sized zero valent iron* '**,** Iran. J. Environ. Health. Sci. Eng., 2011, Vol. 8, No. 2, pp. 175-180.

[5] Xiao-qin Li, Daniel W. Elliott, and Wei-xian Zhang' *Zero-Valent Iron Nanoparticles for Abatement of Environmental Pollutants'* Materials and Engineering Aspects Critical Reviews in Solid State and Materials Sciences, 31:111–122, 2006.

[6] Wan Zuhairi Wan Yaacob, Noraznida Kamaruzaman, Abdul Rahim Samsudin'*Development of Nano-Zero Valent Iron for the Remediation of Contaminated Water'* Chemical Engineering Transactions, VOL. 28, 2012.

[7] A. Akbari, , F. Mohamadzadeh '*New Method of Synthesis of Stable Zero Valent Iron Nanoparticles (Nzvi) by Chelating Agent Diethylene Triamine Penta Acetic Acid (DTPA) and Removal of Radioactive Uranium From Ground Water by using Iron Nanoparticle'*, JNS 2 (2012) 175-181.

[8] Wei-xian Zhang '*Nanoscale iron particles for environmental remediation: An overview* 'Review Journal of Nanoparticle Research **5:** 323–332, 200

Electrochemical preparation process of Mg-La alloys for solid hydrogen storage

M. Sahli[1], K. Chetehouna[2], F. Faubert[3], N. Bellel[1], N. Gascoin[2]
[1]Laboratoire de Physique Energétique, Université de Constantine 1, Algeria
[2]INSA Centre Val de Loire, Univ. Orléans, PRISME, EA 4229, F-18020, Bourges, France
[3]Univ. Orléans, GREMI, UMR 7343, F-18020, Bourges, France
sahlimounir@umc.edu.dz

ABSTRACT

The objective of this work is to characterize Magnesium-Lanthanum alloy elaborated by means of an electrodeposition technique using an aqueous solution based on Magnesium chloride and Lanthanum(III) Nitrate. The Mg-La alloy is deposited on a copper cathode plate used as a cathode. Chemical composition and structure as well as the morphology are investigated respectively by EDS, XRD, FTIR and SEM.

EDS analysis shows the presence of three major elements (Mg, La and O) and a little amount of Cl. Morphological characterization reveals that heterogeneous chemical structures are formed on the surface of sample.

X-ray results showed that the obtained deposit has two phases, which are $Mg(OH)_2$ and $La(OH)_3$.

FTIR analysis confirms the presence of the two phases identified in XRD diffractogram.

This study is a preliminary work to investigate the use feasibility of the obtained samples as potential materials for the hydrogen storage.

Keywords

Mg-La alloys, Electrodeposition, Magnesium hydroxide, Lanthanum hydroxide.

1. INTRODUCTION

Magnesium is the 8th most abundant element in the Earth's crust and the 9th most abundant element in the universe [1].

It is characterized by various properties for instance a low density, a low cost, a very good malleability and ductility and an environmentally friendly nature [2-4]. Magnesium is very chemically active and used in pyrotechnic and incendiary devices.

It is alloyed with other metals such as aluminum, manganese, zircon, zinc, rare-earth metals and thorium. Magnesium and its alloys have the advantageous properties such as low density, high specific strength, good castability, and excellent machinability. They have a broad potential of application and development in marine, automotive, opto-electronic and hydrogen storage materials [5-11]. The addition of rare-earth elements to Mg has attracted considerable attention in the past few years [12-15].

Usually, the elaboration processes of Mg alloys can be classified into three methods: physical, mechanical and chemical. Of these methods, the electrodeposition, which is a much less expensive technique that can be easily implemented on a large scale and can be generally employed over a wide temperature range.

The main objective of this study is to characterize Magnesium-Lanthanum alloys elaborated by means of an electrodeposition technique.

2. EXPERIMENTAL PROCEDURE

Magnesium chloride hexahydrate ($MgCl_2.6H_2O$) and Lanthanum nitrate ($La(NO_3)_3.6H_2O$) from Merck Group were employed as received. The solutions were prepared in deionized water, obtained from a Medica Lab Elga deionizer system. A mass of 16.24 g of $MgCl_2.6H_2O$ and a mass of 4.32 g of $La(NO_3)_3.6H2O$ were dissolved in 34 mL of ultra-pure water at ambient temperature (23 °C). The obtained aqueous solutions with pH=6 were prepared for electrodeposition process.

The electrodeposition process consists in a cylindrical electrolysis chamber. A copper cathode plate and a tungsten thread anode, connected to a conventional potentiometric power source, were used to ensure the deposition of Mg-La alloys. The potential value selected was 3 Volts. The deposition experiment was performed during 8 h at room temperature. Figure 1 shows a photograph and a schematic overview of the described experimental setup.

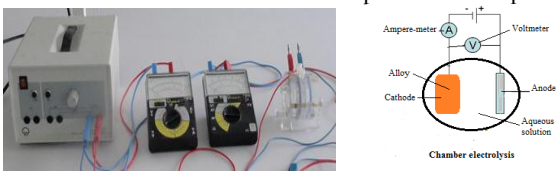

(a) (b)

Figure 1. Illustrations of the electrodeposition experimental setup. (a) Photograph and (b) schematic overview.

The morphology and chemical composition of the obtained alloy were investigated by a scanning electron microscope (SEM, LEO 1455 VP, acceleration voltage of 20 kV) at a working distance of 15 mm equipped with an X-ray energy dispersive spectrometer (EDS, Inca X- sight, Oxford Instrument). The phase identification of the alloy were determined by means of X-ray diffractometer (XRD, Philips X' PERT) using Cu Kα radiation source (λ=1.54 Å, 40 kV, 30 mA) at room temperature. The scanning rate of 0.02°/s within the 2θ range going from 10° to 90° was used in order to increase counting statistics and to improve the signal/noise ratio. Fourier transform infrared (FTIR) spectroscopy of the alloys samples was carried out with a Nicolet 380 FT-IR spectrometer using the ATR technique. All spectra were collected with the resolution of 4 cm^{-1} in the range of 4000-500 cm^{-1}.

3. RESULTS AND DISCUSSION

3.1 EDS analysis

The result of EDS analysis presented in Table 1 give the elemental composition of the Mg-La alloy. These result illustrate clearly the presence of Oxygen, Magnesium, Lanthanum and very little of Chlorine in the studied sample. The elements O, Mg, La and Cl in the as-deposited powder are because of the electrolyte used in electrodeposition experiment. As we can see from this Table, Mg-La alloys are characterized by high contents of Lanthanum (51.4 w.%) and Oxygen (32.4 w.%).

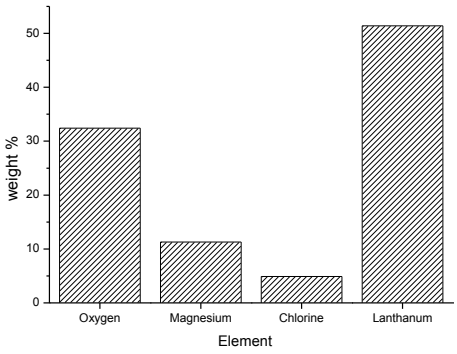

Figure 2. The elemental composition of the obtained alloy in weight percentage.

The morphological characteristics of as-prepared Mg-La alloy are shown in Figure 3. The SEM image exhibits that heterogeneous chemical structures were formed on the surface of the sample. Most of the as-deposited powder shows large aggregates and the different phases seem quite imbricated.

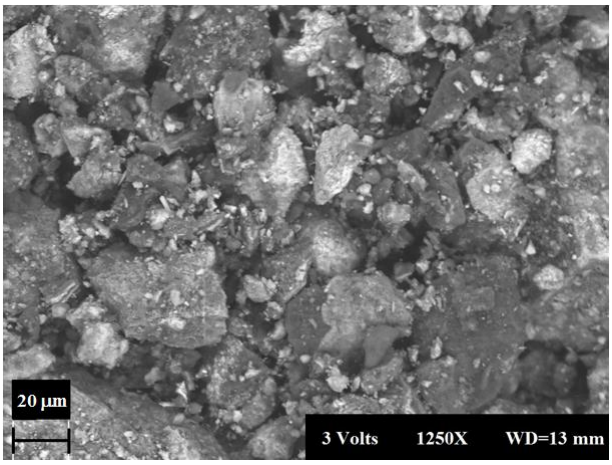

Figure 3. SEM image of the as-deposited powder.

3.2 X-ray diffraction analysis

The different phases of the as-prepared powder are distinguished clearly in Figure 4 through XRD diffractogram. According to the standard data JCPDS, two significant characteristic peaks are detected, which indicate the existence of Magnesium hydroxide ($Mg(OH)_2$) and Lanthanum hydroxide ($La(OH)_3$). As we can see from this Figure, peaks at diffraction angle 2θ of 18.6°, 35.8°, 37.9°, 50.8°, 58.7° and 62.1° are associated to $Mg(OH)_2$ whereas those at 2θ of 15.6°, 27.9°, 39.3°, 46.8°, 48.5° and 54.9° are attributed to $La(OH)_3$.

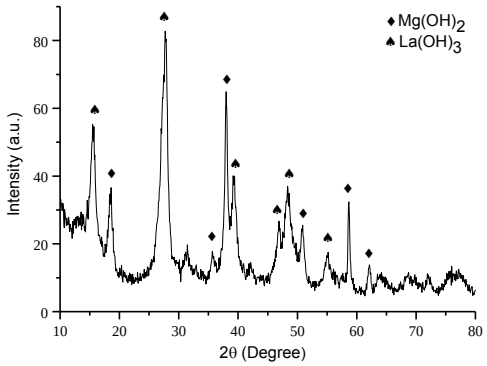

Figure 4. X-ray diffraction pattern of sample.

3.3 FTIR spectroscopy analysis

In addition to the above analyzes, the FTIR spectroscopy study is obvious for the structural confirmation of the as-prepared powder. Figure 5 exhibits the FTIR transition spectrum of the as-deposited Mg-La alloy in the range of 4000-500 cm^{-1} for the electrodepositing voltage of 3 Volts. One can see from this Figure a sharp and strong peak at 3696 cm^{-1} which corresponds to vibrations and stretching of OH bonds in $Mg(OH)_2$ as reported by Jianjun et al. [16] and Gray-Munro and Strong [17]. The band centred at 3606 cm^{-1} is assigned for stretching mode of OH^- in Lanthanum hydroxide [17, 18]. The bands at 3455 cm^{-1} and 1640 cm^{-1} are attributed to the hydroxyl groups in water [17, 19]. The two others distinct bands at about 1434 cm^{-1} and 966 cm^{-1} can be associated to asymmetric stretching vibrations of the carbonate group, which originate from the reaction of the as-deposited powders with CO_2 from air during the FTIR spectroscopy analysis [16, 17, 19].

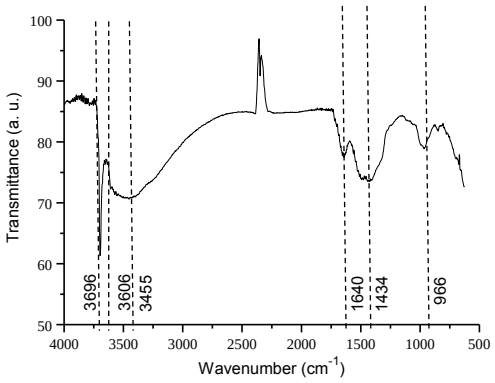

Figure 5. FTIR transition spectrum of the as-prepared powder.

4. CONCLUSION

The preparation of the magnesium-lanthanum powder by electrochemical process at ambient temperature has been successfully treated

As future analyzes, certain parameters would be studied: the concentrations of the electrolyte, the nature of cathode, the current density and electrolysis time; in order to make a comparison and determine the potential material for the hydrogen storage.

5. REFERENCES

[1] A.M. Fekry and R.H. Tammam, Corrosion and impedance studies on magnesium alloy in oxalate solution, *Materials Science and Engineering B*, Vol.176, pp. 792–798, 2011.

[2] B.L Mordike, T Ebert, Magnesium: Properties — applications — potential, *Materials Science and Engineering: A*, Vol. 302, pp. 37-45, 2001.

[3] Kirkland, N T, Magnesium biomaterials: past, present and future, *Corrosion Engineering, Science and Technology*, Vol. 47, pp. 322-328, 2012.

[4] N. Hort, Y. Huang, D. Fechner, M. Störmer, C. Blawert, F. Witte, C. Vogt, H. Drücker, R. Willumeit, K.U. Kainer, F. Feyerabend, Magnesium alloys as implant materials – Principles of property design for Mg–RE alloys, *Acta Biomaterialia*, Vol. 6, pp. 1714-1725, 2010.

[5] V. V. Narulkar, S. Prakash, K. Chandra, Ceramic coated Y1 magnesium alloy surfaces by microarc oxidation process for marine applications, *Bulletin of Materials Science*, Vol. 30, pp. 399-402, 2007.

[6] M. K. Kulekci, Magnesium and its alloys applications in automotive industry, *The International Journal of Advanced Manufacturing Technology*, Vol. 39, pp. 851-865, 2008.

[7] A. Moses Ezhil Raj, C. Ravidhas, R. Ravishankar, A. Rathish Kumar, G. Selvan, M. Jayachandran, C. Sanjeeviraja, Optimized deposition and characterization of nanocrystalline magnesium indium oxide thin films for opto-electronic applications, *Materials Research Bulletin*, Vol. 44, pp. 1051-1057, 2009.

[8] M. Jurczyk, M. Nowak, A. Szajek, A. Jezierski, Hydrogen storage by Mg-based nanocomposites, *International Journal of Hydrogen Energy*, Vol. 37, pp. 3652-3658, 2012.

[9] J. Li , R. Chen, Y. Ma, W. Ke , Effect of Zr modification on solidification behavior and mechanical properties of Mg–Y–RE (WE54) alloy, *Journal of Magnesium and Alloys*, Vol. 1, pp. 346-351, 2013.

[10] A. A. Zaldívar-Cadena, I. Díaz-Peña, J. G. Cabañas-Moreno, Dispersion of niquel on the microstructure in magnesium based alloys for hydrogen storage, *Journal of Magnesium and Alloys*, Vol. 1, pp. 292–296, 2013.

[11] A.A. Luo , Magnesium casting technology for structural applications, *Journal of Magnesium and Alloys*, Vol.1, pp. 2-22, 2013.

[12] J. Kubásek, D. Vojtěch, Structural and corrosion characterization of biodegradable Mg–RE (RE=Gd, Y, Nd) alloys, *Transactions of Nonferrous Metals Society of China*, Vol. 23, pp. 1215-1225, 2013.

[13] T. Liu, Y. Cao, C. Qin, W. Chou, X. Li, Synthesis and hydrogen storage properties of Mg–10.6La–3.5Ni nanoparticles, *Journal of Power Sources*, Vol. 246, pp. 277-282, 2014.

[14] I. Basu and T. Al-Samman, Triggering rare earth texture modification in magnesium alloys by addition of zinc and zirconium, *Acta Materialia*, Vol. 67, pp.116–133 , 2014.

[15] L. Pasquini, E. Callini, M. Brighi, F. Boscherini, A. Montone, T. R. Jensen, C. Maurizio, M. V. Antisari, E. Bonetti, Magnesium nanoparticles with transition metal decoration for hydrogen storage, *Journal of Nanoparticle Research*, Vol. 13, pp. 5727-5737, 2011.

[16] W. Han, Q. Chen, Y. Sun, T. Jiang, M. Zhang, Electrodeposition of Mg-Li-Al-La Alloys on Inert Cathode in Molten LiCl-KCl Eutectic Salt, *Metallurgical and Materials Transactions B*, Vol. 42, pp. 1367-1375, 2011.

[17] B. Xu, M. Zhang, G. Ling, Electrolytic etching of AZ91D Mg alloy in AlCl3–EMIC ionic liquid for the electrodeposition of adhesive Al coating, Surface and Coatings Technology, In Press, 2013.

[18] L. Jianjun, Y. Xiaoyan, C. Jia, L. Xiaowei, F. Chengxing, C. Youfa, The gemmological properties and infrared spectra of brucite, an imitation of nephrite and Shoushan stone, *The Journal of Gemmology*, Vol.32, pp. 67-73, 2010.

[19] J.E. Gray-Munro, M. Strong, A study on the interfacial chemistry of magnesium hydroxide surfaces in aqueous phosphate solutions: Influence of Ca^{2+}, Cl^{-} and protein, *Journal of Colloid and Interface Science*, Vol. 393, pp. 421-428, 2013.

Uncertainty Communication in the Environmental Life Cycle Assessment (LCA) of Carbon Nanotubes (CNTs)

S.Parsons[1,2], R.J. Murphy[1],
J.Lee[1], G.Sims[2]

[1]Centre for Environmental Strategy (CES)
University of Surrey
Guildford, Surrey
E-mail: s.parsons@surrey.ac.uk*, rj.murphy@surrey.ac.uk,
j.lee@surrey.ac.uk
*Corresponding author
[2]National Physical Laboratory (NPL)
Teddington, Middlesex
E-mail: sophie.parsons@npl.co.uk*, graham.sims@npl.co.uk
*Corresponding author

ABSTRACT

Amidst the great technological progress being made in the field of nanotechnology we are confronted potentially by both conventional and novel environmental challenges and opportunities. Several gaps exist in the present state of knowledge or experience with nanomaterials and understanding and managing the uncertainties that these gaps cause in life cycle assessments (LCA) is essential. Traditionally used for more established technology systems, environmental LCA is now being applied to nanomaterials by policy-makers, researchers and industry. However, the aleatory (variability) and epistemic (system process) uncertainties in LCAs of nanomaterials need to be handled correctly and communicated in the analysis, else the results risk being misinterpreted, misguiding decision-making processes and could lead to significant detrimental effects for industry, research and policy-making.

Here, we review current life cycle assessment literature for carbon nanotubes, and identify the key sources of uncertainty which need to be taken into consideration. These include: the potential for non-equivalency between mass and toxicity (potentially requiring inventory and impact models to be adjusted); the use of proxy data to bridge gaps in inventory data; and the often very wide ranges in material performance, process energy and product lifetimes quoted.

Keywords

Life cycle assessment, LCA, uncertainty, carbon nanotubes, environmental impact, decision-making.

1. INTRODUCTION

Research and technical innovation has enabled the design of materials now vital to modern life and society. Understanding environmental life cycle aspects of these materials is regularly becoming an essential perspective in the design process, with the introduction of the Eco-design Directive (2009/125/EC), and more recently the Product Environmental Footprint (PEF). Environmental stewardship (the responsible use and protection of the natural environment) extends further than just a desire to protect the environment. Understanding the potential environmental impacts of new materials used in products can: reduce business risk, through anticipation of unforeseen and costly regulatory compliance; avoid damage to brand image; and can be used to analyse future supply security. Because of this, environmental analysis in the design stage is advisable. However, such early assessments are often prone to challenge due to low levels of practical experience, limited representative data from metrology, monitoring and surveillance and, in many cases, from the inherent novel properties of the materials themselves.

Carbon nanotubes (CNTs) are an emerging class of materials facing environmental scrutiny. CNTs have been relatively well documented in the risk, toxicity and life cycle literature when compared with other nanoparticles. Their small size, leading to large surface area, means toxicity is closely linked with size distribution, chemical composition and functionality. Parallels are often drawn with other ultrafine particulate matter (PM0.1) as CNTs in their dispersed form fit this description. This has led to investigation over their potential toxicity and risk towards human health and the natural environment.

Assessing the environmental life cycle of a product containing CNTs has many uncertainties. These derive from missing data, lack of knowledge on scale-up of production to industrial levels, insufficient measurement of performance and lifetime of products, and the range in physio-chemical attributes which could affect toxicity. This means that currently life cycle assessment (LCA), commonly used to assess the life cycle of a product, cannot be properly applied to CNTs. LCA studies often do not include any consideration of the CNT itself, or if they do, impacts are considered speculatively. This is a major barrier to accurately presenting both the potential environmental issues and the environmental benefits of using CNTs in products. This research describes the uncertainties in environmental assessment, and ranks them in terms of priority for reducing and managing them in LCAs. By doing this, a clear pathway towards developing better, more representative environmental assessments can be delivered.

2. LCA STUDIES ON CARBON NANOTUBES – A REVIEW

2.1 Life cycle assessment and nanomaterials

LCA for the environmental profiling of products and services has been standardized under ISO since 1997 (see ISO 14040: 2006). This technique for environmental systems analysis is now widely used to assess the potential environmental impacts a material might have over its whole 'cradle-to-grave' life cycle. In the last few years there has been much discussion on the use of LCA to assess nanomaterials, with recognition of several key issues summarized below:

2.1.1 Difference in what drives toxicity

For bulk materials this is mass; however, for nanomaterials toxicity can potentially be more closely linked to particle size, shape, size distribution, functionality etc. [1, 2]

2.1.2 Representation of material properties and performance

Nanomaterial properties are dependent on functionalities such as particle size rather than mass, it is important this is taken into account in any LCA study [2, 3].

2.1.3 Limited availability of life cycle inventory (LCI) data

LCAs are data-driven and access to detailed process information, which is often proprietary and very difficult to obtain, is a key requirement. In the absence of direct industrial production and processing information, assumptions regarding scale-up are made [1, 2, 5].

2.1.4 Lack of impact assessment data

Once the inventory data have been compiled for the LCA an assessment of the potential environmental impacts of those inputs and outputs is performed. Due to a lack of well-defined environmental fate and exposure information, this assessment for nano-specific aspects is often speculative or cannot be performed [1, 5].

2.2 Life cycle assessment of carbon nanotubes

A common problem in LCAs of CNTs is the inability to fully represent nano-specific impacts due to lack of data, with major contributions to environmental impact coming from energy demand to produce the CNTs. This is confirmed through performing an LCA study on CNTs in a carbon fibre sports product. The results from contribution analysis are shown in table 1. The impact categories used are those recommended in the International Reference Life Cycle Data System (ILCD).

ILCD impact category	*Percentage (%) contribution to total impact*		
	CNT production	Sports equipment manufacture	Incineration at end-of-life
IPCC global warming, incl biogenic carbon[kg CO_2-equiv]	94.4	5.4	0.3
Resource Depletion, CML 2002[kg Sb-equiv]	98.5	1.5	0.0
Ecotoxicity for aquatic fresh water, USEtox[CTUe]	98.2	1.0	0.8
Human toxicity cancer effects USEtox[CTUe]	98.8	1.0	0.2

Table.1: Contribution analysis: different life cycle stages of lacrosse stick containing CNTs

3. IDENTIFIED AREAS OF UNCERTAINTY

From reviewing the literature relating to LCA of CNT-containing products and from performing a study on CNTs in sports equipment the following areas of uncertainty were identified and ranked in terms of which will achieve the biggest gains first:

1. *Priority 1* – Uncertainty relating to scaling up laboratory processes needs to be addressed, along with product performance in the use phase. Potential releases of CNTs along the life cycle need to be quantified.
2. *Priority 2* – Uncertainty relating assessing impact (fate models and toxicity assessment) coupling these with those uncertainties in priority 1 will allow for evaluation of actual risk levels.
3. *Priority 3* – Continual improvement of data sets collected to include different CNT size distributions and functionalities.

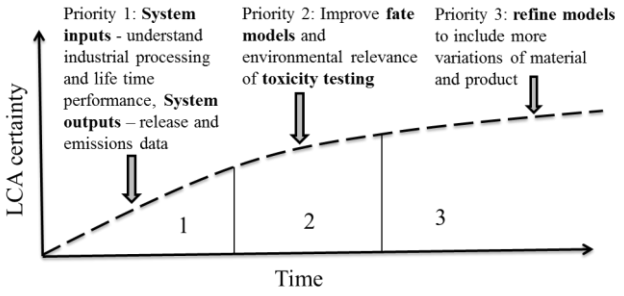

Figure 1: Roadmap for certainty improvement in CNT LCA

4. CONCLUSIONS

LCA is a tool which has been and will be used to assess nanomaterials such as carbon nanotubes and it is therefore important that LCA studies are as representative of the true impacts of CNTs as possible. Lack of data on process scale up, performance in the use phase and environmental release have been identified as initial areas to tackle in reducing CNT-containing products LCA uncertainty. In order to reach this reduction in uncertainty better communication needs to be put in place between LCA practitioners and industry. Further areas of uncertainty needing addressing are those relating to fate and toxicity assessment, and finally the inclusion of a range of different CNT size distributions and functionalities.

5. ACKNOWLEDGMENTS

This work was supported by the National Physical Laboratory (NPL), Teddington, UK, and the Engineering and Physical Sciences Research Council (EPSRC). Research for this paper was carried out as part of an Engineering Doctorate in Sustainability for Engineering and Energy Systems in the Centre for Environmental Strategy, University of Surrey.

6. REFERENCES

[1] Gavankar, S., Suh, S., and Keller, A., *Life cycle assessment at the nanoscale: review and recommendations*. International Journal of Life Cycle Assessment, 2012. **17**

[2] Linkov, I., and Steevens, J., Nanomaterials : risks and benefits, ed. I.Linkov and J.Steevens. 2009: NATO Science for Peace and Security Series C: Environmental Security

[3] Bauer, C., et al., *Towards a framework for life cycle thinking in the assessment of nanotechnology*. Journal of Cleaner Production, 2008, **16**

[4] Hichier, R., and Walser, T,. *Life cycle assessment of engineered nanomaterials: State of the art and strategies to overcoming existing gaps*. Science of the total environment, 2012, 425

[5] Som, C., et al *The importance of life cycle concepts for the development of safe nanoproducts*, Toxicol, 2010, **269**

Humidity sensing based on sol-gel grown Zinc Oxide Thin films

GHANEM Salah[1], TELIA Azzedine[1,] BOUKAOUS Chahra [1] and BENTERROUCHE Lyes[1]

[1]University of Constantine 1, Department of electronic, Laboratory of Microsystems and instrumentation (LMI) Constantine, Algeria

ABSTRACT

Zinc oxide (ZnO) thin films were deposited by sol-gel method on glass substrate. The sols were prepared using zinc acetate,2-Methoxyethanol and monoethanolamine (MEA)as solute ,solvent and stabilizer respectively . The films crystal structure was investigated by means of X-ray diffraction (XRD) analysis. XRD patterns of annealed ZnO thin films exhibit three strong peaks (101), (002) and (100) planes assigned to hexagonal wutrzite structure. ZnO films morphology was investigated by Scanning Electron Microscope (SEM). SEM images reveal that the synthesized ZnO films are composed with irregular fiber-like stripes and a wrinkle network. Relative humidity sensing properties has been studied and determined by variation of electrical resistance measurements at various temperature and humidity levels. Impedance of the sensor decreases with increase in relative humidity (RH) (from 15% to 95%). From humidity sensing tests we inferred that temperature and morphology have a strong influence on the response and recovery times respectively.

Keywords

ZnO, sol-gel, thin films, XRD, SEM, Humidity sensing, Response and recovery time.

1. INTRODUCTION

Physical quantities have been detected using different sensing materials including metal oxides [1] and polyelectrolyte [2]. ZnO is one of the most promising materials for sensor applications due to its chemical sensitivity to volatile gases and low cost synthesis method. It has been proved that ZnO is an excellent sensitive material for detection of toxic gases, such as NO_2 [3] and CO [4], other studies are focused on humidity sensing [1]. ZnO has a special chemical property to adsorb water molecule [5] and it can be grown in different shapes and morphologies such as nanorods [6], flower-like wrinkle network [7], tetrapods [8], nanowires [9], colloid spheres [10] and nanobelts [11]. ZnO thin films with these morphologies have been successfully synthesized and applied in humidity monitoring [8] which is very important for human life in various areas such us food processing. Researchers have developed humidity sensing architectures using different sensing techniques including impedance [12]. Impedance variation is a powerful tool for monitoring of humidity in wide measuring range. For humidity sensors, their electrical impedances change with humidity due to the enhancement of the adsorbed water on sensor surface [13]. A powerful humidity sensor should have high sensitivity, rapid response and recovery times and narrow hysteresis [5]. Many humidity sensors need several tens of seconds for response and recovery times making them unsuitable for lot of applications.

In this work, we prepared a humidity sensor based on ZnO synthesized by sol–gel process. The morphology and crystal structure of ZnO were analyzed by SEM and XRD, respectively. Humidity capabilities of the ZnO thin films were investigated at different temperatures. We have determined hysteresis, response and recovery times to investigate its ability to use as humidity sensor.

2. EXPERIMENTAL PROCEDURE

ZnO sol was prepared using zinc acetate, 2-Methoxyethanol and monoethanolamine (MEA) as solute, solvent and stabilizer respectively. The molar ratio of MEA to zinc acetate was kept at 1.0 and the Zn concentration was 0.5 mol/l. Resulting solution was stirred at 70°C for 2 hours. ZnO thin films were coated by spin coating method on glass substrate at 4000 rpm and annealed at 500°C for two hours. The crystal structure was analyzed by X-ray diffraction. The surface morphology of films was observed using a scanning Electron microscope (SEM).For humidity test sensor was placed on a system of heating into an airtight chamber, air compressor is used to push wet air to the chamber and evacuate it outside chamber via admission valves. To achieve low rates of humidity a vacuum pump was used. For collecting data, a unit impedance measurement was attached to two electrical contacts connected through a hole fitted with a vacuum seal gasket in that chamber. A commercial hygrometer was used to measure the RH inside the chamber.

3. RESULTS and discussions:

3.1 Structural characterization

The films crystal structure was investigated by means of X-ray diffraction, recorded XRD patterns (fig1) of ZnO thin films prepared correspond to three diffraction peaks assigned to (100), (002) and (101) planes where the strongest one is (101). This result reveals that these films have a hexagonal wurzite structure. Chien-Yie et al [14] have reported that undoped ZnO, Ga-, In-, and Zr- doped ZnO thin films have growth oriented along the (101) plane. The crystallites size was calculated using a well-known Scherrer's Formula [14] and it was found 25.62 nm. Surface morphology of the thin films is shown in fig.2. The plan view of SEM micrograph of ZnO thin films shows a large surface with irregular fiber-like and wrinkle network structure. The morphology is homogenous with the wrinkles of a width 300 to 600 nm and length average about 2200 nm. Similar structure has been observed in undoped [7] and in doped ZnO thin films [15]. Wrinkle network structure and high roughness surface lead to much more area, It means that such area has more active sites for

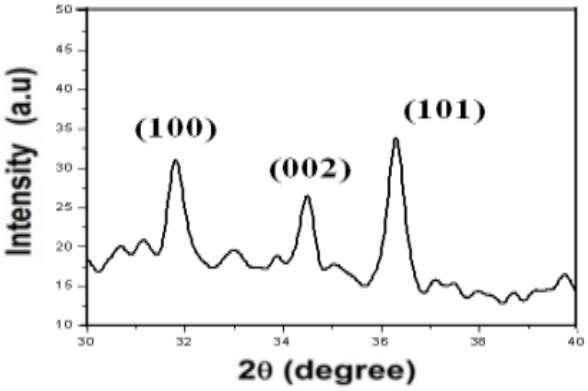

Figure.1 XRD pattern for ZnO films prepared.

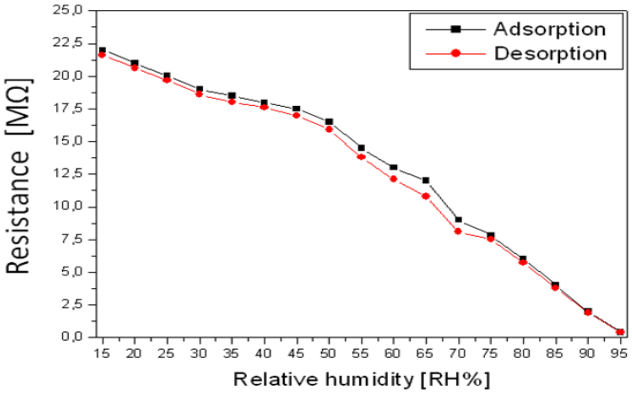

Figure.3 Resistance variation with RH% at 25°C.

dissociation and condensation of water molecules which is interesting for humidity sensing.

3.2 Sensing test

To investigate humidity sensing properties of the device, we have studied the resistance variation measured at 120 Hz and 1V in different humidity levels when sensor temperature was kept at 25°C, 50°C, 75°C and 100 °C. Figures 3 and 4 show resistance variation with respect to humidity levels at 25 and 100C° respectively when RH change from 15 to 95% (adsorption process) and when RH% change from high value to low value (desorption process). As can be seen, the corresponding resistance decreases almost linearly by enhancing humidity during the RH variation. The process of adsorption of water molecules due to RH increase causes the decrease of the impedance. When RH decreases the impedance returns to initial state but not exactly by the same values. In our experiment, a good reliability ZnO sensor indicated by narrow hysteresis was found when heated. At 100°C sensor exhibit an acceptable hysteresis value less than 2%. Sensibility, response and recovery times were evaluated to understand the performance of the humidity sensor and the temperature effect. It is important to note that the time taken by a sensor to achieve 90% of the total impedance change is defined as the response time in the case of adsorption or the recovery time in the case of desorption.

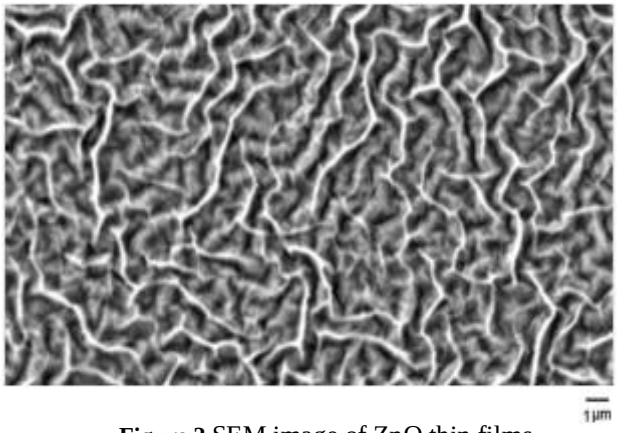

Figure.2 SEM image of ZnO thin films.

We defined the sensitivity S as follow

$$S = ((R_a - R_{Rh})/ R_a)*100) \qquad (1)$$

R_a is the resistance at Rh%=15 and R_{Rh} is the resistance measured at humidity defined. Figure 5 and 6 show the response and recovery times characteristic curves (corresponding to water molecule adsorption and desorption processes) for one cycle for ZnO sensor at 25°C and for five cycles for the sensor heated at 100C°. Results obtained at different temperature of sensor heating are summarized in table1. It is observed that the response time (as the humidity changes from 15% to 95% RH) is about 22 s and it continues to be shorter with the increasing of temperature until 7s at 100 °C, but the recovery time (as the humidity changes from 95 to 15% RH) is about 30 s and it continues to be shorter with the increasing of temperature until the value of 14 s at 100 °C. The recovery time is relatively long even higher than the response time, and generally takes more seconds to completely recover the sensor original state once wet air evacuated; it might be induced by the chemisorptions on the surface of sensing element the adsorbed water might not be easily removed . Temperature of ZnO surface spread toward the water layers and increase the mobility of charges carriers (more rapid) the consequence the response is more rapid.

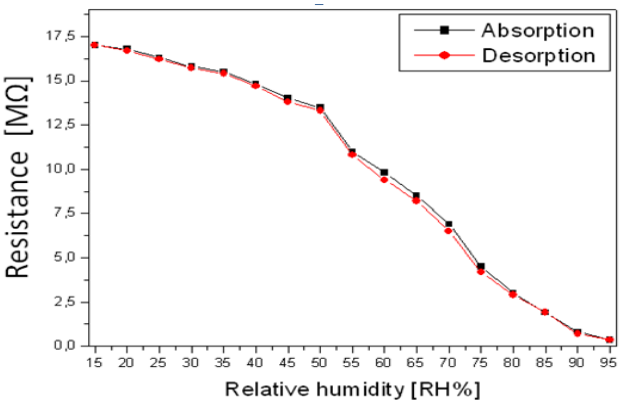

Figure.4 Resistance variation with RH% at 100°C.

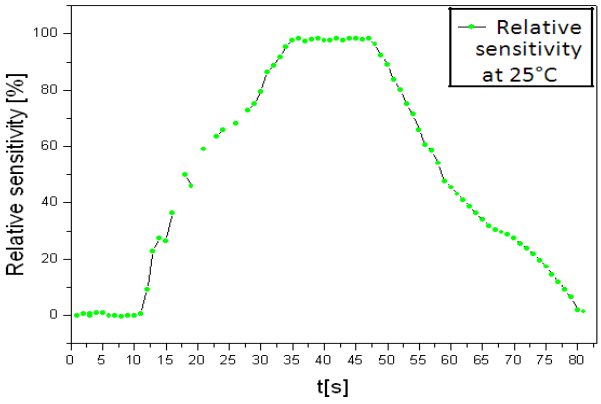

Figure.5 Sensitivity of ZnO humidity sensor at 25°C.

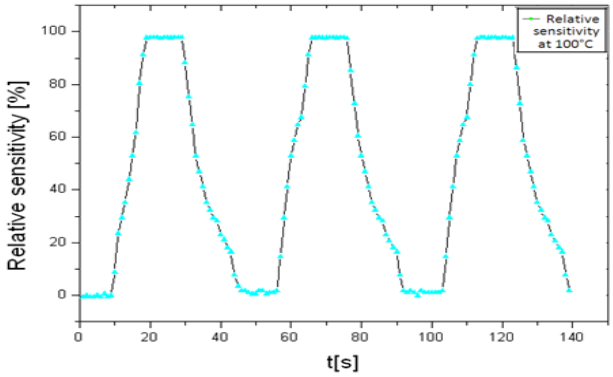

Figure.6 Sensitivity of ZnO humidity sensor at 100°C (5 cycles).

Temperature (°C)	Hysterisis (%)	Response time (s)	Recovery time (s)
25	5.55	22	30
50	4.97	12	19
75	4.3	9	15
100	1.8	7	14

Table.1: Hysterisis, response and recovery times for ZnO sensor

4. CONCLUSION

ZnO thin films with wrinkle network structure were elaborated by sol–gel process. Sensitivity of ZnO thin films to humidity was investigated by resistance variation. Resistance of ZnO sample decrease with the increase of RH%. Shorter response time was observed when samples were heated.

5. REFERENCES

[1] Erol, A., Okurb, S., Comba, B., Mermerc, O., and Arıkan, M.C. 2010. Humidity sensing properties of ZnO nanoparticles synthesized by sol–gel process. *Sensors and Actuators B.* 145 (2010) 174–180.

[2] Kumara, B., Parkb, Y.T. , M. Castroa, M. ,Grunlanb, J.C. , and Feller. J.F.2012. Fine control of carbon nanotubes polyelectrolyte sensors sensitivity by electrostatic layer by layer assembly (eLbL) for the detection of volatile organic compounds (VOC).*Talanta 88* (2012) 396– 402.

[3] Jin Hyung, J., Junggwon,Y., Kyoungah, C., In-Sung H., Jong Heun, L., and Sangsig, K. 2009. Necked ZnO nanoparticle based NO2 sensors with high and fast response. *Sensors and Actuators B 140* (2009) 412–417.

[4] Ting-Jen, H., Yi-Wen, C., Shoou-Jinn, C., Sea-Fue, W., Cheng-Liang, H., Yan-Ru, L., Tzer-Shen L., and I-Cherng, C. 2007. ZnO nanowire based CO sensors prepared on patterned ZnO: Ga/SiO2/Si templates. *Sensors and Actuators B 125* (2007) 498–503.

[5] Fu-Shou T., and Shui-Jinn W. 2014. General Enhanced sensing performance of relative humidity sensors using laterally grown ZnO nanosheets. Sensors and Actuators B 193 (2014) 280– 287.

[6] Polsongkram, D., Chamninok P., Pukird , S., Chowb, L., Lupan, O., Chai, G., Khallaf, H., Park, S., and Schulte, A. 2008 .Effect of synthesis conditions on the growth of ZnO nanorods via hydrothermal method. *Physica B 403* (2008) 3713– 3717.

[7] Chien-Yie,T., Kai-Shiung,F., Yu-Wu, W., Chi-Jung, C., Yung-Kuan, T., and Chung Kwei, L. 2010. Transparent semiconductor zinc oxide thin films deposited on glass substrates by sol–gel process. *Ceramics International 36 (2010)* 1791–1795.

[8] Xiaohua, W., Jian, Z. , Ziqiang, Z., and Jianzhong, Z. 2007. Humidity sensing properties of Pd2+-doped ZnO nanotetrapods. *Applied Surface Science* 253 (2007) 3168–3173.

[9] Fang, F., Zhao, D.X., Zhang, J.Y., Shen, D.Z. , Lu, Y.M. , Fan, X. W., Li, B.H., and Wang, X.H. 2008 .The influence of growth temperature on ZnO nanowire. *Materials Letters 62* (2008) 1092–1095.

[10] Juan, X., Hu, W., Yuanhua, L., Ying, Z., and Yuanpeng, W. 2013. Highly sensitive humidity sensor based on quartz crystal microbalance coated with ZnO colloid spheres .*Sensors and Actuators B 177* (2013) 1083– 1088.

[11] Sadek, A.Z., Supab,C,. Wlodarski,W., Ippolito,S.J., and Kourosh, K. 2007.Characterization of ZnO Nanobelt-Based Gas Sensor for H2, NO2, and Hydrocarbon Sensing. *IEEE SENSORS JOURNAL. 7* (2007) 919.

[12] Qing, Y., Nan, L., Jinchun, T., Xiaotian, L., Rui, W., Tong, Z., and Changlu, S. 2010. Preparation and humidity sensitive property of mesoporous ZnO–SiO2 composite *Sensors and Actuators B 149* (2010) 413–419.

[13] Pranab, B., Souvik, K., Banerji, P., and Bhunia, S. 2013. Super rapid response of humidity sensor based on MOCVD grown ZnO nanotips array. *Sensors and Actuators B 178* (2013) 331– 338.

[14] Chien-Yie, T., and Wen-Che, L. 2013. Effect of dopants on the structural, optical and electrical properties of solegel derived ZnO semiconductor thin films. *Current Applied Physic*s 13 (2013) 60-65.

[15] Chien-Yie, T., Hua-Chi, C., Yen-Ting, T., Wei-Hsing, T., and Chung-Kwei, L. 2008. Effect of Sn-doped on microstructural and optical properties of ZnO thin films deposited by sol–gel method. *Thin Solid Films* 517 (2008) 1032–1036.

Influence of sputtering power on the properties of thin layers of GZO for photovoltaic applications

H. Mahdhi [a], Z. Ben Ayadi [a], J. L. Gauffier [b], K. Djessas[c] and S.Alaya[a,d]

[a] Laboratoire de Physique des Matériaux et des Nanomatériaux appliquée à l'Environnement, Faculté des Sciences de Gabès, Cité Erriadh Manara Zrig, 6072 Gabès, Tunisie.

[b] Département de Physique, INSA de Toulouse, 135 Avenue de Rangueil, 31077 Toulouse Cedex 4, France.

[c] Laboratoire Procédés, Matériaux et Energie Solaire (PROMES-CNRS), Université de Perpignan, Rambla de la thermodynamique, Tecnosud, 66100 Perpignan Cedex, France.

[d] King Faisal University, College of Science, Physics Department, P.O. Box 400, 31982 Hofuf, Saudi Arabia.

E-mail: hayetmahdhi@yahoo.fr

Abstract

In the present work, we have deposited gallium doped zinc oxide thin films by magnetron sputtering technique based nanocrystalline particles elaborated by sol-gel method. In the first step, the nanoparticles were synthesized by sol-gel method using supercritical drying in ethyl alcohol. The structural studied by X-ray diffractometry indicates that GZO has a polycrystalline hexagonal wurzite structure with a grain size of about 30 nm. Transmission

electron microscopy (TEM) measurements have shown that very small particles of GZO are present in the aerogel powder. In the second step, gallium-doped zinc oxide (GZO) films were deposited onto glass substrates by rf-magnetron sputtering at ambient temperature using. The effects of RF sputtering power on structural, electrical, morphological and optical properties were investigated. The obtained films were polycrystalline with a hexagonal wurtzite structure and preferentially oriented in the (002) crystallographic direction. The film deposited at 60 W showed the lowest electrical resistivity of $3.5x10^{-3}$ Ω.cm achieved through the highest Hall mobility of 9.30 cm^2 V^{-1} s^{-1}. All the GZO films in this study showed the optical transmittances higher than 80%.

Keywords: ZnO:Ga ; Transparent conductive oxide films; Magnetron sputtering; Electrical and optical properties.

1. Introduction

During the last years, there has been great interest in the development of transparent conducting oxides, with high visible light transparency and high electrical conductivity. In addition, ZnO films are more stable in activated hydrogen environments than other TCO films such as ITO and SnO_2. Doped zinc oxide materials have been extensively studied, because of its several properties, such as semiconducting and laser emitting devices. It has a large band gap of 3.37eV and a large exciton binding energy of 60 meV, which make it a good candidate for optoelectronic applications [1], and their great potential applications as optically transparent conducting layers as electrodes for thin-film solar cells [2-4]. Various techniques are being used to prepare GZO films such as : Sol–gel [5,6], chemical vapor deposition [7], atomic layer deposition [8], pulsed laser deposition [9], spray pyrolysis [10], molecular beam epitaxy [11], metal organic chemical vapor deposition [12] and sputtering rf-magnetron [13] is commonly used.

In this work, GZO thin films were deposited by rf-magnetron sputtering at room temperature under a pure argon atmosphere using doped nanocrystalline powder synthesized by the sol–gel method. The rf-magnetron sputtering has been used to obtain high-quality Ga-doped ZnO thin films. The effect of power sputtering on the structural, morphological, electrical and optical properties of GZO thin films reported.

2. Experimental details

In the first step, a nanocrystalline GZO aerogel was prepared by dissolving 20 g of zinc acetate dehydrate [$Zn(CH_3COO)_2 \cdot 2H_2O$] as a precursor in 140 ml of methanol. After 15 min under magnetic stirring at room temperature, an adequate quantity of gallium nitrate [GaN_3O_9] corresponding to [Ga]/[Zn] ratios of 0.03 was added. After 20 min under magnetic stirring, the solution was placed in an autoclave and dried in the supercritical conditions of

ethyl alcohol (T_c = 243 °C, P_c = 63.3 bars). The nanoparticles obtained were then treated in a furnace at 500 ° C for 2 h in air.

In the second step, GZO transparent conductive thin films were deposited on glass substrates by using 13.56 MHz rf-magnetron sputtering. Films with thicknesses of approximately 300 nm were deposited. The sputtering chamber was evacuated to a base pressure of 10^{-5} mbar before introducing the sputtering argon gas with 99.9999 % purity without oxygen. The sputtering targets were prepared from the aerogel powders of GZO. During the sputtering process, the target-to substrate distance was fixed at 75 mm, the substrate temperature was set at ambient temperature and the rf power is varied from 40 to 100 Watt. Before deposition, the glass substrates (1 mm thick) were ultrasonically cleaned in HCl, rinsed in deionized water, then subsequently in ethanol. The target was pre-sputtered for 10 min to remove contaminants.

The structural, morphological, electrical and optical properties were studied in this work. The crystal structure was characterized by X-ray diffraction (XRD) using CoKα radiation (1.78901 Å). The crystallite size was calculated from XRD data using Scherrer's formula. The GZO nanoparticles were also characterized by transmission electron microscopy (TEM) using JEM-200CX. The composition studies were performed by Energy Dispersive X-ray Spectroscopy (EDX) using a scanning electron microscope JEOL JSM 5410 type with a probe. Surface morphology and roughness were measured using atomic force microscopy (AFM, Topo Metrix). Electrical resistivity, Hall mobility and carrier concentration were measured at room temperature by a Hall measurement system with the Van der Pauw method. Finally the optical transmittance of the films was determined using a Shimadzu UV-3101 PC spectrophotometer in the wavelength range from 200 to 3000 nm.

3. Results and discussion

3.1. *Structural properties of the GZO aerogel nanopowder*

Fig.1 shows the XRD spectrum of ZnO nanoparticles doped gallium an adequate quantity of gallium corresponding to [Ga]/[Zn] ratios of 0.03 was added. Three pronounced ZnO diffraction peaks, (100), (002) and (101) appear at 2θ = 31.84°, 34.49° and 36.35° respectively, which are very close to wurtzite ZnO ones [14]. This result indicates that GZO aerogel powder has a polycrystalline hexagonal wurtzite structure. Diffraction lines of ZnO were broad, and diffraction broadening was found to be dependent on Miller indices of the corresponding sets of crystal planes. For our samples, the (002) diffraction line was narrower than the (101) line, which is in turn broader than the (100) line. This indicated an asymmetry in the crystallite shape. It was supposed that crystallites were in the form of cylinder (prism), having the height (direction of the crystal *c*-axis) bigger than the basal diameter (crystal axes, *a* and *b*). The average grain size was calculated using Scherrer's formula [15]:

$$G = \frac{0.9\lambda}{B\cos\theta_B} \qquad \textbf{(1)}$$

where λ is the X-ray wavelength (1.5418 Å), θ_B is the maximum of the Bragg diffraction peak (in radians) and B is the full width at half maximum (FWHM) of the XRD peak. The average grain size of the basal diameter of the cylinder-shape crystallites varies from 14 to 20 nm, whereas the height of the crystallites varies from 25 to 34 nm.

TEM measurements (Fig. 2(a)) show that smaller particles are present in the powder. As seen in the TEM images, the majority of GZO particles present in this powder have a size between 20 and 30 nm, this result is comparable to that obtained by XRD.

The EDX analysis shown in is shown in Fig. 2 (b) and table 1 confirmed the presence of gallium in the matrix of ZnO and absence of other impurities. From these analyses, we can conclude that the GZO nanoparticles are homogeneous and quasi-stoichiometric.

3.2 Structural characterization of GZO films

We report in Fig. 3 the XRD patterns of GZO thin films deposited on glass substrates at different rf power values. All films have hexagonal wurtzite structure. A prominent (002) peak indicates that the crystallite structure of the films is oriented with their c-axis perpendicular to the substrate plane [16]. The films are developed without any second phase, indicating that they have a high quality crystalline structure. It is also clearly observed that, the intensity of the (002) XRD peak increases with increasing rf power.

On the other hand, the variation of the peak location (002) as a function of rf power was observed in Table 2. A small detour in (002) peak was observed when the rf power was varied indicating that some residual stresses within the film may exist [17]. By comparing the curves, we see that the rf power of more than 40 W, not only the strong diffraction peak (002) is observed, but also the value of the full width at half maximum (FWHM) of the peak (002) indicating that the GZO thin film quality is improved. This behavior is accompanied by an increase in the average crystallite size (see Table 2). This result can be explained by the increase of the energy of the sputtered atoms, which allows the growth of larger grains with increasing power deposition [18], because a number of atoms are sputtered from the target and gets a higher energy that contributes to the film growth. The average crystallite size for these samples was about 18–32 nm estimated from the XRD spectrum by using Scherre formula [15]. These results indicate that crystallinity is improved at an appropriate sputtering power.

The diffraction peak angles of the ZnO thin films were estimated in Table 2, and the lattice parameter c for this film was calculated from XRD patterns by using the following equation [19]:

$$d_{hkl} = \left(\frac{4}{3} \frac{h^2 + hk + k^2}{a^2} + \frac{l^2}{c^2} \right)^{-1/2} \quad \textbf{(2)}$$

Where a and c are the lattice parameters, h, k and l are the Miller indices of the planes and d_{hkl} is the interplanar spacing. The variations of lattice parameters are shown in Table 2.

The lattice parameters are rf power dependant. This gives rise to a mismatch between the substrate and the deposited thin films. The variation of the interreticular distance d (Table 2), shows that for all the sputtered thin films, the d values are larger than that of ZnO powder which is equal to 0.2603 nm. Thus, we can conclude that all the films exhibit compressive stresses.

Stress of thin films is a very important parameter for the practical application. The total stress in thin films commonly consists of two components. One is the intrinsic stress introduced by impurities, defects and lattice distortions in the crystal, and the other is the extrinsic stress introduced by the lattice mismatch and thermal expansion coefficient mismatch between the film and substrate [20].

$$\varepsilon_z = \frac{c - c_0}{c_0} x\ 100\% \quad \textbf{(3)}$$

where c is the lattice parameter of the ZnO film calculated from (002) peak of XRD pattern and the c_0 is the lattice parameter for the ZnO bulk ($c_0 = 0.52065nm$). The stress in the plane of the films was calculated based on the biaxial strain model,using the following formula [21]:

$$\sigma = \frac{2C^2{}_{13} - C_{33}(C_{11} - C_{12})}{C_{13}} \varepsilon_z \quad \textbf{(4)}$$

where C_{11}= 209.7 GPa, C_{12}= 121.1 GPa, C_{13}=105.1 GPa, and C_{33}=210.9 GPa are the elastic stiffness constant of bulk ZnO. The estimated values of stress σ in the films grown at different sputtering power are listed in Table 2. The total stress in the film commonly consists of two components. One is the intrinsic stress introduced by impurities, defects and lattice distortions in the crystal, and the other is the extrinsic stress introduced by the lattice mismatch and thermal expansion coefficient mismatch between the film and substrate.

Fig. 4 shows the dependence of the growth rate on the sputtering power. It is observed that a clear increase in growth rate as sputtering power increase. The Growth rate and the sputtering power is basically a linear relationship. This increase indicates that the number of atoms sputtered from the target is proportional to the sputtering power [21]. When the sputtering power increase from 40 W to 100 W, the growth rate increase from 4.20 nm/min to 12.80 nm/min.

The sputtering power dependence of crystallinity and crystallite sizes for GZO films was also revealed by their AFM micrographs. Fig.5 show the surface morphologies of the GZO samples deposited at sputtering power values of 40, 60, 80 and 100 W, respectively. From the figure, we can observe that the crystallite sizes increase on elevating the sputtering power because the ions or ion clusters can obtain more energy prior to collision with the substrates. The RMS surface rough nesses were about 3.6, 7.52, 9.2 and 10.2 nm. This also means that the crystallite sizes were increased with elevating the sputtering power. These results are consistent with the XRD observation.

3.3 Optical properties of GZO thin films

The transmission spectra and the reflection spectra of GZO thin films deposited by rf magnetron sputtering to deposit different power are shown in Fig. 6. All spectra show a high transparency in the visible range with a good transmission of the order of 90% and exhibit a low reflection (< 20 %). The steep drop of the transmission for the lower wavelengths at 320 nm, corresponding to absorption in GZO due to the transition between the valence band and the conduction band. This area is used to determine the energy of the optical gap.

The transmission coefficient decreases $\lambda > 1000$ nm, this decrease is due to absorption by free carriers (electrons in the case of ZnO:Ga is n-type) which takes place at the plasma frequency.

The optical absorption coefficient (α) is calculated from the transmittance data where the reflection losses are taken into consideration, by [22]:

$$\alpha = \frac{1}{d} Ln \frac{\sqrt{(1-R)^4 + 4T^2R^2} - (1-R)^2}{2TR^2} \quad \textbf{(5)}$$

Where d is the thickness of the film and R and T are the reflection and the transmission respectively.

In the direct transition semiconductor, the optical absorption coefficient (α) and the optical energy band gap (E_g) are related by [23]:

$$\alpha(h\nu) = C(h\nu - E_g)^{1/2} \quad \textbf{(6)}$$

Where C is a constant for direct transition, and $h\nu$ is the energy of the incident photon.

The optical band gap E_g of the films can be obtained by plotting $(\alpha h\nu)^2$ versus $(h\nu)$ and extrapolating the linear portion of this plot to the energy axis as shown in Fig. 7. We see that the band gap of GZO films increases with increasing rf power from 3.38 to 3.64 eV (Fig.7).

All the values are larger than that of pure ZnO (3.30 eV).With increase in sputtering power, the value of Eg increases. The increase in the optical gap for ZnO doped layers is mainly due to the phenomenon of band filling known as the Burstein-Moss effect [24, 25], which increases the gap (blue shift) with increasing the concentration of charge carriers.

3.4. Electrical properties of GZO films

The variation of the resistivity (ρ), carrier concentration (n) and mobility (μ) of GZO films with rf power are shown in Fig. 8. It is clear that the increase in power deposition from 40 to 100 W causes a decrease in resistivity up to 60 W, and then decreases with further increase of sputtering power. The minimum electrical resistivity is obtained for a power of 60 W deposits, the lower the value of ρ is about 3.5 10^{-3} Ω.cm, his is due to both increase in the mobility around 9.30 $cm^2 V^{-1}s^{-1}$ and carrier concentration to 1.92 10^{20} cm^{-3}. As we previously reported, the grain size increases with the power deposition and subsequent grain boundaries decrease. Therefore increasing the mobility of charge carriers is attributed to the decrease of scattering centers which causes a decrease of the electrical resistivity. In addition, the decrease of the resistivity is due to the increase in the charge carrier concentration (n) from donors Ga^{3+} incorporated in the interstitial or substitutional sites of Zn^{2+} [26, 27]. However, above the sputtering power of 60 W, the resistivity began to slightly increase as a result of the decrease of mobility. The improvement of conductivity was contributed to better crystallinity of GZO film and its dense microstructure with larger grain sizes as seen from the XRD results. Thereby, the carrier concentration and mobility can be increased because of the decrease of impurity scattering and grain boundary scattering. From this study, we conclude that the value of 60 W is the optimal power deposition in our work.

4. Conclusion

The Ga doped zinc oxide thin films were deposited on glass substrates at room temperature by rf-magnetron sputtering process using aerogel nanopowders prepared by sol-gel technique. The effect of the rf power on the structural, electrical and optical properties of GZO films was investigated. All of the obtained films were polycrystalline with the hexagonal structure and had a preferred orientation with c-axis perpendicular to the substrate. Highly transparent films with a visible transmittance higher than 90% and a minimum resistivity of 3.5 $10^{-3}\Omega$.cm were obtained by applying rf power at 60 W. Therefore, it is clear that GZO thin films deposited by rf-magnetron sputtering at room temperature can be used in optoelectronic devices especially in solar cells.

References

[1] A.E. Jiménez, J.A. Soto Urueta, Sol. Energy Mater. Sol. Cells 52 (1998) 345–353.

[2] Y.R. Rye, T.S. Lee, J.A. Lubguban, H.W.White, Y.S. Park, C.J. Youn, Appl. Phys. Lett. 87 (2005) 153504.

[3] A. Maldonado, M.L. Olvera, S. Terado-Guerra, R. Asomoza, Sol. Energy Mater. Sol. Cells 82 (2004) 75.

[4] M. Girtan, M. Socol, B. Pattier, M. Sylla, A. Stanculescu, Thin Solid Films 519 (2010) 573.

[5] K.Y. Cheong, Norani Muti, S. Roy Ramanan, Thin Solid Films 410 (2002) 142–146.

[6] B.M. Ataev, A.M. Bagamadova, A.M. Djabrailov, V.V.Mamedov, R.A. Rabadanov, Thin Solid films 260 (1995) 19.

[7] J. Hu, R.G. Gordon, J. Appl. Phys. 72 (1992) 5381.

[8] S.M. Park, T. Ikegami, K. Ebihara, Thin Solid Films 513 (2006) 90.

[9] K.T.R. Reddy, R.W. Miles, J. Mater. Sci. Lett. 17 (1998) 279.

[10] H. Kato, M. Sano, K. Miyamoto, T. Yao, J. Cryst. Growth 237–239 (2002) 538.

[11] T. Minami, H. Sato, S. Takata, Jpn. J. Appl. Phys. 24 (1985) 781.

[12] M. Miyazaki, K. Sato, A. Mitsui, H. Nishimura, J. Non-Cryst. Solids 218 (1997) 323.

[13] T. Minami, H. Nanto, S. Takata, Jpn. J. Appl. Phys. 23 (1984) 280.

[14] Y. Chem, D.M. Bagnall, H.K. Koh, K.T. Park, K. Hiraga, Z.Q. Zhu, T.Yao, J. Appl. Phys. 84 (1998) 3912.

[15] B. D. Cullity, Elements of X-ray Diffraction, Addison-Wesley, Reading, MA, 1978, p. 102.

[16] Y. Chem, D.M. Bagnall, H.K. Koh, K.T. Park, K. Hiraga, Z.Q. Zhu, T.Yao, J. Appl. Phys. 84 (1998) 3912.

[17] E. M. Bachari, G. Baud, S. Ben Amor, M. Jacquet, Thin Solid Films 348 (1999) 165.

[18] R. C. Chang S. Y. Chu, C. S. Hung and Y. T. Chuang, Surface &Coatings, Technology,200 (2006) 3235.

[19] G.J. Fang, D.J. Li, B.L. Yao, Phys. Status Solidi A 193 (2002) 139.

[20] H.C. Ong, A.X.E. Zhu, G.T. Du, Applied Physics Letters 80 (2002) 941.

[21] M.K. Puchert, P.Y. Timbrell, R.N. Lamb, Journal of Vacuum Science and Technology A 14 (4) (1996) 2220–2230.

[22] D. K. Schroder, Semiconductor Material and Device Characterization, Wiley, New York, 1990.

[23] J.I. Pankove, Optical Processes in Semiconductors, Dover, New York, (1976).

[24] E. Burstein, Phys. Rev. 93 (1954) 632.

[25] T. S. Moss, Phys. Soc. Lond. B 67 (1954) 775.

[26] K. Ellmer, G. Vollweiler, Thin Solid Films 496 (2006) 104.

[27] Y. Igasaki, H. Saito, J. Appl. Phys. 69 (1991) 2190.

Figure captions and Tables

Figure 1: X-ray diffraction spectra of GZO aerogel nanoparticles

Figure 2. Typical TEM photograph (a) and SEM showing (b) the general morphology of GZO aerogel nanoparticles.

Figure 3: X-ray diffraction of GZO thin films with different rf powers.

Figure 4: Growth rate of GZO films as a function of sputtering power.

Figure 5: 2D AFM micrographs ($5\mu m \times 5\mu m$) for the ZnO:Ga films with different sputtering powers.

Figure 6. Transmittance and reflectance spectra of GZO films deposited at various rf powers.

Figure 7. Plots of $(\alpha h\nu)^2$ versus photon energy ($h\nu$) of GZO thin films with various rf powers.

Figure 8. Resistivities, mobility and carrier concentration of GZO thin films as a function of sputtering power.

Table 1. Atomic compositions of GZO nanoparticles.

Table 2: Variation of the (002) peak positions, FWHM, grain size, interreticular distance (*d*) lattice constant (c) and the stress (σ) of the films GZO at different sputtering power.

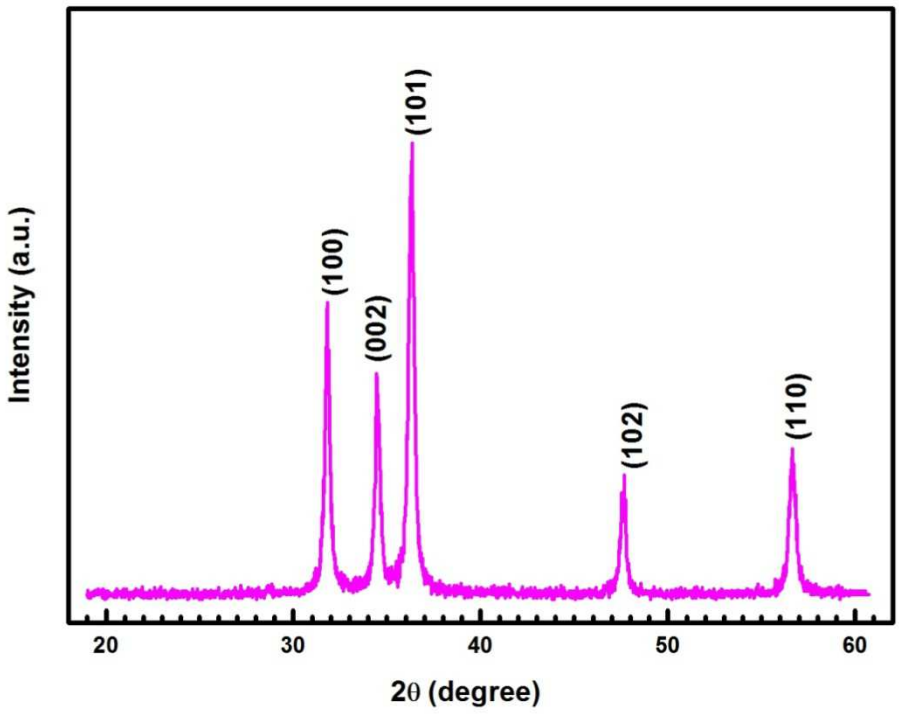

Fig.1: Spectra of X-ray diffraction of the nanoparticles GZO3%.

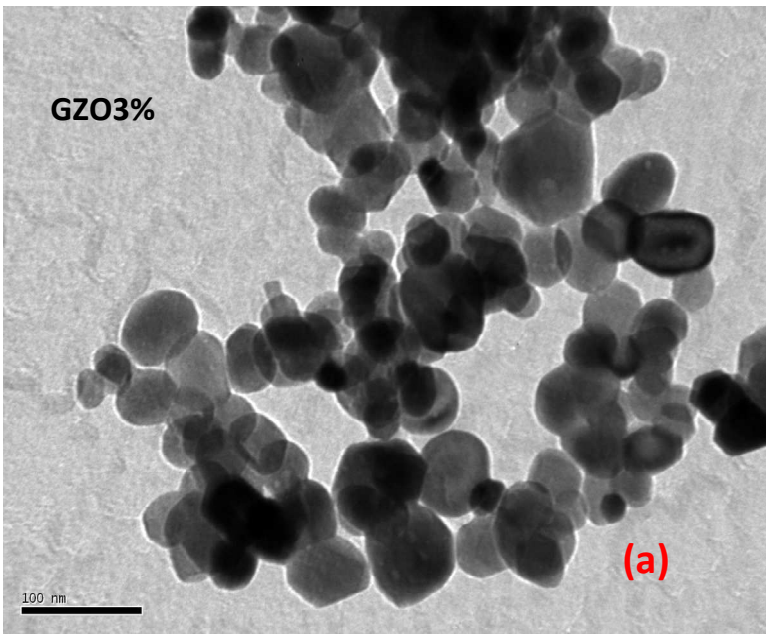

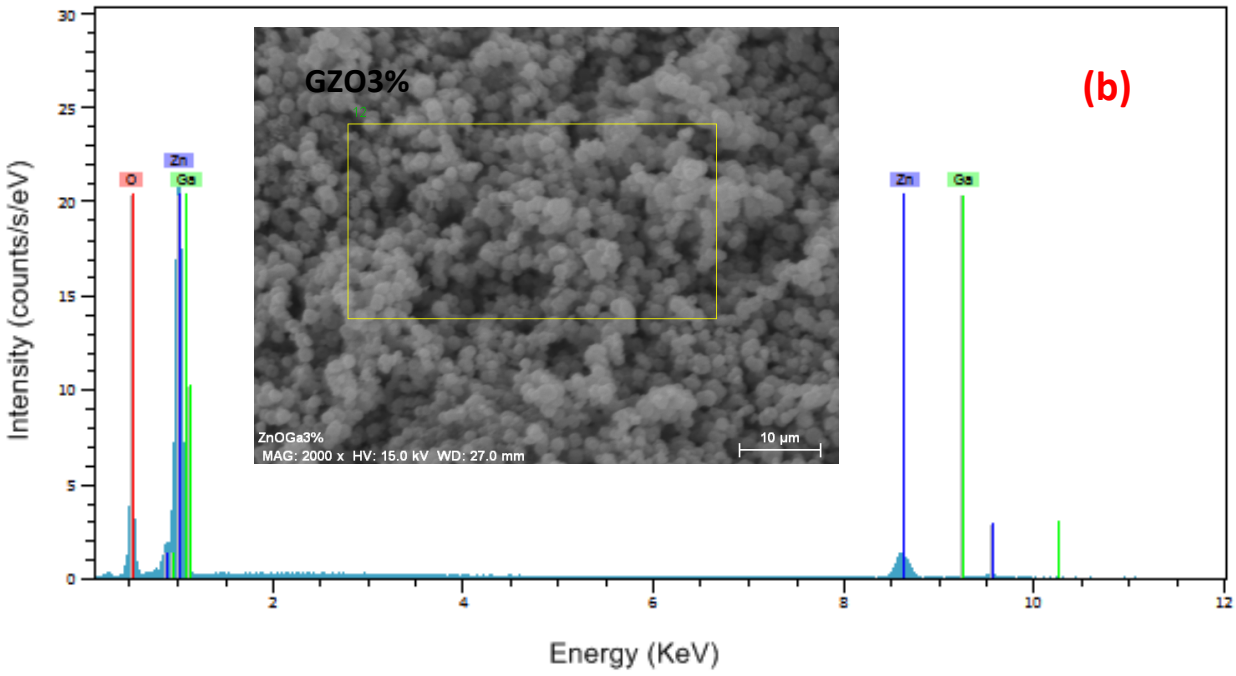

Fig. 2. Typical TEM photograph (a) and SEM showing (b) the general morphology of GZO aerogel nanoparticles.

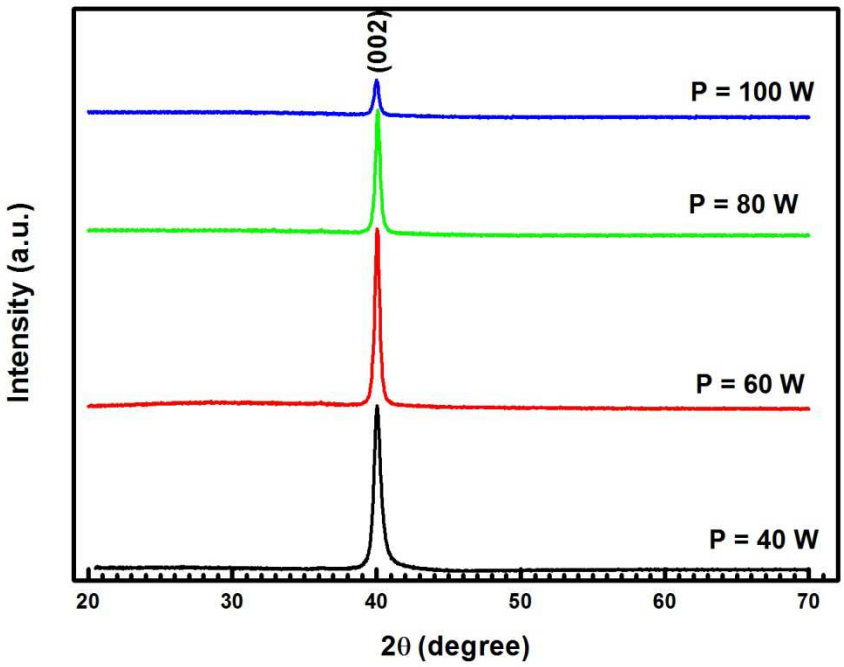

Fig. 3. X-ray diffraction of GZO thin films with different rf powers.

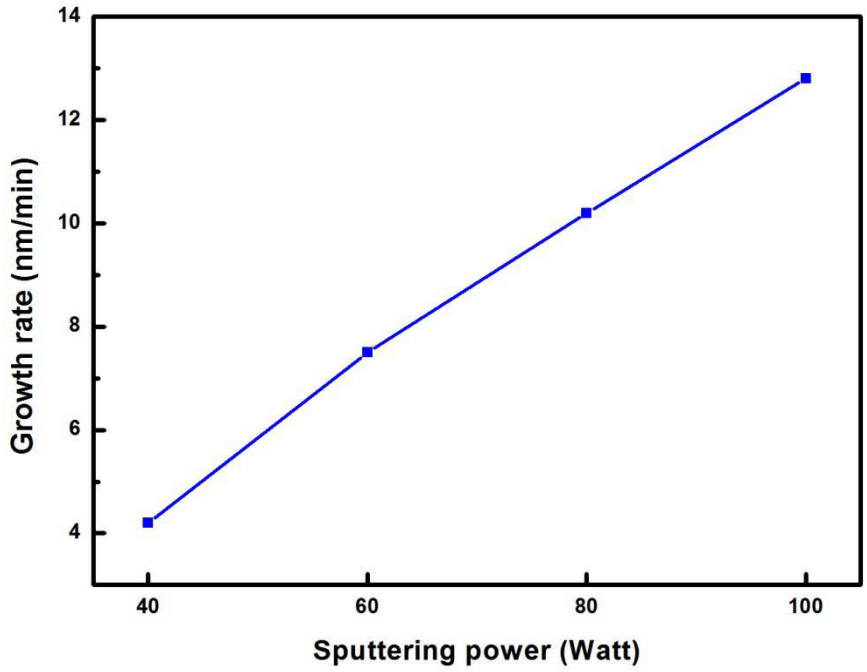

Fig. 4. Growth rate of GZO films as a function of sputtering power.

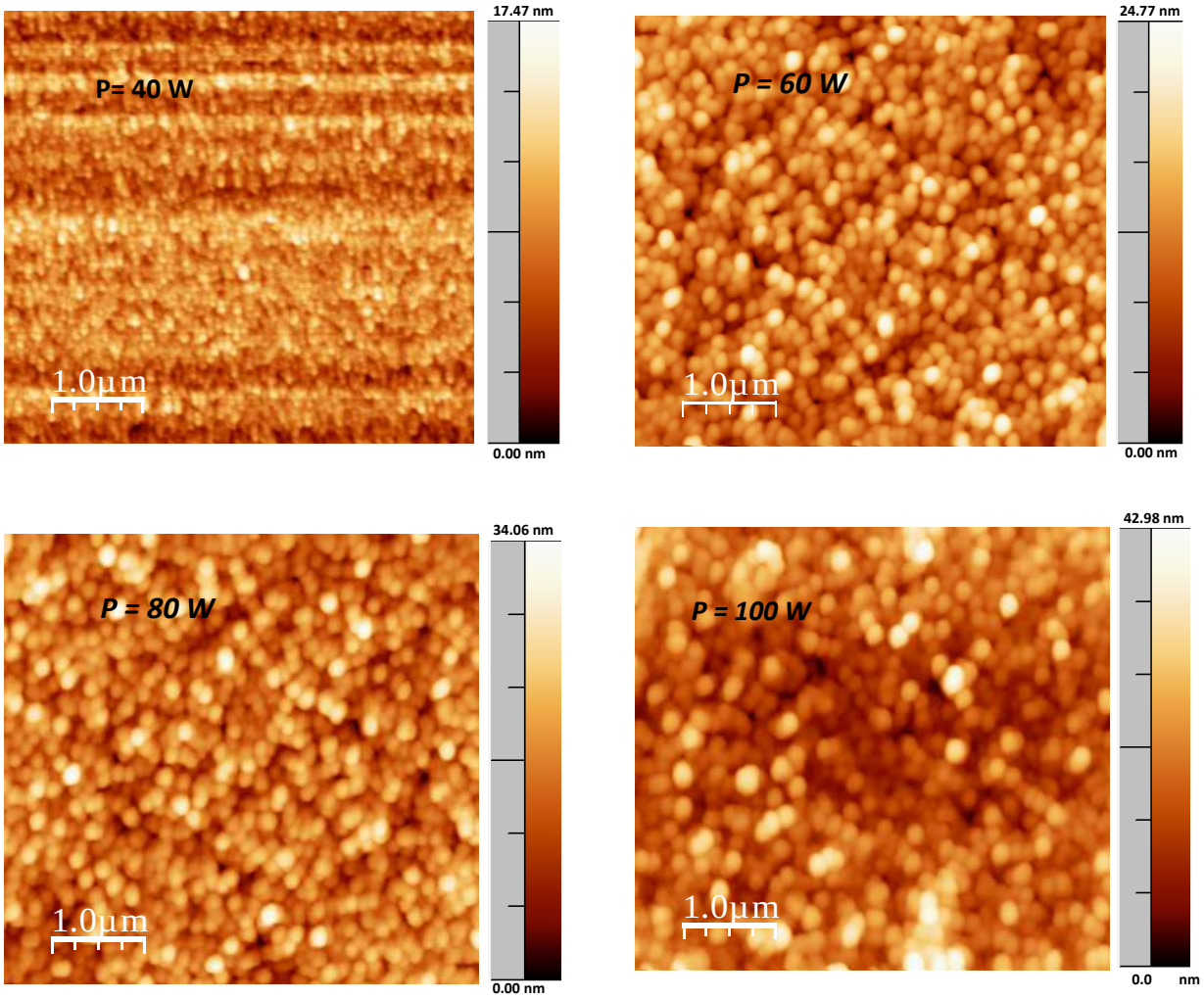

Fig. 5. 2D AFM micrographs ($5\mu m \times 5\mu m$) for the ZnO:Ga films with different sputtering powers.

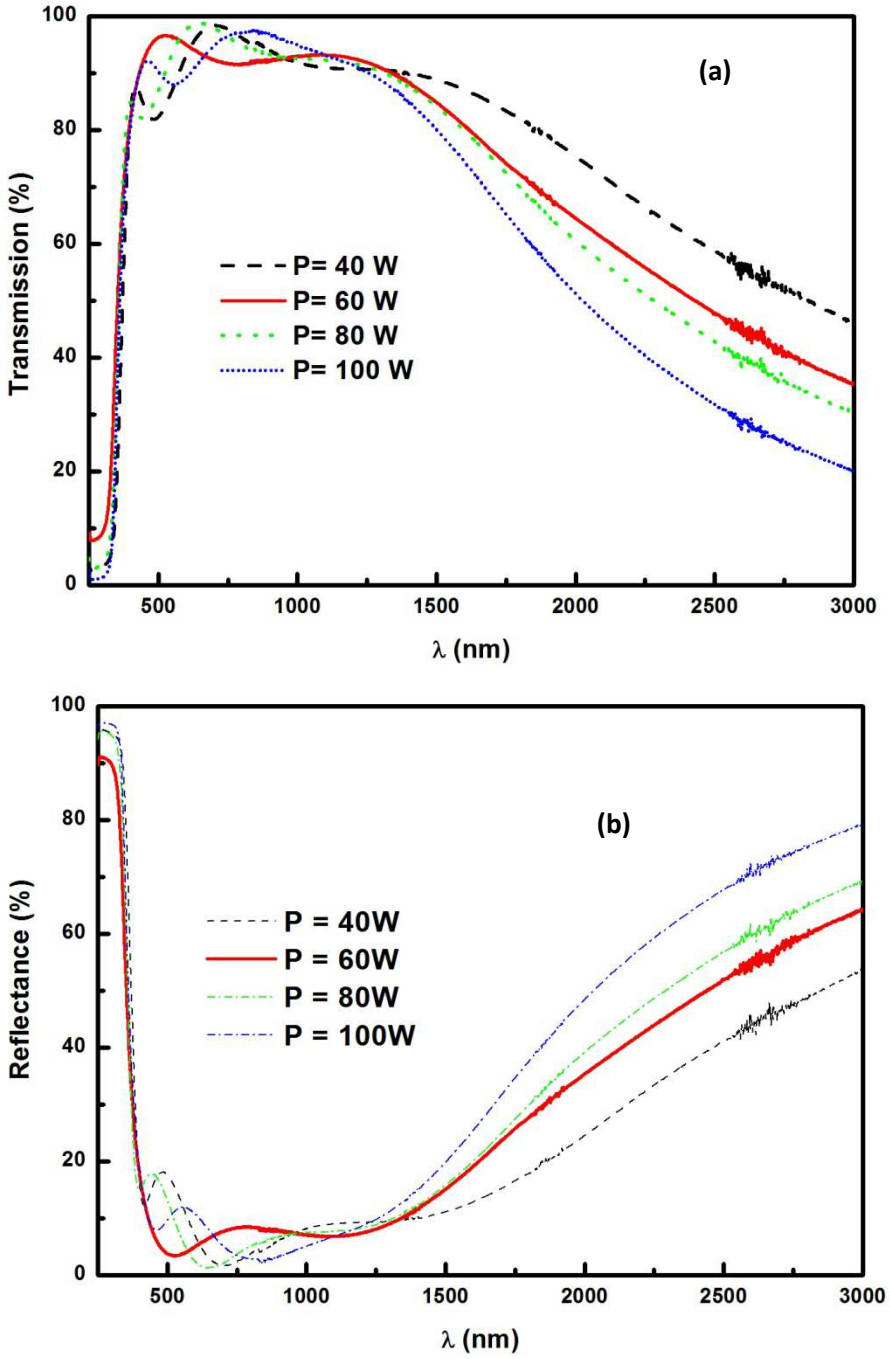

Fig.6. Transmittance and reflectance spectra of GZO films deposited at various rf powers.

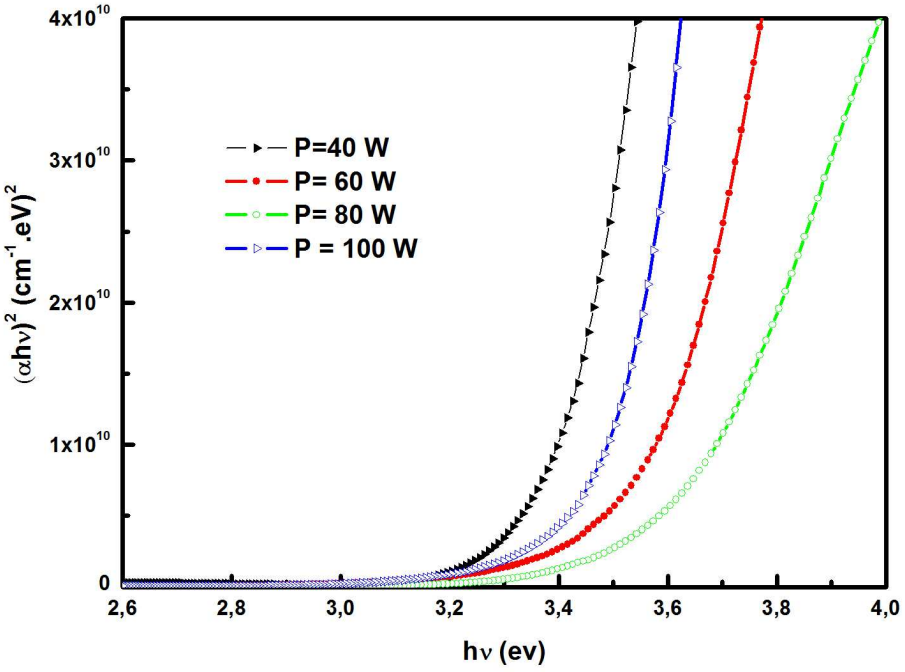

Fig. 7. Plots of $(\alpha h\nu)^2$ versus photon energy ($h\nu$) of GZO thin films with various rf powers.

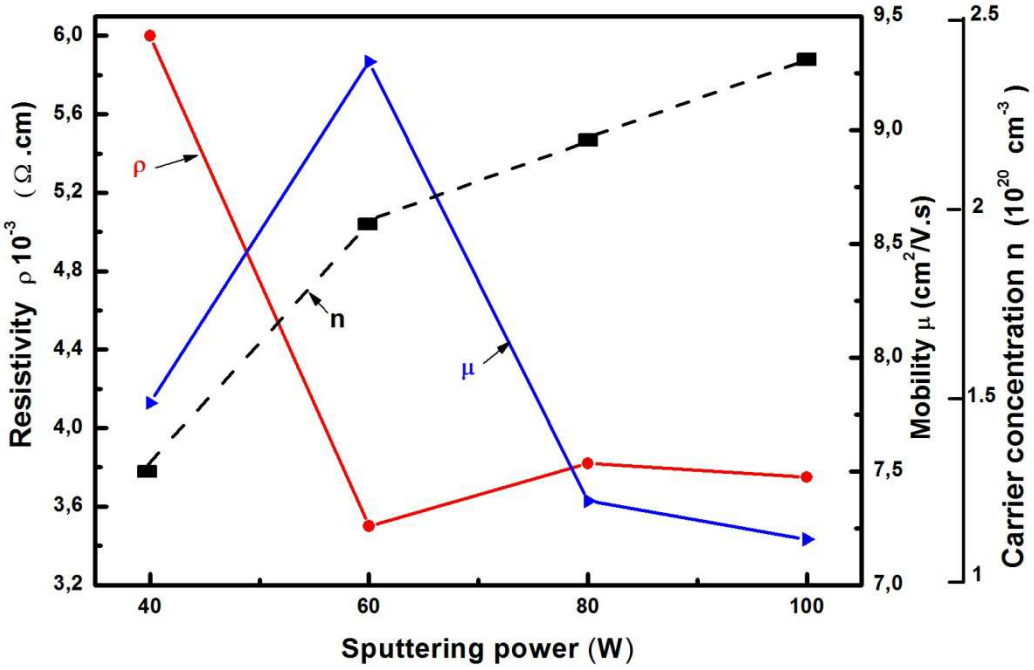

Fig. 8. Resistivities, mobility and carrier concentration of GZO thin films as a function of sputtering power.

Table 1. Atomic compositions of GZO nanoparticles.

Chemical composition in at. %		
Zn	**O**	**Ga**
47.12	51.54	1.34

Table 2: Variation of the (002) peak positions, FWHM, grain size, interreticular distance (*d*) lattice constant (c) and the stress (σ) of the films GZO at different sputtering power.

Rf-power (Watt)	(002)2θ (deg)	β (deg)	G (nm)	d_{hkl} (nm)	c (nm)	σ (GPa)
40	39.97	0.538	18.25	0.2617	0.5234	8.53
60	40.04	0.337	29.20	0.2613	0.5226	6.02
80	40.06	0.331	29.65	0.2611	0.5222	4.80
100	40.04	0.312	31.48	0.2612	0.5224	5.42

Nanotechnology Electrical Behaviour of Antimony Doped layers in silicon as a function of the annealing conditions

[1]T. Alzanki, [1]K. M. Kandil, [1]M. Alenezi, [1]A. Almeshal, [2]B. J. Sealy, and [1]A. Ghoneim
[1]Public Authority for Applied Education &Training (PAAET), P.O. BOX 42325. Safat. Kuwait.
[2]Advanced Technology Institute, University of Surrey, Guildford, GU2 7XH, UK.

ABSTRACT: Antimony implantation is a promising technique for fabricating ultra-shallow n^+/p junctions for extensions of sub-100 nm n-MOSFETs. With the aim of producing shallow n^+ doped layers in p-type silicon substrates, 2keV and 5keV Sb^+ has been implanted at fluences of $5x10^{14}$ and 1×10^{15} cm^{-2} into silicon and annealed using different temperature and time conditions. Electrical characterisations of the samples were done using sheet resistance and Hall effect measurements. 5keV Sb^+ implantation into Si shows the highest electrical activation (60%) as compared to 2keV implants (8%) after annealing at 600 ^oC for 10s. Both energies show a decrease in the electrical activation and an increase in the sheet resistance with increasing annealing temperature from 600^{o}C to 1100^{o}C. There is almost no increase in the electrical activation for both energies with increasing annealing time from 10s to 15mins. Secondary Ion Mass Spectroscopy (SIMS) and a novel Differential Hall Effect (DHE) technique were performed to evaluate the dopant distribution after annealing. Broadening of both 2keV and 5keV profile and a decrease in the carrier concentration is observed for annealing temperatures greater than 900^{o}C.

Keywords: Differential Hall effect, Secondary Ion Mass Spectroscopy, rapid thermal annealing, antimony, ultra shallow junction formation, antimony, silicon

INTRODUCTION: Shallow junctions or ultra shallow junctions are fabricated by many techniques such as, solid phase diffusion, epitaxial doping method, plasma doping method, laser annealing, thermal annealing etc. However, in shallow junction fabrication, ion implantation followed by rapid thermal annealing (RTA), are the conventional techniques used for better controllability, reproducibility and dopant uniformity. To obtain lower projected range, the energy should be low. High temperature annealing at a rapid rate i.e., rapid thermal annealing is preferred to achieve low sheet resistance [1]. Ultra shallow junction formation is one of the key technologies for scaling of MOSFETS. Scaling down of gate length needs a reduction in junction depth for suppression of short channel effects. From the viewpoint of CMOS integration, increase in junction sheet resistance is undesirable, because it leads to increase in parasitic source and drain resistance and prevents performance improvement of MOSFETs by scaling. Source and drain (S/D) junctions for sub 0.1μm CMOS devices are fabricated with As implantation whose energy is less than 10keV **[**2, 3**].** Shibahara et al. **[**4**]**, has reported ultra shallow low-resistive junction formation for sub-100-nm MOSFETs using antimony-doped S/D extensions. However, the electrical characterisation of these shallow n^+/p junctions formations using antimony has not been discussed well in the literature prior to our study **[**5,6**]**. The next generation of sub micrometer MOSFET devices is expected to have a channel length as small as 0.10 μm with S/D extension shallower than 40 nm. In the meantime the management of short channnel effects is expected to have a significant impact on processes used for doping drain extension channels and channel edges. Drain extension doping levels are expected to increase, to minimize parasitic resistance. Conventional rapid thermal annealing has been used throughout this work. It is useful to note that in conventional RTA Sb diffuses exclusively through a vacancy-assisted mechanism. The limited stability of vacancies above 600^{o}C [6]

implies that Sb will not exhibit the transient enhanced diffusion seen with species that diffuse wholly or partly through a Si self-interstitial mechanism. Using Sb for Ultra-Shallow Junction (USJ) purposes may also be advantageous in combination with laser thermal processing (LTP) for high dopant activation and reduction in diffusion [7].

Junction depth is mainly controlled by the implantation energy; however, diffusion during annealing is not negligible especially for the ultra-shallow extension junctions for sub -100nm MOSFETs. Sb is suitable for fabrication of the shallow extensions because of its low diffusivity. However, low thermal equilibrium solid solubility ($1x10^{19}$ cm^{-3} at 850^{o}C and $2x10^{19}$ cm^{-3} at 1000^{o}C [8]) of Sb was the roadblock to use Sb as the dopant for the extension. The details of low energy Sb implantation have not been discussed in terms low diffusion of the profile, junction depth and sheet resistance. In this paper, the effect of post-implant annealing temperature for low (2-5 keV) energy antimony implantation into silicon is discussed. We have also used a modified Differential Hall Effect technique to obtain doping profiles for low implant energies. Thus, the main challenges are to achieve low sheet resistance and high electrical activation of the Sb^{+} implantation into Si.

II. *Experimental*: P-type (100) Si wafers of diameter 200mm with a bulk resistivity of 2-10 Ω.cm were implanted at RT with 2 and 5 keV Sb^{+} at fluences of 1×10^{15} cm^{-2} and 5×10^{14} cm^{-2}. The as-implanted projected range for Sb^{+} implants are respectively 4.8 nm (2 keV) and 7.5 nm (5 keV), and the calculated as-implanted maximum concentrations are respectively 3.1×10^{21} cm^{-3} and 1.1×10^{21} cm^{-3}. The tilt and twist angles of implantation were 7^{0} and 22^{0} respectively. All the implants were performed using a 200 kV Danfysik 1090 accelerator. After implantation the wafers were annealed at temperatures between 600^{o}C and 1100^{0}C for annealing times between 10s and 15 mins. The annealing was performed using a Process Products Corporation RTP system with flowing nitrogen ambient. Following annealing, cloverleaf pattern is

printed on the samples using photolithography and chemical etching solution using a mixture of HNO_3: HF: DI water in the ratio 25: 2: 25. Sheet measurements were performed using a Accent HL5500 Hall system. Electrical Profiles were performed by using a Accent HL5900 Hall system. In/Ga eutectic was used for ohmic contact. For differential Hall effect profiling, we use a native oxide growth and strip process with 2nm resolution. This is achieved by timing the duration that the sample spends in deionised water and air, enabling the growth of a very thin oxide, which is left in place during measurement. Sheet resistance measurements between the HL5500 and HL5900 Hall systems agree within a few percent. SIMS measurements were carried out using a Cameca IMS 6F with a primary beam energy of 750 eV O2+ and 1.5 keV O2+ for samples implanted with antimony at 2 keV and 5 keV respectively.

III. *Results and Discussion*:

Sheet Measurements:

The electrical activation and sheet resistivity measured as a function of the annealing temperatures for the 2 keV and 5 keV Sb^+ implantation into Si at fluences of 1×10^{15} ions/cm^2 and 5×10^{14} ions/cm^2 is shown in figure 1. It is clear that, for the range of annealing conditions investigated, the sheet resistance of the layer decreases with decreasing annealing temperature.

A. For 2 keV Sb^+ implants at a fluence of 1×10^{15} Sb^+cm^2, the highest electrical activity is about 8% after annealing at 600^{o}C for 10s. The lowest sheet resistance value (~1164 Ω/□) however, is found to occur at 800^{o}C but similar low values are obtained at 600^{o}C by increasing the anneal time to 10 mins. The additional time (≥10 mins) is thought to be necessary to complete the solid phase epitaxial re-growth, that is, to complete re-crystallisation of the implanted layer. However, an increase in the electrical activation from 8% to 10% is observed for longer annealing times from 0.5mins to 15mins at 600^{0}C.

B. For 5 keV Sb^+ implants at fluence of 1×10^{15} Sb^+cm^2, the highest electrical activity (~30%) is obtained at the lowest annealing temperatures of 600°C-800°C using an annealing time of 10s. The lowest sheet resistance value (~412 Ω/□) however, occurs at 800°C but similar low values are obtained at 600°C by increasing the anneal time to 10 mins. However, no change in the electrical activation is observed for 5keV antimony implanted samples which are annealed at 600°C for times greater than 10mins.

C. For 5 keV Sb^+ implants at fluence of 5×10^{14} Sb^+cm^2, the highest electrical activity (~60%) is obtained at the lowest annealing temperature of 600°C for annealing time of 10s. The lowest sheet resistance values (~414 Ω/□) however, are found to occur at 800°C but similar low values are obtained at 600°C by increasing the anneal time to 10 mins. However, no change in the electrical activation is observed for samples, which are annealed at 600°C for times greater than 1min.

D. A comparison of the electrical characteristic for antimony (Sb^+) implantation into silicon between our results and those from applied materials is shown in figure 3. Our sheet resistance values is lower than those reported by Collart *et al* [10]. There is a difference of ~14% between the two results**.** Figure 2 shows the effect of electrical activation and sheet resistance as a function of annealing time for both 2keV and 5keV implants. The samples were annealed at times ranging from 10s-15mins. Both implants show similar electrical activation with increasing annealing time from 10s to 15mins. The electrical activation for 5keV implants is three times higher than that of 2keV. We believe that lower implantation energy creates more damage so that the probability of activation is lower. Formation of shallower junction can be achieved by reducing the implantation energy. However, improvement in sheet resistance (R_s) is also important during scaling of the n-doped junction. RTA method is an effective way of improving the sheet resistance [11]. We observe a decrease in the electrical

activation and increase in the sheet resistance with increasing annealing temperature from 600^0C to 1100^0C for both 2 keV and 5 keV implants (table 1). The electrical activation tends to decrease when higher thermal budget is used. As for active fluence, N_d, it tends to decrease with the increase of annealing temperature. This is because of excess thermal energy supplied to activate the dopants. Hence the antimony atoms tend to cluster and/or precipitate together. Thus they are unavailable for electrical activation. During annealing two mechanisms compete: the first one is the re-growth of the damaged layer with the inclusion of the dopant atoms in lattice sites available for electrical conduction; the second is the diffusion of the dopant that tends to nucleate to form inactive precipitates. With increasing thermal energy the second mechanism starts to control over the first one [12].

Electrical profiles:

Figures 4 shows the 2keV Sb at fluence 1×10^{15} /cm^2 carrier concentration profiles following 10s anneals in a nitrogen ambient for various anneal temperatures. Though diffusion of Sb is clearly observed after annealing at 1100^oC, it is apparently negligible in samples annealed at 600^oC and 800^oC, where the profile matches the as-implanted TRIM simulation.

Poor electrical activation (8%) is observed after annealing at 600^oC and 800^oC (table1). Further decrease in electrical activation (4%) is observed for annealing temperatures greater than 900^0C. The decrease is most probably due to out-diffusion and loss of Sb into the native oxide and in the bulk as shown in figure 4. The junction depth, defined here as the depth at which the electron concentration falls to 5×10^{18} cm^{-3}, is about 12 nm for the 2 keV Sb^+ implant after annealing at 600^oC and 800^oC. An increase in the junction depth (>12nm) is observed with increasing annealing temperatures (>900^0C). Figure 5 shows the 5 keV Sb^+ depth profile for a fluence of 1

$\times 10^{15}$ cm^{-2} for various anneal temperatures. The Sb profiles for samples annealed at 600^0C and 800^0C are quite similar to the as-implanted SIMS profile. Similar to 2keV implants, diffusion of Sb towards the surface and in the bulk is observed for higher annealing temperatures (>900^0C). The decrease in activity to 80% at 1100^0C is presumably due to out diffusion and loss of antimony mainly in the bulk as shown in figure 5. The junction depth and sheet resistance is ~15nm and ~450 Ω/□ respectively for samples which have been annealed at temperature lower than 900^0C. This is suitable for future generations of CMOS devices [13].

Figure 6 shows the 5keV Sb^+ depth profiles for a fluence of 5×10^{14} cm^{-2} at various annealing temperatures. Though antimony diffusion is clearly observed for 900^0C and 1100^0C anneals, it is absent in samples annealed at 600^0C and 800^0C, which shows good agreement with the as implanted profile and published data [8]. The sheet resistance measurements for these implants are summarized in Table 1. For 600^0C annealed samples, the electrical activation is two times higher than that of 5keV, $1x10^{15}$ cm^{-2} implanted samples. A decrease in the electrical activation from 60% to 16% is observed with increasing annealing temperatures from 600^0C to 1100^0C. The decrease in activity to 73% at 1100^0C is most probably due to out diffusion and loss of antimony into the native oxide (figure 6).

The junction depth and sheet resistance is ~15nm and ~422 Ω/□ respectively for samples which have been annealed at temperatures lower than 900^0C. Larsen et al [8] has also reported similar profile broadening and a reduction in the peak atomic concentration using Rutherford Backscattering Spectroscopy (RBS) following high temperature anneals (>900^0C) for 80keV Sb^+ implant at fluences in the range of $2x10^{15}$ to $1x10^{16}$ cm^{-2}.

Figure 7 shows a graph of sheet resistance as a function of junction depth for 2keV and 5keV implants. Samples annealed at 800^0C show the lowerest sheet resistance for

both 2keV and 5keV implants. Shibahara et al [4] has also reported similar trend for 10keV Sb implantation into Si for fluences varying from $1x10^{14}$ to $6x10^{14}$ cm^{-2}. They have suggested that annealing temperatures should not exceed 800^0C in order to avoid deterioration of the sheet resistance, which are shown by our results.

IV. *Conclusion*:

Shallow junction formation in silicon using antimony was investigated aiming at applications to sub-100nm MOSFET S/D extensions. The results show that antimony is an interesting candidate for the next generation of n-type ultra shallow junction formation. 5 keV antimony implantation results in lower sheet resistance and higher electrical activation after annealing at 600^0C. The sheet resistance increases with decrease in implantation energy. Almost no change in the sheet resistance and electrical activation is observed for low energies (2-5keV) antimony implanted samples, which are annealed at 600◦C for times between 10s and 15mins. We have found that no diffusion of antimony occurs for annealing temperatures below 900^0C. In contrast, high temperature anneals (>900◦C) produce significant broadening of the electrical profiles. Junction depths of about 10 nm and 20nm have been achieved using 2 keV and 5keV antimony respectively.

References:

1. Takeuchi, K., Hori, A., and Takase, M.: 'Formation of ultra shallow junction by BF_2^+ implantation and spike annealing', Process Manufacturing Department, ULSI Engineering Division, Fujitsu Limited, Japan 2002.
2. Takeuchi, K., Yamamoto, T., Furukawa, A. Tamura, T., and Yoshida, K.: 'High performance sub-tenth micron CMOS using advanced boron doping and Wsi_2 dual gate process', Symp. on VLSI Tech. Digest of Technical Papers, 1995, pp. 9-10.
3. Hori, A., Nakaoka, H., Umimoto, H., Yamashita, K., Takase, M., Shimizu, N., Mizuno, B., and Odanaka, S.: 'A 0.05μm-CMOS with ultra-shallow source/drain junctions fabricated by 5keV ion implantation and rapid thermal annealing', Tech. Digest Int. Elec. Dev. Meeting, 1994, pp. 485-488.
4. Shibahara, K., and Onimatsu, D.: 'Antimony clustering due to high fluence implantation', Mat. Res. Soc. Symp., 2000, 610, pp. B8.5.1-B8.5.6.
5. Shibahara, K.: 'Ultra-shallow junction formation with antimony implantation', IEICE Trans. Elec., 2002, E85-C, pp. 1091-1097.
6. Sai-Halasz, G. A., Short, K. T., and Williams, J. S.: 'Antimony and arsenic segregation at Si-SiO_2 interfaces', IEEE Elec. Dev. Lett., 1985, 6, pp. 285-287.
7. Watkins, G. D.: 'Defect and diffusion in silicon processing native defects and their interaction with impurities in silicon', Mat. Res. Soc. Symp. Proc. 1997, 469, pp. 139-150.
8. Fage-Pedersen, J., Gaiduk, P., Lundsgaard, J., and Nylandsted Larsen, A.: 'Si-self-interstitial injection from Sb complex formation in Si', J. Appl. Phys., 2000, 88, (6), pp. 3254-3259.
9. K. Shibahara, M. Mifuji, K. Kawabata, T. Kugimiya, H. Furumoto, M. Tsuno, S. Yokoyama, M. Nagata, S. Miyazaki and M. Hirose, Tech. Digest lnt. Electron Devices Meeting, pp. 579-582 (1996).
10. E. Collart, D. Kirkwood, W. Vandervorst, B. Brijs, J. A. Van den Berg, M. Werner, T.C. Q. Noakes, "Characterization of Low Energy Antimony (2-5 keV) Implantation into Silicon", Proc. of IEEE for the Intl. Conf. on Ion Implant. Tech., September (2002).
11. T. Alzanki, R. Gwilliam, N. Emerson, A. Smith, R. Webb, & B. J. Sealy, 2006.Electrical profiles of 20nm junctions in Sb implanted silicon. Nuclear Instruments and Methods in Physics Research **B242**: 693-695.
12. B. J. Sealy, A. Smith, T. Alzanki, N.S. Bennett, L. Li, C. Jeynes, B. Colombeau, E. Collart, R. Gwilliam, N. Emerson, & N. Cowern, 2006. Shallow junctions in silicon via low thermal budget processing. IWJT International Workshop on Junction Technology: 10-15.
13. T. Alzanki, R. Gwilliam, N. Emerson, & B. J. Sealy, 2009. Low energy antimony implantation in p-type silicon for ultra-shallow junction formation. Kuwait Journal of Science and Engineering. 36 (2B): 107-115.

Authors' affiliations:

T. Alzanki, K. M. Kandil, M. Alenezi, A. Almeshal and A. Ghoneim
Public Authority for Applied Education &Training, P.O. BOX 42325. Kuwait.
(College of Technical Studies).
E-mail address: th.alzanki@paaet.edu.kw

Figure captions:

Figure 1 Electrical activation and sheet resistance as a function of annealing temperature for 2-5 keV Sb. The annealing time was 10s.

Figure 2 Electrical activation and sheet resistance as a function of annealing time for 2-5 keV, 1×10^{15} Sb^{+} cm^{-2}. The annealing temperature was 600^{0}C.

Figure 3 Comparisons of sheet resistance as a function of annealing temperature between our results and those of Applied Materials. The annealing time was 10s.

Figure 4 Carrier concentration profiles for 2 keV, 1×10^{15} Sb^{+} cm^{-2} as a function of annealing temperature with an annealing time of 10s. The TRIM simulation of the as-implanted atomic profile is included for comparison.

Figure 5 Carrier concentration profiles for 5 keV, 1×10^{15} Sb^{+} cm^{-2} as a function of annealing temperature with an annealing time of 10s. The SIMS as-implanted atomic profile is also included for comparison.

Figure 6 Carrier concentration profiles for 5 keV, 5×10^{14} Sb^{+} cm^{-2} as a function of annealing temperature with an annealing time of 10s. The TRIM simulation of the as-implanted atomic profile is included for comparison.

Figure 7 Sheet resistance as a function of junction depth for 2 and 5 keV Sb^{+} implants into Si at different annealing temperatures.

Table captions:

Table 1 Electrical data for 2 and 5keV Sb^{+} implants into silicon at different annealing temperatures.

Figure 1.

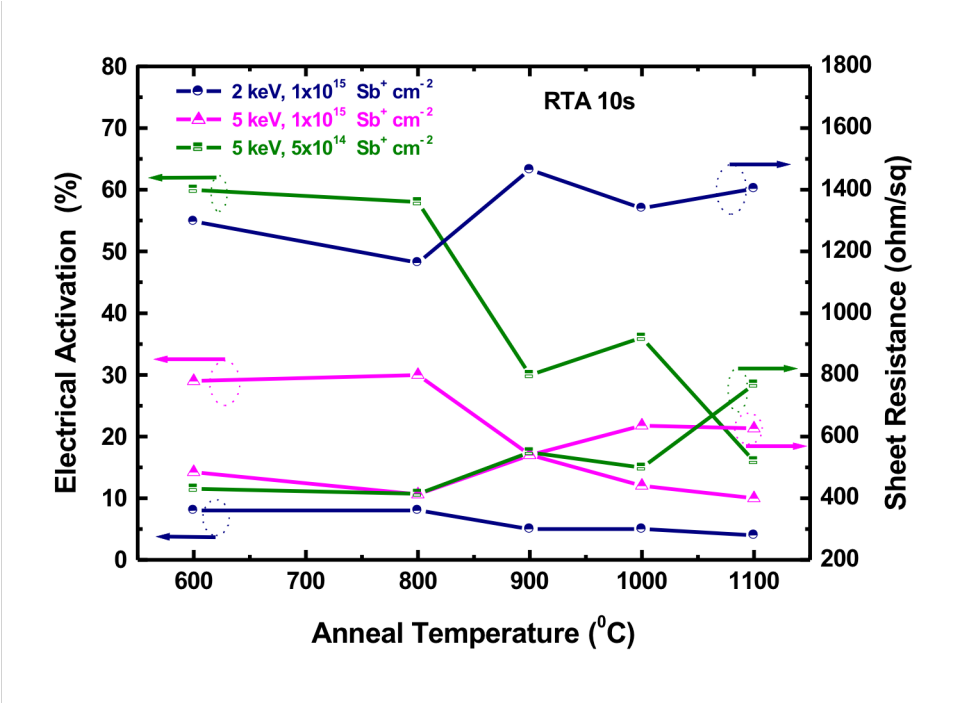
2 keV, 1x10^15 Sb+ cm-2
5 keV, 1x10^15 Sb+ cm-2
5 keV, 5x10^14 Sb+ cm-2
RTA 10s
Electrical Activation (%)
Sheet Resistance (ohm/sq)
Anneal Temperature (0C)
0
10
20
30
40
50
60
70
80
200
400
600
800
1000
1200
1400
1600
1800
600
700
800
900
1000
1100

Figure 2.

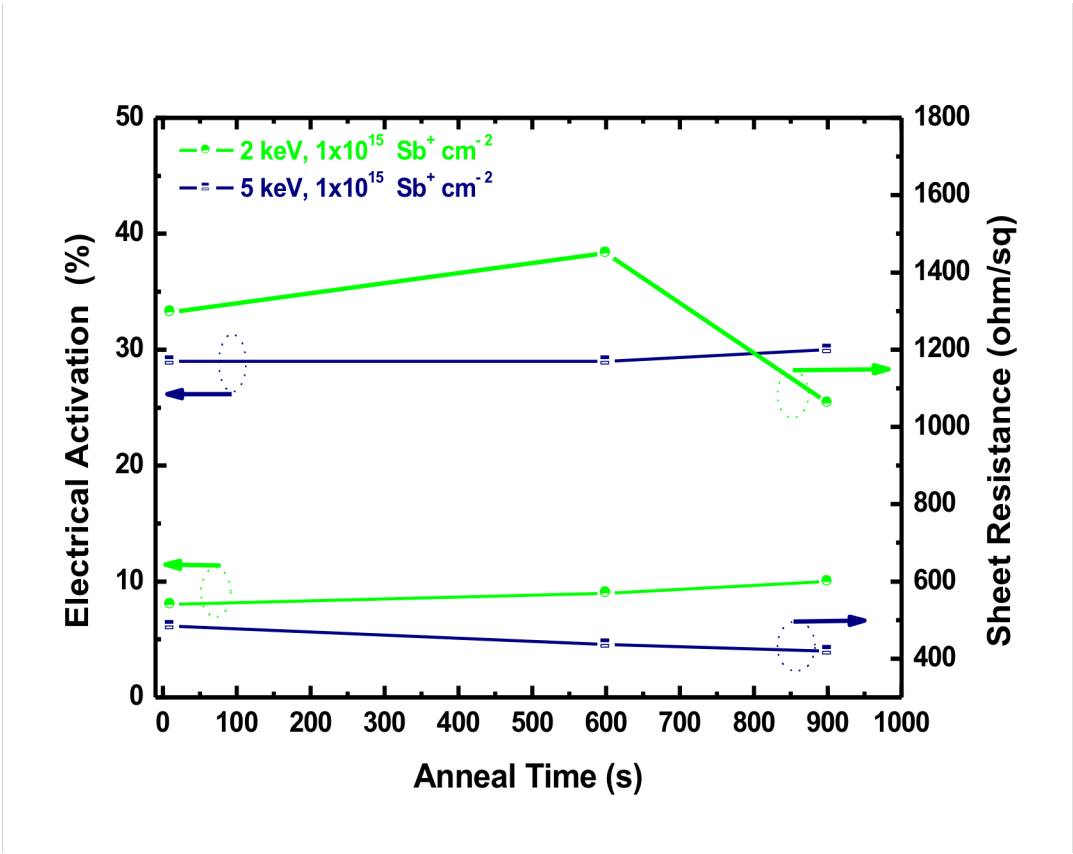
2 keV, 1x10^15 Sb+ cm-2
5 keV, 1x10^15 Sb+ cm-2
Electrical Activation (%)
Sheet Resistance (ohm/sq)
Anneal Time (s)
0
10
20
30
40
50
400
600
800
1000
1200
1400
1600
1800
0
100
200
300
400
500
600
700
800
900
1000

Figure 3.

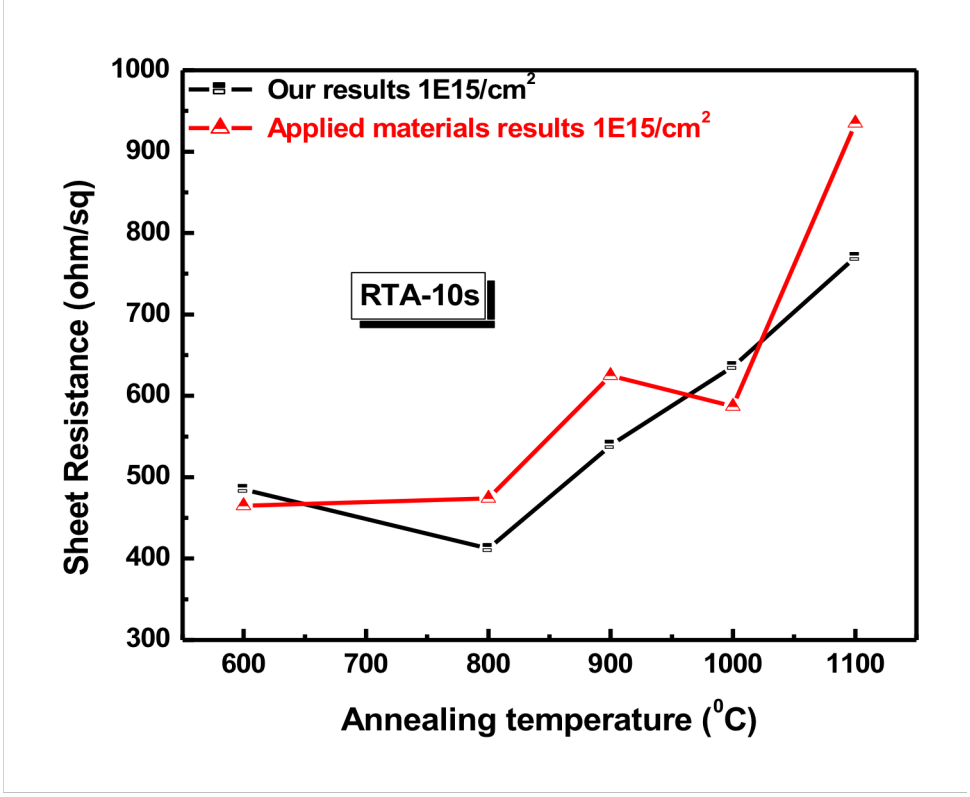
Our results 1E15/cm2
Applied materials results 1E15/cm2
RTA-10s
Sheet Resistance (ohm/sq)
Annealing temperature (0C)
1000
900
800
700
600
500
400
300
600
700
800
900
1000
1100

Figure 4.

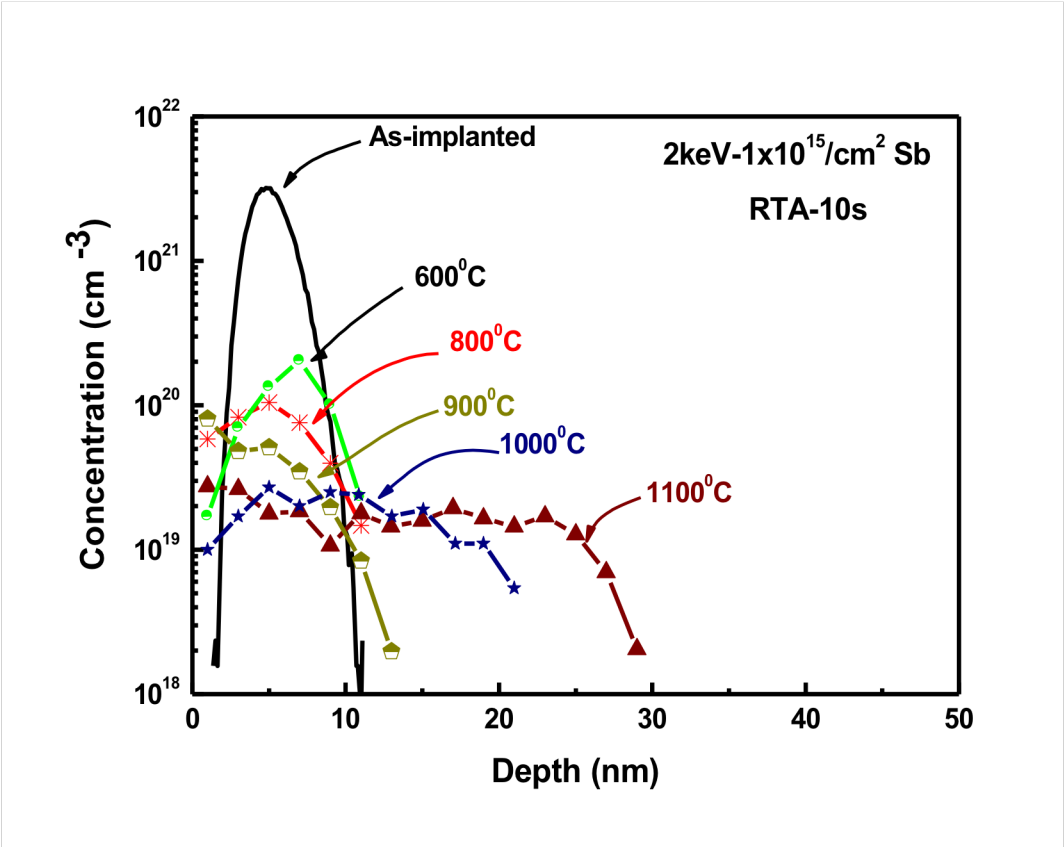
As-implanted
2keV-1x10^15/cm^2 Sb
RTA-10s
600^0C
800^0C
900^0C
1000^0C
1100^0C
Concentration (cm^-3)
Depth (nm)
10^22
10^21
10^20
10^19
10^18
0
10
20
30
40
50

Figure 5.

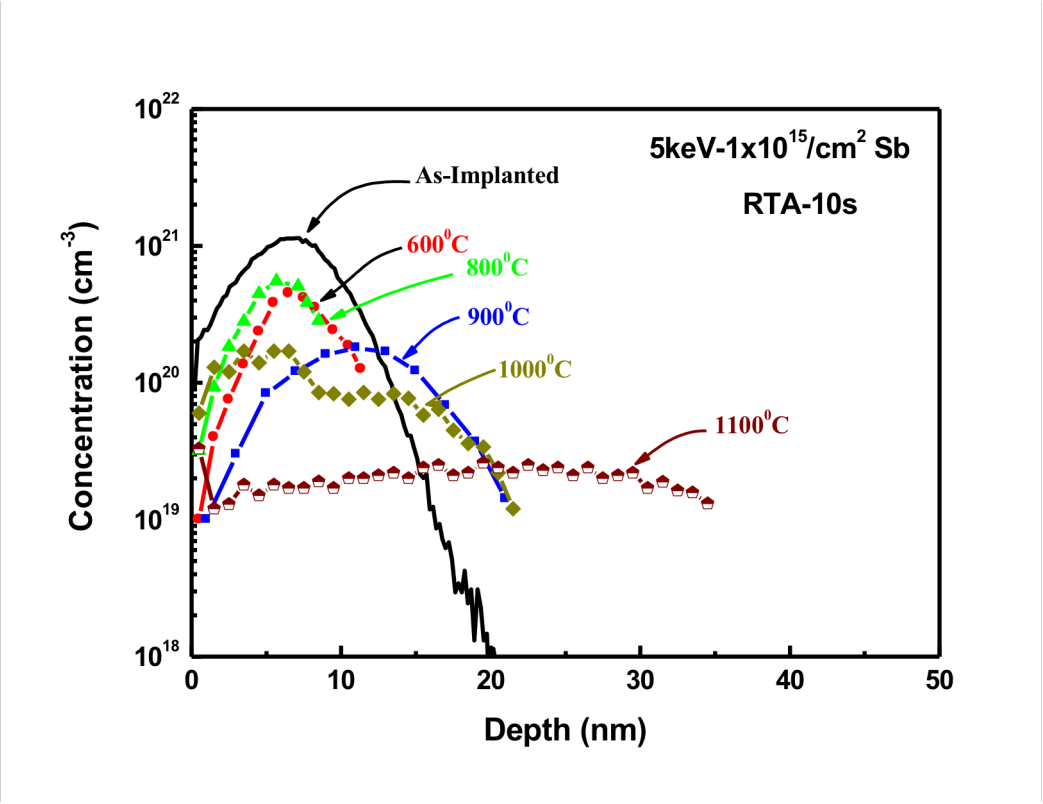
5keV-1x10^15/cm^2 Sb
RTA-10s
As-Implanted
600^0C
800^0C
900^0C
1000^0C
1100^0C
Concentration (cm^-3)
Depth (nm)
10^22
10^21
10^20
10^19
10^18
0
10
20
30
40
50

Figure 6.

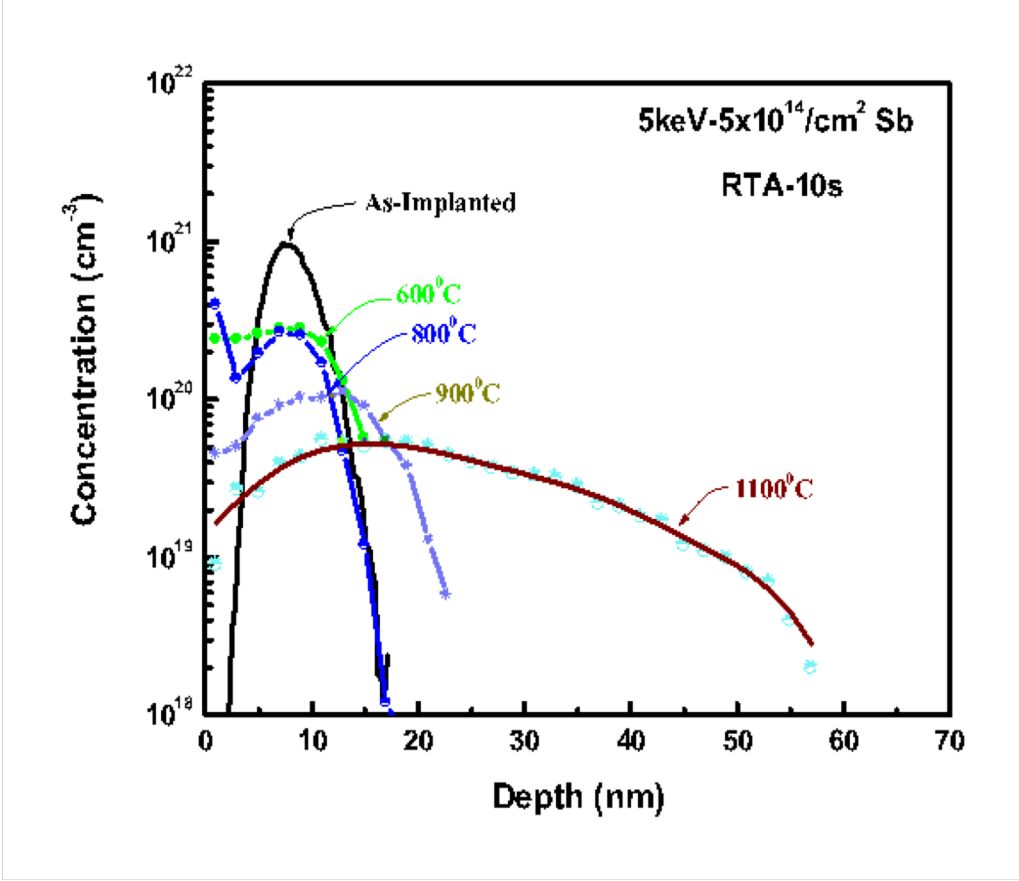
5keV-5x10^14/cm^2 Sb
RTA-10s
As-Implanted
600°C
800°C
900°C
1100°C
Concentration (cm^-3)
Depth (nm)
10^22
10^21
10^20
10^19
10^18
0
10
20
30
40
50
60
70

Figure 7.

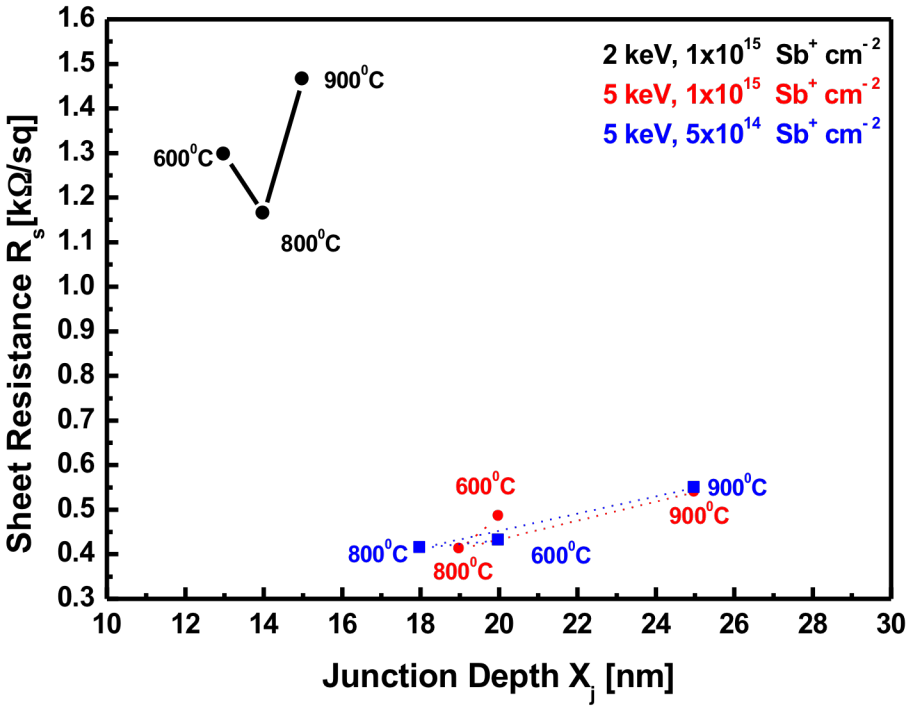
2 keV, 1x10^15 Sb+ cm-2
5 keV, 1x10^15 Sb+ cm-2
5 keV, 5x10^14 Sb+ cm-2
900°C
600°C
800°C
600°C
900°C
900°C
800°C
800°C
600°C
Sheet Resistance Rs [kΩ/sq]
Junction Depth Xj [nm]
1.6
1.5
1.4
1.3
1.2
1.1
1.0
0.9
0.8
0.7
0.6
0.5
0.4
0.3
10
12
14
16
18
20
22
24
26
28
30

Table 1.

Batch	Energy (KeV)	Fluence (Ion/cm^2)	Annealing temperature (^{0}C)	ρ_s (Ω/□)	Mobility (cm^2/V-s)	N_s (cm^{-2}) Active fluence	Peak electron concentration (cm^{-3})	Junction Depth X_j [nm]	Electrical Activation %
Sb^+# 1021	2	1×10^{15}	600	1297	60	8×10^{13}	2×10^{20}	13	8
Sb^+# 1021	2	1×10^{15}	800	1164	69	7.8×10^{13}	1×10^{20}	14	8
Sb^+# 1021	2	1×10^{15}	900	1465	92	4.7×10^{13}	5×10^{19}	15	5
Sb^+# 1021	2	1×10^{15}	1000	1340	96	4.8×10^{13}	2×10^{19}	29	5
Sb^+# 1021	2	1×10^{15}	1100	1404	105	4.2×10^{13}	2×10^{19}	30	4
Sb^+# 1025	5	1×10^{15}	600	485	45	2.88×10^{14}	3×10^{20}	20	29
Sb^+# 1025	5	1×10^{15}	800	412	49	3×10^{14}	6×10^{20}	19	30
Sb^+# 1025	5	1×10^{15}	900	539	69	1.7×10^{14}	2×10^{20}	25	17
Sb^+# 1025	5	1×10^{15}	1000	636	84	1.2×10^{14}	9×10^{19}	29	12
Sb^+# 1025	5	1×10^{15}	1100	770	113	7.3×10^{13}	2×10^{19}	50	7
Sb^+# 1024	5	5×10^{14}	600	431	49	3×10^{14}	2×10^{20}	20	60
Sb^+# 1024	5	5×10^{14}	800	414	53	2.9×10^{14}	2×10^{20}	18	58

Effect of copper to indium atomic ratio on physical properties of Cu-In-S thin films for photovoltaic applications

N. Khemiri[1,2], M. Kanzari,[1]

[1]Laboratoire de Photovoltaïques et Matériaux de Semi-conducteurs- ENIT- Université de Tunis El Manar, BP 37, le belvédère 1002-Tunis, Tunisie

[2]Institut Préparatoire des Etudes d'Ingénieurs El Manar - Université de Tunis El Manar, le belvédère 1002-Tunis, Tunisie

ABSTRACT

In this work, we investigated the physical properties of Cu-In-S thin films with different [In]/[Cu] ratios as promising candidates for thin films solar cells. Cu-In-S compounds with different [In]/[Cu] ratios were synthesized by the horizontal Bridgman method using high-purity copper, indium and sulphur elements. Crushed powders of these ingots were used as raw materials for the elaboration of samples. Cu-In-S thin films were deposited by single source vacuum thermal evaporation onto glass substrates heated at 200 °C. The effect of the [In]/[Cu] ratio on the structural, morphogical, optical and electrical properties of Cu-In-S thin films was investigated using X-ray diffraction (XRD), energy dispersive X-ray (EDX), atomic force microscopy (AFM) and UV-VIS-NIR spectroscopy techniques. XRD results revealed that all the films are polycrystalline. The absorption coefficients of the all Cu-In-S films are in the range of 10^{-4} and 10^{-5} cm^{-1}. The band gap (E_g) of the samples increases from 1.41 to 1.77 eV and then decreases to 1.58 when the [In]/[Cu] ratio increases. The resistivity of Cu-In-S thin films increases by increasing the [[In]/[Cu] ratio and we observe a transition of the type conductivity from p type to highly compensated.

Keywords

Cu-In-S system, thin films, thermal evaporation, optical properties, electrical properties.

1. INTRODUCTION

The Cu-In-S system is very interesting due to the formation of the $CuInS_2$ phase in it ([In]/[Cu] = 1). $CuInS_2$ is a typical semiconductor, which crystallizes in the chalcopyrite structure. Its physical properties are widely studied. Indeed, its direct band gap of 1.5 eV, high absorption coefficient and environmental viewpoint that $CuInS_2$ does not contain any toxic constituents, in comparison with the frequently studied $CuInSe_2$, makes it suitable for terrestrial photovoltaic application [1]. However, in spite of these interesting properties, very little is known about the related In-rich compounds of the Cu-In-S system. Cu-In-S compounds with atomic ratios [In]/[Cu] $\geq$ 1 are formed in the In-rich side of the pseudo-binary Cu_2S-In_2S_3 system [2]. These compounds stabilize due to the ordering of the neutral defect pairs ($2V_{Cu}^{-1}$ + In_{Cu}^{2+}) in $CuInS_2$ phase and this is due to its huge tolerance to off-stoechiometry [3].

In this work, we present results concerning the fabrication of the Cu-In-S thin films with different [In]/[Cu] ratios by the thermal evaporation method and the characterization of the structural, compositional, morphological and optical properties of these materials.

2. EXPERIMENTAL PROCEDURE

Cu-In_S crystals with different [In]/[Cu] atomic ratios were synthesized by direct reaction of high-purity (99.999 %) elemental copper, indium and sulphur. Thin films of Cu-In_S were prepared by thermal evaporation from a tungsten boat on glass substrates of rectangular shape (2.5 x 1.5 cm^2) under 10^{-6} mbar. The substrates were placed directly above the source at a distance of 15 cm and were heated at 200 °C by an insulator heater system. The deposition rate was 0.1 nm/s and the thickness was measured ex situ by a stylus profilometer. The crystalline phase and crystal orientation of the powder and the prepared films were examined using a Philips X'Pert X-ray diffractometer with a monochromatic. $CuK\alpha_1$ radiation (λ = 0.154056 nm and 40 kV, 30 mA). The surface morphology of the films was characterized by atomic force microscopy (AFM) (Veeco Dimension 3100). The optical properties were measured at room temperature and at normal incidence with an UV-VIS-NIR Shimadzu 3100S spectrophotometer in the wavelength range of 300 – 1800 nm. The resistivities of films were measured directly on samples using the Van der Pauw technique. The type of conductivity was determined by the hot probe method.

3. RESULTS AND DISCUSSIONS:

Fig. 1 displays XRD patterns of Cu-In-S thin films with different [In]/[Cu] ratios. It is clear from the Fig. 1 that all the films are polycrystalline with a preferred orientation along the 112 plane for the samples with [In]/[Cu] = 1 and 3 and the 311 plane for those with [In]/[Cu] = 5 and 7 [4]. Using the Scherrer formula [5], we also calculated the crystallite size L of samples from the full width at half maximum (FWHM) of the 112 and 311 peaks (Fig. 2). Although the films are grown at the same substrate temperature, the crystallite size of the sample with [In]/[Cu] = 1 is bigger in comparison to the others. This result suggests that the crystallite size in the Cu-In-S films is related to the In/Cu ratio. Indeed, Cu-excess conditions during film growth results in a higher grain sizes but in In-rich compounds the crystallite sizes are smaller [6].

The AFM analysis results for the surface roughness of the Cu-In-S thin films are shown in Fig. 1. The surface morphologies of the films are quite different. Indeed, the samples with [In]/[Cu] = 3 and 5 show smooth and homogeneous surfaces constituted of densely packed grains. However, the surfaces of the films with [In]/[Cu] = 1 and 7 are rough and constituted of large grains. Fig. 2 shows the root mean square (RMS) values of the surface roughness of the films. It is clear that all the films had a surface roughness of less than 15 nm with a maximum roughness for the film with [In]/[Cu] = 7. Rougher surfaces constituted by larger grains can advance optical scattering and can contribute to the enhancement of the absorption coefficient of films. These

properties are exploited in a number of applications, including semiconductor devices and solar cells [7].

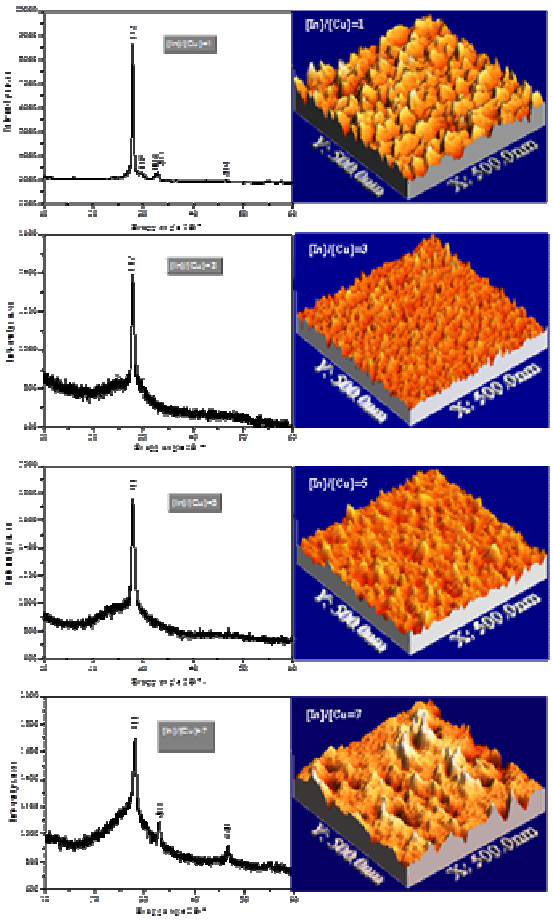

Figure. 1

Fig. 3 shows the variation of the band gap (E_g) versus the [In]/[Cu] ratio. E_g was calculated using the model postulated by Davis and Mott [19]. The band gap (E_g) of the samples increases from 1.41 to 1.77 eV and then decreases to 1.58 when the [In]/[Cu] ratio increases. We also note that the absorption coefficients of the all Cu-In-S films were in the range of 10^{-4} and 10^{-5} cm^{-1}.

The electrical resistivities of Cu-In-S films were measured using the Van der Pauw technique. As is seen in Fig. 4, the resistivity of the films increases from 40 to 1700 Ωcm with the increase in the [In]/[Cu] ratio. This increase can be explained in the light of the increase in the Indium content in the films and the change in the structure because the electrical properties of thin films are mainly governed by the stoichiometry and the structural properties. The conductivity type was identified by the hot-probe measurement technique. The Cu-In-S film with [In]/[Cu] = 1 was found to be p-type whereas the other samples were highly compensated.

In summary, Cu-In-S thin films with different [In]/[Cu] ratios were prepared by thermal evaporation. Our study exhibited that the Cu-In-S materials have important optical and electrical properties that allow those materials to be used in photovoltaic applications.

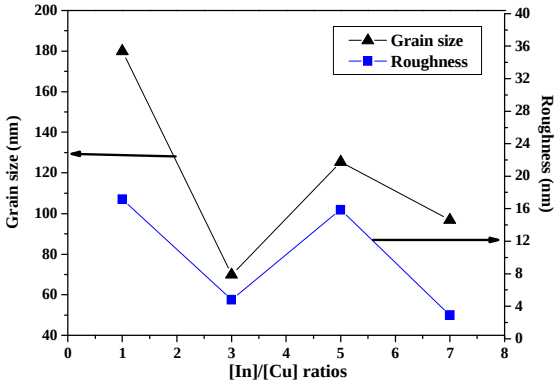

Figure. 2

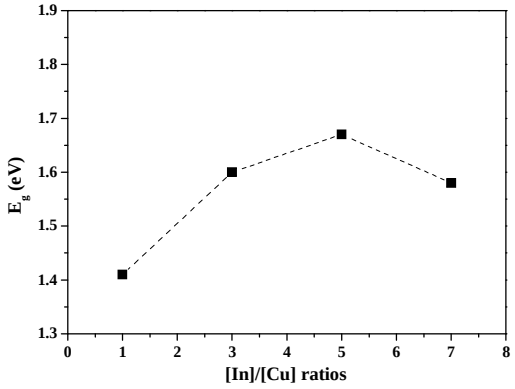

Figure. 3

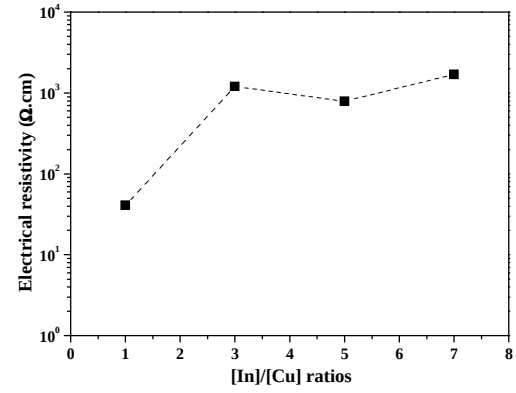

Figure. 4

4. REFERENCES

[1] Zribi, M., Kanzari, M. and Rezig, B. 2006. Optical constants of Na-doped $CuInS_2$ thin films. *Mat. Lett.* 60, (Jan. 2006), 98-103. DOI= http://dx.doi.org/10.1016/j.matlet.2005.08.001

[2] Zhang, S. B., Wie, S. H., Zunger, A. and Katayama-Yoshida, H. 1997. Defect physics of the $CuInSe_2$ chalcopyrite semiconductor. *Phy. Rev. B.* 57, (Apr. 1998), 9642. DOI= http://dx.doi.org/10.1103/PhysRevB.57.9642

[3] Malar, P., Savitha Pillai, S. and Kasiviswanathan, S. 2007. Structural, optical and compositional studies of stepwise flash evaporated $CuIn_3Te_5$ films. *Materials Chemistry and Physics.* 101, (Jan. 2007), 118-123. DOI= http://dx.doi.org/10.1016/j.matchemphys.2006.02.024

[4] Khemiri, N., Khalfallah, B., Abdelkader, D. and Kanzari, M. 2014. X-ray diffraction spectroscopy studies of $CuIn_{2n+1}S_{3n+2}$ thin films. *Int. J. Thin Fil. Sci. Tec.* 3, (Jan. 2014), 7-12. DOI= http://dx.doi.org/10.12785/ijtfst/030102

[5] Ladd, M. and Palmer, R. 2003. *Structure Determination by X-ray Cristallography.* Kluwer Academic, Plenum Publishers, New York.

[6] Khemiri, N. and Kanzari, M. 2010. Comparative study of structural and morphological properties of $CuIn_3S_5$ and $CuIn_7S_{11}$ materials. *Nuclear Instruments and Methods in Physics Research B.* 268, 3-4, (Oct. 2010), 268-272. DOI= http://dx.doi.org/10.1016/j.nimb.2009.10.175

[7] Sze, S. M. and Ng, K. K. 2006. *Physics of Semiconductor Devices.* John Wiley & Sons, Inc., Hoboken, New Jersey.

Memristor-like behavior investigation of the Ag_2S solid-state electrolyte formed by SILAR method

O.V. Pyatilova, S.A. Gavrilov, A.N. Belov, A.V. Zheleznyakova,
R.Yu. Rozanov, P.I. Lazarenko, A.A. Raskin

ABSTRACT
In this paper, we describe the formatting guidelines for Nanotech-MEET Tunisia 2014 conference proceeding.
Thin films of Ag_2S with thickness 15-120 nm were formed by SILAR (successive ionic layer adsorption and reaction) method.
Electrical properties, morphology, and thickness of the films were studied. The measured I-V characteristics that formed layers demonstrate memristor-like behavior suitable for memory cells. It was found that set and reset voltages are direct proportional to layer thickness. Electric field (E) and ionic conductivity (σ_{Ag+}) in Ag_2S films formed by SILAR were estimated. σ_{Ag+} depends on the films with thickness of 90 and 120 nm due to ionic scattering.

Keywords
I-V curves, resistive memory cells, Ag_2S thin films, SILAR deposition method, ionic conductivity.

1. INTRODUCTION
The memory resistor, or memristor based on the solid-state electrolyte (SSE) have roused interest in recent years [1-5]. The resistive switching memory cells efficiency, such as reliability, durability, speed of action, increasing of the specific useful characteristics, and reducing the energy costs, etc., depends on the solid-state electrolyte conductivity [6]. Set and reset phenomena are investigated in Ag_2S as a model system [7, 8]. Electric field and SSE geometric parameters have influence on the set/reset voltage. One of the perspective materials for memristor development is silver sulfide (Ag_2S). It is possible to form this material by different methods [9-13]. A paucity of references relating to the use of memristors based on the Ag_2S formed by SILAR exists [14]. SILAR has become the favored route because of its simpleness, low cost, scalability and reproducibility [15-17]. Thus, in this report we investigated the electrical properties of the Ag_2S thin films with thickness of 15-120 nm formed by SILAR method. The thickness was measured by atomic force microscopy (AFM). Conductance switching properties of Ti/Ag_2S/Au (micro-contact) were measured.

2. Experimental details
Commercially available, pure monocrystal silicon plates (30mm x 30mm x 625μm) were used as the substrate to deposit 15-120 nm-thick nanocrystalline Ag_2S thin films by SILAR. Si wafers were precleaned by a sulfuric acid–hydrogen peroxide mixture (97% H_2SO_4–30% H_2O_2, 1:1 v/v) during 10 min. Then they were rinsed in deionized water and dried by jet of isopropyl alcohol vapor. 500 nm-thick titanium films were deposited on silicon wafers by magnetron sputtering method for adhesion improvement between Si and silver sulphide surfaces. Moreover, the titanium films were used as the bottom contact layers for conductance switching properties measurement.

2.1 Formation of the Ag_2S thin films
Ag_2S thin films were deposed by SILAR method from aqueous solutions, contained Ag^+ and S^-. These solutions are 0,01M $AgNO_3$ and 0,01M Na_2S, respectively. Acidity of the Na_2S solution adjusted to the 7,7 by adding HCl and stirring constantly. This optimum acidity of the solution leads to form Ag_2S films with minimum concentration of impurities as shown for other sulfides in [16].
The process of Ag_2S deposition was an alternate immersing of Si/Ti substrates into:
- 0,01M $AgNO_3$ aqueous solution during 10 seconds;
- deionized water during 10 seconds;
- Na_2S aqueous solution during 10 seconds;
- deionized water during 10 seconds.

AFM and EDS analysis were performed.

2.2 I-V curves measurement
The measurement unit consists of the probe table with contacts, optic microscope Carlzeiss, programmable generator Rigol DG 2041A, and two-channel digital storage oscilloscope Rigol DS 1102E.
Soft golden clamping contacts were used for the interaction with samples. These types of the contacts provide reliable connection to the samples and avoid puncturing the investigated films. The optical microscope is needed to control the supplying probes process. Figure. 1 shows the measurement circuit.

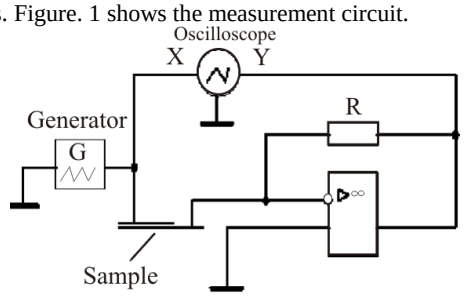

Figure. 1 Scematic diagram of the I-V curves measurement circuit

Electrical measurements of switching were performed perpendicularly across the Ag_2S layer, using a two-probe configuration. A Ti film was used as the bottom electrode and a micrometer-scale probe contact (Au wire, 650 μm^2 square) as the top electrode, applied with a small mechanical load. Measurements were performed by applying a sawtooth voltage (±10 V, 1kHz) to the parallel electrodes at room temperature and atmospheric pressure.

3. RESULTS and discussions:
Figure. 2 shows the surface image of the silver sulfide film deposed by 10 and 70 cycles.

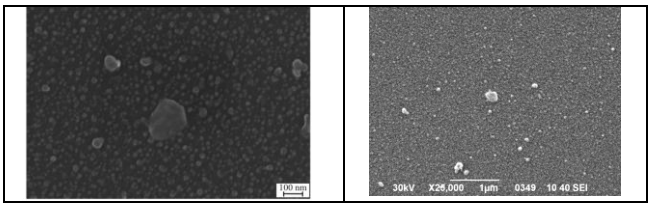

Figure. 2 SEM -images of the silver sulfide film deposed by 10 (a) and 70 (b) cycles

Figure 2 illustrates rough surface of the Ag_2S film. Dependence of film thickness on number of the immersion cycles were controlled by AFM. AFM data were processed by the software Image Analysis. Silver sulfide films` thicknesses were assessed. Thus, the correlation of the films thickness with number of cycles was determined, while also taking into account the surface roughness. The grains sizes (D) were determined and it had a positive correlation with the thickness of the Ag_2S films. The data is presented in Table 1. Film thickness error (Δd) was calculated by software Image Analysis.

№	*Deposition cycles number*	*Films thickness (d±Δd), nm*	*Grains diameter (D), nm*
1	10	15±3	12
2	20	30±3	28
3	30	50±3	40
4	50	90±4	54
5	70	120±5	70

Table.1: The influence of the deposition cycles number on the Ag_2S films thickness and grains diameter

As the film thickness increased, so did the size of the grains. We analyzed the composition of the sample by energy dispersive spectroscopy (EDS) and the results are presented in Figure.3. The EDS spectra confirmed that the sample is composed of Si, Ti, C, O, Ag and S atoms, and with an atomic percentage of 0,91% Ag and 0,38% S. Although the silver in excess on the surface, we assume that silver (I) sulfide composition is Ag_2S.

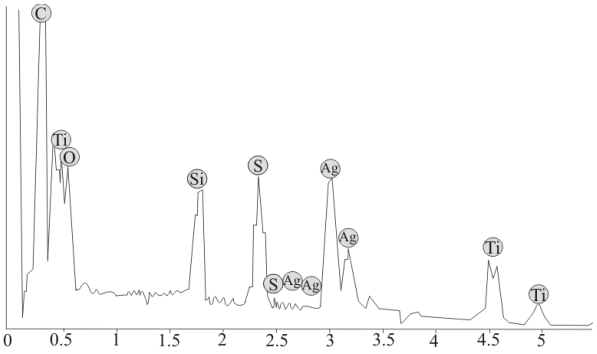

Figure.3 EDS spectrum acquired on the surface

I-V characteristics were measured for films thicknesses in the range of 15-120 nm. The measurements were made three times for every thickness for statistics and error calculation. Figure. 4 shows the I-V curves of the Ag_2S film with a thickness of 90 nm.

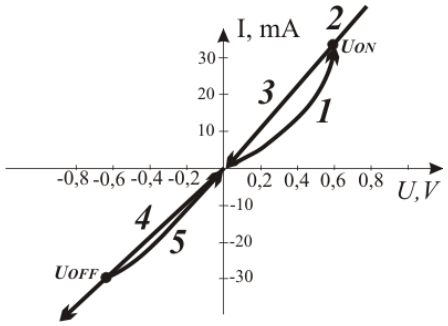

Figure.4 I-V curves of the Ag_2S film with a thickness of 90 nm

Current-voltage (I-V) curves were obtained by applying the voltage from -Vmax → Vmax, where Vmax is the maximum applied bias voltage. Curve section 2 represents the ON state. The set voltage (U_{ON}) equals to 0,6 V. The ON state persists even at moderate negative voltages until -0,64V (reset voltage (U_{OFF})).

Ag_2S thin films show semiconductor behavior at low bias voltages, whereas they exhibit reproducible bipolar resistance switching at higher bias voltages. The transition between both types of behavior is observed by hysteresis in the I-V curves (sections 1→2, 4→5), indicating decomposition of the Ag_2S and formation of a conductive path between the electrodes [7, 8]. Linear I-V characteristics are defined as silver filament formation (section 2). Filament formation is due to ionic transport. Ionic conductivity is the main parameter defined the electrodynamic properties of the films. In this report, we calculated Ag+-ionic conductivity σ_{Ag+} by Eq.1.

$$\sigma_{Ag+} = \frac{d}{R \cdot S}, \qquad (1)$$

where R-resistance is defined by the linear I-V curve 2, S - contact area between Au probe and film is 650 μm^2, d-film thickness.

The Ag^+- ionic conductivity of continuous thin films silver sulfide with thickness of 90 and 120 was calculated and equals to $70 \cdot 10^{-3}$ $Ohm^{-1} \cdot cm^{-1}$ and $74 \cdot 10^{-3}$ $Ohm^{-1} \cdot cm^{-1}$, respectively. Order of magnitude corresponds to the tabular data for solid-state electrolyte. It was incorrectly to calculate the σ_{Ag+} for the ranges 15-50 nm by Eq.1, using S=650 μm^2. It is associated with noncontinuous thin films (<90 nm) surface. Thus, for correct σ_{Ag+} calculations of such films it is necessary to recalculate S considering surface area of the Ag_2S.

Discrepancy of the thin films with thickness 90 and 120 nm ionic conductivity can be explained by the nonuniformity and grained structure of the film. The rough surface on the grain boundaries is carrying the ionic scattering. Therefore, effective grains surface has influence on the ions scattering. As shown by Figure 3, the more the films thickness, the less the carrier scattering. This phenomenon is due to the fact that grains increase in size, as the film thickness increases. It leads to a lower promotion of ion scattering on the effective surface.

One of the main characteristics of the films is electric field E_{ON} and E_{OFF}. It defines the transition between semiconductor and memristor behavior of the solid-state electrolyte. Electric field can be defined by the equation:

$$E = \frac{U}{d}, \qquad (2),$$

where U-set or reset voltage, d-films thicknesses.

Average voltages (U_{ON} ,U_{OFF}) defined by I-V curves (Figure 4) and electric field (E_{ON}, E_{OFF}) was calculated by Eq. (2) for 15-120 nm silver sulfide films are shown in Table 2. Films thickness error was calculated by the Software Image Analysis.

№	d,·10^{-7}cm	U_{ON}, V	U_{OFF}, V	E_{ON},·10^5 V/cm	$\lvert E_{OFF} \rvert$,·10^5 V/cm
1	15±3	0,2	0,28	1,3	1,86
2	30±3	0,4	0,45	1,2	1,5
3	50±3	0,45	0,6	0,9	1,2
4	90±4	0,6	0,64	0,6	0,7
5	120±5	1,4	1	1,16	0,83

Table. 2: The dependence of the U_{ON} , U_{OFF} and E_{ON} , E_{OFF} on the silver sulfide thickness

Although the programming of the Ag_2S memristor is reversible, its "turn-on" and "turn-off" characteristics are not symmetric. As shown in Table 2, E_{ON}, E_{OFF} is not constant for films in the thickness range 15-120 nm. Because of σ_{Ag+} has correlation with d, set and reset electric field has correlation also. Thus, U_{ON}, U_{OFF} is directly proportional to the films thickness, which can be seen in Eq.2 and Table 2.

Set and reset parameters depend on the film composition, surface morphology, thickness, contacts material and size. The contacts contribution was not considered in the current work.

4. CONCLUSIONS

SILAR method was used for silver sulphide rough thin films formation with different thickness. This material exhibits the memristor-like behavior at the high electric field ~10^5 V/cm. The transition between semiconductor and memristor-like behavior of the solid-state electrolyte takes place at the set and reset voltage. The ionic conductivity was calculated for the investigated films. It is consistent with the tubular data for solid state electrolytes (10^{-3} -10^{-2} $\Omega^{-1}cm^{-1}$). The dimensional effects are exhibited for σ_{Ag+} in the films thickness ranging from 90-120 nm. The film thickness has direct influence on the set (U_{ON}) and reset voltage (U_{OFF}). Set and reset parameters depend on the film composition, surface morphology, thickness, contacts material and size. Ag_2S formed by SILAR is a good candidate material for resistive switching memory cells.

5. REFERENCES

[1] Hasegawa, T., Terabe, K., Tsuruoka, T., and Aono, M. 2012. Atomic Switch: Atom/Ion Movement Controlled Devices for Beyond Von-Neumann Computers. *Adv. Mat.*, 24, 252–267.

[2] Yang, J. J., Pickett, M. D., Li, X., Ohlberg A. A., Stewart, D.R. and Williams, S.R. 2008 Memristive switching mechanism for metal/oxide/metal nanodevices. *Nature Nanotechnology*, 3, 429-433.

[3] Thakoor, S., Moopenn, A., Daud, T., and Thakoor, A.P. 1990. Solid-state thin-film memistor for electronic neural networks, *J. Appl. Phys*., 67, 3132-3135.

[4] Terabe, K., Hasegawa, T., Nakayama, T., Aono, M. 2005. Quantized conductance atomic switch, *Nature*, 433,47-50.

[5] Waser, R. and Aono, M. 2007. Nanoionics-based resistive switching memories, *Nature Materials*, 6, 833-840.

[6] Simmons, J. G. and Verderber, R. R. 1967. New conduction and reversible memory phenomena in thin insulating films, *Proc. R. Soc. Lond. A.*, 301, 1464, 77-102.

[7] Morales-Masis, M., Wiemhoferb, H.-D. and J. M. van Ruitenbeeka. 2010. Towards a quantitative description of solid electrolyte conductance switches, *Nanoscale*, 2, 2275–2280.

[8] Morales-Masis, M., S.J. van der Molen, and J. M. van Ruitenbeek, Hasegawa, T. 2011. Bulk and Surface Nucleation Processes in Ag2S Conductance Switches, *Phys. Rev. B.* = DOI: 10.1103/physrevb.84.115310.

[9] Shen, Sh., Guo, L., Chena, X., Rena, F., Maoa, S.S. 2010. Effect of Ag2S on solar-driven photocatalytic hydrogen evolution of nanostructured CdS, *International Journal of Hydrogen Energy*, 35, 13, 7110–7115.

[10] Lokhande, C. D., Bhad, V. V. and Dhumure, S. S. 1992. Conversion of tin disulphide into silver sulphide by a simple chemical method, *J. Phys. D: Appl. Phys*., 25, 315-318.

[11] Grozdanov, I. 1995. Solution growth and characterization of silver sulfide films, *Appl. Surface Science*, 84, 325-329.

[12] El-Nahass, M.M., Faraga, A.A.M., Ibrahim, E.M., Abd-El-Rahman, S. 2004. Structural, optical and electrical properties of thermally evaporated Ag2S thin films, *Vacuum*, 72, 453–460.

[13] Dlala, H., Amlouka, M., Belgacema, S., Girarda, P. and Barjona, D. 1998. Structural and optical properties of Ag2S thin films prepared by spray pyrolysis, *The European Physical Journal Applied Physics*, 2, 1, 13-16.

[14] Pathan, H.M., Salunkhe, P.V., Sankapal, B.R., Lokhande, C.D. 2001. Photoelectrochemical investigation of Ag2S thin films deposited by SILAR method, *Materials Chemistry and Physics*, 72, 105–108.

[15] Pathan, H. M. and Lokhande, C. D. 2004. Deposition of metal chalcogenide thin films by successive ionic layer adsorption and reaction (SILAR) method, *Bull. Mater. Sci.*, 27, 2, 85–111.

[16] Kravtchenko, D. A., Gavrilov, S.A., Zheleznyakova, A.V. 2006. Synthesis of $A^{II}B^{VI}$ semiconductor nanocrystals by electrochemical deposition and SILAR techniques, *Proceedings of SPIE - The International Society for Optical Engineering*, art. no. 62600E.

[17] Gavrilov, S.A., Zheleznyakova, A.V., Redichev, E.N., Popenko, N.I.2010. The influence of solution-precursors on optical properties of In_2S_3 films deposited by successive ionic layer adsorption and reaction, *Semiconductors* , 44, 13, 1649-1653.

Spin Orbit Torque (SOT) nanodevice for ultra energy efficient and non-volatile applications

K. Jabeur, G. Prenat, G. Di Pendina
Univ. Grenoble Alpes & INAC-SPINTEC, CNRS & INAC-SPINTEC, CEA & INAC-SPINTEC,
F-38000 Grenoble, France

Abstract:
Magnetic Random Access Memory (MRAM) is a promising candidate to be the universal non-volatile (NV) storage device. The Magnetic Tunnel Junction (MTJ) is the cornerstone of the NV-MRAM technology. The 3-terminal Spin Orbit Torque (SOT) MTJ has recently been considered as a hopeful device which can revolutionize the use of MRAMs. In this work, we highlight the benefits brought by the SOT device to increase the reliability of MTJ based ICs. Moreover, a macrospin compact model in Verilog-A has been developed to describe the behavior of the SOT-MTJ device and enable its integration into semiconductor commercial design flows to realize hybrid CMOS/magnetic ICs. Simulations results show the great potential of SOT-MTJs to improve the writing energy by 3× to 6× compared with Spin Transfer Torque (STT-MTJs) at 40 nm and 28 nm dimensions, respectively.

Keywords: Spintronics, MRAMs, Magnetic tunnel junction, spin transfer torque, spin orbit torque, modeling, simulation, Verilog-A, ASICs

Introduction:
The discovery of the giant magnetoresistance (GMR) (awarded Nobel Prize Physics 2007) was the founding step of Spintronics. Afterward, the giant step advancing Spintronics came from creating the magnetic tunnel junction (MTJ) (Moodera *et al.*; 1995). The discovery of MTJs induced a rapid development era on spin-based integrated circuits (ICs), such as magnetic random access memory (MRAM). MTJ-based MRAMs are the promising technology candidate to govern the future storage market. It provides a combination of fast access time, non-volatility (NV), data retention, zero-standby power, endurance and high density. The first two generations of MRAMs were based on Field Induced Magnetic Switching (FIMS) and Thermally Assisted Switching (TAS), consecutively (Kang et al.; 2014). Now, a great interest is given to MTJs based on Spin Transfer Torque (STT) (Kang et al.; 2014). The scalability is improved and the required storage current is decreased over previous MTJ generations (FIMS and TAS). However, the common write and read path through STT-MTJs decreases their reliability. Recently, SPINTEC researchers have proved that such an issue seems to be avoided by the demonstration of Spin-Orbit-Torques in ferromagnetic thin films (Miron et al,; 2011).
Section 1 describes the structure of the SOT device and its behavioral model through a Verilog-A based compact model. Secion 2 illustrates an example of a hybrid CMOS/magnetic application.

SOT nanodevice description:
Figure 1 shows the SOT-MTJ with a 3-terminal architecture alleviating the stress on the barrier by separating the read path from the write path. Figure 2 shows the behavior of the model that we developed which corresponds to the theoretical switching of the magnetization (m_z); m_z switchs from parallel 'P' to antiparallel 'AP' and vice versa depending on the current direction applied during the time.

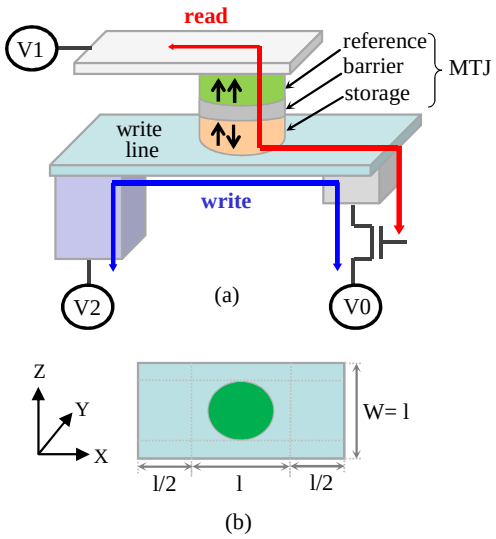

Figure 1: 3-terminal SOT device (a) two independent paths for write and read operations. The reference layer magnetization is pinned. The storage layer magnetization is programmable (up or down); In-plane current injection through the write line induces the perpendicular switching of the storage layer. When the reference and the storage layers have a parallel magnetization state, the resistance of the MTJ is R_{min} (logic '0'). When the reference and the storage layers have anti-parallel magnetization state, the resistance of the MTJ is R_{max} (logic '1') (b) top view of the SOT-MTJ with experimental dimension assumptions.

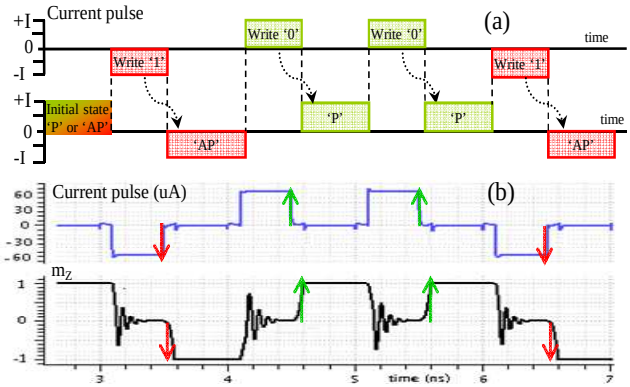

Figure 2: SOT-MTJ model validation (a) Theoretical behavior (b) model behavior

SOT nanodevice based standard cell:

We propose the use of SOT-MTJs to add the non-volatility (NV) feature to flip-flops (FFs). The basic architecture of the NVFF corresponds to the usual CMOS flip flop circuit. An extension is added to integrate the SOT-MTJs as shown in figure 3. In (Jabeur et al.; 2014), the architecture of the NVFF, as well as its operating modes, have been detailed. This hybrid FF offers the possibility to use the standard CMOS functionality of a flip-flop to fully exploit the performance of silicon with an extra possibility to omit the input data (D) and load the magnetic data stored from a previous state or written by the user thanks to additional signals (S/W, R). Derived architectures of the proposed flip-flop are in their way to be patented.

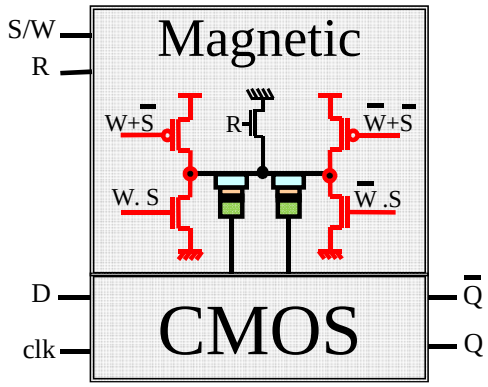

Figure 3: An example of a hybrid CMOS/magnetic circuit: non-volatile flip-flop based on SOT devices

The writing mechanism of the SOT-MTJ is different from its STT counterpart since an in-plane current is applied through the stripe line conductor avoiding the passage through the junction. Thus, the electrical stress on the barrier is relaxed and endurance is improved. Benefits in terms of energy per bit-cell can be also observed; since, the writing stripe is highly conductive (Pt, W, Ta), the writing path has a very low resistance (R_w). If we consider Ic the critical writing current and τ =1ns the width of the writing pulse, the energy per bit-cell can be calculated as ($E= R_w \times Ic^2 \times \tau$). In our study, we consider the case of Platinum (Pt) with low resistivity value (20 μΩ.cm). An improvement of 3× and 6× is observed in favor of the SOT device when compared with the energy required for the STT device at 40 nm and 28 nm dimensions, respectively. This ratio could be diminished if we use other heavy materials such as the Tantalum (Ta) or the Tungsten (W) which have a resistivity nearly 10× higher than Platinum (Jabeur et al.; 2014).

Conclusion:

Simulation results of hybrid CMOS/magnetic circuits based on SOT nanodevices are very encouraging for future complex systems targeting Array Specific Integrated Circuits (ASICs) and memories. Portable applications such as mobile phones and digital cameras are among the possible device candidates in the market which can profit from the power efficieny, and the instant on/off of the SOT nanodevice. Furthermore, the intrinsic hardness to radiation of MTJ based MRAMs is a very interesting asset for aerospace and military applications

References:

Moodera,J,S., Kinder,L,R., Wong, T,M., Meservey,R. (1995) magnetoresistance at room temperature in ferromagnetic thin film tunnel junctions,´ *Phys. Rev. Lett, Vol. 74, PP. 3273-3276.*

Kang,W., Zhao,W., Klein,J-O., Wang,Z., Y,Zhang., Zhang,Y.,Ravelosona, D.,Chappert,C. (2014), An Overview of Spin-based Integrated Circuits, *Procs. Of IEEE ASP-DAC.*

Miron, I.M., Garello,K., Gaudin,G., Zermatten, P-J., Costache, M-V., Auffret, S., Bandiera, S. Rodmacq, B., Schhuhl, A., Gambardella, P., (2011) , Perpendicular switching of a single ferromagnetic layer induced by in-plane current injection", *Nature 476.*

Jabeur, K., Di Pendina, G., Prenat, G., (2014), Ultra-energy-efficient CMOS/magnetic non-volatile flip-flop based on spin-orbit torque device, Electronics letters, vol 50, issue 8, pp 585-587.

Jabeur, K., Di Pendina, Bernard-Granger, F,G., Prenat, G., (2014), Spin Orbit Torque Non-Volatile Flip-Flop for High Speed and Low Energy Applications, Electron Device Letters, IEEE (Volume:35 , Issue: 3), pp 408 – 410.

Enhanced Performance of Optoelectronic Memory Devices Based on Carbon Nanotube Transistors

N. Ismail[1,2], A. Kalboussi[2], S. Lenfant[3] and D. Vuillaume[3]
[1]INSAT, University of Carthage, Tunis, Tunisia
[2]Laboratory of Microelectronic and Instrumentation, Faculty of Sciences of Monastir, University of Monastir, Tunisia
[3]IEMN-CNRS, BP60069, Avenue Poincaré, 59652 Villeneuve d'Ascq, France

ABSTRACT
We have studied an optically-gated CNTFET with carbon nanotubes deposited on an oxidized Undecenyltichlorosilane molecules. We have observed that this device presents a large hysteresis in the drain source current versus the gate source voltage characteristic which can enhances the performance of optoelectronic memory devices based on carbon nanotube transistors.

Keywords
Field-effect transistors (FETs), carbon nanotubes, polymer, CNTFET, optoelectronics, traps.

1. INTRODUCTION
Organic electronics and optoelectronics have progressed rapidly, driven by the tremendous potential of these devices for future low-cost, large-area, flexible, and transparent technologies.[1]

In parallel, there has been tremendous progress in the performance of carbon nanotube field-effect transistors (CNTFETs). The CNTFETs can be used to emit or detect[2, 3] infrared photons. In these experiments, the optical properties of the device are defined by the band structure of the carbon nanotube, i.e., by its atomic structure. To extend the capabilities of CNTFETs to optoelectronics, light sensitivity at a tunable wavelength must be achieved, for example, by functionalizing the nanotubes with chromophores[4] or photosensitive polymers.

2. THE OPTICALLY GATED CNTFET
Figure 1 presents the optically-gated CNTFET structure. A 10nm of oxide has thermally grown on a Si substrate. A thick oxide layer is deposited to isolate the source and drain contacts from the substrate. A molecular layer (SAM), representing the Octadécyltrichlorosilane (OTS) or the oxidized Undecenyltichlorosilane (UETS) molecules, is grafted on the thermal oxide. The carbon nanotubes (nT) are then deposited on the molecular layer. Finally, the device is coated by a polymer film P3HT.

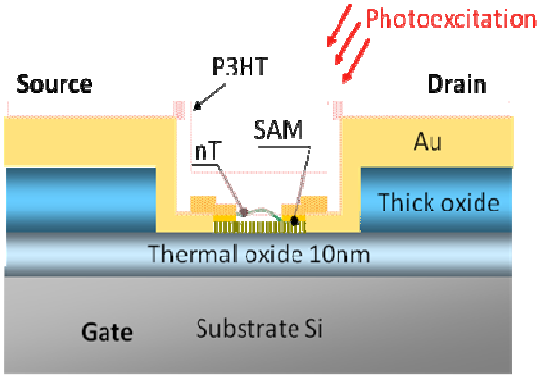

Figure 1: The OG-CNTFET structure.

Star et al. have demonstrated that carbon nanotube networks coated with polymers can act as memory devices [5]. This approach has resulted in the development of a device named optically-gated CNTFET (OG-CNTFET) [6]. Indeed, when the transistor is photoexcited, the photogenerated electrons in the polymer film are trapped at the polymer/SiO2 interface, in the vicinity of the nanotube. These trapped electrons act as an "optical gate" for the nanotube transistor and apply the equivalent of a very negative potential which induces the switch of the device from off state to on state regime. When the photoexcitation is turned off, the photogenerated electrons remain trapped and the device remains at the on state regime. Figure 2 presents an AFM image of the fabricated OG-CNTFET.

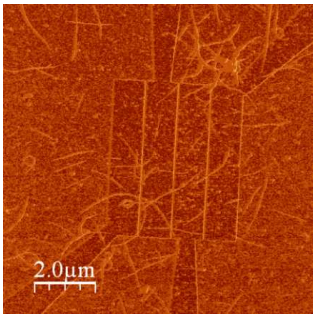

Figure 2: AFM image of the OG-CNTFET

3. RESULTS and discussions:

Our purpose is to enhance the performance of the OG-CNTFET by a chemical modification of the dielectric/polymer interface. We have fabricated three kinds of OG-CNTFET devices. A first device with carbon nanotubes deposited on Octadécyltrichlorosilane (OTS) molecular layer. A second device with carbon nanotubes deposited on the thermal oxide layer. A third device with carbon nanotubes deposited on an oxidized Undecenyltichlorosilane (UETS) molecular layer.

We have observed that the first device doesn't present an hysteresis in the drain-source current versus the gate-source voltage Ids-Vgs characteristic. This is attributed to the fact that the OTS molecules end with a CH3 chemical bond that doesn't allow electrons to be trapped around the carbon nanotubes. Furthermore, we have observed that the third device presents an hysteresis in the Ids-Vgs characteristic larger than the hysteresis corresponding to the second device. This phenomenon can be explained by the fact that the oxidized UETS molecules end with a COOH chemical bond increasing the trapping rate of electrons around the carbon nanotubes (Figure 3).

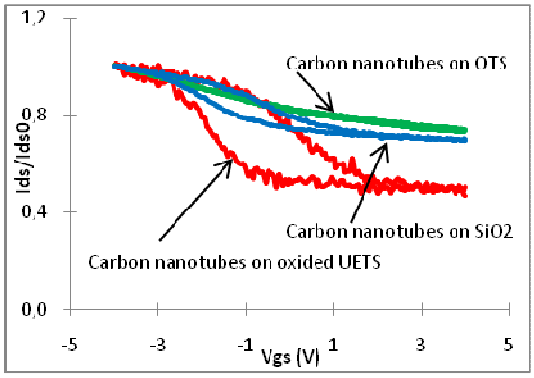

Figure 3: The Ids/Ids0 versus Vgs chartacteristics measured for the three kinds of devices. Ids_0 is the initial value of Ids.

Table 1 presents the maximum hysteresis width in the drain source current versus the gate source voltage characteristic measured for the three kind of devices. We have observed that the device with carbon nanotubes deposited on an oxidized Undecenyltichlorosilane (UETS) molecular layer presents the more important maximum hysteresis width compared with the other devices.

	Maximium hysteresis width (V)
Carbon nanotubes on OTS molecules	0
Carbon nanotubes on SiO2	1,1
Carbon nanotubes on oxided UETS molecules	2

Table 1 : The maximum hysteresis width in the drain source current versus the gate source voltage characteristic measured for the three kind of devices.

In order to confirm this result, we have measured the drain source current versus the gate source voltage characteristics for many samples corresponding to the three kinds of OG-CNTFET. We have observed that for all samples with carbon nanotubes deposited on Octadécyltrichlorosilane (OTS) molecular layer, the hysteresis width is close to zero voltage. For samples with carbon nanotubes deposited on the thermal oxide layer, the maximum hysteresis width average is close to 1V. Whereas for samples with carbon nanotubes deposited on an oxidized Undecenyltichlorosilane (UETS) molecular layer, the maximum hysteresis width average is close to 2V (Figure 4).

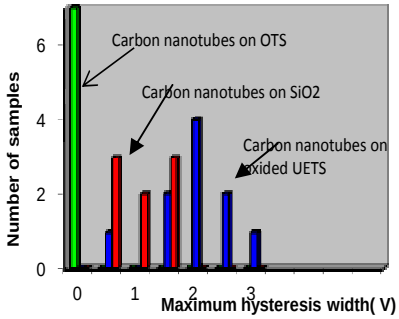

Figure 4 : Histogram of the sample number of the different kind of devices in function of the maximum hysteresis width.

We concluded that we can enhance the performance of the OG-CNTFET device operating as a memory by depositing the carbon nanotubes on an oxidized Undecenyltichlorosilane molecular layer.

4. ACKNOWLEDGMENTS

Our thanks to the IEMN Laboratory in France for allowing us to fabricate the CNTFET device.

5. REFERENCES

[1] Forrest S. R. 2004. The path to ubiquitous and low-cost organic electronic appliances on plastic. Nature, 428, 911.

[2] Freitag M., Martin Y. 2003. Photoconductivity of Single Carbon Nanotubes, *Nano Lett.*, *3*, 1067.

[3] Qiu X., Freitag M., Perebeinos V. 2005. Photoconductivity Spectra of Single-Carbon Nanotubes: Implications on the Nature of Their Excited States, *Nano Lett.*, *5*, 749.

[4] Guo X. F., Huang L. M., O'Brien S., Kim P., Nuckolls C. 2005. Directing and Sensing Changes in Molecular Conformation on Individual Carbon Nanotube Field Effect Transistors, *J. Am. Chem. Soc.*, *127*, 15045.

[5] Star, A., Lu, Y., Bradley, K., Grüner, G. 2004. Nanotube Optoelectronic Memory Device, *Nano. Lett.* , 4, 1587-1591.

[6] Borghetti, J., Derycke, V., Lenfant, S., Vuillaume. 2006. Optoelectronic Switch and Memory Devices Based on Polymer-Functionalized Carbon Nanotube Transistors, *Adv. Mater.*, 18, 2535-2540.

Few Layer Graphene on Copper Substrate Developed By Atmospheric Chemical Vapor Deposition

Hatem Abuhimd[1], Mushtaq A. Dar[2]

[1]National Nanotechnology Center, King Abdulaziz City for Science and Technology
P.O Box 6086, Riyadh 11442, Saudi Arabia
habuhimd@kacst.edu.sa
[2] Center of Excellence for Research in Engineering Materials, Advanced Manufacturing Institute, King Saud University, P.O Box 800, Riyadh 11421, Saudi Arabia
mdar@ksu.edu.sa

ABSTRACT

The graphene growth by chemical vapor deposition route on metal substrates has attaracted the attention of the research community due to its capability to prepare large scale samples composed of single layer graphene (1-3). Graphene is a recently discovered 2-D material with its interesting and unique properties such as high surface area, electrical conductivity, high flexibility, and better mechanical strength (4). It is alo providing single-atom-thick substrate for functional nanomaterials' growth (5). The synthesiszed graphene can be coated on other appropriate substrates for specific application. In this research work, standard copper foil was used as a catalyst for the graphene growth (6).

In the graphene growth experimental procedure, we used 9 µm thick Cu foil (99.99%, MTI-USA) as the substrate. The Cu foil samples where cleaned ultrasonically in acetone, ethanol and double distilled water. The cleaned samples were loaded into the CVD system. To avoid oxidation of the loaded Cu samples at 950 C for 40 min, ambient gas atmosphere were maintained which involves hydrogen (H_2) (99.99%) and argon (Ar) (99.99%).

Methane (CH4) (99.99%) precursor gas was flown for 10 min. The CVD system was cooled down to room temperature naturally. Various types of chatracteriziation techniques were utilized to understand the nature of the resulted product which includes X ray diffraction (XRD), Raman microscopy, transmission electron microscopy (TEM), Scanning electron microscopy (SEM) and atomic force microscopy (AFM). The SEM results show that the grain size of the resulting graphene obtained was found to 70 microns (Fig. 1).

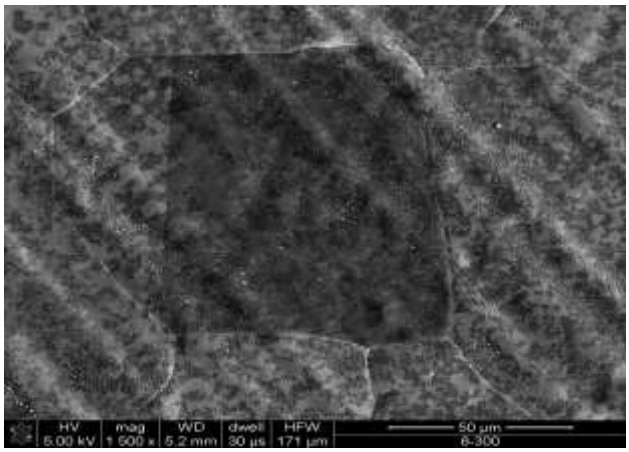

Fig. 1. A representative SEM image of the CVD grown graphene on copper.

Almost defect free graphene layers were observed by Raman spectroscopy. AFM measurements were employed to understand the surface of the grown graphene (Fig. 2). The Average root mean square (RMS) roughness of Graphene on Cu foil surface as estimated from AFM is ~21.72 nm.

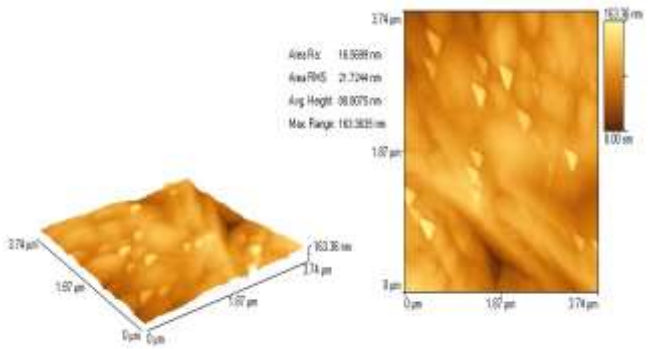

Fig.2 AFM image of the multilayer graphene sheets

Acknowledgement

The authors would like to acknowledge King Abdulaziz City for Science and Technology for funding this work.

References:

1. Y. Yao, Z. Li, Z. Lin, K.-S. Moon, J. Agar, C. Wong, J. Phys. Chem. C 115 (2011) 5232–5238.
2. X. Li, C.W. Magnuson, A. Venugopal, R.M. Tromp et. al., J. Am. Chem. Soc. 133 (2011) 2816–2819.
3. J.W. Suk, A. Kitt, C.W. Magnuson, Y. Hao et. al., ACS Nano 5 (2011) 6916–6924.
4. Z.G. Wang, Y.F. Chen*, P.J. Li*, X. Hao et. al., Vacuum 86 (2012) 895-898
5. J.R. Miller, R.A. Outlaw, B.C. Holloway, Science 329 (2010) 1637.
6. Z. G. Wang, Y. F. Chen, P.J. Li et. al., Vacuum 86 (2012) 895-898

PAN/CNT/AgNP composite nanowebs: Effect of CNT functionalization and Ag^+ reduction on properties of composite nanofiber webs

N. Kizildag[1*], N. Ucar, [1] I. Karacan, [2] A.Onen[1]

[1]Istanbul Technical University, Istanbul, Turkey

[2]Erciyes University, Kayseri, Turkey

ABSTRACT

In this study, composite nanofibers from a solution of polyacrylonitrile (PAN), carbon nanotubes (CNTs) and silver nanoparticles (AgNPs) in dimethylsulfoxide were successfully produced by electrospinning method (Figure 1). The use of amino-functionalized CNTs was investigated and compared to that of pristine CNTs. Chemical reduction using an aqueous solution of hydrazinium hydroxide was conducted for the in situ synthesis of silver nanoparticles and the effect of the reduction on the morphology, conductivity and mechanical properties of the nanowebs was also investigated. Scanning electron microscopy, conductivity meter and tensile tester were used for the characterization of the nanofibers.

Keywords

Carbon nanotube, electrospinning, functionalization, nanofiber, nanocomposite, silver nanoparticles, silver reduction.

1. INTRODUCTION

Silver (Ag), and carbon nanotubes (CNTs) have been increasingly incorporated into polymers with the aim of producing functional materials. Nanocomposites with silver nanoparticles are reported to acquire catalytic, optical, and especially antibacterial properties. Through different methods of preparing a polymeric matrix containing silver nanoparticles, in situ reduction of metal ions have attracted much attention. Chemical reduction using aqueous solution of sodium borohydride, hydrazinium hydroxide, photo reduction, and heat treatment are some of the methods used for in situ reduction of silver nanoparticles [1,2]. On the other hand, the combination of superior mechanical, thermal, and electronic properties makes CNTs an ideal candidate as an advanced filler material in nanocomposites. A significant challenge for getting maximum benefit of CNTs in polymer composites is to achieve a good dispersion. The functionalization of CNTs is an effective way for better dispersion and bonding of the CNTs within a polymer matrix. There are several approaches for functionalization of CNTs such as defect functionalization, covalent functionalization, and noncovalent functionalization [3,4]. In this study, composite nanofibers from a solution of polyacrylonitrile (PAN), carbon nanotubes (CNTs) and silver nanoparticles (AgNPs) in dimethylsulfoxide were successfully produced and the effects of the use of amino-functionalized CNTs, pure CNTs and chemical reduction method with aqueous solution of hydrazinium hydroxide on the morphology, conductivity and mechanical properties of the nanowebs were investigated. Scanning electron microscopy, conductivity meter and tensile tester were used for the characterization of the nanofibers.

2. EXPERIMENTAL

2.1 Materials

Polyacrylonitrile (PAN) (Sigma Aldrich, 181315, average Mw:150.000g/mol), AgNO3 (Alfa Aesar Premion, 10858), dimethylsulfoxide (DMSO) were used as received. Multi-walled carbon nanotubes (MWCNTs) (diameter: 60-100 nm, length: 5-15 μm) were used both as received and after functionalization. For functionalization, they were carboxy-functionalized and then amino-functionalized.

2.2 Methods

2.2.1 CNT functionalization

The CNTs were firstly carboxyl functionalized and then amino functionalized. Gao et al.'s method was used to carboxyl-functionalize carbon nanotubes [5]. For amino functionalization of CNTs, Zhao et al.'s method was used [6].

2.2.2 Solution Preparation

The required amount of CNT-NH_2 and $AgNO_3$ were added to the required amount of DMSO and homogenized with ultrasonic tip for 10 minutes and with ultrasonic bath for 45 min. Then PAN was added to this dispersion and dissolved by stirring with a magnetic stirrer at 40˚C, 300 rpm for 3 hours. The concentration of PAN was kept constant as 7 w% (with respect to the weight of the solution).

2.2.3 Electrospinning

Electrospinning of nanofibers was performed on a horizontal electrospinning setup. It contained a syringe pump, a high voltage power supply (0–50 kV), and a grounded rotating collector. Electrospinning solutions were fed through a capillary tip with a diameter of 1.25 mm, using a syringe of 10 ml. During electrospinning, the applied voltage was 15 kV, the distance between the tip and the collector was 10 cm and the flow rate of the spinning solution was 1 ml/h.

2.2.4 Silver reduction

Half of the as-spun nanowebs was immersed into the aqueous solution of hydrazinium hydroxide (1:20 hydrazinium hydroxide: distilled water) for 30 min at room temperature, then washed with 100 mL distilled water two times and dried in room temperature to obtain composite nanofibers containing Ag nanoparticles.

2.2.5 Characterization

Scanning electron microscopy (SEM; EVO MA 10) was used to obtain SEM images of the samples. The samples were sputter coated with gold layer before SEM analysis. The diameters of at least 50 randomly selected nanofibers were measured on SEM photomicrographs and analyzed using Image Analysis Software to obtain the average fiber diameter. Tensile strength, breaking elongation and modulus of the webs were measured using a tensile tester with a 100N load cell at a crosshead speed of 20 mm/min. The length and width of the specimens were 35 mm and 5 mm, respectively. The gage length was 15 mm, and at least 10 specimens were tested for each sample. The thicknesses of the specimens were measured with a Mitutoyo digital micrometer. Resistance measurements were performed using a two-circular-prob system connected to Microtest 6370 LCR meter. From the volume resistance value measured and the geometric dimensions of the samples, conductivity in S/cm was calculated. The thicknesses of the samples were measured with the integrated thickness meter during the conductivity measurements.

3. RESULTS and DISCUSSIONS

3.1 Morphology

SEM images of some selected samples can be seen in Figure.1. The nanofibers were uniform and beadless.

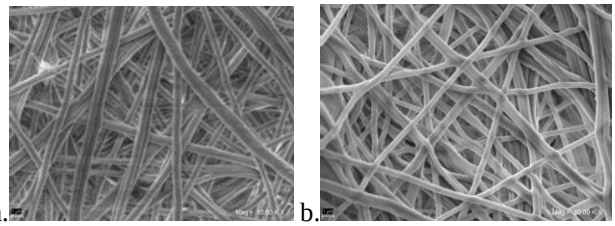

Figure.1 SEM image of the composite nanowebs containing a.1% CNT-NH_2 and 1% $AgNO_3$; b. 1% CNT-pristine and 1% $AgNO_3$.

The diameters of the nanofibers are presented in Table 1.

Samples	Diameter (nm)
100% PAN	515.34
PAN-0.5%CNT-NH_2-0.5%$AgNO_3$	540.87
PAN-0.5%CNT-NH_2-0.5%$AgNO_3$ - after reduction	531.60
PAN-1%CNT-NH_2-1%$AgNO_3$	674.00
PAN-1%CNT-NH_2-1%$AgNO_3$ - after reduction	559.35
PAN-0.5%CNT-pristine-0.5%AgNO3	520.81
PAN-0.5%CNT-pristine-0.5$AgNO_3$ - after reduction	546.91
PAN-1%CNT-pristine-1%$AgNO_3$	529.11
PAN-1%CNT-pristine-1%$AgNO_3$ - after reduction	529.99

Table.1: Diameters of the electrospun nanofibers

Additives generally cause an increase in diameter due to the increased substance concentration. Besides affecting concentration, charge carriers such as conductive filler particles have an influence on the conductivity of the solution; thus having an opposite effect. The diameter of the nanofibers depends on the phenomena which is dominant. In our study, for the nanowebs electrospun with CNT-NH_2, nanofiber diameter increased as the additive content increased while the diameter of the nanofibers were very slightly affected for the nanofibers produced with pristine CNTs. Chemical reduction process had a thinning effect on the nanofibers produced with CNT-NH_2 while it had no effects for the others.

3.2 Mechanical Properties

Mechanical properties of the nanofibers are presented in Table.2.

Samples	Breaking strength N/mm^2	Breaking elongation %	E-modulus N/mm^2
100% PAN	10.58	8.47	69.78
PAN-0.5%CNT.NH_2-0.5%AgNO3	7.36	26.89	33.86
PAN-0.5%CNT.NH_2-0.5%AgNO3 - after reduction	8.78	11.59	42.75
PAN-1%CNT.NH_2-1%AgNO3	5.74	35.25	35.80
PAN-1%CNT.NH_2-1%AgNO3 - after reduction	6.80	11.81	31.15
PAN-0.5%CNT-pristine-0.5%$AgNO_3$	7.19	26.63	45.64
PAN-0.5%CNT-pristine-0.5$AgNO_3$ - after reduction	9.48	20.73	42.15
PAN-1%CNT-pristine-1%$AgNO_3$	4.64	48.16	32.03
PAN-1%CNT-pristine-1%$AgNO_3$ - after reduction	7.09	10.77	35.88

Table.2: Mechanical properties of the electrospun nanofibers

Both MWCNT addition and $AgNO_3$ addition are reported to improve the mechanical properties of the nanofibers [10-12]. In our study, MWCNT-NH_2 and $AgNO_3$ are used in combination and this resulted in a decrease in tensile stress of the nanofiber webs. This was most probably due to the void formation and agglomeration of the nanoparticles which acted as stress points during tensile testing. The decrease in tensile stress was higher with the pristine CNTs. The silver reduction process resulted in an increase in tensile stress. When dimensional deformation was measured, 3% shrinkage was observed in nanoweb dimensions during the reduction process. The structure became more compact and less porous, thus became stronger. With the effect of the additives, the breaking elongation increased which is considered to be result of the void formation around the agglomerates. The increase in elongation was higher for the samples produced with pristine CNTs. After reduction process, breaking elongation decreased because of the decrease in molecular mobility due to the metallic silver nanoparticles. E-modulus values decreased as the tensile stress decreased and elongation increased; thus the nanowebs became less rigid.

3.3 Conductivity

The conductivity values are summarized in Table.3.

Samples	Conductivity S/cm
100% PAN	*
PAN-1%CNT.NH_2	2.79E-08
PAN-0.5%CNT.NH_2-0.5%$AgNO_3$	1.60E-07
PAN-0.5%CNT.NH_2-0.5%$AgNO_3$ - after reduction	1.30E-07
PAN-1%CNT.NH_2-1%$AgNO_3$	2.17E-07
PAN-1%CNT.NH_2-1%$AgNO_3$ - after reduction	4.02E-07
PAN-0.5%CNT.pristine-0.5%AgNO3	1.89E-07
PAN-0.5%CNT.pristine-0.5$AgNO_3$ - after reduction	1.37E-07
PAN-1%CNT.pristine-1%$AgNO_3$	3.64E-09
PAN-1%CNT.pristine-1%$AgNO_3$ - after reduction	8.60E-08

Table.3: Conductivity of the electrospun nanofibers

The presence of CNT-NH_2 and $AgNO_3$ provides conductive properties into PAN nanofiber which is normally an insulator with a conductivity value of 10^{-12}S/cm [12]. The conductivity of the nanofibers increased with respect to neat PAN nanofibers with the addition of conductive additives, but was not much affected with the increase in additive content, especially for the samples which are produced using amino-functionalized CNTs. The use of amino functionalized CNTs resulted in higher conductivity value which was attributed to the better dispersion of functionalized CNTs. For the samples produced with pristine CNTs, conductivity decreased as the additive content increased which might have been due to the possible agglomeration of the additives. Silver reduction had no pronounced contribution to the improvement of conductivity except for the sample with 1%pristine CNT and 1%$AgNO_3$. As the structure became more compact during the reduction process, the conductive particles might have become closer which resulted in an increase in conductivity. Results obtained in this study indicated that the combined use of CNTs and $AgNO_3$ improved the formation of conductive network as AgNPs might have acted as bridges between the carbon nanotubes and facilitate the electron transfer.

4. ACKNOWLEDGEMENTS

We would like to thank to TUBITAK for supporting this study with Project (112M877).

5. REFERENCES

[1] Mahapatra, A., Garg, N., Nayak, B.P., Mishra, B.G., Hota, G. 2012. Studies on the Synthesis of Electrospun PAN-Ag Composite Nanofibers for Antibacterial Application. *J. Appl. Polym. Sci.* 124, 1178–1185.

[2] Sichani G.N., Morshed, M., Amirnasr, M., Abedi, D. 2010. In Situ Preparation, Electrospinning, and Characterization of Polyacrylonitrile Nanofibers Containing Silver Nanoparticles. *J. Appl. Polym. Sci.* 116, 1021–1029.

[3] Coleman, J.N., Khan, U., Gun'ko, Y.K. 2006. Mechanical Reinforcement of Polymers Using Carbon Nanotubes. *Adv. Mater.* 18, 689–706.

[4] Sahoo, N.G., Chenga, H.K.F., Caia, J., Li, L., Chan, S.H., Zhaob, J., Yub, S. 2009. Improvement of mechanical and thermal properties of carbon nanotube composites through nanotube functionalization and processing methods. *Mater. Chem. Phys.* 117, 313-320.

[5] Gao, C.; Vo, D. C.; Jin, Z. Y.; Li, W.; Armes, S. P. 2005. Multihydroxy Polymer-Functionalized Carbon Nanotubes: Synthesis, Derivatization, and Metal Loading. *Macromolecules*. Vol. 38, No.21, pp. 8634-8648.

[6] Zhao, Z.; Yang, Z.; Hu, Y.; Li, J.; Fan, X. 2013. Multiple functionalization of multi-walled carbon nanotubes with carboxyl and amino groups. *Applied Surface Science*. Vol.276, pp.476-481.

[7] P. Heikkilä, A. Harlin. 2009. Electrospinning of polyacrylonitrile (PAN) solution: Effect of conductive additive and filler on the process. *eXPRESS Polymer Letters.* Vol.3, No.7, 2009, 437–445.

[8] X.H. Qin, E.L. Yang, N. Li, S.Y. Wang. 2007. Effect of different salts on electrospinning of polyacrylonitrile (PAN) polymer solution. *Journal of Applied Polymer Science*. Vol.103, 2007, 3865–3870.

[9] T. Lin, H. Wang, H. Wang, X. Wang. 2004. The effect of surfactants on the formation of fibre beads during the electrospinning of polystyrene nanofibres. *Polymer Fibres 2004*, Meetings management' Manchester, UK, 4

[10] J.S. Jeong, J.S. Moon, S.Y. Jeon, J.H. Park, P.S. Alegaonkar, and J.B. Yoo. 2007. Mechanical properties of electrospun PVA/MWNTs composite nanofibers. *Thin Solid Films*. Vol.515(12), 5136-5141.

[11] Ge, J.J., Hou, H., Li, Q., Graham, M.J., Greiner, A., Reneker, D.H., Harris, F.W., Cheng S.Z.D. 2004. Assembly of Well-Aligned Multiwalled Carbon Nanotubes in Confined Polyacrylonitrile Environments: Electrospun Composite Nanofiber Sheets. *Journal of American Chemical Society*, Vol.126, 2004, 15754-15761.

[12] S. Almuhamed, N. Khenoussi, L. Schacher, D. Adolphe, H. Balard. 2012. Measuring of Electrical Properties of MWNT-Reinforced PAN Nanocomposites, *Journal of Nanomaterials.* 1-7.

Synthesis and Thermal Characterization of Metal Filled Alumina Composites with Different Concentration of Nanowires

Yu. Shilyaeva, V. Bardushkin, M. Silibin, V. Yakovlev, A. Shulyat'ev, and S. Gavrilov
National Research University of Electronic Technology
Bld. 5, Pas. 4806, Zelenograd, Moscow, Russia
shyliaeva@gmail.com

ABSTRACT

It is necessary to take into account the real structure of nanocomposite materials while simulating thermodynamic and thermoelastic properties. The concentration of metal inclusions in the bulk of the matrix is one of the main structural characteristics along with the radius of the inclusion for the heterogeneous systems "porous alumina - metal". Considering not only the radius of nanowires, but also their concentration allows us to quantify the influence of the matrix material on the properties of metal nanowires and the composite as a whole. In order to consider the concentration of nanowires there has been introduced the corresponding parameter of the structure that can be easily controlled during the synthesis of the material, and can be directly measured with sufficient accuracy.

In this work, indium, tin, and zinc nanowire arrays have been synthesized by electrochemical deposition using anodic aluminum oxide templates with different porosity. Thus, the alumina-metal composites with different concentration of nanowires have been fabricated and characterized using the method of X-ray diffraction analysis and scanning electron microscopy. Melting of metal nanowires within the pores of refractory matrix has been investigated by means of differential scanning calorimetry, and there has been obtained the dependence of the melting temperature on the nanocomposite structural parameter.

Keywords

Nanowires, anodic aluminum oxide, electrochemical deposition, differential scanning calorimetry, melting temperature, structural parameter.

1. INTRODUCTION

The investigation of new functional materials with valuable properties is one of the main challenges of modern materials science. In recent years, metal one-dimensional nanostructures (nanowires) have attracted a great number of scientists and researchers because of their unique electrical, thermoelectrical, optical, magnetic and chemical properties, which are different from those of the corresponding bulk materials [1]. The investigation of properties of nanowires is of fundamental importance, and it is necessary from the point of view of their application. Low-melting point metal nanowires are often chosen as convenient objects for studying the thermodynamic and mechanical properties. Besides, arrays of low-melting point nanowires have attracted considerable interest in the view of obtaining semiconductor one-dimensional nanostructures on their basis by means of treatment method at temperatures close to the melting point [2]. The obtained arrays of semiconductor nanowires can find various applications in nanoelectronics and photonics as a part of devices and instruments [3].

Metal nanowire arrays with high aspect ratio, reproducible size, shape, and high degree of spatial order can be fabricated by electrochemical deposition by means of nanoporous matrices of anodic aluminum oxide (AAO). Template synthesis method is simple, cost-effective and low temperature, and therefore, it is widely used [4]. However, the enclosure of particles inside the pores of matrix-refractory is accompanied by additional phenomena associated with the presence of interfaces which affect the properties of nanostructures and require a detailed study.

In the published papers related to the thermal characterization of metals inside the pores of alumina matrix, the authors have presented the size dependence of the melting temperature [5,6]. Nevertheless, the influence of matrix material was not discussed. As it is shown in our previous papers [7,8], the influence of matrix on the thermoelastic characteristics can considered by introducing the structural parameter associated with the concentration of nanowires in the bulk of the matrix.

The results of the microscopy show that alumina composites have cellular structure consisting of hexagon-like cells adjoining each other along their sides. Thus, in the considered unidirectionally reinforced nanocomposite, the components are isotropic and the position of nanowires in the bulk of the matrix is random; on the whole, however, the material is assumed to be statistically homogeneous. This results in an existence of the average distance between nanowires that may be related to their concentration. Thus, it is possible to completely characterize the structure of the composite by introducing h/r parameter, representing the ratio of half the distance between the nanowires to the nanowire radius, as illustrated in Figure 1.

In this paper, we have synthesized In, Sn, and Zn nanowire arrays with different radius and concentration in the bulk of the matrix. Fabricated composites have been investigated by X-ray diffraction (XRD), scanning electron microscopy (SEM), and differential scanning calorimetry (DSC). There has been established the dependence of the melting temperature of the embedded metal nanowires on the nanocomposite structural parameter taking into account their radius and concentration.

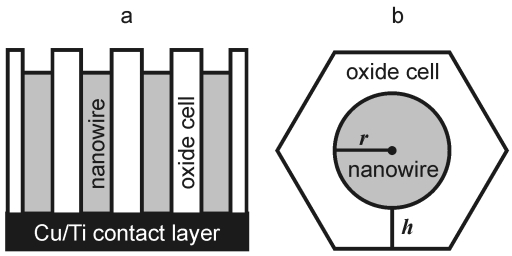

Figure. 1 Schematic representation of the material's structure: (a) side view of several elementary volumes and (b) an elementary volume in the cross-section plane

2. EXPERIMENTAL PROCEDURES

2.1 Sample Preparation

Porous AAO was fabricated by using a two-step anodization process [9] in the solution containing 40 g/l of oxalic acid. Anodization was conducted at the constant temperature of 18 °C. Then, thoroughly washed and dried the porous AAO templates were treated with the solution containing 3 wt. % H_3PO_4 at the temperature of 35-37 °C for 0, 15, 25, 35 and 45 min to form matrices with different porosity. Table 1 shows the values of pore radius and structural parameter depending on the etching time obtained by means of scanning electron microscope. Stand-alone AAO membranes were obtained after dissolving the unreacted Al on the back of the substrate in 0.1M $CuCl_2$ solution containing 10 wt.% HCl. To remove the barrier oxide layer that is also formed in the anodization process, there was applied 0.5M NaOH solution. The metal contact on one of the sides of the membrane consisting of 100 nm titanium layer and 200 nm copper layer was formed by means of magnetron sputtering.

etching time, min	*h*/*r*	*r*, nm
0	1.11	18
15	0.82	22
25	0.64	23.5
35	0.50	26
45	0.22	32

Table.1: Values of the structural parameter and pore radius of the alumina matrix depending on the etching time

Electrochemical deposition of In, Sn, and Zn into the AAO was carried out at room temperature in a two-electrode cell that provides contact of the solution only on one of the sides of the template. Deposition was performed from sulfate solutions, the anode material was identical to the metal being deposited, the current density was 5 mA/cm^2. The process was being carried out up to the moment when the metal film appeared on the surface of the sample, which was removed by the soft polishing material. The samples were then rinsed with deionized water and dried.

2.2 Crystalline Structure

The structure of arrays of In, Sn, Zn nanocrystals enclosed in the AAO pores was characterized by means of X-ray diffraction analysis. In the diffractograms there are diffraction peaks corresponding to polycrystallites of the deposited metals In, Sn, Zn, as well as peaks corresponding to unreacted aluminum which remained after etching. The morphology of the formed nanocomposites and pores fillability were analyzed using scanning electron microscopy. Microphotographs of the top view and cross-section view of the metal-filled AAO matrix are shown in Fig. 2. As it follows from the results of the microscopy, the deposited metal completely fills the pores, and the diameter of the built-in nanowire may be supposed to be equal to the pore diameter of the anodic oxide.

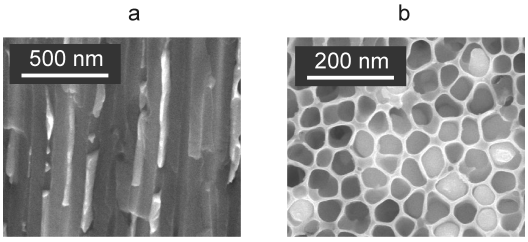

Figure. 2 SEM cross-section view (a) and top view (b) of AAO-Zn nanocomposite

2.3 Differential Scanning Calorimetry

3-5 mg samples were studied using differential scanning calorimeter DSC 204 F1 Phoenix (Netzsch). Heating was carried out in press-fitted aluminum crucibles at a rate of 10 K/min in argon atmosphere. An empty Al crucible was used as a reference. The phase transition temperature in the structures was determined according to the beginning point of the endothermic peak. DSC analysis included experiments under similar conditions with an empty matrix and electrochemically deposited bulk films of indium, tin, and zinc for correct explanation of the observed temperature effects.

3. RESULTS AND DISCUSSIONS

DSC signals of the composite samples with different structural parameter in comparison with those of the bulk metal films are given in Fig. 3. There is endothermic peak corresponding to the melting of metals in each curve. In the curves it is clearly seen that the beginning point of the melting peak shifts to the area of lower temperatures when the structural parameter increases.

As can be seen in Fig. 3, with the increase of *h*/*r* and corresponding decrease of nanowire radius the melting temperature decreases, and this is caused by both the size effects and the influence of the "matrix-nanowire" interface. This effect is primarily determined by the mechanical stresses caused by the differences between the thermal coefficients of linear expansion of the heterogeneity elements during heating. And this fact should necessarily be taken into account in the future when simulating the melting temperature of the embedded nanowires.

In the process of our research there have been obtained alumina composites with indium, tin, and zinc nanowires with different structural parameter *h*/*r*. The melting of the nanowires enclosed in the matrix pores was studied depending on the structural parameter *h*/*r*.

In order to consider the influence of the matrix material on thermodynamic properties of the metal nanowires, it was offered to introduce the structural parameter *h*/*r* associating the radius of nanowires with the distance between the nanowires in the composite, since this data can be directly obtained by means of scanning electron microscopy. Using the parameter *h*/*r* will allow in the future to derive equations convenient for numerical analysis when predicting thermodynamic properties without losing information about the structure of the composite.

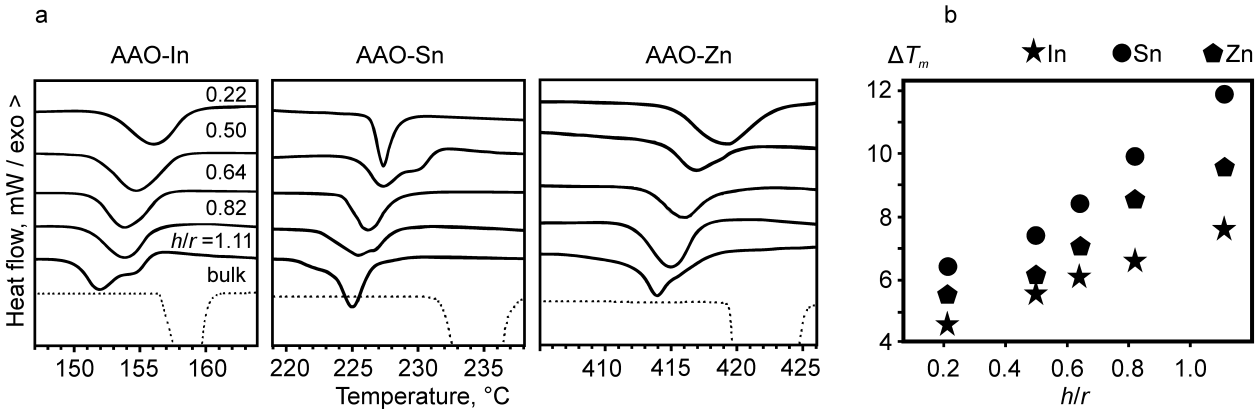

Figure. 3 DSC traces of composites with various *h*/*r* (a); melting temperature change as a function of *h*/*r* (b)

4. ACKNOWLEDGMENTS

This work was supported by the Ministry of education and science of the Russian Federation (Code: 122-GZ-MFE), the Russian Foundation for Basic Research (Grants No. 13-08-00672 A, 14-08-00654 A), and the European FP7 project PIRSES-GA-2011-295273-NANEL.

5. REFERENCES

[1] Sarkar, J., Khan, C.G., Basumallick, A. 2007. Nanowires: properties, applications and synthesis via porous anodic aluminium oxide template. *Bull Mater Sci.* 30, 3 (June 2007), 271-290.

[2] Gavrilov, S., Nosova, L., Sieber, I., Belaidi, A., Dloczik, L., Dittrich, Th. 2005. Synthesis of semiconductor nanowires by pulsed current electrodeposition of metal with subsequent sulfurization. *Phys. Status Solidi A.* 202, 8 (June 2005), 1497-1501.

[3] Gudiksen, M.S., Lauhon, L.J., Wang, J., Smith, D.C., and Lieber, C.M. 2002. Growth of nanowire superlattice structures for nanoscale photonics and electronics. *Nature.* 415 (Feb. 2002), 617-620.

[4] Jessensky, O., Müller, F., Gösele, U. 1998. Self-organized formation of hexagonal pore arrays in anodic alumina. *Appl. Phys. Lett.* 72 (Mar. 1998), 1173-1175.

[5] Xu, S. H., Fei, G. T., Zhang, Y., Li, X. F., Jin, Z., Zhang, L. D. 2011. Size-Dependent Melting Behavior of Indium Nanowires. *Phys. Lett. A*. 375 (Mar. 2011), 1746–1750.

[6] Wang, X. W., Fei, G. T., Zheng, K., Jin, Z., Zhang, L. D. 2006. Size-Dependent Melting Behavior of Zn Nanowire Arrays. *Appl. Phys. Lett*. 88 (Apr. 2006), 173114 (3pp).

[7] Shilyaeva, Yu. I., Bardushkin, V. V., Silibin, M. V., Gavrilov, S. A., Yakovlev, V. B., Pyatilova, O. V. 2013. Effect of the Structure and Thermoelastic Properties of Components on the Average Stress in Anodic Aluminum Oxide Having Pores Filled With Metallic Nanowires. *Inorg. Mater.* 49 (July 2013), 676–680.

[8] Shilyaeva, Yu. I., Bardushkin, V. V., Silibin, M. V., Gavrilov, S. A., Yakovlev, V. B., Pyatilova, O. V. Bulk Density of the Energy of Deformation in an Anodic Aluminum Oxide with Pores Filled by Threadlike Metal Nanocrystals. *Russ. J. Phys. Chem. A.* 87 (Nov. 2013), 1870–1874.

[9] Masuda, H., Fukuda, K. 1995. Ordered metal nanohole arrays made by a two-step replication of honeycomb structures of anodic alumina. *Science.* 268 (June 1995), 1466-1468.

Detection of adulteration of extra virgin olive oil with pomace olive oil by Fourier Transform Infrared Spectroscopy

S.NIGRI, R.OUMEDDOUR

ABSTRACT

Adulteration of edible oils has been a chronic illness in food adulteration for many years. It not only causes serious health problems, but also undermines the integrity and orderly economy. To discriminate among different oils as well as to detect adulteration, many analytical techniques can be used. Recently, the application of FTIR spectroscopy has increased in food studied, and particularly has become a powerful analytical tool in the study of edible oils and fats. In this study, Fourier-transform infrared spectroscopy (FTIR), followed by multivariate treatment of the spectral data, was used to establish the composition of binary mixtures of extra virgin olive oil (EVOO) with pomace olive oil. The wavelength scale of the FTIR spectra of the oils was divided in 26 wavelengths. The spectral regions where the variations were observed were chosen for developing models. The performance of the model was evaluated by the coefficient of determination R^2 and the root mean square error of cross validation RMSECV. Using PLS and MLR regression we could find models, selected by cross validation with a high determination coefficient of $R^2 > 0.99$. The methodology presented in this study is a useful tool for analysis and quantifying adulteration of extra virgin olive oil with pomace olive oil.

Keywords

Extra virgin olive oil, adulteration, FTIR spectroscopy, MLR, PLS.

1. INTRODUCTION

Today, olive oil has received great attention because of its nutritional and sensory characteristics. Numerous components of olive oil may contribute to its beneficial effect for human health [1]. It's characterized by consisting of monounsaturated fatty acids as well as by its elevated content in antioxidant agents. Extra virgin olive oil is the most sought after on account of the organoleptic and nutritional properties and is therefore the most expensive grade. For this latter reason, it's a potential target for adulteration or mislabeling [2]. Thus, the adulteration of the extra virgin olive oil undermines the confidence of consumers and also increases the profit of unscrupulous producers [3]. The edible oils widely employed in virgin olive oil adulteration can be lower quality of olive oil such as refined and pomace olive oil or others vegetable oils such as sunflower, corn, palm, hazelnut, soya, soybean, and canola oils due to their close resemblance to virgin olive oil composition [4,6]. To discriminate among different oils as well as to detect adulteration, many techniques can be used [7]. Now, the development of new rapid and sensitive methods instead of traditional time-consuming and expensive analysis techniques is required. There are several studies about new emerging methods mainly focusing on this subject. Due to their properties as fingerprint techniques, vibrational spectroscopies like infrared and Raman have been considered deal analytical methods for food studies, including the authenticity of high price edible fats and oils [8-11].

Fourier transform infrared (FTIR) spectroscopy combined with various chemometric techniques has been used for the identification of olive oil adulterated with some vegetable oils namely hazelnut [12], canola oil [13], corn, soybean, and sunflower oils [14] and with sunflower and corn oils [15]. Besides, FTIR spectroscopy can also be exploited for quantitative analysis of EVOO in quaternary mixture systems with other plant oils [16]. The aim of this study was to evaluate the potential of the FTIR spectrometry for detection and quantification of POO with the aid of multivariate calibrations.

2. MATERIALS AND METHODS

2.1 Sample preparation

Extra virgin olive oil (EVOO) and pomace olive (POO) were purchased from the local supermarket in Guelma, Algeria. To quantify the concentration of adulterant agents, binary mixtures composed of EVOO and POO oils were prepared.

2.2 Quality indices

Free acidity expressed as percentage of oleic acid, peroxide value (PV) expressed as millequivalents of active oxygen per kilogram of oil ($meqO_2/kg$) and extinction coefficients (K232 and K270) were determined according to European commission regulation EEC 2568/91. Absorption at 232 and 270 nm was measured; chlorophylls and carotenoids were evaluated according to the procedure described by Mosquera et al [17] by their absorption at 670 and 470 nm respectively, using a UV spectrophotometer (Jasco V-630).

2.3 FTIR spectra

A Perkin-Elmer Spectrum one spectrophotometer equipped with a deuterated triglycerine sulphate (DTGS) detector was used to collect FTIR spectra with a resolution of 4 cm^{-1} at 10 scans. A small quantity of the oil samples was directly deposited between two well-polished KBr disks, creating a thin film. Duplicated

spectra were recorded for all the oil samples and binary mixtures. Spectra were scanned in the absorbance mode from 4000 to 450 cm^{-1} and processed with the computer software program Spectrum for Windows (Perkin-Elmer). In order to reduce the variability associated with total amount of oil sample used, and to minimize other sources of variance affecting the intensity of peaks, spectra were normalized.

2.4 Chemometrics analysis

Chemometrics analysis, including quantification with MLR and PLS models were performed using the software MINITAB 16. The spectral regions where the variations were observed chosen for developing the model calibrations. The optimum number of PLS factors was determined by cross validation.

3. RESULTS and discussions:

The quality of the selected olive oil was evaluated by acidity index, peroxide value and the spectroscopic indices K232 and K270 are reported in table 1.

Acidity	PV (meq:kg)	K232	K270	Chlorophylls (mg/kg)	Carotenoids (mg/kg)
0.37	12	1.46	0.19	3.51	1.27

Table 1: Initial characteristics of the selected olive oil.

All quality parameters were markedly bellow the limits fixed by the EU regulation for olive oil to be labeled as “extra virgin”.

The measurements of the FTIR signals in the 4000–450 cm^{-1} spectral region were recorded on the butter samples of the calibration set. The collected spectra, cumulated in Figure. 1 show small differences among them and only in limited regions.

Figure.1 exhibits FTIR spectra of EVOO and POO between 4000 and 450 cm^{-1}. At first glance, the spectra are similar; this is due to the chemical composition very close. However, structural differences must be revealed.

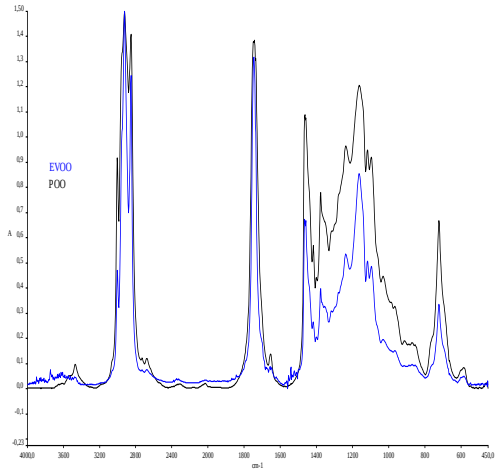

Figure. 1: FTIR spectra of EVOO and POO at frequency of 4000-450 cm^{-1}

The presence of small amounts of adulterant oil in EVOO is evidenced by small variations in the values of peak intensity of specific bands in the spectra. FTIR spectra of EVOO and POO show that there exist notable differences in the band around 3007 cm^{-1} assigned to the C-H stretching vibration of the cis-double bond. The height of this band for the EVOO is smaller than it for POO and changed with the percentage of the adulterant agent. Moreover, the clear shift of the 2926.82 cm^{-1} band for EVOO, attributed to the symmetric stretching vibration of the aliphatic CH_2 group, to the 2925.83 cm^{-1} bands for POO. The height of large peak around 1745 cm^{-1} is attributed to C=O stretching which varies between oils with higher absorbance values for POO. Based on these observations, quantify the percentage of vegetable oil added to extra virgin olive oil could be using FTIR Spectra.

The analysis of the variations in FTIR spectra for extra virgin olive oil (EVOO) and pomace olive oil (POO) is not very easy, because of the weak changes. PLS is one of the most used tools for the study of the adulteration of extra virgin olive oil with edible oils. PLS was used for the study of the adulteration of EVOO with POO.

In the PLS calibration models, the evaluation of the method linearity was carried out in order to show a proportional relationship between responses versus analyte concentrations. The frequency regions of 3010-2675 cm^{-1} and 1745-1030 cm^{-1} were used for the quantification of POO in EVOO. The performance of the model was evaluated by the coefficient of determination R^2 and the root mean square error of cross validation RMSECV.

In order to validate the developed model, cross validation using leave one out technique was used.

Figure.2 exhibits the scatter plot for the relationship between actual value and FTIR-predicted value (%) of POO in EVOO.

As indicate in figure.2, PLS was able to find a very good correlation with $R^2 > 0.99$, this confirm the goodness of fitting of the model.

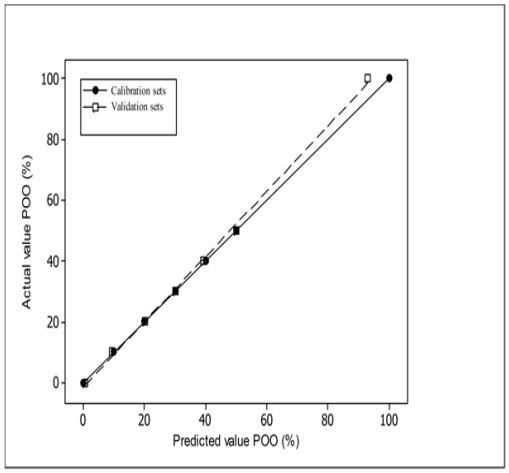

Figure 2: Correlation plot of the predicted versus the actual value (%) of POO in EVOO

The PLS method has an excellent predictive ability for the determination EVOO purity at frequencies of 3006 cm^{-1} caused by =C-H stretching vibration of the cis-double bond, 2679, 1746 cm^{-1} ascribed to –C=O groups, 1654 cm^{-1} assigned to C=C (cis), 1417 cm^{-1} attributed to =C-H (cis) and 1032 cm^{-1} assigned to the -C-O stretching vibration in FTIR spectra.

FTIR spectroscopy combined with PLS as multivariate method can be a powerful tool to monitor the adulteration of extra virgin olive oil with vegetable oil like pomace olive oil.

4. REFERENCES

[1] Dankowska, A., Malecka, M. 2009. Application of synchronous fluorescence spectroscopy for determination of extra virgin olive oil adulteration. Eur. J. Lipid Sci. Technol. 111 (sep. 2009), 1233-1239. DOI=10.1002/ejlt.200800295.

[2] Aparicio, R.; McIntyre, P. 1998. Oils and Fats. In Food Authenticity: Issues and Methodologies; Lees, M., Ed.; Eurofins Scientific: France, 1998; pp 231-269.

[3] Zhang, Q.,Liu, C.; Sun, Z., Hu, X., Shen, Q.,Wu, J. 2012. Authentication of edible vegetable oils adulterated with used frying oil by Fourier Transform Infrared Spectroscopy. Food Chem. 132 (jun. 2012), 1607-1613. DOI=http://dx.doi.org/10.1016/j.foodchem.2011.11.129.

[4] Shurst, P. R. and Dennis M. J. 1996. Food authentication. Blackie Academic and professional, London (UK).

[5] Guimet, F., Ferré, J.and Boqué, R. 2004. Application of unfold principal component analysis and parallel factor analysis to the exploratory analysis of olive oils by means of excitation-emission matrix fluorescence spectroscopy. *Anal. Chim. Acta.* 515 (2004), 75-85. DOI= http://dx.doi.org/10.1016/j.aca.2004.01.008

[6] Guimet, F., Ferré, J. and Boqué, R. 2005. Rapid detection of olive-pomace oil adulteration in extra virgin olive oils from the protected denomination of origin "Siurana" using excitation-emission fluorescence spectroscopy and three-way methods of analysis. *Anal. Chim. Acta.* 544 (2005), 143-152.DOI=http://dx.doi.org/10.1016/j.aca.2005.02.013

[7] Rohman, A. and Che Man, Y. B. 2012. Application of Fourier Transform Infrared Spectroscopy for Authentication of Functional Food Oils. *Appl. Spectros. Rev*. 47, 1 (2012), 1-13. DOI=10.1080/05704928.2011.619020

[8] Reid, L. M., O'Donnell, C. P. and Downey, G. 2006. Recent technological advances for the determination of food authenticity. *Trends Food Sci. Technol.* 17 (2006), 344–353. DOI= http://dx.doi.org/10.1016/j.tifs.2006.01.006

[9] Baeten, V. and Dardenne, P. 2002. Spectroscopy: developments in Instrumentation and Analysis. *Grasas Aceites.* 53 (2002), 45–63

[10] Zhang, X., Qi, X., Zou, M. and Liu, F. 2011. Rapid authentication of olive oil by Raman Spectroscopy using principal component analysis. *Anal. Lett.* 44 (2011), 2209–2220. DOI=10.1080/00032719.2010.546030.

[11] Bunaciu, A. A., Aboul-Enein, H. Y. and Fleschin, S. 2010. Application of Fourier transform infrared spectrophotometry in pharmaceutical drugs analysis. *Appl. Spectros. Rev.* 45 (2010), 206–219. DOI= 10.1080/00387011003601044.

[12] Groselj, N., Marjan Vracko, M., Fernandez Pierna, J. A., Baeten, V. and Novic M. 2008. The use of FT-MIR spectroscopy and counter-propagation artificial neural networks for tracing the adulteration of olive oil. *Acta Chim. Slovenia*. 55 (2008), 935–941.

[13] Rohman, A., Che Man, Y. B. and Yusof, F. M. 2014. The Use of FTIR Spectroscopy and Chemometrics for Rapid Authentication of Extra Virgin Olive Oil. *J. Am. Oil Chem. Soc.* 91 (2014), 207–213. DOI= 10.1007/s11746-013-2370-5

[14] Lerma-Garcı´a, M. J., Ramis-Ramos, G., Herrero-Martı´nez, J. M. and Simo´Alfonso, E. F. 2010. Authentication of extra virgin olive oils by Fourier-transform infrared spectroscopy. *Food Chem.* 118 (2010),78–83. DOI= http://dx.doi.org/10.1016/j.foodchem.2009.04.092

[15] Gurdeniz, G. and Ozen, B. 2009. Detection of adulteration of extra virgin olive oil by chemometric analysis of mid-infrared spectral data. *Food Chem.* 116 (2009), 519–525. DOI= http://dx.doi.org/10.1016/j.foodchem.2009.02.068

[16] Rohman, A. and Che Man, Y. B. 2011. Determination of extra virgin olive oil in quaternary mixture using FTIR spectroscopy and multivariate calibration. *Spectroscopy.* 26, 3 (2014), 203–211.DOI= 10.3233/SPE-2011-0538

[17] Minguez-Mosquera, M.I., Rejano-Navarro, L., Gandul-Rojas, B.; Sánchez-Gómez, A.H. and Garrido-Fernandez, J. 1991. Color pigment correlation in virgin olive oil. *J. Am. Oil Chem. Soc.* 68 (1991), 332-336.

Corresponding author : Laboratoire d'Analyses Industrielles et Génie des Matériaux,

Université 8 mai 1945 Guelma, B.P 401 Guelma 24000 Algeria.

E-mail: nigri_s@yahoo.fr

Ab initio calculation of polarization, piezoelectric constants and elastic constants of InAs and InP semiconductors

C. Hajlaoui,[1,2,*] F. Raouafi,[1] F. Ben Cheikh Laarbi[1], J-M. Jancu[2]

[1]Faculté des sciences Tunis el Manar, laboratoire physico-chimie des microstructures et microsystèmes LPCMM-IPEST La Marsa, Tunis, Tunisie.

[2]Université Européenne de Bretagne, INSA-RENNES, CNRS, UMR 6082 FOTON-OHM, Rennes, France.

ABSTRACT

We report, in this work, first principles density functional calculations of the spontaneous polarizations, piezoelectric stress constants and elastic constants for the III-V wurtzite structure semiconductors InAs and InP. Using the density functional theory implemented in the VASP code, we obtain polarization values of -0.011 and -0.013 C/m^2, and piezoelectric constants e_{33} (e_{31}) of 0.091 (-0.026) and 0.012 (-0.081) C/m^2 for structurally relaxed InP and InAs respectively. These properties are consistently smaller than those of nitrides. Therefore we predict a smaller internal field in such structures.

Keywords

DFT simulation, VASP, semiconductors, elasticity, piezoelectricity, spontaneous polarization, nanowires, heterostructure, Berry phase method.

1. INTRODUCTION

Despite significant advances achieved in Si-photonics with based materials, the III-V compounds have superior optoelectronic properties and exhibit unique features (direct and tunable band gap) for light emission and detection. This represents some real advanges for optoelectronic functionalities (LEDs, lasers, photo detectors, photovoltaic) [1] to operate with a high efficiency at various optical wavelengths. The integration of III-V materials in this field is based on epitaxial growth of nanowires.

When a nanowire heterostructure is epitaxially grown from materials with different lattice constants, an elastic strain field will be created inside the material system. This strain field can in general modify the electronic structure of the material system and can therefore be employed to tailor the electronic and optoelectronic properties of the nanowire heterostructure for applications. This strain can induce spontaneous polarization and piezoelectric fields with significant effects on the electronic and optoelectronic properties of the systems. Thus, it is in general of great importance to consider strain and piezoelectricity simultaneously when studying epitaxially grown, strained nanowire heterostructures.

In this work we calculate the spontaneous polarizations, piezoelectric coefficients and elastic constants of wurtzite-structure InAs and InP using the standard local density approximation to density functional theory as implemented in the VASP package [2]. The polarizations are obtained using the widely-used Berry phase method [3], and the piezoelectric coefficients and elastic constants are obtained from the calculated dependence of polarization and energy on the appropriate strain.

Our polarizations are reported relative to the conventional reference structure of the zinc blende structure with the same ratio of *c* lattice constant to unit cell volume [4], and care is taken to avoid problems associated with the branch dependence of the polarization by extracting the so-called *proper* piezoelectric response for the e_{13} coefficients [5].

2. POLARIZTION and piezoelectric effects:

Typical bulk III-V compound semiconductors grow preferentially in the zinc blende phase (Figure 1). Bulk wurtzite (Figure 1) crystals of III-V compound semiconductors are rare in nature (except for III-nitride materials). Nevertheless, it have been shown that it is possible to selectively grow thin III-V compound semiconductor nanowires in either zinc blende or wurtzite phase, or in a superlattice form of these two phases. However, it is very challenging to experimentally establish the elastic and piezoelectric properties of wurtzite III-V compound semiconductors because of the lack of bulk wurtzite crystals of these materials in nature. Thus theoretical calculation seems to be a good solution of such problems.

As We know, when a wurtzite structure semiconductor is constrained by epitaxial matching to a substrate or in a heterostructure, its total polarization is the sum of its intrinsic spontaneous polarization P_{sp} (that is the polarization that it would have in an unstrained bulk sample) plus the polarization induced as a result of the strain P_{pz} (ε). The strain-induced component depends strongly on the strain ε and hence on the lattice mismatch between the epitaxial layers. In the linear regime, it is related to the piezoelectric tensor *e* by:

$$P_{pz}(i) = \sum_j e_{ij}\varepsilon_j$$

Both the intrinsic and strain-induced contributions can be calculated accurately from first principles calculations and have been shown to be large in the III-V nitrides [4].

In the case of wurtzite symmetry, this tensor contains three independent elements P_x, P_y and P_z.

Thanks to intrinsic symmetry rules of hexagonal lattice, many coefficients of piezoelectric tensor are equal to zero, only three coefficients are not equal to zero : e_{33} , e_{31} and e_{15}.

e_{33} and e_{31} characterizes polarization along the **z** axis (P_z), e_{15} (shearing term) characterizes polarizations along **x** and **y** axis (P_x and P_y) which are in general neglected.

$$P_z = 2\left(e_{31} - \frac{C_{13}}{C_{33}} e_{33}\right)\varepsilon_{\perp}$$

C_{13} and C_{33} are the elastic constants. To note that, in the hexagonal symmetry, the elastic tensor contains six elements not equal to zero : C_{11} , C_{12}, C_{13}, C_{33}, C_{44} and C_{66}.

3. RESULTS and discussions:

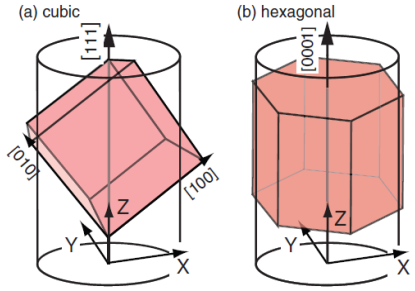

Figure. 1 Schematic illustration of (a) a cubic symmetric zinc blende and (b) an hexagonal wurtzite unit cell with respect to the coordinate system employed in this work. The Z axis is defined to be along the growth direction of materials: the [111] direction of the zinc blende and the [0001] direction of the wurtzite crystal.

We begin by calculating the polarization and piezoelectric constants (e_{33} and e_{31}) at the calculated LDA equilibrium structures for InP (a = 4.12 Å, c = 6.72 Å and u = 0.3705) and InAs (a = 4.21 Å, c = 7.02 Å and u = 0.3703). Our results are reported in table 1. For comparison we also report these value for GaN since we have results in literature to compare with. This is how we validate our method.

	InP	InAs	GaN
e_{31} (C/m^2)	- 0.026	- 0.081	- 0.35
e_{33} (C/m^2)	0.091	0.012	1.27
P (C/m^2)	- 0.011	- 0.013	- 0.029

Table.1: Polarizations P and piezoelectric constants e_{33} and e_{31} for InP, InAs and GaN calculated at the theoretical LDA equilibrium lattice parameters.

We note that, contrarily to the gallium nitride, InP and InAs materials have very small polarization and piezoelectric coefficients. These values can be related to the low ionic character of In-As and In-P binding. For the III-nitrides, the binding is highly ionic due to the big size of the azote atom, which gives a large spontaneous polarization for nitrides.

The piezoelectric effect is related to the stress state of the material and the lattice mismatch. In fact, in the case of InAs/InP system, the lattice mismatch is about 3% but it can reach 7% in the case of nitride (the InN/GaN system as example), that is why InP and InAs piezoelectric constants are smaller than those of nitrides.

Since the polarization in the InAs/InP system is very small, we can affirm the absence of an internal electric field, and this is a good news for optoelectronic applications based in such systems.

		C_{11}	C_{12}	C_{13}	C_{33}	C_{44}	C_{66}
ZB	InAs	80.3	43.3	-	-	36.9	-
	InP	98.4	45.4	-	-	39.5	-
WZ	InAs	99.1	43.6	31.9	114.5	22.0	27.7
	InP	116.7	50.9	38.2	135.9	27.0	32.9

Table.2 Elastic constants in GPa for wurtzite (WZ) and zinc Blende (ZB) structures of InP and InAs calculated at the theoretical equilibrium lattice parameters and atomic positions.

Finally, we report in table 2, the elastic constants obtained by calculating the change in energy with strain for five different strain configurations. The details of the strain configurations used and the procedure for extracting the elastic constants are described in Ref [6] For comparison, we include the values of elastic constants in the cubic phase since we have experimental results to compare with.

In the case of zinc blende phase, the values of elastic constants are in good agreement with experimental ones [7] which was expected since the LDA (Local Density Approximation) describes precisely the energetic properties of the ground state. In the case of the wurtzite phase, we have no experimental data to compare with but we expect our calculated values to be similarly appropriate.

4. ACKNOWLEDGMENTS

This work was performed using HPC resources from GENCI CINES and IDRIS 2013-2013096724. The work is supported through the participation of the INSCOOP ANR project.

5. REFERENCES

[1] Tomioka, K., Yoshimur, M., Fukui, T. (2012). A III-V nanowire channel on silico for high-performance vertical transistors, *Nature*, **488**,189-192.

[2] Kresse, G., Furthmuller, J. (1996). Efficient iterative schemes for *ab initio* total energy calculations using a plane wave basis set, *Phys. Rev. B*, **54**, 11169.

[3] King-smith, R., D., Vanderbilt, D., (1993). Electric polarization as a bulk quatity and its relation to surface charge, *Phys. Rev. B*, **48**, 4442.

[4] Bernardini, F., Fiorentini, V. and Vanderbilt, D., (1997). Spontaneous polarization and piezoelectric constants of III-V nitrides, *Phys. Rev. B*, **56**, R1024.

[5] D. Vanderbilt, (2000). Berry-phase theory of proper piezoelectric response, *J. Phys. Chem. Solids*, **61**, 147 (2000).

[6] A, F. Wright, (1997). Elastic properties of zinc Blende and wurtzite AlN, GaN and InN. *J. Appl. Phys*. **82**, 2833 (1997).

[7] M. Krijin, (1991). Heterojunction band offsets and effective masses in iii-v quaternary alloys. *Semicond. Sci. Technol***, 6**, 27, (1991).

Modeling and Simulation of Radial Piezoelectric Transducer

Sawsen Rouabah [1], Abdelhafid Chaabi [1] and Toufik Mordjana [1]

1 Laboratory of Hyperfrequencies and Semi-conductor(LHS),
Electronic department, Constantine 1 University, Algeria

ABSTRACT

Piezoelectric ceramics are characterized as smart materials and have been widely used in the area of actuators, sensors and piezoelectric transformers.

In this study, we focus on piezoelectric transformers, for the advantages they have over conventional magnetic transformers: high power density, high efficiency, low profile, small size, light weight and electro-magnetic noise free operation.

There are many types of piezoelectric transformers: Rosen type, circular (radial) type and in thickness mode… We took in this work an example of radial type for its good characteristics. It can be miniaturized to a greater degree since the energy is stored by the elastic vibration.

The characterization of radial piezoelectric transformer (RTP) such as the total displacement in different axes, resonance frequency, and efficiency were shown using COMSOL MULTIPHYSICS. It was used as a tool to design, characterize this RPT, to simulate and to show the 1D plots.

Using this model, the electric voltage is applied to the driving piezoelectric transformer that is radially polarized in a cylindrical coordinate system.

Selected material in our study is Lead Zirconate Titanate PZT 5H that has a good benefit especially when it offers high sensitivity and good response.

The output parameters (voltage and efficiency) are studied according to the input ones (load and frequency). We have tried to compare with another software: Matlab Simulink using the equivalent circuit parameter.

Keywords

Piezoelectricity, materials, transducer, piezoelectric transformer, COMSOL Multiphysics, voltage, frequency, displacement.

1. INTRODUCTION

Piezoelectric transformer has been developed in recent years [1]. It is a combination between a piezoelectric actuator on the primary side and a piezoelectric transducer on the secondary side [2].

Piezoelectric transformers can be categorized as one of the three major types: Rosen type [3], thickness vibration mode [4,5], or radial vibration mode [6]. Because of their different vibration modes and mechanical structures, all the three types of piezoelectric transformers have different mechanical and electrical characteristics [7].

This paper focus on radial vibration mode using the simulation of Comsol Multiphysics. The radial mode piezoelectric transformers provide high power density and wide range of voltage gain. It can be used in many applications like: AC/DC or DC/DC converter [8].

2. RADIAL PIEZOELECTRIC TRANSFORMERS:

The basic of piezoelectric transformers is revealed with focus on Electrical parameters. They are based on piezoelectric materials which have an electromechanical coupling and through this coupling a charge displacement is generated. It is proportional to the deformation of the material [2].

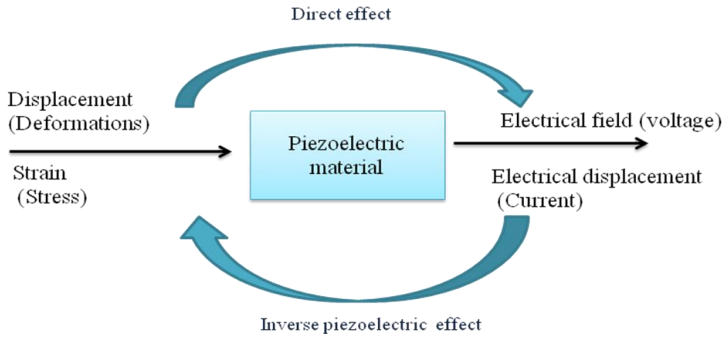

Figure. 1 principle of operation of a piezoelectric transformer

In this paper, we have taken one model which is the radial mode piezoelectric transformer. It is the construction between two discs of piezoelectric ceramic which are bonded to copper electrodes using an adhesive. This additional piezoelectric ceramic can then made together to create a path for the energy to be transferred between the actuators and transducers.

Figure 1 shows the structure of radial piezoelectric transformer [4]

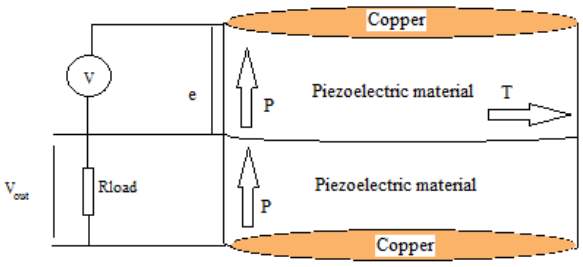

Figure. 2 Radial piezoelectric transformer's structure

2.1 Constitutive Equations

The following linear piezoelectric equations (1) and (2) can describe the behavior of the radial piezoelectric transformer which is the piezoelectric actuator and piezoelectric transducer [9].

$$S = c^E.T + e.E \quad \ldots\ldots\ldots\ldots\ldots\ldots(1)$$

$$D = e.T + \varepsilon^T.E \quad \ldots\ldots\ldots\ldots\ldots\ldots(2)$$

The table 1 shows the characteristic of the radial piezoelectric transformer [10].

S	Mechanical strain
c^E	Elastic compliance at constant electric field (N/m^2)
E	Electric field (V/m)
e	Piezoelectric constant (C/m^2)
T	Mechanical stress (N/m^2)
D	Electric displacement (C/m^2)
ε^T	Permittivity at constant mechanical stress (F/m)

Table.1: Piezoelectric constitutive equation symbols

2.2 Electrical equivalent circuit

To analyze the radial mode piezoelectric transformer, it is useful to apply the electrical equivalent circuit which includes constant voltage power and load resistance R_l. Figure 2 shows the lumped constant equivalent circuit with C_{d1} and C_{d2} which are the damped capacitance of the input and the output parts, respectively. The circuit contains the R, L and C which are the equivalent mechanical resistance, the equivalent mass and the equivalent compliance of the input, respectively. All this parameter is developed on [11]

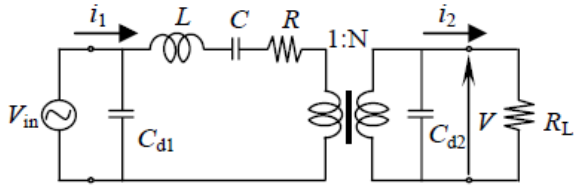

Figure. 3 lamped constant equivalent circuit

The voltage gain [2] is the ration of output voltage to input voltage which defined as following:

$$G = \frac{1}{N\sqrt{\left(\frac{1}{N^2}+\frac{C_{d2}}{C_m}-\omega^2 L_m C_{d2}+\frac{R_m}{R_{load}}\right)^2+\left(\omega\left(R_m C_{d2}+\frac{L_m}{R_{Load}}\right)-\frac{1}{\omega C_m R_{load}}\right)^2}} \quad \ldots(3)$$

With N which is transformer-turn ratio

The efficiency η [2] is expressed by the relation (4):

$$\eta = \frac{R_{load}}{(1+r^2)N^2 R_m + R_{load}} \quad \ldots\ldots\ldots\ldots(4)$$

3. RESULTS and discussions:

3.1 Using Comsol Multiphysics

Comsol multiphysics is used as a tool to design our structure and extract the output parameters which are the total displacement and the voltage gain according to the input ones (frequency and load).

For simulating the radial piezoelectric transformer in Comsol multiphysics, the "piezoelectric devises" and "Electrical circuit" physics under structural mechanics are used. The type of study required for a frequency sweep is the "Frequency domain".

We have drawn our piezoelectric transformer with the dimensions of the radius of 8mm and the thickness of 1mm which shown on figure 4.

After the design is buit, we polarise the piezoelectric transfomer with V=10sin(ωt)(V).

The load resistance R_{load} is 10^5 Ohm.

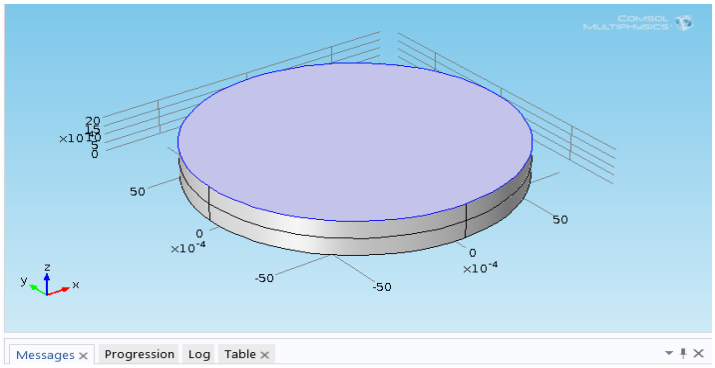

Figure.4 The architecture of radial mode piezoelectric transformer using Comsol multiphysics

Material selected is Lead Zirconate Titanate (PZT 5H), it has a good benefit especially when it offers high sensitivity and good response [12].

The range of frequency is between 400kHz and 900kHz, it depends on the thickness of our structure.

After meshing of our piezoelectric transformer which is shown on figure 5

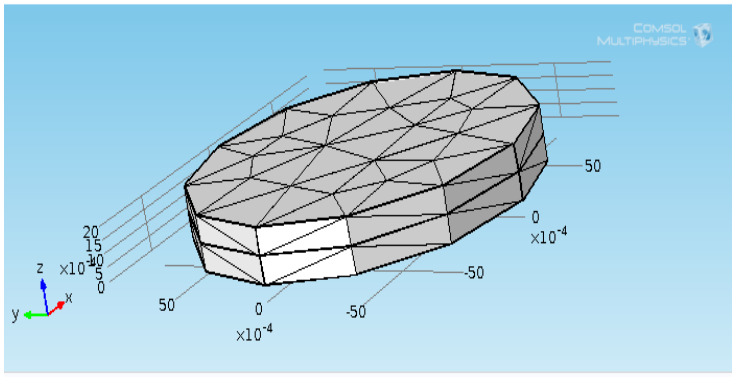

Figure. 5: Mesh

The figures 6, 7 and 8 show the total displacement with the different deformations depending on different frequencies on 3D.

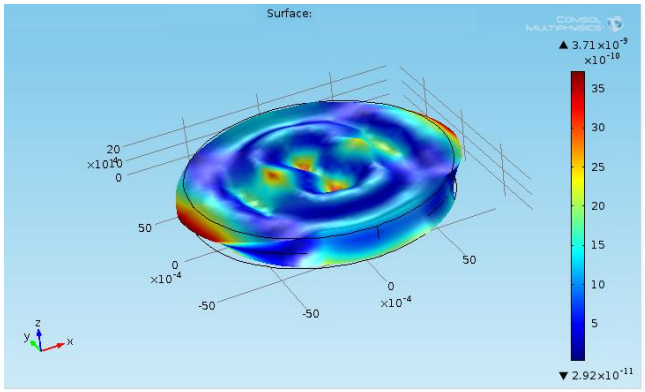

Figure. 6 3D modeling for total displacement at the 400kHz

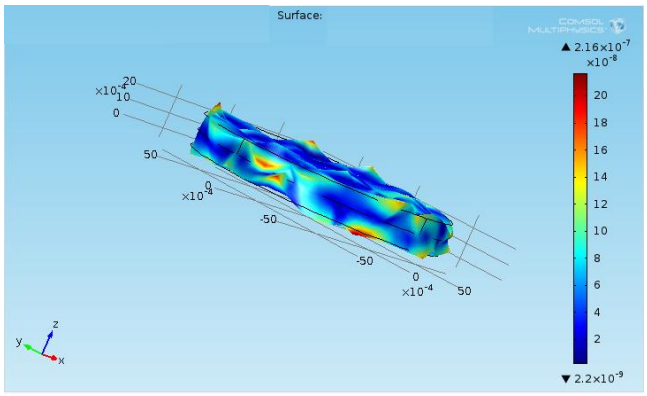

Figure. 7 3D modeling for total displacement at resonance frequency f=640kHz

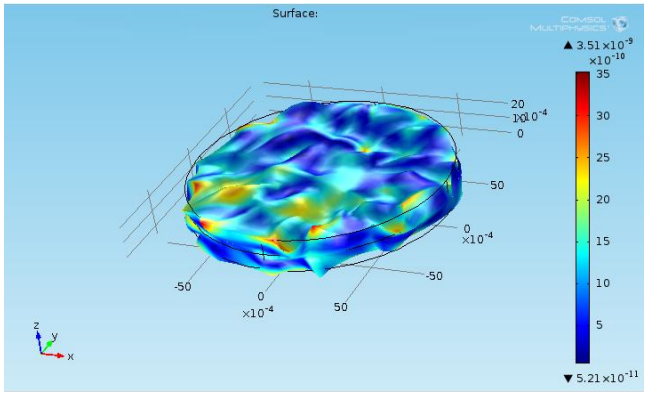

Figure. 8 3D modeling for total displacement at 900kHz

Figure. 9 total displacement

Figure 9 shows the resonance plot of total displacement at first mode which set on 640 kHz.

At the resonance frequency, we see that the gain voltage is high which is shown on figure 10. That is why those Radial mode piezoelectric transformers have a good benefit and advantages.

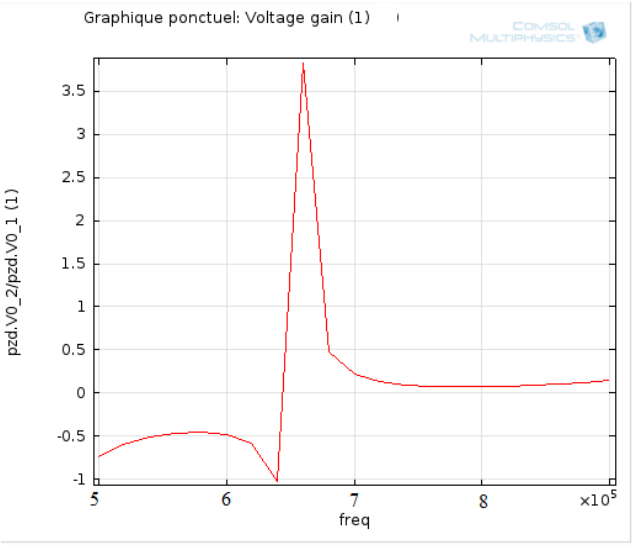

Figure. 10 gain voltage according to the frequency

When we change the load resistance, figure 11 shows that the piezoelectric transformer doesn't affect according to the value with R_l=1000 and 10 kOhm.

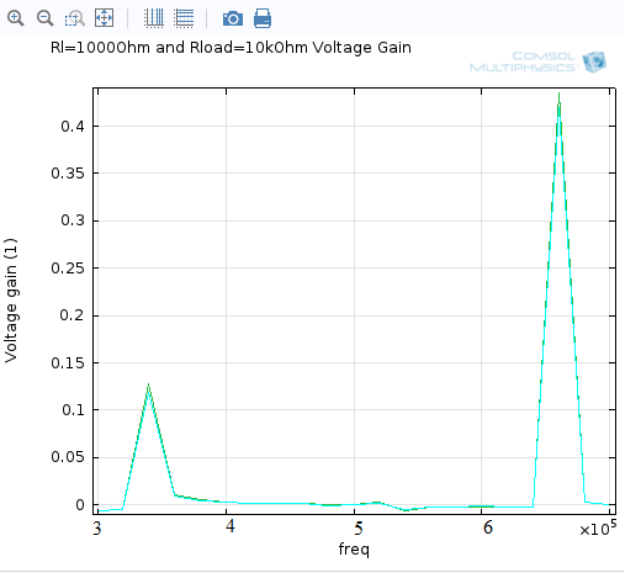

Figure. 11 Voltage gain with two different load resistance

4. CONCLUSION

A Radial piezoelectric transformer is simulated using Comsol Multiphysics software, which is very useful for this study. After the simulation, we have worked on the radial piezoelectric transformer. We have obtained different resonance frequencies which vary from load resistor to another. That is why the electrical and mechanical variables of the piezoelectric transformer depend on the frequency.

The results indicate that the voltage gain obtained has a high number which means that we can minimize our radial piezoelectric transformer as much as possible according to a high frequency.

5. REFERENCES

[1] A. Chérif, M. Meddad and S.Belkhiat, CEM. D 2008. Radial piezoelectric Trasnformer Study, International Journal of Sciences and techniques of automatic control and computer engineering.

[2] E. M.Baker. 2002. *Design of radial mode piezoelectric transformers for lamp ballast applications*. Doctoral thesis. University of Virginia.

[3] C. Y. Lin, 1997. *Design and analysis of piezoelectric transformer converters*. Doctoral Thesis. Blacksburg. University of Virginia.

[4] T. Zaitsou, O.Ohnishi. T. Inoue. M. Shoyama. T. Ninomiya. F.C Lee. G.C. Hua. IEEE, 1998. *Piezoelectric Transformer operating in Thickness Extensional Vibration and Its application to switching Converter*. P585-589.

[5] E. Sarraute. D. Vasic. F.Costa. 2004. *Piezoelectric Static Trasnformers*. Techniques of engineers.

[6] W.Huang. 2003. *Design of a radial mode piezoelectric transformer for a charge pump electronic ballast with high power factor and zero voltages witching*. Doctoral thesis. University of Virginia.

[7] R.L. Lin. M.J. 2011. A Family of piezoelectric Transformer Based Bridgeless continuous conduction mode charge pump power factor correction electronic ballasts. IEEE Transactions of industry applications. Vol 47. NO. 3. DOI= 10.1109/TIA.2011.2126034.

[8] Y. Huang. Z. Miao. X. Chen. W. Huang. D 2012. A verification and parametric analysis of an analytical model of a flexural vibration mode piezoelectric transformer. IEEE Transactions of ultrasons, ferroelectrics and frequency control. Vol. 59. (12, December 2012). DOI= 10.1109.TUFFC.2012.2514.

[9] G.Farong .H. Hong ping.H.Yuantai. X.Caihua. 2007. *An analysis of a cylindrical thin shell As a piezoelectric transformer*. Acta Mechanica Solida Sinica, Vol. 20, No. 2, June, 2007. Published by AMSS Press, Wuhan, China. DOI= 10.1007/s10338-007-0719-8.

[10] T. Anderson. M.A.E. Anderson. O.C.Thomson. 2012. Simulation of piezoelectric transformers with COMSOL. In *Proceeding of the 2012 COMSOL conference In Milan*

[11] A. Chérif. 2012. *Optimization of the piezoelectric transformer. Application: semi-passive vibration control* Doctoral Thesis. University of Setif.

[12] Sinocera. Typical values of standard piezoelectric ceramic materials. On http://www.sinocera.net/en/piezo_material.asp.

Sterilization of polymers surface contaminated by Bacillus bacteria using atmospheric DBD plasma

L. Benterrouche[1], N. Kacem Chaouche[2], S. Sahli[1], S. Benhassine[2], M. T. Benabbas[1], A. Benhamouda[1]

[1] University Constantine 1, Laboratory of Microsystems and Instrumentation, Faculty of Technology Sciences, Route de Ain El Bey, 25017 Constantine, Algeria

[2] University Constantine 1, Laboratory of Mycology, Biotechnology and Microbial Activity, Constantine, Algeria

ABSTRACT

A dielectric barrier discharge (DBD) plasma generated in air at atmospheric pressure in a controlled chamber and using a low cost homemade pseudo-pulsed high voltage power supply was used to inactivate Bacillus bacteria. The bacteria were spread-out on the surface of low density Polyethylene films. Effects of plasma treatment time variations and plasma treatment modes on the germicidal effect (GE) of the created DBD plasma have been investigated. Furthermore, surface properties of the polymer pre-treated films have been characterized by water contact angle measurements. The GE of the created plasma was found strongly dependent on the investigated parameters. A decrease of about 4 decades of the survival bacteria was observed after 16 min of DBD plasma treatment. Moreover, it appears that the polymer surface wettability has a significant role in the bacterial cells distribution and adhesion on the polymer media and then on the germicidal effect of the created plasma. In the other hand, it has been shown that the contaminated substrates position in the reactor has an effect on the bacteria treatment efficiency. An optimum GE was obtained on polymer substrates pre-treated with DBD plasma in direct discharge mode.

Keywords

Dielectric barrier discharge, plasma, Polymer surface, Low Density Polyethylene (LDPE), Bacillus bacteria, sterilization.

1. INTRODUCTION

Dielectric Barrier Discharges (DBDs) at atmospheric pressure are commonly used in the last ten years in many biomedical applications [1]. Because of their ambient working conditions, great interests have been focused on the use of these type of cold plasmas for developing a new sterilization processes especially for heat sensitive polymer materials [2, 3]. Moreover, due to their safety use for both the operator and the medical sensitive devices, the plasma sterilization process has become an alternative promising technique to other conventional sterilization methods such as those using chemical agents, gamma ray irradiation, UV and thermal sterilization. Generated at room temperature and atmospheric pressure, many sorts of plasma reactive species, such as radicals, UV photons, atoms, electrons, positive and/or negative ions, can directly or indirectly interact with microorganisms and thus lead to the death of not only pathogenic bacteria, but also highly resistant microorganisms [4].

In this study, an atmospheric pressure DBD plasma in air, generated in a controlled chamber using a low cost homemade pseudo-pulsed high voltage power supply, was used to inactivate Bacillus bacteria spread-out on the surface of low density Polyethylene (LDPE) films. Effects of plasma treatment time, plasma treatment modes (substrates placed in direct discharge mode or in post-discharge mode) and the polymer surface wettability on the microorganisms' inactivation efficacy of the created DBD plasma have been investigated.

2. MATERIALS AND METHODS

2.1 Experimental Setup

The experimental set up used for the sterilization process consists of a DBD reactor constituted from two plane-parallel metallic electrodes with 80 mm diameter spaced by a gap varying from 1 to 5 mm (Figure 1).

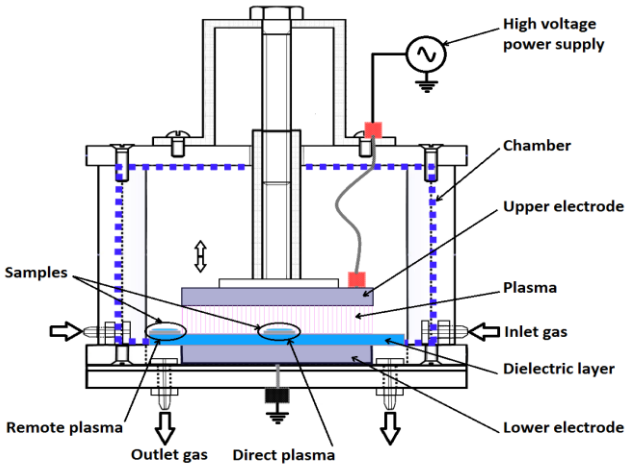

Figure. 1: Schematic illustration of the atmospheric Dielectric Barrier Discharge (DBD) reactor.

The lower electrode used as a substrate holder was grounded and covered with a glass plate of 1.3 mm of thickness and 110 mm of diameter. The upper electrode was connected to a pseudo-pulsed high voltage power supply to generate the DBD plasma in the atmospheric air gap. The DBD plasma device was installed in a homemade ambiance controlled chamber with the dimensions of 140 mm (width) x 140 mm (depth) x 100 mm (height) where air was used as a discharge gas.

2.2 Sample preparation

Bacillus Sp bacteria were cultured on a solid surface (agar) containing a nutrient culture medium, washed in saline, then their density was adjusted between 10^6 and 10^7 cells/ml. In this study, two types of media were used. In the first case, the bacteria were spread out on nutrient culture medium in Petri dishes and then exposed in direct mode to air DBD plasma for different treatment time to show the Bacillus bacteria inactivation kinetics. In the second case, bacteria were spread out on polymeric media; for this purpose, transparent low density polyethylene (LDPE) films of 50 µm of thickness were used. First, the films were cut into small square pieces of 20 x 20 mm^2 area, each one was washed successively in bleach, methanol and twice in distilled water and then dried naturally at room temperature. Some of these pieces films were then pretreated by a DBD plasma in atmospheric air. Next, 100 µl of Bacillus bacteria was transferred and spread out on the surface of both the only washed and the plasma pre-treated LDPE films, then dried at room temperature for 1 h. After that, the contaminated LDPE samples were exposed during different time to air DBD plasma in direct or indirect mode. In the direct plasma mode, the samples were placed on the lower electrode directly exposed to the plasma and in the indirect plasma mode, called also remote or post-discharge plasma mode, samples were placed outside the plasma discharge zone as shown in figure 1.

In order to count the surviving cells, the plasma treated films were washed in sterile saline solution to recover the survival bacteria, then they were diluted and a drop from this solution were transferred to a Petri dish contained nutritional agar and incubated at 37 °C for 48 h. Germicidal effect (GE) was calculated as follows [5]:

$$GE = \text{Log } N_0 - \text{Log } N_t$$

Where N_0 and N_t represent the number of colony forming units of control and sterilized samples, respectively.

During all the experiments, the applied high voltage, its frequency and the electrode discharge gap were fixed to 9 kV, 0.2 kHz and 5 mm respectively.

2.3 Contact angle measurements

To investigate the wettability effect of polymeric substrates on the inactivation efficacy, the contact angle technique was used. All the measurements were carried out at 20 °C and 57 % RH. A distilled water drop was delivered by a micro syringe onto the films surface immediately after plasma treatment experiments. To lessen the effect of gravity, the volume for each drop was regulated to 5 µl. The contact angles were measured at least five different locations on the treated samples and a maximum error less than ±2 ° has been recorded.

3. RESULTS AND DISCUSSIONS:

The GE of the created plasma was studied in the direct mode. It was found strongly dependent on the plasma treatment time; figure 2 reports the influence of this parameter on the inactivation of Bacillus bacteria. A decrease of about 4 decades of the survival bacteria is observed after 16 min of DBD plasma treatment. This behaviour of the Bacillus inactivation kinetic by different plasma systems is similar to that observed by other works [6, 7]. The necessary time to reduce the initial Bacillus bacteria population by 90% (called also: The decimal reduction time D-value) is approximately 1.15 min. Using a similar plasma system and parameters, Kostov et al. [8] have found on Staphylococcus aureus and Escherichia coli bacteria a slightly lower value of D and a complete sterilization was achieved in about 20 min. In our case, the Bacillus bacteria were completely removed from the surface substrate after only about 16 min of air plasma treatment.

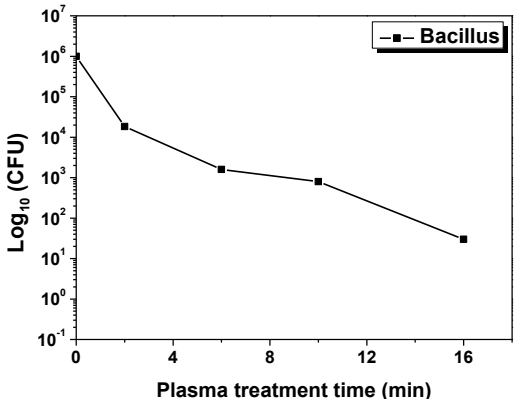

Figure. 2: Inactivation kinetics of the Bacillus bacteria using atmospheric pressure air DBD plasma.

The little difference between the D values found in our work and that found by Kostov et al. can be explained by the less resistant of Staphylococcus aureus and Escherichia coli bacteria compared to Bacillus bacteria [9].

In order to evaluate the sterilization efficacy of the air DBD plasma on polymeric materials, the GE was investigated as function of the plasma treatment time and the plasma treatment modes. Figure 3 shows that the GE is strongly depend on these parameters.

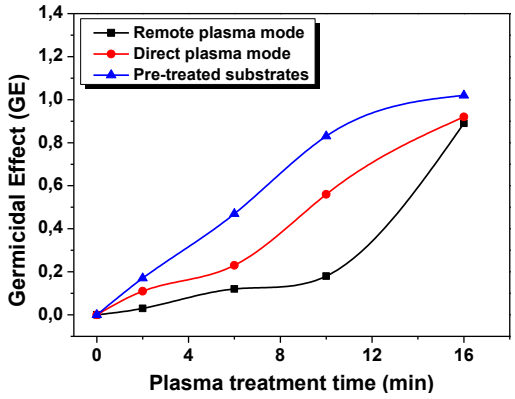

Figure. 3: Variations of the GE as a function of plasma treatment time using Direct and Remote plasma mode.

An increase of the plasma treatment time in the direct plasma mode induces an increase of the GE reaching a value of 0.92 after 16 min of plasma treatment. In this case, Bacillus bacteria were exposed directly to plasma reactive species (such as hydroxyl radicals (OH), ozone...), to UV radiation and to charged particles. This improve the consumption process of the bacterial cells by the plasma reactive species [10] and can lead to a sputtering effect of the bacterial structure by the charged and/or the energetic plasma species [11]. This increase of the GE with the increase of the plasma treatment time is less pronounced when the bacteria were exposed to a plasma in the remote mode. As it is shown on figure 3, until 10 min, the efficiency of this sterilization effect is not significant (about 0.1); however, it increases quickly beyond 10

min, reaching a value of 0.89 for a treatment time of 16 min. This behavior may be due to a less exposition of the polymer films to the charged and energetic plasma species (in the remote plasma mode, species are generally less energetic and less reactive) and to the UV radiations [12].

The GE induced by our DBD plasma on the Bacillus bacteria contaminated LDPE films is more pronounced when these substrates were first treated directly by atmospheric pressure air DBD plasma during 15 min and then the bacteria were spread out on it. The GE increases more rapidly with the increase of the plasma treatment time for these pre-treated substrates, reaching a value of 1.02 after 16 min of plasma treatment in direct plasma mode (Figure 3). This increase in the efficiency of the plasma sterilization may be due to the improvement of the LDPE films surface wettability by the DBD plasma pre-treatment process, leading to a more homogenous bacteria distribution on the polymer surface. The concentration of the bacteria directly exposed to the micro discharges is then more important than that on the untreated LDPE films. In this latter case (untreated LDPE films), because the hydrophobicity of the surface films, the bacteria are unevenly distributed on the surface, increasing then the probability of finding islands of bacteria layers on some places of the LDPE surface. In these places, the bacteria layers are thicker and therefore, take more time to be completely eliminated [13]. In order to confirm the wettability improvement of the LDPE films by air atmospheric pressure DBD plasma pretreatment, contact angle measurements were carried out on no contaminated LDPE films immediately after their exposition to DBD plasma treatments.

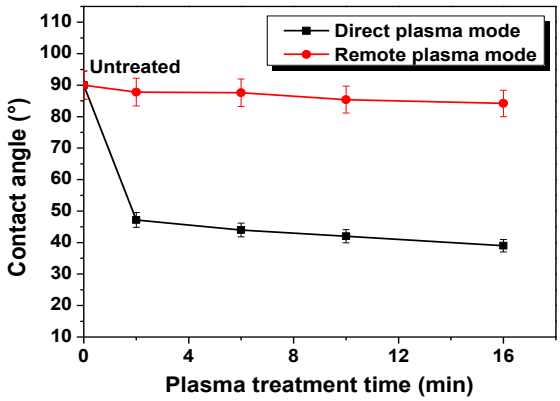

Figure. 4: Effect of plasma treatment time on the contact angle of the LDPE films using direct and remote plasma mode.

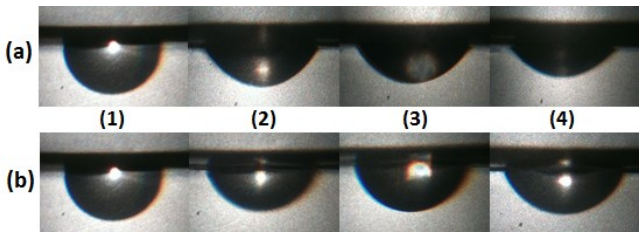

Figure. 5: Photographs of the water drops on the surface of LDPE films: (1) Untreated; (2) 6 min; (3) 10 min; (4) 16 min using:

(a) Direct plasma mode ; **(b)** Remote plasma mode.

As it is shown on figure 4, a strong dependence of the contact angle on the plasma treatment time in direct mode is observed. From about 90° measured on untreated LDPE surface films, the contact angle of plasma treated LDPE films decreased significantly with increasing the plasma treatment time, reaching a value of 39° for samples treated in the direct plasma mode during 16 min of DBD plasma treatment and 84° for those treated in the remote plasma mode, using the same discharge parameters. This behavior appears clearly on the photos of the water drops represented on figure 5. This decrease in the contact angle with the increase of the plasma treatment time may be due to the creation of polar groups such carbonyl (C = 0) [14] or hydroxyl (-OH) on the surface of plasma treated LDPE films. This polymer surface modification is improved by free radicals and charged species present with high concentrations in the case of direct plasma treatments. However, in the remote plasma, the LDPE surface modification is less pronounced because of a poor presence of charged particles and free radicals far from the DBD discharge [15].

4. ACKNOWLEDGMENTS

This work was supported by the Algerian Thematic Agency of Research in Sciences and Technology (ATRST ex ANDRU).

5. CONCLUSION

The sterilization of Bacillus Sp bacteria on the surface of low-density polyethylene (LDPE) films by DBD plasma at atmospheric pressure using air as a discharge gas and the surface modification properties of the treated films was investigated in this study. It has been revealed that the plasma treatment time, the plasma treatment mode (direct or indirect plasma mode) and the initial state (substrates pre-treated or not) have a strong effect on the sterilization efficiency. Results show a strong dependence of these parameters on the germicidal efficiency of the air DBD plasma.

6. REFERENCES

[1] Fridman, G., Friedman, G., Gutsol, A., Shekhter, A. B., Vasilets, V. N. and Fridman, A. 2008. Applied Plasma Medicine. *Plasma Process. Polym.* 5 (2008), 503–533.

[2] Heise, M., Neff, W., Franken, O., Muranyi, P. and Wunderlich, J. 2004. Sterilization of polymer foils with dielectric barrier discharges at atmospheric pressure. *Plasmas and Polymers* 9, 1 (March 2004), 23–33.

[3] Benterrouche, L., Sahli, S., Rebiai, S., Benhamouda, A. and Sebihi, F. Z. 2013. Inactivation of E. coli bacteria by atmospheric dielectric barrier discharge. *Int. J. Nanotech.*10, 5/6/7 (2013), 543–552.

[4] Philip, N., Saoudi, B., Crevier, M. C., Moisan, M., Barbeau, J. and Pelletier, J. 2002. The respective roles of UV photons and oxygen atoms in plasma sterilization at reduced gas pressure the case of N2–O2 mixtures. *IEEE Trans. on Plasma Science* 30, 4 (August 2002), 1429–1436.

[5] Sureshkumar, A., Sankar, R., Mandal, M. and Neogi, S. 2010. Effective bacterial inactivation using low temperature radio frequency plasma. *International journal of pharmaceutics* 396 (2010), 17–22.

[6] Deng, X., Shi, J. and Kong, M. G. 2006. Physical Mechanisms of Inactivation of Bacillus subtilis Spores Using

Cold Atmospheric Plasmas. *IEEE Trans. on Plasma Science* 34, 4 (August 2006), 1310–1316.

[7] Roth, S., Feichtinger, J. and Herte, C. 2010. Characterization of Bacillus subtilis spore inactivation in low-pressure, low-temperature gas plasma sterilization processes. *Journal of applied microbiology* 108 (2010), 521–531.

[8] Kostov, K. G., Rocha, V., Koga-Ito, C. Y., Matos, B. M., Algatti, M. A., Honda, R. Y., Kayama, M. E. and Mota, R. P. 2010. Bacterial sterilization by a dielectric barrier discharge (DBD) in air. *Surface and Coatings Technology* 204 (2010), 2954–2959.

[9] Sung, S. J., Huh, J. B., Yun, M. J., Chang, B. M. W., Jeong, C. M. and Jeon, Y. C. 2013. Sterilization effect of atmospheric pressure non-thermal air plasma on dental instruments. *J Adv Prosthodont* 5 (2013), 2-8.

[10] Laroussi, M. 2005. Low temperature plasma-based sterilization: Overview and state-of-the-art. *Plasma Process. Polym.* 2, 5 (2005), 391–400.

[11] Opretzka, J., Benedikt, J., Awakowicz, P., Wunderlich, J. and Von Keudell, A. 2007. The role of chemical sputtering during plasma sterilization of Bacillus atrophaeus. *Journal of Physics D: Applied Physics* 40, 9 (2007), 2826–2830.

[12] Miao, H. and Jierong, C. 2009. Inactivation of Escherichia coli and properties of medical poly(vinyl chloride) in remote-oxygen plasma. *Applied Surface Science* 255 (2009), 5690–5697.

[13] Miao, H. and Yun, G. 2011. The sterilization of Escherichia coli by dielectric-barrier discharge plasma at atmospheric pressure. *Applied Surface Science* 257 (2011), 7065–7070.

[14] Ziari, Z., Bellel, A., Sahli, S., Segui, Y. and Raynaud, P. 2008. A comparative study on the effect of VUV radiation in plasma SiOx-coated polyimide and polypropylene films. *Progress in Organic Coating* 61 (2008), 326-332.

[15] Xia Liu, H. and Rong Chen, J. 2008. Analysis of surface sterilization and properties of medical poly (tetrafluoroethylene) in remote argon plasma. *IEEE Trans. on Plasma Science* 36, 1 (February 2008), 230-236.

Spatial Resolved Measurements of the Local Efficiency in CIGS Thin-Film Based Solar Cell

M. Haggui [1], B. Reinhold [2], P. Andrä [1,2], M. Schmid [2], P. Fumagalli [1]
[1]Freie Universität Berlin, Institut für Experimentalphysik, Berlin 14195, Germany.
[2]Helmholtz-Zentrum Berlin für Materialien und Energie, Berlin 14109, Germany.

ABSTRACT

We report the application of Scanning Near field optical Microscopy (SNOM) to the mapping of the photocurrent produced by $Cu(In,Ga)Se_2$ solar cells under local monochromatic illumination. We demonstrate the influence of the presence of inhomogeneities on the top surface of the sample on the local current generation.

Keywords

SNOM, Photovoltaic, CIGS thin-film Solar Cell, Photocurrent.

1. INTRODUCTION

$Cu(In,Ga)Se_2$ (CIGS) based Solar Cells are well known as one of the highest efficient solar devices. The highest efficiency for CIGS solar cells, according to the National Renewable Energy Laboratory (USA), is 20.8%. Nevertheless, Scientific literature shows that there are still many basic questions in CIGS research intensely debated such as grain boundaries [1], and the presence of defects [2]. Exploiting these questions could increase the efficiency and reduce the production costs.

A large variety of experimental techniques have been used in order to characterize photovoltaic devices such as Transmission Electron Microscopy (TEM) [3], Atomic Force Microscopy (AFM) [3], Scanning Transmission X-ray Microscopy [4], near-field cathodoluminescence [5] and Scanning Near-field Optical Microscopy (SNOM) [6]. SNOM is a powerful technique that scans a tapered optical fiber across the sample, illuminating only that area of the sample that lies directly under the tip aperture (~200nm). Kept within few nanometers of the surface, the tip illuminates the sample in the near field allowing the collection of optical information, better than the diffraction limit of the operating light, of the surface of the sample. Topographic information are equally obtained. In addition, this technique could be used in order to perform spatial resolved photocurrent measurements on solar cell samples [7].

2. EXPERIMENT

A home-made Aperture-SNOM was used for this experiment. A monochromatic modulated light (λ=532nm) is injected into an optical fiber, which is shaped at the other extremity to form a tip. The tip is coated with aluminum leaving only a nanometric aperture at the end playing the role of a local nanosource of light and hardly glued on a tuning-fork. Tips with aperture of 200nm were used. The local photocurrent generated by the sample when illuminated through the tip aperture is detected with a Lock-in Amplifier and transmitted to the computer, which allows the analogue current signal to be converted to digital signal that can be stored. The topographic information are measured with a second Lock-in by detecting the shear-forces, resulting from the interaction between the tip and the sample surface, via a tuning-fork feedback system.

The studied sample is a typical Copper Indium Galium Selenide solar cell. It is a module cell constituted of a back electrode made of Molybdenum (800nm) deposited on a glass substrate. On top of it, is deposited a Cu(In,Ga)Se2 layer (1.5-2μm), then a thin film of Cadmium Sulfide (20-50nm) and finally the top electrode which is a Zinc Oxide Aluminium doped layer (~800nm).

3. RESULTS

Using our setup, topographic and photocurrent images are obtained. The figure 1 displays two maps: the first one (Figure 1a) represents the topography measured with the SNOM tip. This picture shows clearly that the Zinc Oxide top layer is not homogeneous and that is constituted of grains of different size varying from few tenths of nanometers to many hundreds of nanometers. The second one shows the distribution of the local photocurrent generated by this region of the sample under local illumintation through the tip aperture. The usage of 200 nm aperture tips shows that the big “islands” contribute significantly less to the overall produced current than the surrounding regions. The photocurrent map shows that the produced photocurrent in such regions is three to four times smaller than the current produced in other regions (Figure 1b).

In the opposite, regions presenting small aggregates show more uniform current on the length scale of few hundreds of nanometers. This demonstrates that the local efficiency of the solar cell depends on the morphology of the top electrode surface also.

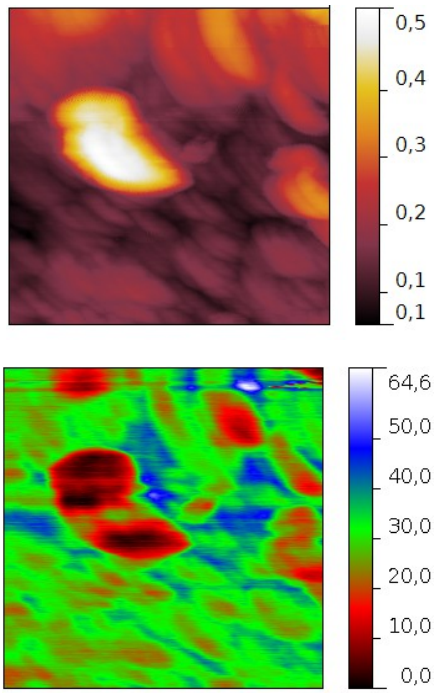

Figure 1. Topographic (top) and Photocurrent (bottom) images of a CIGS photovoltaic device. Large regions (bright on the topographic image) correspond to big aggregates producing lower current (red-dark on the current map) and smaller aggregates producing much higher current. The scale bar is 10X10μm^2. The color scale is expressed in *μm* (top) and in *nA* (bottom).

This variation of local efficiency of the photodiode to producing photocurrent could have several reasons. Among them, a local variation of the transmission of the top electrode could lead to this photocurrent change. To reach the buried p-n junction, the light coming from the aperture will travel more distance through the large grains than through the small ones and could be diffract somewhat before reaching it. Thus, the parts of the p-n junction that are lying under large grains would receive less light and then produce less current. In the other hand, the regions that are covered by small grains produce much higher current because they will absorb more light.

Another hypothesis is a changing of local physical properties of the Zinc Oxide doped Aluminum layer. For example, a variation of the local conductivity could be another reason for the observed behavior of the local photocurrent generated by the photovoltaic device. A deep investigation of such hypothesis would be a helpful for understanding the obtained results.

4. CONCLUSIONS

We performed a Scanning Near field Photocurrent Measurement on a Cu(In,Ga)Se_2 solar cell. We studied the effect of the morphology of the top electrode on the local efficiency of the solar cell to produce photocurrent. We found that the efficiency depends on the size of the grains constituting the Zinc Oxide top layer. The regions containing grains of large size contribute significantly less than the regions of small grains.

This study could be of interest for better understanding the local properties of photovoltaic devices based on CIGS thin films.

5. ACKNOWLEDGMENTS

This work was supported by the Helmholtz-Energie Allianz, Hybrid Photovoltaic Project.

6. REFERENCES

[1] Rau, U., Taretto, K., Siebentritt, S. (2009) Grain boundaries in Cu(In,Ga)(Se,S)$_2$ thin-film solar cells. *Applied Physics A,* 96, 221–234.

[2] Igalson, M., Urbaniak, A., Edoff, M. (2009) Reinterpretation of defect levels derived from capacitance spectroscopy of CIGSe solar cells. *Thin Solid Films,* 517, 2153–2157.

[3] Hoppe, H.; Glatzel, T.; Niggemann, M.; Schwinger, W.; Schaeffler, F.; Hinsch, A.; Lux-Steiner, M. C.; Sariciftci, N. S. (2006) Efficiency limiting morphological factors of MDMO-PPV:PCBM plastic solar cells. *Thin Solid Films*, 511, 587-592.

[4] McNeill, C. R.; Watts, B.; Thomsen, L.; Belcher, W. J.; Kilcoyne, A. L. D.; Greenham, N. C.; Dastoor, P. C.(2006) X-ray Spectromicroscopy of Polymer/Fullerene Composites: Quantitative Chemical Mapping. *Small*, 2, 1432-1435.

[5] Yoon, H. P.; Lee, Y.; Bohn, C. D.; Ko, S. H.; Gianfrancesco, A. G.; Steckel, J. S.; Coe-Sullivan, S.; Talin, A. A.; Zhitenev, N. B. (2013) High-resolution photocurrent microscopy using near-field cathodoluminescence of quantum dots. *AIP Advances*, 3, 062112.

[6] Hecht, B.; Sick, B.; Wild, U. P.; Deckert, V.; Zenobi, R.; Martin, O. J. F.; Pohl, D. W. (2000) Scanning near-field optical microscopy with aperture probes: Fundamentals and applications. *J. Chem. Phys*., 112, 7761-.

[7] Feron, K., Nagle, T.-J., Rozanski, L.-J.,Gong, B.-B., Fell, C.-J. (2013) Spatially resolved photocurrent measurements of organic solar cells: Tracking water ingress at edges and pinholes, *Solar Energy Materials & Solar Cells*, 109, 169–177.

Electrical Porous Silicon Sensor for Detection of Various Organic Molecules

Farid A. Harraz[1,2*], Adel A Ismail[1,2], Huocine Bozid[1,4,5], S. A. Al-Sayari[1,3], A. Al-Hajry[1,4]

[1] Promising Centre for Sensors and Electronic Devices (PCSED), Advanced Materials and Nano-Research Centre, Najran University, P.O. Box: 1988, Najran 11001, Saudi Arabia
[2] Nanostructured Materials and Nanotechnology Division, Central Metallurgical Research and Development Institute (CMRDI), P.O. Box: 87 Helwan, Cairo 11421, Egypt
[3] College of Science and Arts-Sharoura, Najran University, Saudi Arabia
[4] Department of Physics, College of Science and Arts, Najran University, Saudi Arabia
[5] Laboratoire des Matériaux Ferroélectriques, Faculté des Sciences de Sfax, Route Soukra Km 3,5, B.P.802, F-3018 Sfax, Tunisia

[*]E-mail: fharraz68@yahoo.com

ABSTRACT

Electrical sensor based on porous silicon (PSi) layers for detection of various organic molecules is demonstrated. PSi layers with a thickness of ~4.5 µm and pore sizes in the range of 30 nm were initially synthesized by the electrochemical anodization of silicon wafer in hydrofluoric acid based-solution. For a proper sensor operation, the surface of PSi was passivated via electrochemical oxidation process. The as-fabricated electrical sensors exhibit a sensitive and reversible conductance response upon exposure to polar solvents (ethanol, methanol, acetone and acetonitrile), whereas the sensing behavior towards non-polar molecules (*n*-hexane and toluene) was irreversible. Conductance was found to increase in case of polar solvents; however a conductance decrease was detected in case of non-polar molecules. A comparative study between sensing behavior is discussed in terms of the change in dielectric constant of porous layer upon solvents infiltration, together with the effect of dipole moment and a redistribution of surface charge. The sensor could be re-used efficiently for ten cyclic tests for acetone, indicating excellent repeatability of the device.

Keywords

Porous silicon; Electrical sensor; Organic molecules.

1. INTRODUCTION

Porous silicon (PSi) is an ideal material for sensing applications [1], principally due to ease of fabrication [2,3], large internal surface area and surface reactivity [4,5], wide range of accessible and adjustable pore sizes [6,7] and compatibility with existing silicon technologies [8,9]. The sensing principle using PSi layer is based primarily on monitoring the variation in electrical and/or optical properties upon infiltration of target molecules into the porous matrix. In contrast to electrical properties, the changes in optical characteristics of PSi have been extensively employed, probably due to the faster response time and more safety of implementation, especially for sensing flammable gases and vapors.

Some arising challenges still exist for electrical PSi-based sensors including the fabrication of efficient ohmic contacts, surface stabilization and enhancement of sensor recyclability. In addition, the sensing via conductance measurement has not been studied previously in details. In the present work, electrical sensor based on electrochemically fabricated PSi is designed to detect various polar and non-polar target molecules. The electrical contacts were created directly onto the front surface. A comparative study of sensing behavior between polar and non-polar molecules is provided.

2. RESULTS AND DISCUSSIONS

Figure.1 shows top and cross-sectional views of FE-SEM images of as-synthesized PSi layer with 30 nm pore size and 4.5 µm pore thickness.

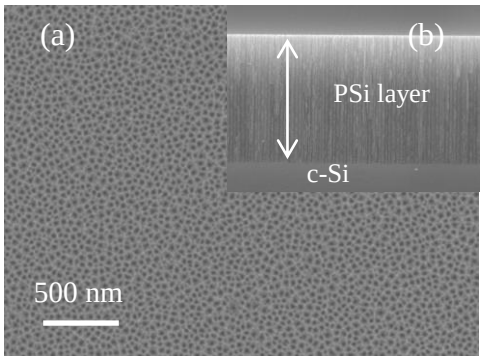

Figure. 1 FE-SEM images of PSi; (a) top and (b) cross-sectional view as an inset.

The as-formed PSi sample was electrochemically oxidized to form a thin oxide layer which is necessary for a better device performance. FTIR and XPS (not shown here) were measured to confirm the formation of surface oxide.

Figure 2 shows the real time conductance response of the sensor towards polar organic molecules. In all cases, the response is reversible with a remarkable conductance increase. Due to the different vapor pressure of examined solvents, the order of

response time was; acetone < methanol < acetonitrile < ethanol. The conductance shift is likely related to the change in dielectric constant after the solvent infiltration into the pores.

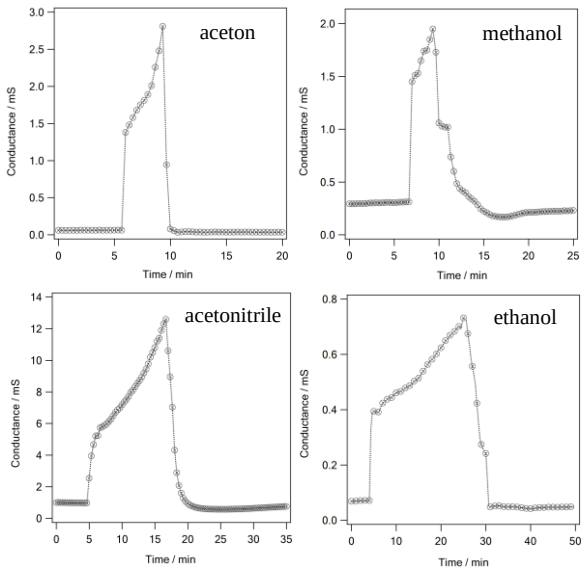

Figure. 2 Conductance response for PSi sensor upon exposure to various organic molecules

The sensing response towards non-polar solvents (*n*-hexane and toluene) was found to be completely different than polar molecules. A conductance decrease was observed with irreversible behavior. The finding can be related to the effect of very small values of dielectric constant as well as the small dipole moment of non-polar solvents.

Figure 3 shows the direct conductance measurement for PSi device during ten consecutive exposures to acetone. During exposure to acetone, the conductance is rapidly increased and remained higher than the baseline, before returning to its original value after solvent evaporation. This experimental result ensures excellent re-use and cycling behavior of the present sensor. The sensitivity remained sufficiently high during ten cyclic tests. We believe that these data will be useful in the development of chemical sensors based on PSi layers or modified PSi surfaces.

3. ACKNOWLEDGMENTS

Authors would like to acknowledge the support of the Ministry of Higher Education, Kingdom of Saudi Arabia for this research through a grant (PCSED-019-12) under the Promising Centre for Sensors and Electronic Devices (PCSED) at Najran University, Kingdom of Saudi Arabia.

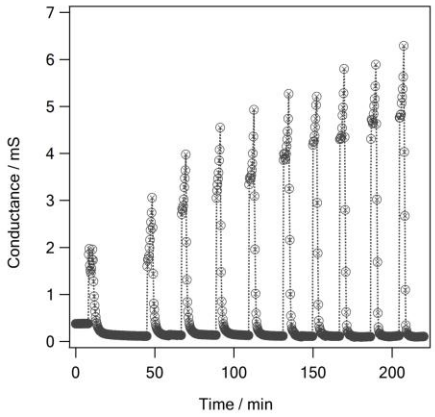

Figure. 3 Durability for repeated use of porous silicon sensor, showing the device stability after ten cyclic tests of acetone.

4. REFERENCES

[1] Ouyang, H., Christophersen, M., Viard, R., Miller, B.L. and Fauchet, P.M. (2005) 'Macroporous silicon microcavities for macromolecule detection', *Adv. Funct. Mater.*, Vol. 15, pp.1851-1859.

[2] Fukami, K., Harraz, F.A., Yamauchi, T., Sakka, T. and Ogata, Y.H. (2008) 'Fine-tuning in size and surface morphology of rod-shaped polypyrrole using porous silicon as template', *Electrochem. Commu.*, Vol. 10, pp.56-60.

[3] Ogata, Y.H., Koyama, A., Harraz, F.A., Salem, M.S. and Sakka, T. (2007) 'Electrochemical formation of porous silicon with medium-sized pores', *Electrochemistry*, Vol. 75, No. 3, pp. 270-272.

[4] Harraz, F.A., Salem, A.M., Mohamed, B.A., Kandil, A. and Ibrahim, I.A. (2013) 'Electrochemically deposited cobalt/platinum (Co/Pt) film into porous silicon: Structural investigation and magnetic properties', *Appl. Surf. Sci.*, Vol. 264, pp.391-398.

[5] Harraz, F.A., Salem, M.S., Sakka, T. and Ogata, Y.H. (2008) 'Hybrid nanostructure of polypyrrole and porous silicon prepared by galvanostatic technique', *Electrochim. Acta*, Vol. 53, pp.3734-3740.

[6] Harraz, F.A., El-Sheikh, S.M., Sakka, T. and Ogata, Y.H. (2008) 'Cylindrical pore arrays in silicon with intermediate nano-sizes: A template for nanofabrication and multilayer applications', *Electrochim. Acta*, Vol. 53, pp.6444-6451.

[7] Ogata, Y.H, Sasano, J., Jorne, J., Tsuboi, T., Harraz, F.A. and Sakka, T. (2000) 'Immersion plating of copper on porous silicon in various solutions', *Phys. Stat. Sol. (A)*, Vol. 182, pp.71-77.

[8] Buriak, J.M. (2002) 'Organometallic chemistry on silicon and germanium surfaces', *Chem. Rev.*, Vol. 102, No. 5, pp.1271-1308.

[9] Sasano, J., Schmuki, P., Sakka, T. and Ogata, T. (2005) 'Maskless patterning of various kinds of metals onto porous silicon', *Phys. Stat. Sol. (A)*, Vol. 202, No. 8, pp.1571-1575.

Resonant Tunneling Transport in $Al_{0.5}Ga_{0.5}N/ In_xGa_{1-x}N/Al_{0.5}G_{0.5}N/In_{0.1}Ga_{0.9}N$ quantum structures

[1]A. Rached[*], [1]A. Bhouri, [1]H. Belmabrouk and [2]J.-L. Lazzari

[1] Laboratoire d'Electronique et Microélectronique, Faculté des Sciences de Monastir, 5019 Monastir, Tunisia.

[2] Centre Interdisciplinaire de Nanoscience de Marseille (CINaM), UMR 7325 CNRS – Aix-Marseille Université, Case 913, Campus de Luminy, 13288 Marseille cedex 9, France.

ABSTRACT

In this work we present calculations of vertical transport in $Al_{0.5}Ga_{0.5}N/In_xGa_{1-x}N/Al_{0.5}Ga_{0.5}N/In_{0.1}Ga_{0.9}N$ quantum structures in the ballistic regime. Using the transfer matrix formalism we investigate the effect of the conduction band discontinuities and internal field on the transmission coefficient and the current-voltage characteristics by varying indium contents in the central quantum well. We demonstrate that an optimal design in terms of thicknesses, doping and compositions of these resonant tunneling diodes may allows a peak-to-valley ratio as high as 564 @1.3-1.6Volts.

Keywords

Nitride materials, Piezoelectricity, Quantum wells, Self Consistent calculations, Resonant Tunneling Diodes, Negative Differential Resistance, Peak to Valley Ratio.

1. INTRODUCTION

In the last decade, GaN/Al(In,Ga)N heterostructures have received considerable attention in the nanoelectronics and nanophotonics research communities. Owing to their outstanding properties, III-nitrides are excellent candidates for instance the fabrication of high temperature THz quantum cascade lasers [1-5]. All these key applications require the study of vertical transport using basically the double-barrier (DB) Resonant Tunneling Diode (RTD), which displays a Negative Differential Resistance (NDR). The large NDR observed at Room Temperature in Al(Ga)N/GaN diodes has been interpreted as related to resonant tunneling but found to be sensitive to the internal electric field present in wurtzite III-nitride compounds and to the depleted space charge GaN region on one side contact of the RTD structure (piezoelectric effect).

2. DESCRIPTION OF THE MODEL:

In this work, we investigate the vertical electron transport at room temperature in the pseudomorphic $Al_{0.5}G_{0.5}N/In_xGa_{1-x}N/Al_{0.5}G_{0.5}N/In_{0.1}Ga_{0.9}N/GaN$ quantum stack that is designed with a 6nm thick lateral $In_{0.1}Ga_{0.9}N/GaN$ n-type contact corrected spacer. First, the conduction-band profile at the Γ point along the growth direction is performed using a Schrödinger-Poisson solver with periodic boundary conditions far outside the active region.

3. RESULTS and discussions:

Using the transfer matrix formalism [4], the transmission coefficient T(E) and the current density J(V) are then computed for different indium composition in the $In_xGa_{1-x}N$ central well in order to optimize the resonant current peak-to-valley-ratio (PVR). Results are shown in Figure 1. The inset of figure 1(a) displays the heterostructure conduction band profiles investigated for different indium composition. It is worth noting that the internal field breaks the symmetry of the potential profile and unlike

depletion regions are formed on the two sides of the contact region. The transmission coefficient presented in Fig.1 (a) shows different peaks where the first resonant peak series is attributed to the resonant tunneling through the fundamental quasi-bound state in the QW, while the second series is due to the tunneling through the excited quasi-bound state or a continuum state near the DB edge. As one can note, when increasing In composition $(0.05 \leq x \leq 0.15)$ in the central well, the resonant peaks are shifted towards low energies and their transmission values decrease.

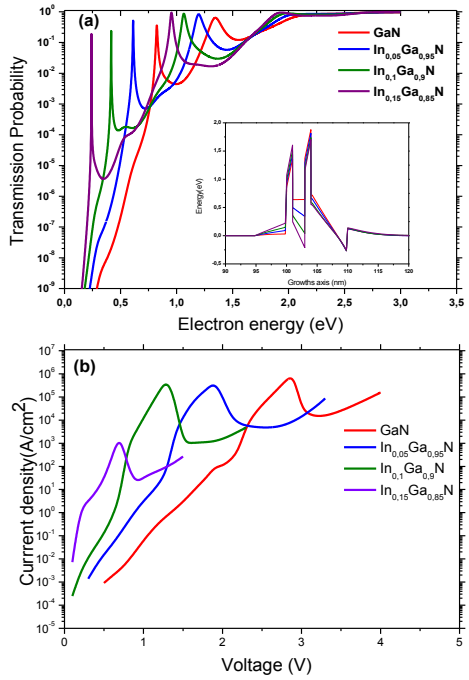

Figure. 1: (a) Transmission probability vs. longitudinal electron energy and (b) Theoretical current density vs applied voltage characteristics for different In compositions in the $n^{+}(5.10^{18}$ $cm^{-3})$–GaN/5nm undoped GaN/1nm undoped $Al_{0.5}G_{0.5}N$/2nm undoped $In_xGa_{1-x}N$/1nm undoped $Al_{0.5}G_{0.5}N$ /n^{+} $(5.10^{18}$ $cm^{-3})$6nm $In_{0.1}Ga_{0.9}N/n^{+}$ $(5.10^{18}$ $cm^{-3})$GaN quantum. The inset of fig(a) plots the corresponding conduction band diagrams.

As shown in fig1(b), for all In compositions, theoretical current-voltage characteristics reveal the presence of a sharp NDR due to the resonant tunneling between the Fermi level (E_F) and the quantum confined levels. Furthermore, the current peak (fig1(b)), progressively shifts to lower voltages with increasing In content. The PVR is also strongly affected by x and increases with In composition from 62 for $x = 0.05$ to 564 for $x = 0.1$. In fact, when In composition increases, the QW is pushed down near the conduction band edges in the contact layers, and the right contact depletion region reduces meanwhile the left one becomes larger. Hence, the applied bias is red-shifted and the value of the valley current is strongly reduced which enhances the PVR. We point out that the current peak value is also reduced when increasing x but in a less extend due to its resonant nature. The results are listed in Table I.

In (%)	Current density (A/cm^2)		Tension (V)		PVR
	Peak	Valley	Peak	Valley	
0	$9{,}04\times10^{5}$	$1{,}46\times10^{4}$	2,90	3,20	62.00
5	$4{,}30\times10^{5}$	$4{,}80\times10^{3}$	1,90	2,60	90.00
10	$5{,}72\times10^{5}$	$1{,}01\times10^{3}$	1,30	1,60	564.00
15	$2{,}57\times10^{3}$	19,56	0,70	0,90	131,40

Table I: Values of the current density and tension for peak and valley and their corresponding PVR with different In concentration in the central quantum well.

In conclusion, we demonstrate that an appropriate choice of a 10% In composition in the central well and a 6nm thick lateral $In_{0.1}Ga_{0.9}N$/GaN n-type contact corrected spacer achieves a peak current density of 5.72×10^{5} A/cm^2 and a pronounced 564 PVR value which arises from the large decrease in the valley current. This makes this RTD design very interesting for power devices.

3. REFERENCES

[1] E. Bellotti, K. Driscoll, T.D. Moustakas, and R. Paiella, Appl. Phys. Lett 92, 101112 (2008).

[2] H. Machhadani, Y. Kotsar, S. Sakr, M. Tchernycheva, R. Colombelli, J. Mangeney, E. Bellet-Amalric, E Sarigiannidou, E. Monroy, and F.H. Julien, Appl. Phys. Lett. 97, 191101 (2010).

[3] S. Sakr, E. Warde, M. Tchernycheva, L. Rigutti, N. Isac, and F. H. Julien, Appl. Phys. Lett 92, 142103 (2011) .

[4] S. Sakr, E. Warde, M. Tchernycheva, and F. H. Julien, J. Appl. Phys. 109, 023717 (2011).

[5] C. Bayram, Z. Vashaie, and M. Razeghi, Appl. Phys. Lett. 97, 181109 (2010)

Fractal Morphology of $LiFePO_4$ Particles for Use as Cathode in LIB

Z. Cabán-Huertas[1], O. Ayyad[1]*, P. Gómez-Romero[1]*
[1]Catalan Institute of Nanoscience and Nanotechnology, ICN2(CSIC-ICN) Campus UAB, ICN2 Building 08193 Bellaterra, Barcelona, Spain
*omar.d.h@gmail.com, *pedro.gomez@cin2.es

ABSTRACT
During the last few months our efforts were directed to develop a synthesis method for $LiFePO_4$ capable of generating a new morphology and a nanostructure. We study the effect of the morphology on the electrochemical properties of this material. An optimal microstructure of micron-sized particles formed by self-assembled nanoparticles was prepared. This fractal granularity material was coated with carbon to improve the behavior of the inorganic phase as a synergic hybrid material.

Keywords
Lithium Ion Batteries, Lithium Iron Phosphate, X-Ray Diffraction, Scanning Electron Microscope, Transmition Electron Microscopy, Thermal Analysis.

INTRODUCTION
$LiFePO_4$ is a material of great interest for lithium ion batteries[1], it is considered as the most promising cathode materials, especially for its great potential for the next-generation large-scale lithium ion batteries to be applied in electric vehicles and/or hybrid electric vehicles. $LiFePO_4$ has high theoretical capacity (170 $mAhg^{-1}$), high safety, environmental benignity, low cost, and high temperature stability owing to the highly covalent bonding between oxygen and phosphorus. $LiFePO_4$ undergoes a two-phase reaction ($LiFePO_4$ /$FePO_4$) at a constant voltage of about 3.45 V vs. Li (metal). $LiFePO_4$ offers technological advantages over commercial $LiCoO_2$ and other metal oxide cathode systems because of its tolerance to overcharge and over discharge [2]. One of the main drawbacks of $LiFePO_4$ is its poor electronic conductivity, so conductive surface coating on the $LiFePO_4$ is required to increase the electronic conductivity of the material. Coating with metals such as Ag, conductive polymers and carbon has been applied until now. Carbon coating approach reasonable one, because carbon is of low cost, exhibits high conductivity with low concentrations, is simple to be introduced in-situ or ex-situ, and is highly chemically stable in a battery. In general, $LiFePO_4$ is synthesized by a solid-state reaction or soft chemistry method (solution chemistry approach) such as hydrothermal synthesis. $LiFePO_4$ offers technological advantages it is important to improve the cycling characteristics of $LiFePO_4$, to allow it to gain wide acceptance in the lithium ion battery market.

EXPERIMENTAL
$LiFePO_4$ microspheres were synthesized by a one-step low-temperature hydrothermal reaction as described below. The precursor solution was divided into two fractions. In the first fraction, 5 wt.% polyimine aqueous solution of FeSO4.7H2O and H_3PO_4 was prepared. The second fraction of EG solution of $CH_3COOLi.2H_2O$ was prepared simultaneously, and slowly added to the first fraction under vigorous mechanical stirring for 10 min. Molar ratio of Li:Fe:P was 3:1:1. The obtained homogeneous, green-whitish colloidal solution was placed in a glass inlet of a Teflon lined autoclave which was then sealed and heated up in an oven to 200 ºC under autogeneous pressure for 24 hours. Precipitation of $LiFePO_4$ microspheres took place inside the autoclave during hydrothermal process, and the reactor was allowed to cool down to room temperature. The supernatant was carefully decanted; the collected greenish precipitate was washed thoroughly with water and ethanol, and dried under vacuum at 80 ºC overnight. The obtained $LiFePO_4$ powders were dispersed in the D-glucose (20 wt.%) water solution with magnetic stirring. After water evaporation, the $LiFePO_4$/glucose mixture was heated at 700 ºC for 9 hours in N_2 atmosphere to prepare the carbon-coated $LiFePO_4$ nanoparticles. No surfactants or other growth-directing agents were used during the synthesis. The final pristine LiFePO4 microsphere powders were very fine and greenish, while the final $LiFePO_4$/C composites were black in color. Structure and morphology of the prepared $LiFePO_4$ materials was characterized using a combination of X-ray diffraction, SEM and TEM microscopy. Electrochemical test cells (Swagelok-type) were assembled in an argon-filled glove box with the coated Al disk as working electrode, lithium metal foil as the counter/reference electrode, and 1 M solution of $LiPF_6$ in a 1:1 vol/vol mixture of ethylene carbonate and diethyl carbonate as the electrolyte. Glass microfiber filter paper was used as separator. For Electrochemical battery test, the batteries were charged and discharged galvanostatically in the fixed voltage window between 2.5 V to 4 V at room temperature (charge and discharge rate respectively the same). The formula of the prepared electrode was composed of 80% $LiFePO_4$/C composites, 15% carbon black and 5% binder.

RESULTS and discussions:
Figure 1 presents the X-ray diffraction pattern of LFP@200: $LiFePO_4$ sample, synthesized by hydrothermal process, at 200 ºC before heat treatment (Red Line); and LFP@700C: $LiFePO_4$ sample prepared at 200 ºC and then followed by heat treatment in presence of glucose under N_2 atmosphere at 700 ºC for 9 hours (Black Line). All the peaks can be indexed to orthorhombic olivine $LiFePO_4$ with space group (Pnma) (JCPDS card No.01-083-2092) without any detectable impurities such as $Fe_2P_2O_7$, Fe_2O_3 or Li_3PO_4. There is no obvious carbon diffraction peaks due to the small amount of amorphous carbon present in $LiFePO_4$/C composite. It is worth mentioning that, even at low temperatures (200ºC), the pristine $LiFePO_4$ material X-ray diffraction (XRD) analysis reveals well crystalline single phase $LiFePO_4$ without detectable impurity phases (all peaks could be indexed according to ICDD card No. 01-083-2092).

SEM images of pristine $LiFePO_4$ and $LiFePO_4$/C powder are shown in Figure 2A and 2B, respectively. The $LiFePO_4$ material has sphere-like morphology of ca. 5-10 μm with fractal granularity composed of microsized secondary particles built-up of nanosized primary particles (Figure 2 inset).This morphology is expected to provide interconnected porous structure that could reduce the lithium ions diffusion path, contact resistance between $LiFePO_4$ particles and could favour the electrolyte impregnation.

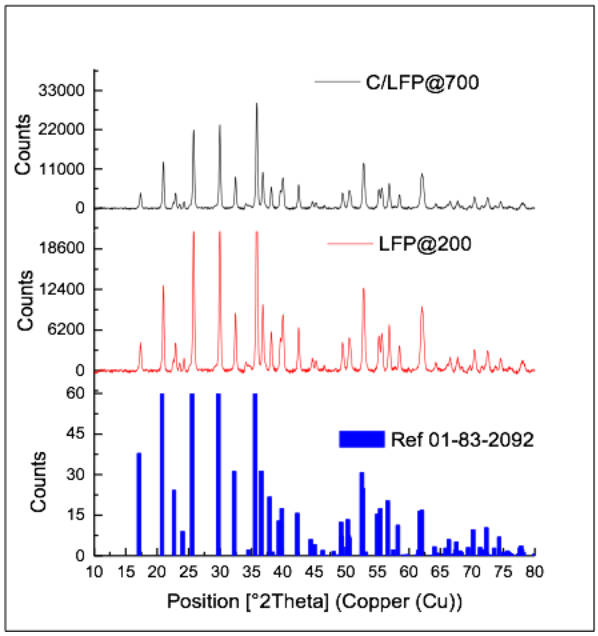

Figure 1. X-ray diffraction

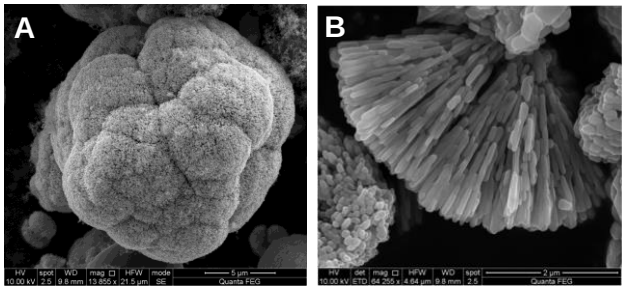

Figure 2. SEM images of A) as-prepared $LiFePO_4$ microspheres (LFP@200); B) $LiFePO_4$/C microspheres after sintering at 700ºC/9 hours in N_2 atmosphere (LFP@700C).

As seen in Transmission electron microscopy (TEM) (Figure 3A), the $LiFePO_4$ nanoparticles that assemble to form the microspheres have a diameter of around 40 nm and a length of around 120 nm, which is also confirmed by SEM images (Figure 2C). Figure 3A confirm the presence of carbon in the final $LiFePO_4$ material. As can be shown in Figure 3B, the $LiFePO_4$ particle is coated with an amorphous carbon layer of 2-3 nm thickness, which suppresses aggregation and at the same time it is thin enough not to block Li transport. All carbon coated single crystalline $LiFePO_4$ nanoparticles are loosely connected with each other to form a three-dimensional microspheres network (Figure 2B).

Fig. 4 shows TGA curves of pristine $LiFePO_4$ and C/$LiFePO_4$ composite, respectively. TGA experiments were performed under flowing air atmosphere. Water was removed in the temperature range 0-200 ºC with no significant structural rearrangement for both samples. These experiments were carried out primarily to determine the exact amount of carbon coated on the olivine from our process. The TGA curves (Fig. 4) show a weight gain of 4.03% for the $LiFePO_4$ and 2.33% for the C-$LiFePO_4$ between 250-700 ºC. The difference in the weight uptake of prisitine $LiFePO_4$ material could be explained by the following oxidation reaction[3]:

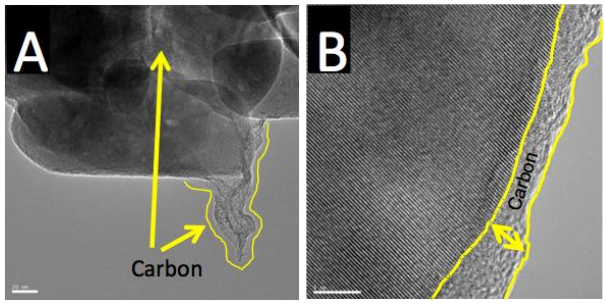

Figure 3. A) Overview TEM micrograph showing $LiFePO_4$/C nanoparticles with a diameter of around 40 nm and a length of around 120 nm. Non-uniform carbon coating on the surface of $LiFePO_4$ is shown; B) HRTEM image of carbon coated $LiFePO_4$ nanoparticle synthesized hydrothermally and further annealed under nitrogen flow at 700ºC (LFP@700C).

$$LiFe^{II}PO_4 + 1/4\,O_2 \uparrow \rightarrow 1/3Li_3Fe_2^{III}(PO_4)_3 + 1/6Fe_2^{III}O_3$$

Finally, % carbon is equal to total weight gain of LiFePO4 minus total weight gain of C-$LiFePO_4$. Using this approach the amount of carbon in our sample with carbon is 1.73%.

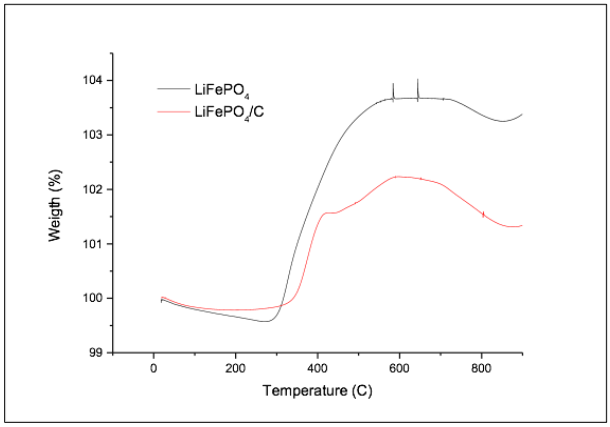

Figure 4. TGA curves of the pristine $LiFePO_4$ and $LiFePO_4$/C.

The 3-D network structure of $LiFePO_4$ results in a good discharge capacities and rate performance, e.g., 159 (0.1 C), 127 (0.25 C), 113 (0.5 C), 99 (1 C), 86.5 (2 C) and 72.5 mAh/g (5 C) at room temperature (charge and discharge profiles as shown in Figure 5). Note that the capacity at 0.1 C (159 mAh/g) is close to the theoretical one of 170 mAh/g (93.5% of the theoretical capacity). As shown in Figure 6, LFP@700C shows excellent cycling stability, after 100 cycles at 1C rate, that could be attributed to the single-crystalline properties of the LFP@700C particles, as ordered atom arrangement in single-crystalline nanoparticles enables fast and reverse Li+ ion intercalation/deintercalation. A capacity as high as 110 mAh/g can be obtained after 100 cycles at 1C discharge rate (65 % of the theoretical capacity). Figure 7 shows that the final discharge capacity at 1C discharge rate is slightly increased in comparison with the initial discharge capacity at 1C discharge rate (99 mAh/g) due to improved kinetics. Figure 8 shows the rate performance of LFP@700C microsphere cathode material.

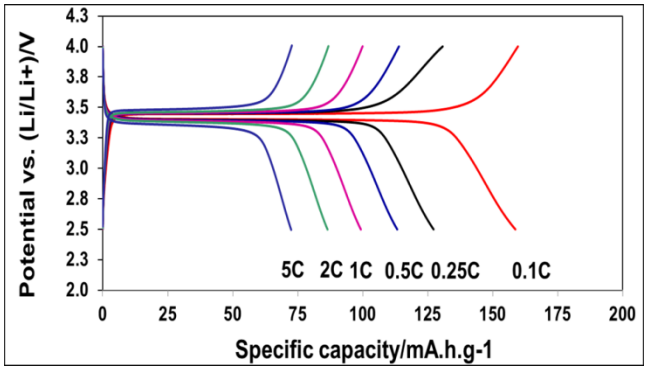

Figure 5. Charge and discharge profiles of $LiFePO_4$/C at different C-rates.

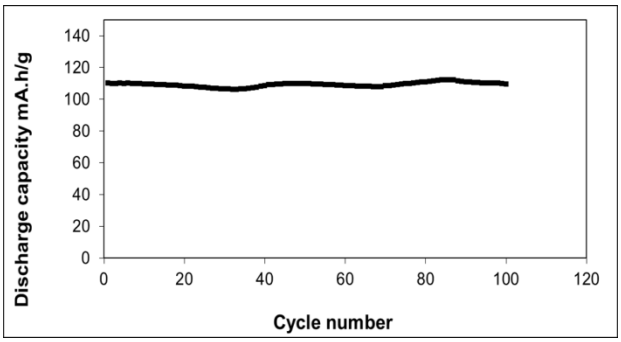

Figure 6. Cycling stability of LFP@700C at 1C rate at room temperature.

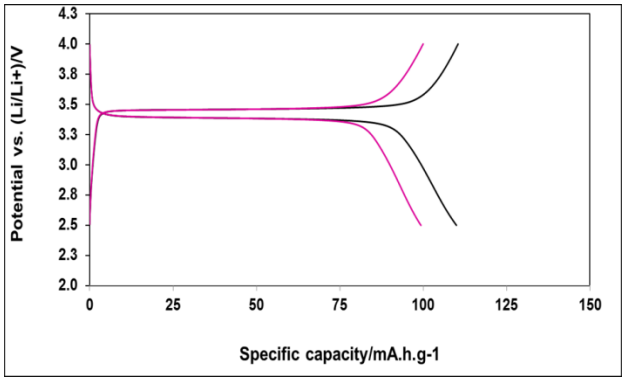

Figure 7. Initial (pink) and final (black) charge and discharge profiles of $LiFePO_4$/C at 1C-rate (cycle no. 5).

CONCLUSIONS

$LiFePO_4$ microspheres cathode material (hierarchical structures formed by assembled nanoparticles) was synthesized by simple hydrothermal method. The obtained product is pure and single crystalline $LiFePO_4$ olivine phase. Particles morphology revealed from SEM images shows sphere-like morphology of ca. 5-10 µm with fractal granularity composed of microsized secondary particles built-up of nanosized primary particles. Electrochemical analyses show good cycling performance. The discharge capacity at 0.1 C (159 mAh/g) is close to the theoretical one of 170 mAh/g (93.5% of the theoretical capacity). As shown in TEM micrograph, the carbon coating on the surface of $LiFePO_4$ particles is not sufficiently homogenous and still need to be optimized in order to enhance the charge and discharge capacity as well as the rate capability at different C-rates.

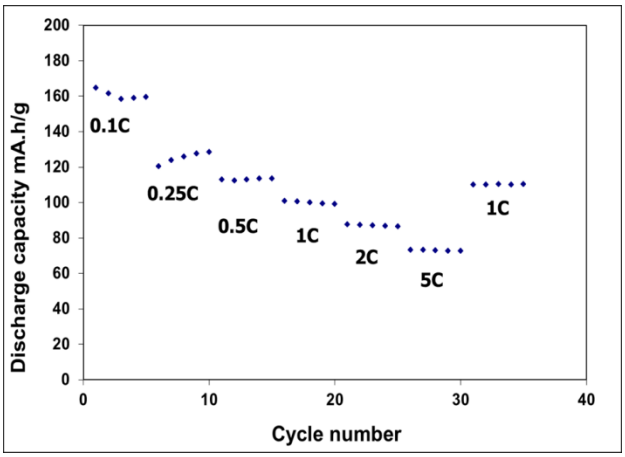

Figure 8. Rate performance of LFP@700C microspheres.

ACKNOWLEDGMENTS

Project SOMABAT (Development of novel SOlid MAterials for high power Li polymer BATteries) funded by the EC (VII FP) CP 266090 .

REFERENCES

[1] Padhi, A. K.; Nanjundaswamy, K. S.; Goodenough, J. B. *Journal of The Electrochemical Society* **1997**, *144*, 1188.
[2] Imachi, N.; Takano, Y.; Fujimoto, H.; Kida, Y.; Fujitani, S. *Journal of The Electrochemical Society* **2007**, *154*, A412.
[3] Belharouak, I.; Johnson, C.; Amine, K. *Electrochemistry Communications* **2005**, *7*, 983.

Simulation study of an Operational Amplifier with non-Ideal CNTFET

W. Makni[1], M. Najari[2], H. Samet[1]

[1] National School of Engineering of Sfax , Laboratory of Micro-Electro Thermal Systems (METS), Sfax, Tunisia

[2] Faculty of Sciences of Gabes , Department Of Physics, Gabes, Tunisia

Abstract: Carbon Nanotube Field-Effect Transistor (CNTFET) is a promising candidate for future electronic devices thanks to its ballistic transport, high current, high speed and low power dissipation [21] [32]. Among these characteristics ballistic transport should verify the following condition: the channel length of nanotube should be smaller than the mean free path of acoustic phonon at low bias and optical phonon scattering at high bias voltage [3] [4] [-5]. If this condition is not satisfied, electron phonon scattering effect will be important.

In order to have an accurate model we should to take into account the electron phonon scattering effect.

Two scattering mechanisms have been identified to be important in CNT which are acoustic phonon scattering and optical phonon scattering. Under high bias and for short channel length, optical phonon scattering is the most important mechanism due to its short mean free path (λ_op~15nm) [6]. However, under low bias, acoustic phonon scattering is the dominant scattering mechanism inside the long nanotube due to the long mean free path (λ_ap~0.6µm-1.5µm) depending on the chirality indices and the temperature range [7].

In this study, CNTFET long channel lengths are used. Therefore only the AP scattering will be considered due to working at low bias (V_GS<0.55V) [7]. In order to determine the impact of this effect on electronic circuit operations, Operational Amplifier (Op Amp) is designed and performances are scaled.

The main contribution of this study is to complete the Raychowdhury model by adding AP scattering equation and to analyze the impact of this effect on Operational Amplifier (Op Amp) circuit performances. Finally to compare these results with ballistic Op Amp model. For this purpose, the Verilog-A language [8] is used to implement the CNTFET behavioral model under the ADS environment [9].

Keywords: Carbon nanotube field effect transistor, Acoustic phonon scattering, Verilog-A, Operational Amplifier.

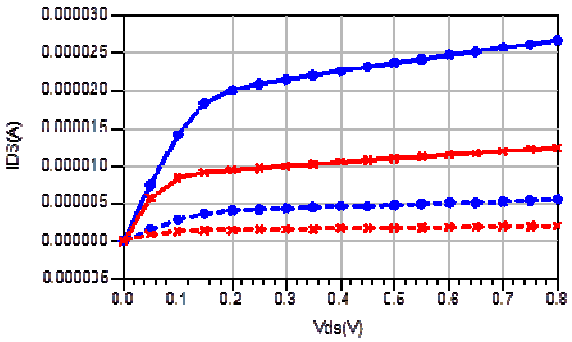

Figure 1. Drain-current I_ds versus drain-source V_ds for gate voltage (V_GS=0.5 V): comparison between ballistic compact model (solid line with circle for d=1.48 nm and with x for d=1.25 nm) and AP scattering compact model CNTFET (dashed line with circle for d=1.48 nm and with x for d=1.25 nm) for (L_ch=1µm)

At low bias and for channel length longer than the mean free path for AP scattering λ_{APhi}, AP scattering effect is the dominant mechanism in the device [7]. This AP scattering mean free path λ_{APhi} is a function of the temperature range and the chirality indices. For example, a temperature variation from 200K to 400K and for chirality indices scaling from (from (13, 0) to (22, 0)), λ_{APhi}variation will be from 659 nm to 1120 nm [7].

Table 1 calculates the different values of the AP scattering mean free path corresponding to different CNT chirality, i.e. diameter.

Using the Landauer equation the current drain I_{nSAP} is calculated.

The AP scattering model is included in the compact model simulation of Raychowdhury's et al, and compared with ballistic model of CNTFET. VERILOG-A language is used to implement the compact model in the ADS software. Fig. 1 shows the comparison of I_{ns}current with ballistic model simulation and with simulation including AP scattering for diameter equal 1.25nm and 1.4878nm for low bias $V_{GS} = 0.5$ V. We can observe with AP scattering model that the current I_{ns}decreases with a ratio of 0.2 compared with the ballistic current. Since neglecting the AP scattering lead to an overestimation of more than 20% of the current I_{ns}.

In order to analyze the impact of AP scattering on analog circuit performances, two-stage Op Amp circuit design using AP scattering model CNTFET has been simulated to

determine their performances and compared them with Op Amp using a ballistic model.

The design of ballistic Op Amp is tuned in order to have a compromise between the gain (27.4 dB), bandwidth (15.5MHz) and low power dissipation. Practical robust design values of load (CL) and miller compensation (Cc) capacitances are chosen as 1f F and 0.01pF respectively. The chosen values of these capacitances allow the stability in term of phase margin more than 45 degrees. The different CNTFET Op Amp simulated parameters, using ADS environment are gain, phase margin , -3dB gain frequency, unity gain frequency, common mode rejection ratio (CMRR), Power Supply Rejection Ratio (PSRR), Input common mode voltage range (ICMR) , Vout swing, output resistance (Rout) and power dissipation.

We act on the CNT diameter since diameter is the main parameter that affects CNTFET performances. Table II shows the different diameters and channel lengths used in Op Amp simulation. These diameters are implemented in Op Amp design, for both cases of the ballistic and the AP scattering models. The chosen value of channel length is based on having the scattering case.

We remark that there is a degradation of Op Amp performances with Ap scattering model compared with ballistic model therefore neglecting the AP scattering lead to have not an accurate results.

References:

[1] A. Raychowdhury, S. Mukhopadhyay, K. Roy, "A circuit-compatible model of ballistic carbon nanotube field effect transistor. " IEEE Trans Computer –Aided Design, 2004, vol. 12, n. 10, pp. 1411-1420.

[2] J. Guo, M. Lundstrom, S. Datta, "Performance projections for ballistic carbon nanotube field-effect transistors". Applied Physics Letters, 80, pp. 3192-3194. 2002

[3] P. Avouri, J. Appenzeller, R. Martel, S. J. Wind. "Carbon nanotube electronics" Proceeding of the IEEE, 2003, vol. 91, n. 11, pp. 1772-1784.

[4] A. Javey,J. Guo, M. Paulsson, Q. Wang, D. Mann, M. Lundstrom, H. Dai, " High-field, quasi ballistic transport in short carbon nanotube". Physics Letters, 2004, 92, 106804.

[5] A. Javey, P. Qi, Q. Wang, H. Dai, " Ten-to 50- nm long quasi ballistic carbon nanotube devices obtained without complex lithography" PNAS, 2004, vol. 101, n. 37, pp. 13408-13410.

[6] J. Guo, M. Lundstrom, "Role of phonon scattering in carbon nanotube field-effect transistor." Applied Physics Letters, 2005, vol. 86, pp. 193103.

[7] S. Fregonese, J. Goguet, C. Maneux, T. Zimmer, " Implementation of electron –phonon scattering in a CNTFET compact model" IEEE Transaction On Electron device , 2009, vol. 56 n. 6.

[8] Verilog-A Reference Manual, Agilent Technologies September 2004.

[9] Advanced Design System (ADS) The website of ADS, http:// www.home.agilent.com

The Use of Different Solvent Types for Electrospinning of Polycaprolactone Tubular Scaffolds

I. Yalcin,[1] J. Horakova,[2] T. Gok Sadikoglu[1]

[1] Istanbul Technical University, Textile Technologies and Design Faculty, Textile Engineering Department, Istanbul, Turkey.

[2] Technical University of Liberec, Faculty of Textile Engineering, Department of Nonwovens and Nanofibrous materials, Liberec, Czech Republic.

ABSTRACT

In this study, polycaprolactone (PCL) with differing molecular weights dissolved in acetic acid, formic acid and chloroform:ethanol solvents seperately at a concentration of 20 w/v % solution. Tubular scaffolds were produced by using electrospinning apparatus modified with rotating mandrel. Produced scaffolds were examined morphologically by scanning electron microscope (SEM) to investigate its availability of usage for vascular grafts.

Keywords

polycaprolactone, nanofiber, tubular scaffolds, electrospinning

1. INTRODUCTION

For the improvement of cell attactment and proliferation on scaffolds, it is essential to mimic extra cellular matrix [ECM]. In this case, electrospun nanofibrous matrices play an important role due to their resemblance to the natural ECM and fiber morphology become important task while designing such a nanofibrous scaffold [1]. As a polymer, biodegradable materials provide a key advantage for tissue engineering. Polycaprolactone is one of the most promising synthetic biodegradable polymers for medical applications owing to its biocompatibility and high elastic behavior. Moreover, its hydrophobic nature and the high level of crystallinity results in a long degradation time which provides prolonged mechanical support for cells to infiltrate [2, 3].

The modification of an electrospinning process with a rotating mandrel type collector results in deposition of nanofibers onto tubular scaffolds of various inner diameters. A promising material for vascular grafts can be obtained with combination of favored properties of PCL and the desired characteristics of electrospun nanofibrous structures [4, 5]

In this study, PCL with 45000 and 90000 molecular weights dissolved in acetic acid, formic acid and chloroform:ethanol at a concentration of 20 w/v % solution were investigated morphologically to examine its availability of usage in multilayered tubular scaffolds for small diameter vascular grafts.

2. MATERIALS & METHODS

Poly-ε-caprolactone (Mn 45000 and Mn 90000 / Sigma–Aldrich) was dissolved in acetic acid, formic acid and chloroform:ethanol (9:1, v:v; Sigma–Aldrich) at a concentration of 20 w/v % solution. Solutions stirred 8 hour by magnetic stirrer and immediately spun

The custom-designed electrospinning apparatus consists of positive high-voltage power supply (Matsusada Precision Inc., Japan), a syringe pump (Model NE-1000x; New Era Pump Systems Inc., USA) a 10 ml plastic syringe, a hypodermic needle and grounded stainless steel rotating mandrel collector. Electrospinning apparatus modified with a rotating mandrel type collector enables the production of fibrous tubular scaffolds. Schematic view of designed electrospinning apparatus can be seen at Figure 1.

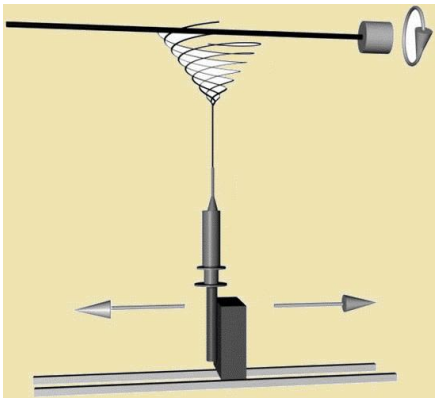

Figure 1. Schematic view of custom design electrospinning apparatus.

During production, electrospinnig parameters were fixed at 2 ± 0.5 ml/h flowrate, 10 cm distance and 7.5 kV applied voltage while using 0.6mm needle diameter. Rotational speed of the collector was adjusted to 250r/min for 6mm diameter rotating mandrel (peripheral speed is 4.71m/min). Spinning time was varied from 5min to 60min in order to get a tubular scaffold with adequate wall thickness. Temperature and relative humidity 20 ± 3 ºC and 34 ±4%.

Morphology of the fibrous scaffolds were examined by using scanning electron microscopy (SEM; FEI Company) and fiber diameters were measured from 100 fibers for each sample by NIS Elements Software System (Phenom, Nikon Inc.).

3. RESULTS and DISCUSSIONS

3.1 Fabrication of scaffolds

In this study, monolayer PCL tubular scaffolds with length up to 10 cm, inner diameter of 6mm and with 150-300 µm wall have been successfully fabricated (Figure 2).

Except formic acid solution, all tubular scaffolds could be easily removed from the rotating mandrel due to the characteristics of PCL.

Figure 2. Macroscopic image of PCL tubular scaffolds

3.2 Fiber Morphology

According to the results, average fiber diameters were measured as 172.92 ± 39nm; 229.41 ± 61nm and 2.08 ± 0.98µm for formic acid, acetic acid and chloroform: ethanol solvent systems respectively.

3.2.1. 20% PCL (90000Mn.) in Acetic Acid

Average fiber diameter was measured as 229.41± 61nm while bead-like nanofibrous structure was observed dominantly when acetic acid was used as solvent for PCL (Figure 3).

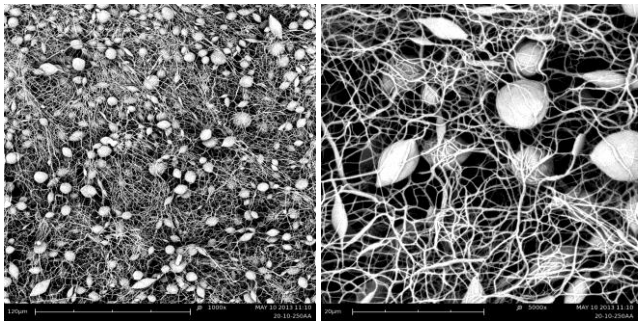

a. ***b.***

Figure 3. Morphological analysis of PCL in acetic acid solution. *Scale bars **a)**1000x and **b)**5000X*

3.2.2. 20% PCL (90000Mn.) in Formic Acid

When formic acid was used as a solvent, average fiber diameter was measured as 172.92± 39nm which results in problems while pulling the scaffold out from mandrel in tubular form.

Damaged scaffold can be seen in Figure 4. For this reason, SEM images were achieved from flat surfaces of the scaffolds.

Figure 4. Damaged inner surface of the scaffold of PCL in formic acid solution. (Scale bar 400x)

PCL fibers produced from formic acid solution leads to less in amount beads in comparison with PCL-acetic acid solution (Figure 5).

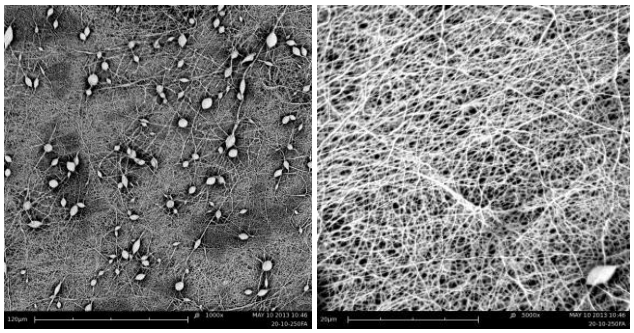

a. ***b.***

Figure 5. Morphological analysis of PCL in formic acid solution. *Scale bars **a)**1000X and **b)**5000X*

3.2.3. 20% PCL (45000Mn.) in Chloroform:ethanol

In PCL-chloroform: ethanol solution, continuous and smooth fibers with 2.08 ± 0.98µm average fiber diameter and without any bead-like formation were achieved that results in better morphology (Figure 6).

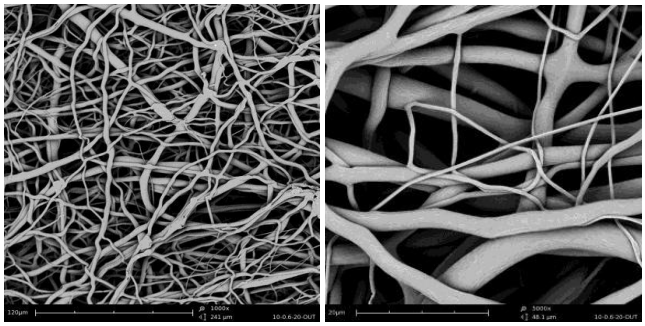

a. ***b.***

Figure 6. Morphological analysis of PCL in chloroform:ethanol solution. *Scale bars **a)**1000X and **b)**5000X*

4. CONCLUSION

In this study, monolayer PCL tubular scaffolds were successfully fabricated. According to the results, average fiber diameters were measured as 172.92 ± 39nm; 229.41 ± 61nm and 2.08 ± 0.98µm for formic acid, acetic acid and chloroform:ethanol solvent systems respectively.

Bead-like nanofibrous structures were observed dominantly in acetic acid and notably in formic acid. In PCL chloroform:ethanol solution, continuous and smooth fibers without any bead-like formation were achieved that results in better morphology.

The use of chloroform-ethanol solvent system results in microfibers which can be used in tunica media and adventitia layers of vascular grafts owing to their larger pore sizes[6].

Fiber diameters are reduced by using acidic solvents. However, its usage in tunica intima seems unappropriate based on its beadlike formation and problems in achieving tubular scaffolds without deformation.

Since chloroform is one of the solvent that is most often used for electrospinning of PCL due to its less hazardous properties, there

is risk of acidic solvent residues in the scaffold that can cause change of tissue's pH when it is implanted so, it must be studied before invivo analysis.

For futher studies, mixtures of acidic solvents with chloroform are aimed to be studied to reduce fiber diameter with better morphology of PCL fibrous scaffolds.

5. ACKNOWLEDGMENTS

We would like to thank Technical University of Liberec for proving us their laboratory opportunities and sharing with us their experiences.

6. REFERENCES

[1] Walkenström, P., Thorvaldsson A., (2008) "Electrospinning of Nanofibers for Biomedical Applications", *Textile Journal*, 22-29.

[2] Edwards, M.D., Mitchell, G.R., Mohan, S.D., Olley, R.H. (2010) Development of orientation during electrospinning of fibres of poly(e-caprolactone). *Eur Polym J*, 46, 1175–1183.

[3] McClure, M.J., Sell, S.A., Simpson, D.G., Walpoth, B.H., Bowlin, G.L., (2010) A three-layered electrospun matrix to mimic native arterial architecture using polycaprolactone, elastin, and collagen: A preliminary study. *Acta Biomater*, 6, 2422–2433.

[4] Schueren, L.V., Schoenmaker, B., Kalaoglu, O.I., Clerck, K., (2011) An alternative solvent system for the steady state electrospinning of polycaprolactone, *Eur Polym J*, 47, 1256–1263.

[5] Wu, H., Fan, J., Chu, C., Wu, J., (2010) Electrospinning of small diameter 3-D nanofibrous tubular scaffolds with controllable nanofiber orientations for vascular grafts, *J Mater Sci: Mater Med*, 21, 3207–3215.

[6] Gaudio C.D., Bianco, A., Folin, M., Baiguera, S., Grigioni, M. Structural characterization and cell response evaluation of electrospun PCL membranes: Micrometric versus submicrometric fibers, *J of BiomedMater Res Part A.*, 1028-1039.

Investigating effects of an argon-based non-thermal atmospheric pressure plasma jet on inactivation of E. coli bacteria

M. T. Benabbas[1], S. Sahli[1], S. Mouissat[1], N. Kacem Chaouche[2], L. Benterrouche[1], M. Kara Ali[2]

[1] University Constantine 1, Laboratory of Microsystems and Instrumentation, Constantine, Algeria

[2] University Constantine 1, Laboratory of Mycology, Biotechnology and Microbial Activity, Constantine, Algeria

ABSTRACT

In this work, some investigations have been carried out to generate an argon-based non-thermal atmospheric pressure plasma jet (ANAPPJ). The argon gas was injected through the inner electrode of a homemade dielectric barrier discharge-based cylindrical reactor linked to a high voltage pulse generator Redline G2000. A plasma jet length varying from 0 to 6 cm has been obtained by applying an excitation voltage in the range 6 - 10 kV with a signal frequency in the range 10 - 50 kHz. This argon-based non-thermal atmospheric pressure plasma jet has been applied to inactivate Escherichia coli (E. coli) bacteria in order to determinate its action field around the impact point on the contaminated surface by measuring the inhibition zone diameter (I.Z.D).

Keywords

Argon-based non-thermal atmospheric pressure plasma jet, micro-organisms inactivation, E. coli bacteria, inhibition zone diameter.

1. INTRODUCTION

During the last decade, non-thermal plasmas have been widely studied for several medical applications such as sterilization [1 - 2], blood coagulation, teeth whitening [3], dermatology [4] and cancer healing [5]. Atmospheric plasmas created in air or in a noble gas remain the most promising plasmas for biomedical applications because of their safety to use under low temperatures, near the ambient. The creation of plasma in open air leads to the production of several reactive species such nitrogen oxide (NO), atomic oxygen (O) and ozone (O_3) besides to the ultraviolet (UV) radiations. Several works have shown that these plasma species have high bactericidal effects [6 - 7]. Recently, a large number of plasma sources were designed for specific applications in the biomedical field. Among the studied cold plasma techniques for medical applications, plasma jet sources are the most attractive.

These kind of atmospheric cold plasmas were considered as indirect plasmas. Indeed, the electrical discharge is created between two electrodes inside a tube and then the used plasma for the treatment is transported in a gas flow until it reaches the area to be treated. The size of the jet can be modulated and can have a small section (less than a millimeter), allowing then the plasma jet to be used for a very located treatment. Although several works have been recently devoted to the plasma jet sources and their potential applications in the biomedical field, however their precision in the treated area remains not well controlled.

In this work, a homemade argon plasma jet is developed. Results of some investigations carried out on the effect of some plasma jet parameters on the inhibition zones diameter created by the jet on a surface previously contaminated by E. coli colonies are presented.

2. EXPERIMENTAL DETAILS

The schematic representation of the elaborated homemade argon-based non-thermal atmospheric pressure plasmas jet reactor is reported in Figure. 1(a). The reactor is constituted by a glass tube (glass thickness = 1 mm) as dielectric barrier, a stainless steel tube (6 mm of external diameter and 1 mm of thickness) inserted into the glass tube as inner electrode and a coiled tungsten wire of 0.5 mm of diameter placed around the neck of the glass tube as an outer electrode. The argon gas was injected through the inner electrode to the discharge area between the two electrodes. The inner and the outer electrodes are linked to a high voltage pulse generator Redline G2000. Samples contaminated by E. coli bacteria are exposed to the argon plasma jet. Each sample is constituted from a 100 µl of E. coli bacteria spread out on the surface of an agar plate contained in a petri dish and then dried at room temperature. The samples were exposed to the plasma jet during different times and different distances from the source of the plasma jet. The photo of the created plasma jet is represented on Figure. 1(b). During all the experiments, the applied voltage and its frequency were fixed at 8 kV and 18 kHz respectively.

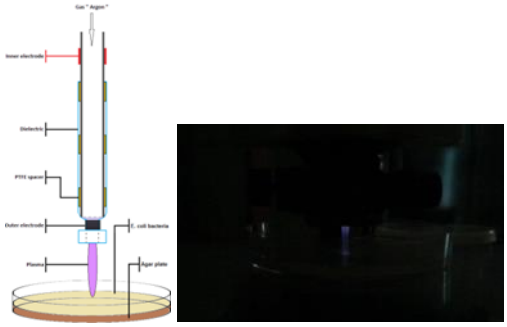

(a) **(b)**

Figure. 1: Schema (a) and photo (b) of the homemade plasma jet set up.

3. RESULTS AND DISCUSSION

It is well known that the plasma jet shape, length and energy depend on the applied voltage value and its frequency, on the surrounding air humidity and the nature of the working gas [8 - 9]. In this work, we have generated at room temperature and humidity, an argon-based non-thermal atmospheric pressure plasma jet of about 27 mm of length. We have exposed an E. coli

contaminated surface to this plasma jet. In the following, we will present the effect of the plasma source – sample distance variation and the effect of exposure duration to this plasma jet, on the diameter of the inhibition zone created on the E. coli contaminated surface.

3.1 Effect of the distance variation between the plasma jet nozzle and the contaminated surface

Petri dishes containing E. coli bacteria spread out on agar plates were exposed to the generated plasma jet (27 mm of length) for 10 minutes. The contaminated surface was placed at 10, 20, 30 and 40 mm away from the nozzle of the plasma jet. At 10 and 20 mm, the samples were completely immersed in the plasma jet and by consequence, directly exposed to the jet. At 30 and 40 mm, the contaminated surface was located far from the plasma jet extremity of about 3 mm and 13 mm respectively. Figure. 2 shows the distance plasma source - samples effect on the contaminated surface. A zone without manifest bacteria is created on the petri dishes surface. The diameter of this area decreases when the contaminated surface is more far from the plasma jet nozzle.

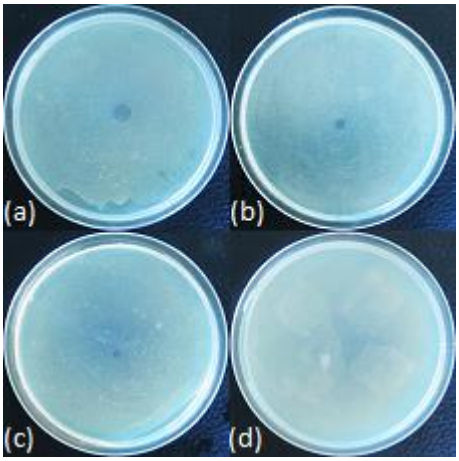

Figure. 2: Photos of the E. coli contaminated surface after its exposition to the plasma jet at different distances from the jet nozzle. (a):10 mm, (b): 20 mm, (c): 30 mm, (d): 40 mm.

Figure. 3 shows the evolution of the inhibition zone diameter versus the distance between the contaminated surface and the plasma jet nozzle. The increase of this distance induces a decrease of the I.Z.D created on the treated samples. From 7 mm at a distance of 10 mm from the plasma jet nozzle, the I.Z.D decreases to near 0 mm for a sample treated at 40 mm far from the nozzle. The presence of this deserted area shows a disappearance of the bacteria from the treated zone, because of their cadaver consumption by the plasma species created in the argon gas and the ambient air. Many works have revealed that the interaction of bacteria with a cold plasma may have different effects leading to their inactivation and/or removal from the contaminated surface. UV radiations emitted by the plasma can damage the DNA of the bacteria cells causing their inactivation, the reactive species react chemically with their membranes inducing an oxidation of their constituents and the electrostatic forces produced by the charged particles of the plasma accumulated on the outer surface of the bacteria cells, can induce the rupture of their membrane and this last phenomenon is more pronounced with gram-negative bacteria [10 - 12].

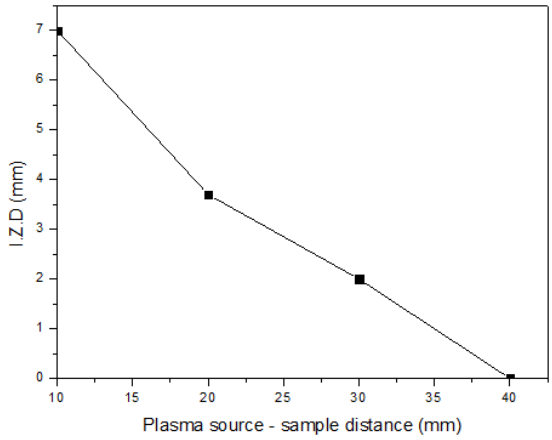

Figure. 3: Effect of the distance between the plasma jet nozzle and the contaminated petri dishes surface on the inhibition zone diameter (exposure time: 10 min).

The variation of the I.Z.D depends on the plasma jet diameter and species nature, energy and density. In the direct mode (at 10 and 20 mm), the effect of these parameters is more pronounced when the treated surface is close to the nozzle and decreases when the contaminated surface is placed far from the nozzle. In the indirect mode (samples placed at 30 and 40 mm), since there is no contact between the plasma jet and the treated samples surface, charged particles have little effect on the bacteria [13]. The removal bacteria from only a little area on the contaminated surface may be due to the effect of less reactive oxygen species reaching the petri dishes surface compared to that produced in the direct mode. Especially, the ozone created by the plasma can have an important effect because of its longer lifetime compared to that of atomic oxygen O and OH groups [14].

3.2 Effect of the exposure time

In this study, petri dishes containing E. coli bacteria spread out on agar plates were immersed in a plasma jet at 10 mm from the plasma jet nozzle, during different treatment times. Figure. 4 shows the treatment time effect on the contaminated surface.

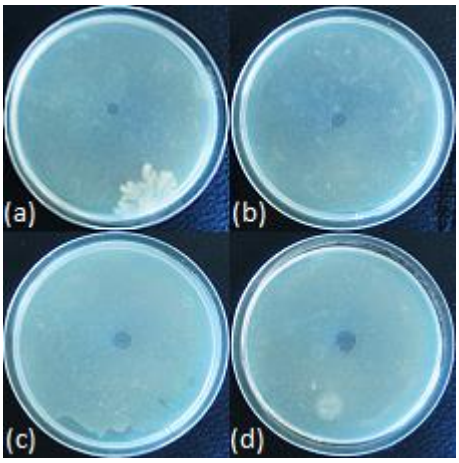

Figure. 4: Photos of the time effect on the treated area on the E. coli contaminated samples. (a): 2 min, (b): 6 min, (c): 10 min, (d): 14 min.

The plasma jet creates a circular zone without any visible E. coli micro-organisms. The diameter of this zone increases with the increase of the exposure time to the plasma jet, showing then

more bacteria inactivation. On figure 5 is represented the variation of the diameter of the inhibition zone induced by the plasma jet as function of exposure time.

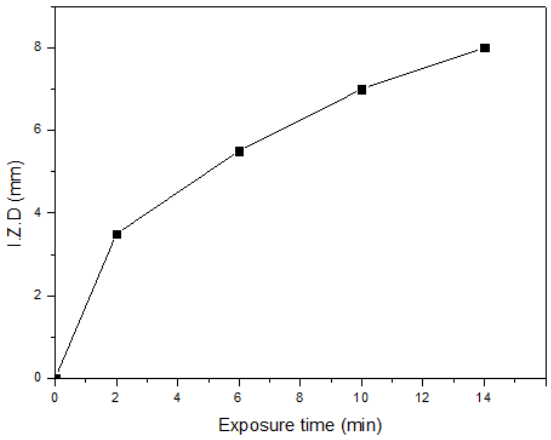

Figure. 5: Effect of the exposure time on the inhibition zone diameter (distance from the plasma jet nozzle: 10 mm).

When the plasma jet exposure time increases from 2 to 14 min, the I.Z.D curve variation shows two behaviours. The first one in the treatment time range 0 – 2 min, presents a pronounced I.Z.D increase (from 0 to near 3.5 mm) and the second one in the range 6 – 14 min, shows a less pronounced I.Z.D increase (from 5.5 to about 8 mm). Beyond 14 min, a quasi-saturation I.Z.D variation is reached. This quasi-saturation of the I.Z.D can be explained by the short lifetime of the plasma species at atmospheric pressure. Because of the high pressure, the plasma species cannot diffuse sufficiently far from the centre of the plasma jet impact zone and lose their reactivity, even if the treatment time is increased.

4. CONCLUSION

An argon-based non-thermal atmospheric pressure plasma jet (ANAPPJ) has been generated using a homemade DBD-based plasma jet reactor and a high voltage pulse generator. This ANAPPJ has been used to inactivate E. coli bacteria in order to determine its field of action. The efficiency of the plasma jet and in E. coli inactivation process and its field of action depend on exposure time, treatment mode (direct or indirect) and plasma source – sample distance. A plasma jet with a controlled action field diameter can be obtained and allows then the use of this plasma jet for a very localized treatment.

5. ACKNOWLEDGMENTS

This work was supported by the Algerian Thematic Agency of Research in Sciences and Technology (ATRST ex ANDRU).

6. REFERENCES

[1] Uhm, H. S., Hong, Y. C. 2011. Various microplasma jets and their sterilization of microbes. *Thin Solid Films* 519, 20 (Aug. 2011), 6974–6980.

[2] Benterrouche, L., Sahli, S., Rebiai, S., Benhamouda, A., Sebihi, F. Z. 2013. Inactivation of E. coli bacteria by atmospheric dielectric barrier discharge. *Int. J. Nanotech.*10, 5–7, (Apr. 2013), 543–552.

[3] Park, G. Y., Park, S. J., Choi, M. Y., Koo, I. G., Byun, J. H., Hong, J. W., Sim, J. Y., Collins, G. J., Lee, J. K. 2012. Atmospheric-pressure plasma sources for biomedical applications. *Plasma Sources Sci. Technol.* 21, 4 (Aug. 2012), 043001.

[4] Heinlin, J., Morfill, G., Landthaler, M., Stolz, W., Isbary, G., Zimmermann, J. L., Shimizu, T., Karrer, S. 2010. Plasma medicine: possible applications in dermatology. *J. Dtsch. Dermatol. Ges.* 8, 12 (Dec. 2010), 968-976.

[5] Han, X., Klas, M., Liu, Y., Stack, M. S., Ptasinska, S. 2013. DNA damage in oral cancer cells induced by nitro-gen atmospheric pressure plasma jets. *Appl. Phys. Lett*. 102, 23 (Jun. 2013), 233703.

[6] Sousa, J. S., Girard, P-M., Sage, E., Ravanat. J-L., Puech. V. 2012. DNA Oxidation by Reactive Oxygen Species Produced by Atmospheric Pressure Microplasmas. In *Plasma for Bio-Decontamination, Medicine and Food Security*, Z. Machala *et al*, Ed. NATO Science for Peace and Security Series A: Chemistry and Biology. Springer, Dordrecht, 107–119.

[7] Lackmann, J., Schneider, S., Narberhaus, F., Benedikt, J., Bandow, J. 2012. Characterization of damage to bacteria and bio-macromolecules caused by (V)UV radiation and particles generated by a microscale atmospheric pressure plasma jet. In *Plasma for Bio-Decontamination, Medicine and Food Security*, Z. Machala *et al*, Ed. NATO Science for Peace and Security Series A: Chemistry and Biology. Springer, Dordrecht, 17–29.

[8] Shao, X. J., Zhang, G. J., Zhan, J. Y., Mu, H. B. 2011. Investigation on Spurt Length of Atmospheric-Pressure Plasma Jets. *IEEE T. Plasma Sci.* 39, 11 (Nov. 2011), 2340 – 2341.

[9] Li, L., Nikiforov, A., Xiong, Q., Britun, N., Snyders, R., Lu, X., and Leys, C. 2013. OH radicals distribution in an Ar-H2O atmospheric plasma jet. *Phys. Plasmas* 20, 9 (Sep. 2013), 093502.

[10] Mahasneh, A., Darby, M., Tolle, S. L., Hynes, W., Laroussi, M., Karakas, E. 2011. Inactivation of Porphyromonas gingivalis by Low-Temperature Atmospheric Pressure Plasma. *Plasma Med*. 1, 3–4 (2011), 191–204.

[11] Mendis, D. A., Rosenberg, M., Azam, F. 2000. A note on the possible electrostatic disruption of bacteria. *IEEE T. Plasma Sci*. 28, 4(Aug. 2000), 1304–1306.

[12] Laroussi, M. 2002. Nonthermal decontamination of biological media by atmospheric pressure plasmas: Review, analysis, and prospects. *IEEE T. Plasma Sci.* 30, 4 (Aug. 2002), 1409–1415.

[13] Lu, X., Ye, T., Cao, Y., Sun, Z., Xiong, Q., Tang, Z., Xiong, Z., Hu, J., Jiang, Z., Pan, Y. 2008. The roles of the various plasma agents in the inactivation of bacteria. *J. Appl. Phys*. 104, 5 (Sep. 2008), 053309.

[14] Seo, Y. S., Mohamed, A-A. H., Woo, K. C., Lee, H. W., Lee, J. K., Kim, K.T. 2010. Comparative Studies of Atmospheric Pressure Plasma Characteristics Between He and Ar Working Gases for Sterilization. *IEEE Trans. Plasma Sci.* 38, 10 (Oct. 2010), 2954–2962.

Nano-powder deposited on polyimide and silicon surface by PECVD deposition technique from HMDSO precursor

I.Nouicer[1], S.Sahli[1], M.Kihel[1], Z.Ziari[1], A.Bellel[2], P.Raynaud[3], B.Lantin[3]

[1] Université Constantine 1, Laboratoire Microsystèmes et Instrumentation, Faculté des Sciences de la Technologie, 25017 Constantine-Algeria.

[2] Université Constantine 1, Laboratoire d'Etude des Matériaux Electroniques pour Applications Médicales (LEMEAMED), Faculté des Sciences de la Technologie, 25017 Constantine-Algeria.

[3] Universitiés de Toulouse - Laboratoire Plasma et Conversion d'Energie (LAPLACE)- CNRS, Université Paul Sabatier, 118 Route de Narbonne, 31062 Toulouse cedex, France.

ABSTRACT

Plasma polymerization of hexamethyldisiloxane (PPHMDSO) was used to deposit micro and nano structured thin layers on silicon (Si) and polyimide (PI) substrates, using low pressure and low frequency plasma discharge. The effect of several plasma deposition conditions (plasma chamber pressure, discharge power, deposition time) on the films characteristics has been studied. Thickness, chemical structure and surface properties of the elaborated thin layers were analyzed by means of numerical microscopy, profilo-meter, Scanning Electron Microscopy (SEM), Fourier Transform InfraRed spectroscopy (FTIR) and static contact angle measurements. For some deposition parameters, nano-powder of different concentrations and size was observed over the elaborated surface thin layers. FTIR analysis has revealed that the chemical formula of the deposited thin layers was SiOxCyHz like structure. Water contact angle measurements showed that the increase of the deposition pressure leads to the growth of a super-hydrophobic layer on polyimide substrates due to the increase of the powder concentration on the deposited film surface as revealed by SEM images.

Keywords

Nano-powder, super-hydrophobic surface, HMDSO, plasma polymerization, FTIR, SEM.

1. INTRODUCTION

In recent years, hydrophobic surface with water contact angles (CAs) greater than 150° has attracted considerable attention [1,2]. Superhydrophobic surfaces is desirable for various industrial applications such as antibiofouling paints for boats, antisticking of snow (or ice) for antennas, self-cleaning of windshields, anti-rusting, reduction of friction resistance and so forth [2]. In nature, the superhydrophobic property is observed on several cases as lotus leaves [4] and some animals organs like pond skater's legs [3], elephant ear, butterfly wings and duck feathers [3]. Daniele C. Bastos et al, explain that the contact angle is highly dependent on the surface roughness and the microstructure created on the surface [5] and to get a superhydrophobic surface, it's important to control the surface roughness and structure in both small and large scales [6].

In polymer materials, hydrophobic surfaces can be obtained by increasing hydrocarbon content and/or surface roughness [7]. If a surface is initially hydrophobic, introducing roughness to that surface will make it even more hydrophobic.

In this paper, we have carried out some investigations on the effect of Plasma-Polymerized Hexamethyldisiloxane (PPHMDSO) thin layers on the wettability of silicon and polyimide substrates. PPHMDSO nanoparticles have been grown during the deposition process and their effect on the hydrophobicity improvement of the coated substrates surface has been studied.

2. EXPERIMENTAL DETAILS

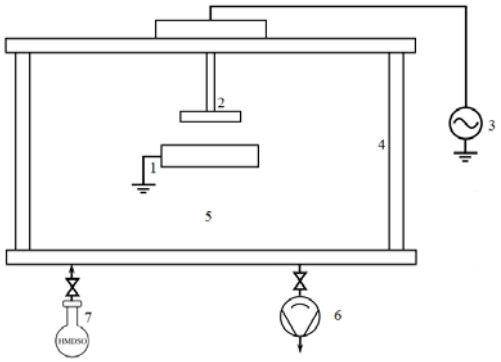

Figure. 1: Schematic drawing of the plasma chamber. 1: grounded electrode; 2: powered electrode; 3: low frequency power generator; 4: Pyrex cylinder; 5: vacuum chamber; 6: pumping unit; 5: HMDSO vapors inlet.

Figure 1 shows the plasma reactor used for the deposition of the PPHMDSO thin layers on silicon and polyimide surface substrates. The discharge experiments were carried out in a capacitively coupled plasma (CCP) reactor using a low frequency (LF) of 2 kHz. The pressure in the deposition chamber was monitored by mean of Pirani gauge and controlled using a microneedle valve gas. The pumping unit was composed of Alcatel primary pump. First, the reactor chamber was pumped down to 10^{-2} mbar and then the gas precursor was introduced without any gas carrier using a monomer inlet system. The substrates were placed on the grounded electrode spaced from the upper electrode of about 3cm. The experiments were performed at the ambient temperature using a fixed plasma polymerization power of 50 W and two chamber pressure values (0.2 and 0.5 mbar). The process parameters used for the growth of the PPHMDSO thin layers are summarized in **Table 1**.

Polyimide thin films substrates with a thickness of about 50 µm (Kapton ® HN from DuPont Nemour) were cut into rectangular shaped (6.5×1 cm^2) and silicon substrates wee cut in a square shape (2x2 cm^2). Before any thin layers deposition and in order

to eliminate any dusts on their surfaces, the used substrates were cleaned and then dried using nitrogen gas jet. Silicon substrates have been used for thin layers thickness and roughness measurements (using a KLA-Tencor Alpha-step IQ and surface Profiler, respectively) and for scanning electronic microscopy using a JEOL JMS-6060 LV Scanning Electron Microscopy analysis. Fourier transform infrared spectroscopy (FTIR) was used to investigate the chemistry and bond structure of the produced nanoparticles using a Thermo Nicolet Avatar 360 spectrometer in the range of 4000-400 cm^{-1}.

Sample	Deposition time (sec)	P_{moy} (W)	Pr (mbar)
WP01	30	50	0.2
WP02	60	50	0.2
WP03	120	50	0.2
WP04	240	50	0.2
WP05	420	50	0.2
WP06	900	50	0.2
P01	120	50	0.5
P02	300	50	0.5
P03	600	50	0.5
P04	1200	50	0.5
P05	1800	50	0.5

Table.1: Discharge plasma parameters values (WP : without powder, P ; powder).The wettability of the treated samples was characterized by contact angle measurements on 5µl droplets of deionized water dripped onto the treated surface. All contact angle measurements were performed at atmospheric pressure and room temperature and were averaged from five measurements.

3. RESULTS AND DISCUSSIONS

3.1 Contact angle measurements

The static contact angle measurements have been carried out to evaluate the wettability of PPHMDSO thin layers deposited at a chamber pressure of 0.2 mbar. **Figure 2** illustrates the variation of the water contact angle as a function of deposition time.

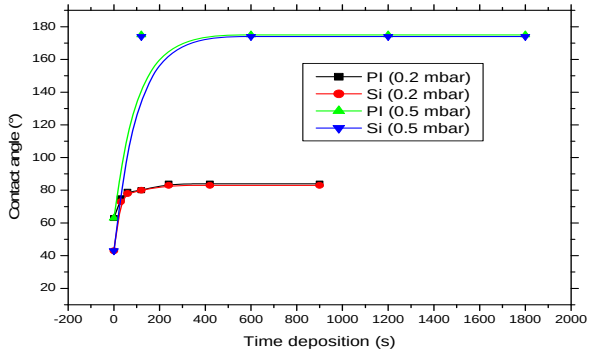

Figure. 2 : Variation of the contact angle as a function of deposition time.

The variation shows that the water contact angle increases significantly with increasing treatment time. From 63° for untreated PI, the contact angle increases to about 84° after 240 s of deposition time, then remains unchanged for treatment times greater than 240 s. However, for a deposition chamber pressure of 0.5 mbar, the evolution of water contact angle showed a significant increase. After less than 200 s of the deposition time, its value reaches a value of about 175° for both coated Si and Pi substrates. This super hydrophobicity character remains constant in all explored deposition time range over near 200 s and it appears independent of the substrate nature.

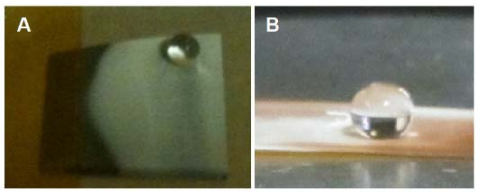

Figure. 3: Images of water drop shapes deposited on: (A) Si, (B) PI substrates.

3.2 Fourier transform infrared spectrometer analysis

Figure 4 shows the absorption infrared spectra of plasma polymerized HMDSO films as a function of deposition time. The assignation of the main peaks vibration of the spectra is reported in table 2 [9].

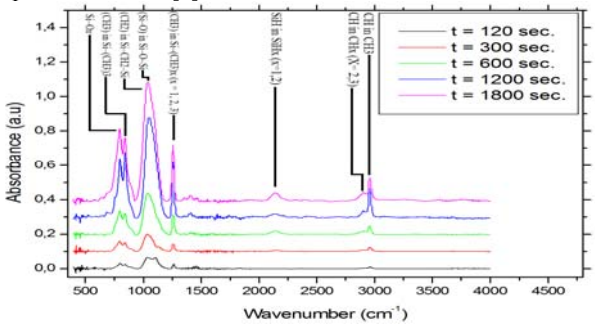

Figure. 4: Infrared absorption spectra of plasma polymerized HMDSO thin layers for different deposition times.

Peak position (cm^{-1})	Band assignment
2960	va (C–H) in CH_3
2900	vs (C–H) in CH_x (x = 2, 3)
2120	v (Si–H) in Si–H_x (x = 1, 2)
1260	δa (CH_3) in Si–$(CH_3)_x$ (x = 1, 2, 3)
1025-1110	δa (Si–O) in Si–O–Si
1025	w (CH_2) in Si–CH_2–Si
840	ρ (CH_3) in Si–$(CH_3)_3$
800	v (Si–C) in Si–$(CH_3)_2$
740	v (Si–C) in Si–$(CH_3)_x$ (x = 1, 2, 3)

Tableau.2 : FTIR bands assignment of plasma polymerized HMDSO thin layers (v : stretching ; δ : bending ; ρ : rocking ; w : wagging ; a : asymmetric ; s : symmetric).

The principal absorption bands are very different between deposited layers at 120 and 300 s and deposition time higher than 300 s. This difference indicates that the material have a different structure and/or chemical composition. Moreover, we notice an overlapping of the absorption bands of Si-O-Si and Si-CH_2-Si when the deposition time increases. The infrared spectra show that the structure of the deposited nanoparticles contains carbon (Si-C and CH_x (x = 1,2,3)). The surface area of the absorption bands associated to the C-H bonds of CH_x (x = 1,2,3), Si-C and Si-H is very weak for films deposited at 2 min and increases with increasing plasma discharge time. Young-Yeon Ji et al have observed that, the increase of deposition time leads to an increase of Si-C, Si-$(CH_3)_2$ and Si-O-Si bonds inducing more water-repellent property on the treated surfaces [9,10]. Our results are in good agreement with those reported in this latter work.

3.3 Roughness evolution

The measurements of surface roughness as a function of deposition time are reported in **Figure 6**. The thin layers deposited at a pressure of 0.2 mbar were smooth in all the explored deposition time. In contrary, for a chamber pressure of 0.5 mbar, the deposited thin layers were less smooth and their roughness was dependent on the deposition time. The surface of the coated PI and silicon substrates at this chamber pressure value was covered with white powder. The surface roughness changes linearly from a nanometer scale for the smooth PPHMDSO surface elaborated at 0.2 mbar to around one hundred nanometer scale for the rough surface for thin layers deposited during 30 min at 0.5 mbar.

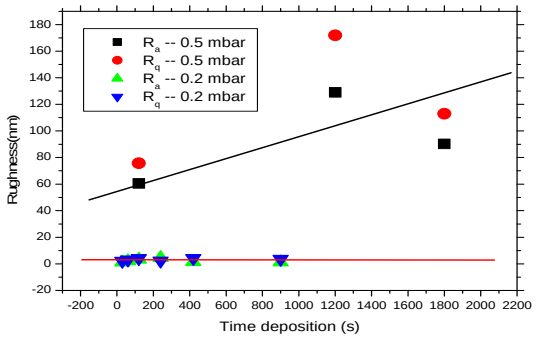

Figure. 6: Surface roughness evolution of as function of deposition time.

3.4 Surface morphology analysis

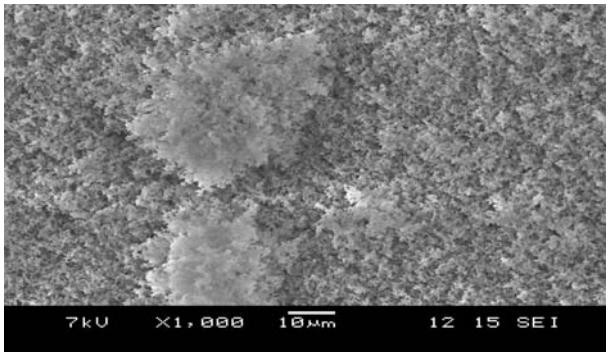

Figure. 7: SEM image of nano-powder processed from the HMDSO monomer.

Figure 7 shows SEM micrographs of nano-particles produced with plasma polymerization of HMDSO monomer with time deposition of 1200 seconds at pressure of 0.5 mbar. SEM images show highly agglomerated large microstructures consisting of primary nano-particles that have non-spherical shape. The particle size is in the range of about 500 nm, while the agglomerate size ranges between few microns to about 60 µm. The growth of the powder can be explained by a more collisions of the monomer molecules fragments in the deposition chamber because of this high pressure value, leading to the formation of primary clusters [11] that are deposited on the surface as island-like structure. In our case, the surface substrate was partially covered with white powder for a deposition time of 2 minutes and completely covered at a deposition time greater than 20 minutes. The same observation has been reported in a recent work [10,12] for a deposition time greater than 30 minutes and a chamber pressure of 0.4 mbar. The presence of this powder on the deposition thin layers of PPHMDO improves their hydrophobicity and allows to reach a super hydrophobicity character.

4. CONCLUSION

Super hydrophobic property has been successfully produced on polyimide and silicon surfaces using plasma enhanced chemical vapor deposition technique. The increase in the deposition time at a pressure of 0.2 mbar leads to the increase of the contact angle from 64° for untreated polyimide and 43° for untreated silicon to 84° and 83° for coated PI and Si, respectively. Surface roughness measurements showed that the increase of plasma pressure from 0.2 mbar to 0.5 mbar leads to the production of nano-powder on PI and Si surface with the increase of the surface roughness leading to the formation of super-hydrophobic surface. The contact angle of water drop increases to 175° after 120 seconds of deposition time for both substrates.

5. REFERENCES

[1] Xiu-Fang Wen. 2011. Organic–inorganic hybrid superhydrophobic surfaces using methyltriethoxysilane and tetraethoxysilane sol–gel derived materials in emulsion. Applied Surface Science, 258, 991– 998.

[2] Sanjay S. 2010. Porous superhydrophobic silica films by sol–gel process. Microporous and Mesoporous Materials, 130, 115–121.

[3] Bharat Bhushan. 2011. Natural and biomimetic artificial surfaces for superhydrophobicity, self-cleaning, low adhesion, and drag reduction. Progress in Materials Science, 56, 1–108.

[4] Xianfeng Wang et al. 2011. Engineering biomimetic superhydrophobic surfaces of electrospun nanomaterials. Nano Today, 6, 510-530.

[5] Daniele C. Bastos. 2013. Inducing surface hydrophobization on cornstarch film by SF6 and HMDSO plasma treatment. Carbohydrate Polymers, 91, 675-681.

[6] Y.Y. Yan. 2011. Mimicking natural superhydrophobic surfaces and grasping the wetting process: A review on recent progress in preparing superhydrophobic surfaces. Advances in Colloid and Interface Science, 169, 80-105.

[7] M. Drabik. 2007. Composite SiOx/hydrocarbon plasma polymer films prepared by RF magnetron sputtering of SiO2 and polyimide. Vacuum, 81, 920‑ 927.

[8] E. Vassallo. 2006. Structural and optical properties of amorphous hydrogenated silicon carbonitride films produced by PECVD. Applied Surface Science, 252, 7993–8000.

[9] Young-Yeon Ji. 2008. Formation of super-hydrophobic and water-repellency surface with hexamethyldisiloxane (HMDSO) coating on polyethyleneteraphtalate fiber by atmosperic pressure plasma polymerization. Surface & Coatings Technology, 202, 5663-5667.

[10] Young Yeon Ji. 2009. Water-repellent improvement of polyester fiber via radio frequency plasma treatment with argon/hexamethyldisiloxane (HMDSO) at atmospheric pressure. Current Applied Physics 9, 253-256.

[11] Christian Roth.2012. Nanoparticle Synthesis and Growth in a Continuous Plasma Reactor from Organosilicon Precursors. Plasma Process. Polym, 9, 119–134.

[12] Z. Ziari. 2013. Chemical and electrical properties of HMDSO plasma coated Polyimide, Vacuum, 93, 31-36.

Modeling and Simulation of AlGaAs/InGaAs Tandem Solar Cell

… S.Slimani [1], B. Djellouli[2]

ABSTRACT

Photovoltaic electricity is obtained by direct transformation of the sunlight into electricity by means of photovoltaic cells. Tandem cells are containing several p-n junctions. Each junction is tuned to a different wavelength of light, reducing one of the largest inherent sources of losses, and thereby increasing efficiency. By solving the Poisson equation in an AlGaAs/InGaAs and AlGaAs /AlGaAs/InGaAs monolithic cascade solar cells, we have established a classical calculation of conduction and valence band edge and the electron and hole densities. These calculations were performed within the framework of the Nextnano[1].

Keywords

solar cell**;** nextnano3d**;** AlGaAs /AlGaAs/InGaAs**;** Photovoltaic

1. INTRODUCTION

.The advantage of solar cells fabricated by forming a monolithic crystalline stack of materials with the desired bandgaps is the simplicity in processing. The disadvantage is that there are a limited number of materials combinations which can be epitaxially grown in device quality form.

The experimentally-measured conversion efficiencies are up to 40.7% [2] and 40.8% [3] . The monolithic, series interconnected multi-junction (MJ) solar cells based on group III-V semiconductor material system are proven to be very attractive for many space and terrestrial applications [4,5)

Due to the importance of the tunnel junction on the overall conversion efficiency, this paper presents the comparison of the Energy band diagram characteristics for the AlGaAs/InGaAs tunnel junction and AlGaAs /AlGaAs/InGaAs .

In this work, based on Nextnano simulator, dimensional (1D) simulation has been performed on AlGaAs/InGaAs and AlGaAs /AlGaAs/InGaAs solar cell devices. This paper is organized as follows. In section 2, the device structure and simulation details are explained. The simulator Nextnano..Modeling results, analyses and discussion are presented in section 3. Finally, a summary is given in section 4.

Good simulation software could usually help to obtain a better understanding of the performance characteristics and predict the operational condition for these solar cells

…2. DEVICE STRUCTURE AND SIMULATION DETAILS …

AlGaAs/InGaAs solar cells were fabricated on a GaAs substrate , based on a experimental results of US patent [6],AlGaAs and InGaAs single junction solar cells and AlGaAs tunnel junction also Possible design optimization of triple-junction (TJ) solar cell is suggested by simulation in order to enhance the efficiency starting from the bottom, the TJ solar cell is constructed with three subcells, namely AlGaAs AlGaAs and InGaAs junctions stacked in series. An anti-reflective coating (ARC) layer is at the very top

The tunnel junction is implemented and placed between two subcells. Although the actual device growth uses thin GaAs .

simulating the device. The geometry of the device is completely specified in the input file Each model can be accompanied by a full set of its parameters and each material can be doped by any dopant to the desired concentration. This can be done in a regular uniform way, in a linear or even a Gaussian distribution.

starting from the bottom, the TJ solar cell is constructed with three subcells, namely AlGaAs AlGaAs and InGaAs junctions stacked in series. An anti-reflective coating (ARC) layer is at the very top The tunnel junction is implemented and placed between two subcells. Although the actual device growth uses thin GaAs .

AlGaAs layer is the first layer which is heavily doped (10^{18} -10^{19} cm^{-3}) with a 1.920 eV band at the surface graded to 1.890 eV. The top cell is p-n homojunction $Al_{0.14}$ $Ga_{0.86}$ As moderately doped (10^{17} cm^{-3}), and exhibit 1.590 eV bandgap.

n-doped Al GaAs, heavily doped (10^{18} cm^{-3}), bandgap of greater than 1.62 eV, is inserted between the top cell and tunnel junction. the tunnel homojunction$Al_{0.141}$ $Ga_{0.859}$ As material heavily doped (10^{19} -10^{21} cm^{-3}cm) to provide a minimum 1.62 eV bandgap .the heavily p-doped AlGaAs(10^{18} cm^{-3}), is between the tunnel junction and bottom cell which has a bandgap lower than the bandgap of the first layer is $In_{.0.388}Ga_{0.612}$ homojunction are moderately doped (10^{17} cm-3) to provide a bandgap of 0.954 eV for the second layer. The homojunction InGaAs graded material is between the bottom cell and n-doped GaAs on which the cell has been formed. the effects of mismatch can be minimized by use of graded layers between the voltage producing layers Similarly for AlGaAs /AlGaAs/InGaAs solar cells Two tunnel junctions are placed between each pair of subcells. Efficiencies of 30-40% can be achieved.

the Poisson equation is solved in an AlGaAs/InGaAs and AlGaAs /AlGaAs/InGaAs monolithic cascade solar cells**,** we have established a classical calculation of conduction and valence band edge and the electron and hole densities. These calculations were performed within the framework of the Nextnano3 [7] The basic Semiconductor equations is by the solving the Schrödinger, Poisson, current continuity equations for electrons and holes and the current relations for electrons and holes

Our calculation results show the band edges diagram and electron and hole densities in the vicinity of the tunnel junction of AlGaAs/InGaAs monolithic cascade solar cell.The built-in potential has been calculated to be 1.83 V at zero bias and We assumed that all materials are strained with respect to the GaAs substrate, a graded p-type AlGaAs layer has been used to generate an electric field of 3 kV / cm (= 30 meV / 100 nm)[8,9].

3. RESULTS

Most of the photons that are absorbed in the semiconductor produce such electron-hole pairs. these electron-hole pairs generate photocurrent and in the presence of a built-in field, and the photovoltage of the solar cells.

In the figures below we show as examples of our calculation results the band edges diagram and electron and hole densities in the vicinity of the tunnel junction of AlGaAs/InGaAs monolithic cascade solar cell. The band edges diagram of AlGaAs/InGaAs monolithic cascade solar cell is showed in Fig1.Also the band edges diagram of AlGaAs/ AlGaAs/InGaAs monolithic cascade solar cell is showed in Fig2, we can see clearly that the degeneracy of heavy and light hole valence band edges is lifted, especially inside the InGaAs regions

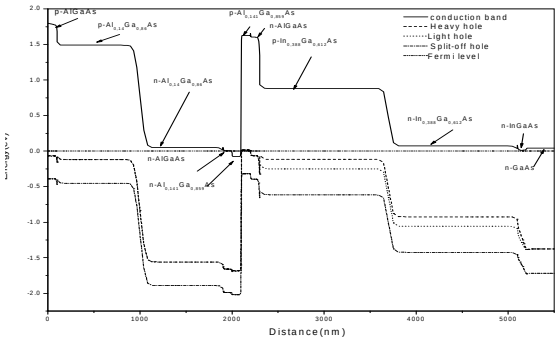

Fig.1. conduction band edges of AlGaAs/InGaAs monolithic cascade solar cell

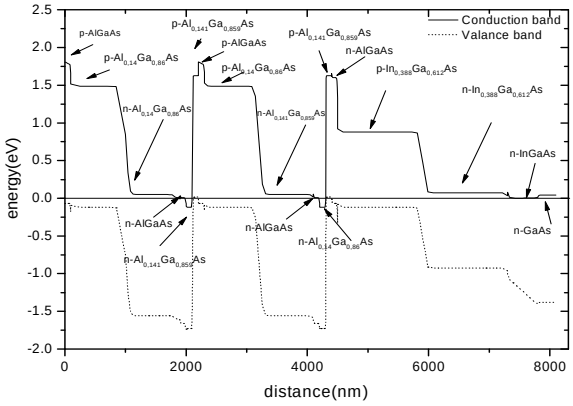

Fig.2. conduction band edges of AlGaAs/ AlGaAs /InGaAs monolithic cascade solar cell

Its well known that photons energies in excess of the threshold energy gap or band gap between the valence and the conductions bands are dissipated as heat; thus they are wasted specifically, there is a fixed quantum of potential energy difference across the band gap in the semiconductor.The band gap of AlGaAs/InGaAs as a function of distance is shown in the following Fig.3

Tunnel junctions play an important role in the MJ solar cells by facilitating the current transfer from one subcell to another. A thin tunnel junction could be simply created by doping either side of the junction very heavily.

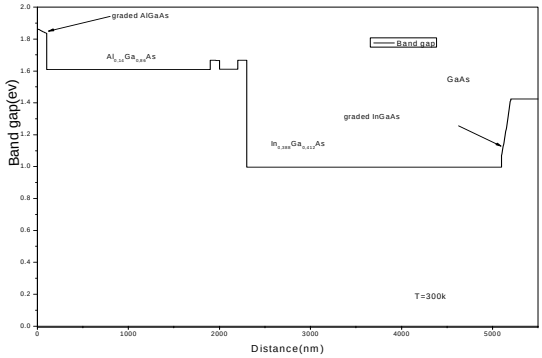

Fig.3. Band gap of AlGaAs/InGaAs monolithic cascade solar cell[2]

If both sides of the junction are sufficiently doped, the conduction band and valence bands may cross the Fermi level to align the electrons with empty states[10]. Energy band diagram for the AlGaAs tunnel junction at 0 V bias, where the electron and hole quasi-Fermi levels are superimposed and the depletion region is highlighted.Fig.4. . It is difficult to obtain high tunnelling peak current with wide gap tunnel junction, so thinning depletion layer width by formation of highly doped junction is quite necessary. the depletion layer in Fig.4 is 15nm. We could notice the band diagram near the tunnel junctions where the conduction band electrons could be aligned with the valence empty states.

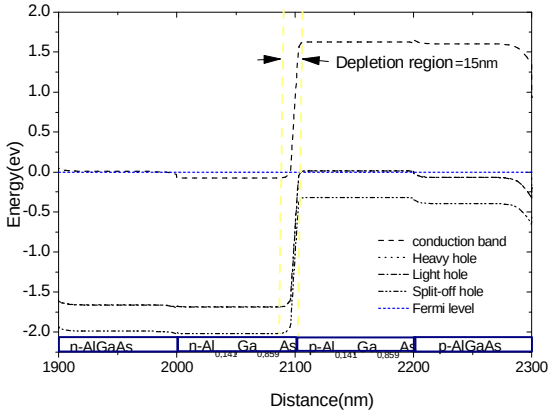

Fig.4.Energy band diagram for the AlGaAs/InGaAs tunnel junction at 0 V bias

the density has been calculated classically the density and the potential are calculated self-consistently from Poisson equation.The electron and hole densities in the vicinity of the tunnel junction for the AlGaAs/InGaAs Tandem cell are shown in Fig.5. Absorption of light near the surface of the semiconductor creates electron-hole pairs. By varying the doping density in the semiconductor, carrier density gradient can be created and Mobility Enhanced.. Also in the figure 6 allows more photogenerated current to be collected at the contact due to double tunneljunction.

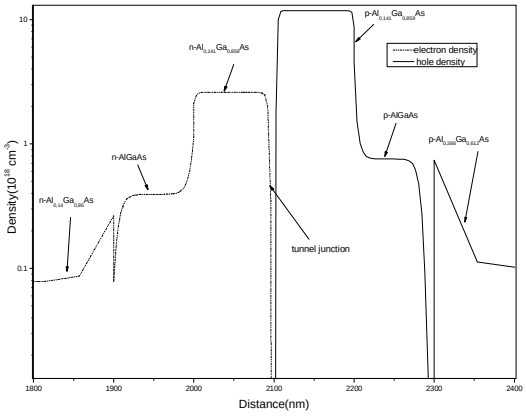

Fig.5. electron and hole densities of AlGaAs/InGaAs monolithic cascade solar cell

Fig.6. shows the simulated densities for AlGaAs/ AlGaAs/InGaAs tandem cell AlGaAs/InGaAs monolithic cascade solar

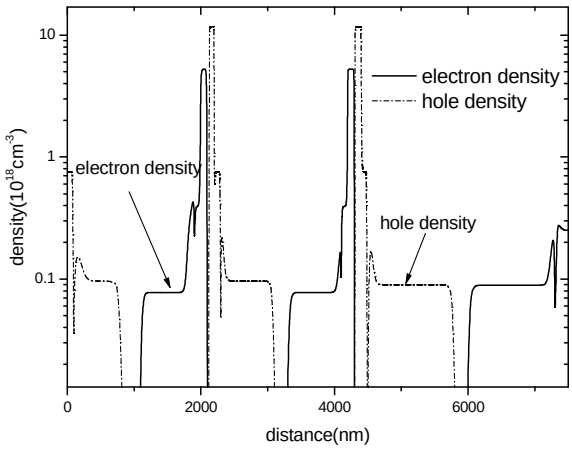

Figure 6 Electron density of AlGaAs/ AlGaAs/InGaAs /ell

4. Conclusion

Designing efficient solar cells is very important. By several key criterions in designing high quality solar cells Semiconductor materials should be chosen targeting certain wavelength of the solar radiation spectrum. This will Minimize optical losses and maximize photon absorption, reduce recombination losses in the quasi-neutral and depletion region. The implications of these two-junction or three-junction cascade solar cells to obtain maximum efficiency for terrestrial applications

5. ACKNOWLEDGMENTS

The authors would like to thank the support of the LLMC of Saida University and also the anonymous reviewers for their critical comments

6. REFERENCES

[1] Walter schottky Institute(T33),Technical university of Munich nextnano[3],Prof Peter vogl Am coulombwall 3 d-85748 Garching Germany .nextnano3@Wsi.tum.de,05/01/06

[2] R. R. King, D. C. Law, K. M. Edmondson, C. M. Fetzer, G. S. Kinsey, H. Yoon, R. A. Sherif and N. H. Karam, "40%

[3] J. F. Geisz, D. J. Friedman, J. S. Ward, A. Duda, W. J. Olavarria, T. E. Moriarty, J. T. Kiehl, M. J. Romero, A. G. Norman and K. M. Jones, "40.8% efficient inverted triple-junction solar cell with two independently metamorphic junctions", *Appl. Phys. Lett.*, 93, 2008, pp. 123505.

[4] J. M. Olson, S. R. Kurtz, A. E. Kibbler, and P. Faine, "A 27.3% efficient Ga0.5In0.5P/GaAs tandem solar cell," *Appl.Phys. Lett.* 56, pp. 623-625 (1990).

[5] D. J. Friedman, S. R. Kurtz, K. A. Bertness, A. E. Kibbler, C. Kramer, J. M. Olson, D. L. King, B. R. Hansen, and J. K. Snyder, "GaInP/GaAs monolithic tandem concentrator cells," in *Proc. 1st World Conf. PVEC*, p. 1829 (1994).

[6] US patent 4,179,70: Cascade solar cell

[7] S. Birner, Nextnano3, next generation 3D nanodevice simulator Available : http://www.nextnano.de/nextnano3l/tutorial.htm.

[8] Alex Trellakis ,Tobias Zibold,Till AndlauerE"The 3Dnanometer device project nextnano:concepts ,methods,results" spriger science+business Medias ,LLC 2006.

[9] The 3D nanometer device project nextnano: Concepts, Methods, Results Stefan Birner, Tobias Zibold, Till Andlauer, Tillmann Kubis, Matthias Sabathil, Alex Trellakis, and Peter Vogl Journal of Computational Electronics 5 (4), 285 (2006)

[10] K. Jandieri, S. D. Baranovskii, W. Stolz, F. Gebhard, W. Guter, M. Hermle, and A. W. Bett, "Fluctuations of the peak current of tunnel diodes in multi-junction solar cells," J. Phys. D Appl. Phys. **42**(15), 155101 (2009).

Design of a UV-Protected Nonwoven Fabric with Anti-mosquito Property

H. Sezgin,[1] I. Yalcin,[1] T. Gok Sadikoglu,[1]
G. Ozcan,[1] O. B. Berkalp[1]

[1]Istanbul Technical University, Textile Technologies and Design Faculty, Textile Engineering Department, Istanbul, TURKEY.

ABSTRACT

In this study, UV protected nonwoven fabrics with anti-mosquito (AntiM) property were designed by using both nano and conventional finishings to investigate their effects on mechanical and comfort properties.

Keywords

UV protection factor, anti-mosquito, air permeability, nonwoven, permetherin.

1. INTRODUCTION

There are various factors that affects the clothing's level of sun protectiveness, such as; fabrics' weave, color, weight, wetness, and also any UV absorbers that are added to enhance the level of UV protection [1,2]. The protection extended by the textile materials is denoted by Ultraviolet Protection Factor (UPF) [3]. UPF measures the amount of UV radiation that reaches the skin. UPF ranges and their protection category levels are given in Table 1. For ex; a fabric with a UPF 15 indicates that this fabric allows 1/15th of the UV-radiation to penetrate the skin [4].

Protection Category	UPF Range
Moderate	10 - 19
High	20 - 29
Very High	30 - 39
Maximum UPF	≥ 50

Table.1: UVR ratings [5].

Also ultra-violet (UV) degradation is one of the major problems of textile materials which are constantly exposed to sunlight [6].

Mosquito-borne diseases have plagued civilization for thousands of years. To diminish these diseases many chemicals are used. Permethrin is the only insect repellent used for factory treatment of clothing. It is a broad spectrum, non-systemic, synthetic pyrethroid insecticide [7].

The aim of this study is to design UV protected nonwoven fabrics with anti-mosquito (AntiM) property by using both nano and conventional finishing to investigate their effects on UPF value, tensile strength, air permeability, permethrin amount and colour fastness to light of samples.

2. MATERIALS & METHODS

100% polyester spunbond nonwoven fabrics (30 g/m^2) were used in this study. Nonwoven fabrics preffered instead of woven fabrics because it was found that non-woven fabrics have better UV resistance property than woven fabrics [8].

Type of Finish	Chemical Structure	Trade name
UV1	Anionic	UV-SUN® PES
UV2	Nano	Nonax
Mosquito Repellant	Nonionic	BEMATİN 988

Table 2. Properties of finishes.

Two types of UV protective finishes and one type of AntiM finish were used on 100% polyester spunbond nonwoven fabrics with a concentration of 10g/l. The properties of finishes are shown in Table 2. While UV1 is a conventional finish which is a dispersion of triazine, UV2 is a nano finish which is composed of ZnO. Also BEMATIN 988 was used as a AntiM finish. All finishing treatments were done by padding process. Six samples codes and their finish types are shown in Table 3.

Sample No	Type of Finish
1	-
2	UV1
3	UV1-AntiM
4	UV2
5	UV2-AntiM
6	AntiM

Table 3. Sample codes.

UPF rating, tensile strength, air permeability, permethrin amount and colour fastness to light of samples were analyzed due to AS/NZS 4399:1996, BS 2576, D 737, WHO/IS/3.1821.2, BS EN ISO 105 B02 standards respectively.

3. RESULTS & DISCUSSIONS

UPF values of the fabrics were measured by UV spectrophotometer. The results are given in Table 3. When UPF results are examined, it is clearly seen that while sample 2 has the highest value, sample 6 has the lowest one which shows that AntiM finish has a negative effect on ultraviolet protection of the samples.

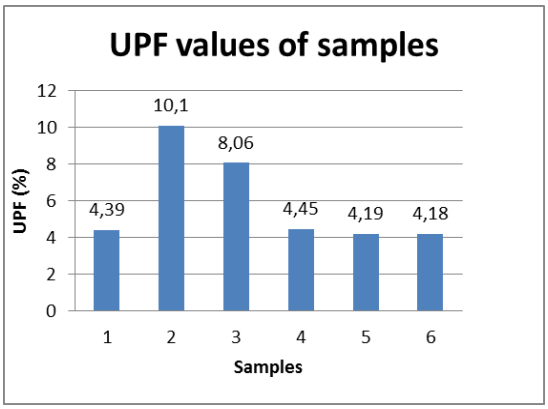

Figure 1. UPF rating results.

On the other hand, when the tensile strength results are examined from Table 4, it is seen that although there is not a significant difference between samples, samples that are UV1 treated have higher tensile strength values at both direction (MD: Machine Direction, CD: Cross Direction).

Sample No	Tensile Strength MD (N/cm)	Tensile Strength CD (N/cm)
1	13,39	5,79
2	16,62	6,45
3	15,30	8,15
4	13,26	6,04
5	12,55	6,30
6	11,25	6,39

Table 4. Tensile strength test results.

Air permeability of fabric samples were evaluated by Air Permeability Tester. All finished samples have lower air permeability values than sample 1 which is not treated shows that all of the finishes (Figure 2).

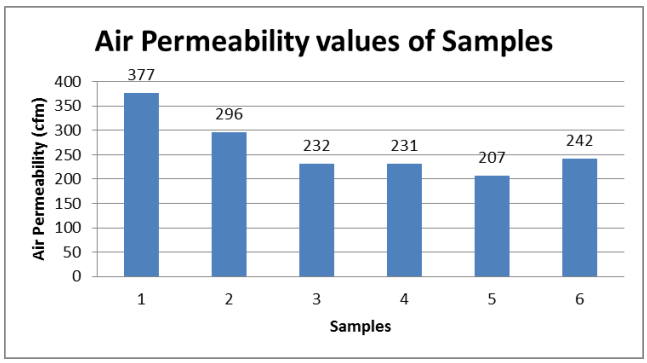

Figure 2. Air permeability test results.

The amount of permethrin was evaluated by using gas chromatography. Permethrin amount was found adequate to put away mosquitos from the specimens which have AntiM finish (Table 5).

Sample No	Permethrin Amount (%)
3	**0,6**
5	**0,18**
6	**0,17**

Table 5. Permethrin test results.

Finally, colour fastness test results showed that, all of the samples have colour fastness of 4 or 5 which confirms the fabric has high resistivity to light (Table 6).

Sample No	Colour Fastness to Light
1	5
2	5
3	4
4	5
5	4
6	4

Table 6. Colour fastness to light test results.

4. CONCLUSION

In this study, UV protected nonwoven fabrics with anti-mosquito (AntiM) property were designed as a mosquito repellent curtain. As mentioned above, when the results are examined it is seen that, colour fastness to light of all samples show that they have high resistivity to light and convenient for curtain fabric.

Also it is seen from literature that, to keep away the mosquitos from fabric, it is enough to have a little amount of permethrin on it and it is seen our results that samples that have treated AntiM finish have permethrin on them. Conventionel finished samples have higher permethrin on them when compared with nano finished samples.

UPF values show that there is not a significant difference between not treated and nano finished samples' UPF values. But conventional UV treated samples (UPF – 10) have higher UPF values than others (UPF - 4). When Table 1 is taken into consideration, it is seen that UPF values of our samples are lower than "Moderate Protection Category" . Since our samples will not be used directly to the skin, UPF values that we obtained can be adequate for such kind of applications like curtains.

Tensile strength results indicates none of the finishes has an effect on the tensile strength of samples. Also it is observed that tensile strength of samples are enough for usage as a curtain.

It is seen from results that air permeability of all conventional finished samples are higher than nano finished samples.

Although nano finished samples have lower physical and chemical properties, it is realized that both samples are convenient for the application of curtain.

REFERENCES

[1] Reinert, G., Fuso, F., Hilfiker, R., Schmidt, E. 1997. UV-Protecting Properties of Textile Fabrics and their Improvement, *Textile Chemist and Colorist*, 29 (12), 37-43.

[2] Hoffmann, K., Laperre, J., Avermaete, A., Altmeyer, P., Gambichler, T. 2001. Defined UV Protection by Apparel Textiles, *Arch Dermatol*, 137(8), 1089-1094.

[3] Saravanan, D. 2007. UV Protection Textile Materials, *AUTEX Res. J.*, 7, 53-62.

[4] http://www.indiantextilejournal.com/articles/FAdetails.asp?id=2837

[5] Das, B. R. 2010. UV Radiation Protective Clothing, *The Open Textile J.*, 3, 14-21.

[6] Harini, D., Sharada Devi, A., Anitha, D. 2012. Non-woven Drapery Lining With Ultra Violet Resistance, *J.Res. Angrau*, 40(3), 33- 36.

[7] http://www.epa.gov/pesticides/factsheets/factory-treated-clothing.html

[8] Srinivasan, R. 2001. Nonwoven fabric having both UV stability and flame retardancy, Patent no:US 6,309,97 B1. October 30:1-16.

Reduction of graphene oxide using a natural polymer

F. Khili[1, 3], R. Boukherroub[3], A. Dakhlaoui Omrani[2,*]

1. Laboratoire des Physiques des Matériaux Lamellaires et Nanomatériaux Hybrides (PMLNH), Faculté des Sciences de Bizerte, Tunisie

2. Centre National des Recherches en Sciences des Matériaux, Technopole Bordj Cedria, Hammam-Lif BP 73, 8027, Soliman, Tunisie.

3. Institut de Recherche Interdisciplinaire (IRI), Parc de la Haute Borne, 50 avenue de Halley – BP 70478, 59658 Villeneuve d'Ascq Cédex, France

* dakhlaoui_amel@yahoo.fr

ABSTRACT

Graphene oxide (GO) has been elaborated using purified graphite powder then reduced by nanocrystalline cellulose (NCC) to reduced graphene oxide (rGO). The structure and the microstructure of the as-elaborated products were investigated by X-ray diffraction (XRD), Fourier transform infrared (FTIR) spectroscopy, UV-visible (UV-VIS) spectrometry and scanning electron microscopy (SEM).

Keywords: Graphene oxide, reduced graphene oxide, green reduction.

1. INTRODUCTION

Graphene has attracted much attention among researchers due to its promising electrical, optical, chemical, mechanical, thermal and catalytic properties [1]. Up to now, various physical and chemical methods have been developed to produce graphene [2, 3]. However, most of them require high temperatures and expensive equipments. The method based on the reduction of graphene oxide (GO) is a promising and economically synthetic approach for the large scale production of graphene.

This paper, reports on the synthesis of GO and its reduction to rGO using a low-cost and largely abundant natural polymer, nanocrystalline cellulose. The X-Ray Diffraction (XRD), the UV-vis spectrometry and FTIR spectroscopy permit to confirm the total reduction of the exfoliated GO to rGO and thus the effectiveness of the process adopted here.

2. EXPERIMENTAL

2.1. Nanocrystalline cellulose preparation

The NCC used in this study was prepared by sulphuric acid hydrolysis of microcrystalline cellulose (MCC) according to the following process: 52 mL of concentrated sulphuric acid was added drop wise to 10 g of MCC dispersed in 50 mL of distilled water. The cellulose suspension obtained was heated at 44 °C while stirring for 10 min. After that, it was diluted with cold distilled water to stop the acid hydrolysis, centrifuged five times at 5000 rpm and finally dialysed against ultra-pure water for 2 to 4 days using cellulose membranes to neutral pH. The precipitate collected at the end of these processes was dried in an oven at 50 °C for 12 hours.

2.2. Graphene oxide preparation

GO was prepared using graphite powder according to the modified Hummers and Offman method [4]: 3g of graphite powder and 18 g of $KMnO_4$ were added to a mixture of concentrated sulfuric and phosphoric acids then heated at 50 °C under constant stirring. The mixture obtained after 12 h of reaction was transferred in a beaker containing glacial milli-Q-water and 30 % H_2O_2 solution to form graphite oxide suspension. The precipitate collected by centrifugation at 6000 rpm was washed successively with different solvents (HCl, milli-Q-water until neutral pH, ethanol and ether) then dried in the oven at 50 °C

2.3. Reduction of GO using NCC

The reduction of GO to rGO has been realized as follow: typically 20 mg of NCC was added to an aqueous solution of GO. The mixture was and then magnetically stirred at 100 °C. The black precipitate obtained at the end of the reaction was separated from the aqueous supernatant by centrifugation at 5000 rpm for 10 mn, washed several times with ethanol then dried in an oven at 50 °C.

2.4. Material characterization

FTIR spectra of the as-elaborated product were obtained using a Nicolet Avatar 360 spectrophotometer en mode ATR. The XRD diffraction patterns were given by a BRUKER D8 ADVANCE powder diffractometer equipped with a cupper anticathode ($\lambda_{CuK\alpha}$= 1.5406Å). Data were collected in the 2θ range 5 - 40° at an increment step of 0.02°. Morphological studies of our materials have been performed using an ULTRA 55 field emission Scanning electron microscope. The UV-vis spectra were recorded on a Perkin Elmer UV-vis spectrophotometer. The wave length range was 200-800 nm.

3. RESULTS AND DISCUSSIONS:

3.1. Nanocrystalline cellulose

SEM image of the as-prepared cellulose nanoparticles (Fig. 1) shows rods with about 11 nm in diameter and 180 nm in length. Their FTIR spectrum (Fig. 3a) shows typical bands of cellulose: The broad bands at 1386 cm^{-1} and 1325 cm^{-1} were assigned to $–CH_2$ and OH bending vibration, band at 1370 cm^{-1} corresponds to the C-H asymmetric deformation and the band near 1250cm^{-1} corresponds to the axial asymmetric strain of -C-O-C. The XRD pattern of the as-elaborated nanocrystalline fibers (Fig. 5a) is characteristic of cellulose II with high degree of cristallinity.

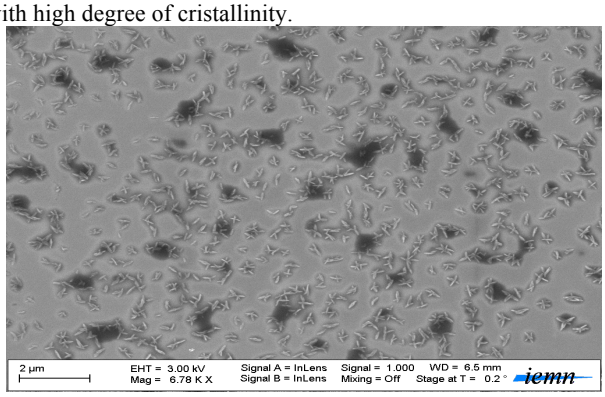

Figure1: SEM image of the as-prepared cellulose nanofibers.

3.2. Graphene oxide and reduced graphene oxide

The reduction of GO involves essentially the removal of hydroxyl, epoxy and carboxyl groups. It has been reported in the literature that the color change of the GO suspension is the first visible characteristic indicating the formation of the rGO. In our case, the fully reduction of

GO with NCC, indicated by a color change of the reaction mixture from brown (GO) to black (rGO) (Fig.2), was obtained after 48 h of reaction at 100 °C. This reduction was further evidenced by FT-IR spectroscopy (Fig. 3), UV-vis spectrometry (Fig. 4) and XRD (Fig. 5). The most attractive difference between the FT-IR spectra of the as-prepared GO and rGO was the disappearance of the bands at 1746 and 1634 cm^{-1} corresponding respectively to the stretching frequencies of the carbonyl groups, and the appearance of a new band at 1582 cm^{-1} due to the C=C stretching vibration in the rGO.

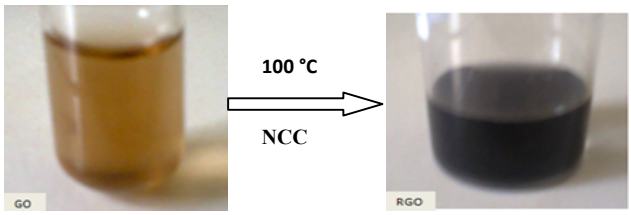

Figure 2: Photos of GO and rGO aqueous suspensions.

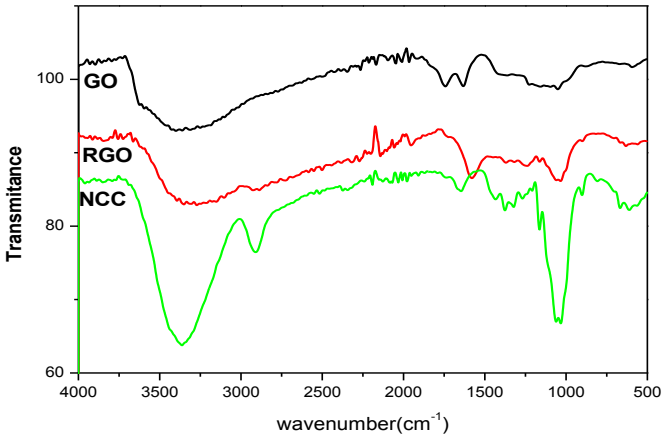

Figure 3: FTIR spectra of the NCC, GO and r GO.

The UV-vis absorption spectra of GO and rGO suspensions are given in figure 4. GO shows an absorption band at 228 nm and a shoulder at 300 nm corresponding, respectively, to the Π-Π* and n-Π* absorption transition bands. The clearly red-shift of a Π-Π* absorption band upon reaction of GO with NCC indicates the remove of some groups on the GO surface and the restoration of the conjugated structure [5].

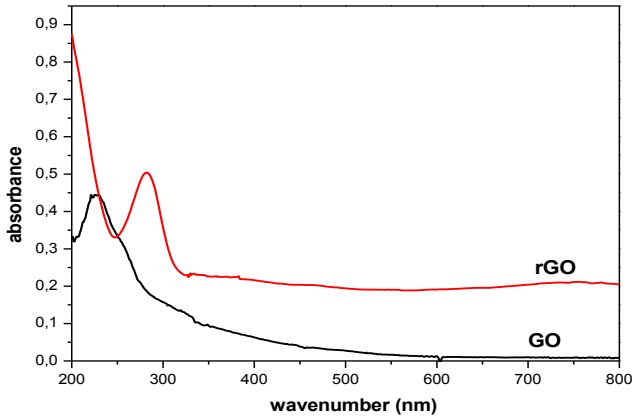

Figure 4: UV –VIS spectra of GO and rGO aqueous suspensions.

The X-Ray diffraction patterns of the GO and rGO are reported in figure 5. GO diffractogram exhibits an intense peak at 10.34° which drastically shift to higher 2θ upon reduction.

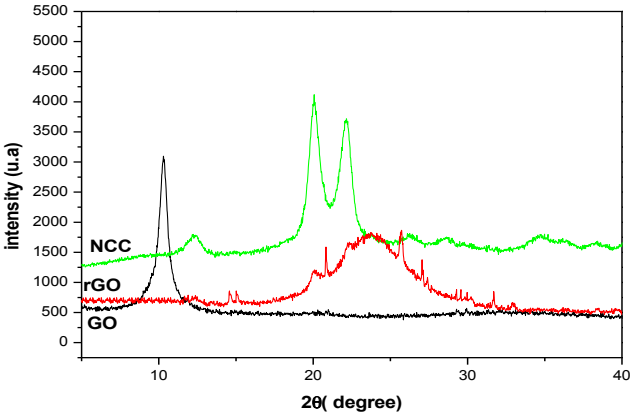

Figure 5 : X-ray diffraction patterns of NCC, GO and rGO.

5. REFERENCES

[1] H. Liu, L. Zhang, Y. Guo, Ch. Cheng, L. Yang, L. Jiang, G. Yu, W. Hu, Yunqi Liu and D. Zhu, *J. Mater. Chem. C*, 1 (**2013**) 3104.

[2] Ch. K. Chua and M. Pumera, *Chem .Soc. Rev.*, 43 (**2014**) 291.

[3] T. Kuila, A. K. Mishra, P. Khanra, N. H. Kim and J. H. Lee, *Nanoscale*, 5 (**2013**) 52.

[4] W.S. Hummers, R.E. Offeman, *J. Am. Chem. Soc*. 80 (**1958**) 1339-1339.

[5]- Qi Wang Musen.Li,S. Szunerits and Rabah Boukherroub, Electroanalysis, 26 (2014), 156–163.

Anisotropic Fabry-Pérot transmission resonance in undoped twisted bilayer graphene

A. Daboussi [1], L. Mandhour [1], and S. Jaziri [1,2]

[1] Laboratoire de Physique de la Matière Condensée, Faculté des Sciences de Tunis, Université de Tunis El Manar, Campus Universitaire Tunis, El Manar, 2092 Tunis, Tunisia.

[2] Laboratoire de Physique des Matériaux, Faculté des Sciences de Bizerte, Université de Carthage, Jarzouna, 7021 Bizerte, Tunisia.

ABSTRACT

We investigate tunneling across non doped twisted bilayer graphene. Femi line in twisted bilayer graphene at zero-energy is transformed into two separated points positioned along the transverse direction of the reciprocal space. We show that this change in the topology of low-energy band-structure affects drastically the zero-energy transmission resonances. We report the appearance for a magic twist parameter of a new kind of transmission resonances: Fabry-Pérot like resonance in addition to the Klein-like resonances characterizing the perfectly Bernal stacked bilayer graphene at zero-energy. This unusual transmission resonance shows a strong dependence on the orientation of the reservoirs interfaces and the twisted bilayer strip.

Keywords

Twisted bilayer graphene, two mini-Dirac cones, Fabry-Pérot resonance, Klein-like resonance, anisotropic.

1. INTRODUCTION

Let us consider the problem of a particle trying to pass over a potential barrier higher than its incidence energy. A classical particle would be totally reflected and then has no chance to pass over the barrier region. However, in quantum mechanics this particle has some finite probability to penetrate the barrier region. And in the context of the quantum electrodynamics (QED), a normally incident particle to a potential barrier is perfectly transmitted over the barrier region regardless its height and width: this reefers to the so-called Klein paradox which is one of the most exotic and counter-intuitive consequences of the QED.

Shortly after the first isolation of graphene [1], it has been reported [2], that Klein tunneling effect can be tested in the condensed matter context using an electrostatic barrier in single and bilayer graphene.

While a normally incident non chiral particle of a gapless semiconductor exhibits a transmission probability across the barrier region oscillating between 0 and 1 as a function of the width of the barrier (Fabry-Pérot like resonances), the massless Dirac fermion of a monolayer graphene, is perfectly transmitted at normal incidence through a potential barrier. This feature is related to Klein tunneling effect and can be understood in terms of a conversion of an electron state to a hole state at the barrier interface. And for the case of the AB stacked bilayer graphene where quasiparticles behave as massive chiral particles with quadratic dispersion relation, at normal incidence, there is a perfect reflection while the perfect transmission occurs at oblique incidence, this could be seen as another incarnation of the Klein-paradox [2].

Another kind of quasiparticles in graphene based systems, which is the coupled Dirac fermions, has been reported to describe the quasiparticles of the low-energy excitations in a rotationally faulted bilayer graphene (twisted bilayer graphene) regarding to the perfect Bernal-stacked bilayer configuration [3-6]. In what follows, we study how could be affected the zero-energy transmission resonances across twisted bilayer graphene.

2. Model

Starting from the perfect Bernal stacked bilayer graphene, keeping the bottom layer fixed and rotating the top layer by some small twist angle θ, transforms each parabolic band crossing of the perfect Bernal bilayer into pairs of Dirac cones separated by 2α along the transverse momentum direction k_y [7].

We consider a two terminal wide geometry of undoped twisted bilayer graphene with a width L_x along the x direction and a height L_y along the y direction $L_x << L_y$, connected to two strongly n-doped reservoirs made out of AB bilayer graphene. The interfaces between electrode regions and twisted bilayer strip are oriented parallel to y axis making an angle φ with respect to the symmetry axis of the twisted bilayer lattice as indicated in Figure. 1 (a). So the two mini-Dirac cones are positioned along a direction making φ regarding to the k_y momentum direction (see Figure. 1 . (b)).

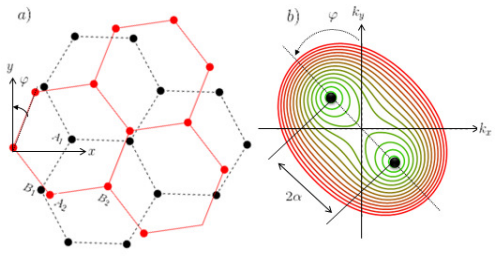

Figure. 1: (a) The twisted bilayer lattice structure projected onto the x-y plane; φ is the angle between the lattice symmetry and the y-axis. (b) Isoenergy curves and positions of the two Dirac points in the momentum space (k_x, k_y) close to a single valley.

We are interested by the effect of the twist defect and the orientation of the electrodes and the lattice symmetry axis on the transmission resonance across an undoped bilayer structure. So we consider: $V(x)=\begin{cases} 0 & 0<x<L_x \\ \dfrac{\hbar^2 k_F^2}{2m_*} & elsewhere \end{cases}$, as a potential profile along the x direction that divides the space in three different regions.

The solutions of the Schrödinger equation $H\psi = E\psi$ in the various regions of the device are given by:

$$\psi(x,y)=e^{ik_y y}\begin{cases} e^{ik_F x}\begin{pmatrix}1\\1\end{pmatrix}+re^{-ik_F x}\begin{pmatrix}1\\1\end{pmatrix}+Ee^{k_F x}\begin{pmatrix}1\\-1\end{pmatrix} & For \quad x<0 \\ Ae^{\left(k_y x+ie^{i\left(\varphi-\frac{\pi}{2}\right)}\alpha x\right)}+Be^{\left(k_y x-ie^{i\left(\varphi-\frac{\pi}{2}\right)}\alpha x\right)} \\ Ce^{\left(-k_y x+ie^{i\left(\varphi-\frac{\pi}{2}\right)}\alpha x\right)}+De^{\left(-k_y x-ie^{i\left(\varphi-\frac{\pi}{2}\right)}\alpha x\right)} & For \quad x<0<L_x \\ te^{ik_F(x-L_x)}\begin{pmatrix}1\\1\end{pmatrix}+Fe^{-k_F(x-L_x)}\begin{pmatrix}1\\-1\end{pmatrix} & For \quad x>L_x \end{cases}$$

Where:

$$H=\frac{\hbar^2}{2m_*}\begin{pmatrix}0 & k_-^2\\ k_+^2 & 0\end{pmatrix}+\frac{\hbar^2}{2m_*}\begin{pmatrix}0 & \alpha^2\\ \alpha^2 & 0\end{pmatrix}$$

We note that the complex wave vectors $k_\pm = e^{\mp i\varphi}\left(k_x \pm ik_y\right)$ depend on the misorientation angle φ.

One should stress that, in the central region, the k_y evanescent waves for the case of the undoped perfect Bernal bilayer $(\alpha=0)$ are replaced, when $\varphi=\frac{\pi}{2}$, by a mixture of α-oscillating and k_y evanescent waves in the presence of the rotational defect.

Matching the boundary conditions at the interfaces $x=0$ and $x=L_x$, we calculate the transmission coefficient across the twisted bilayer region. The total transmission probability is then directly deduced from the transmission amplitude using the relation $T=|t|^2$

3. RESULTS and discussions:

In this section we present our findings for the zero-energy transmission resonance across twisted bilayer graphene.

We show in Figure.1 the transmission probability across the twisted bilayer strip as a function of the incidence angle for a misorientation angle $\varphi=\frac{\pi}{2}$ and for three given values of the twist momentum αL_x .

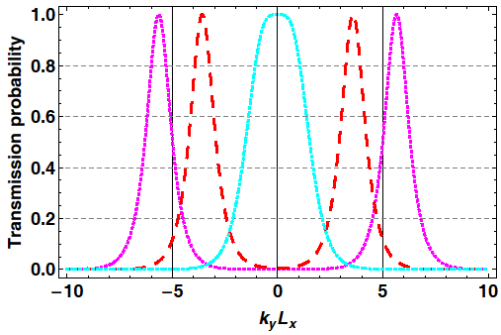

Figure. 2: (Color online) Transmission probability of the twisted bilayer when $\varphi=\frac{\pi}{2}$ as a function of the perpendicular momentum $k_y L_x$ for three different values of the twist momentum: $\alpha L_x = 0$ (dotted magenta), $\alpha L_x = \pi$ (dot-dashed cyan) and $\alpha L_x = \frac{5\pi}{2}$ (dashed red). The doping of the reservoirs is taken such that $k_F L_x = 200$.

From Figure. 2, one can distinguishes two kinds of transmission resonances, corresponding to peaks with unit value, when comparing the form, the position and the number of these peaks. For $\alpha L_x \neq \pi$, there are two narrow peaks occurring at oblique incidences. These transmission resonances correspond to Klein-like resonances since they originate from transmission via evanescent waves across the barrier region [7].

For $\alpha L_x = \pi$, the transmission resonance (only one wide peak) occurs at normal incidence. This resonance is unusual as compared to the zero-energy transmission resonances for the case of the monolayer and the perfect Bernal stacked bilayer graphene since the perfect transmission at normal incidence is the signature of the Klein tunneling effect in monolayer graphene [8-10] whereas the perfect reflection at normal incidence characterizes the Klein-like tunneling in the bilayer structure [11-12]. This resonance ($\alpha L_x = \pi$) originates from the constructive interference of the oscillating waves inside the barrier in between the two reservoirs. The potential barrier can be assimilated to a cavity made of two interfaces as the well-known optical Fabry-Pérot interferometer. The observation of the Fabry-Pérot resonance at zero-energy and normal incidence constitutes a striking effect of the twist on the bilayer grapheme [7].

Figure. 3 shows the effect of the misorientation angle φ on this Fabry-Pérot transmission resonance. The Fabry-Pérot resonance finds a strong dependence on φ. In fact, Fabry-Pérot resonance appears only for $\varphi=\left(n+\frac{1}{2}\right)\pi$; where n is an integer. This corresponds to the two mini-Dirac cones positioned along the longitudinal momentum direction k_x. As soon as the direction connecting the two mini-cones no longer coincides with the k_x-direction, the twisted bilayer strip becomes a perfectly reflecting device.

Controlling the orientation of the interfaces of the reservoirs and the symmetry lattice axis permits to switch between a perfect

transmission and a perfect reflection through the undoped twisted bilayer strip.

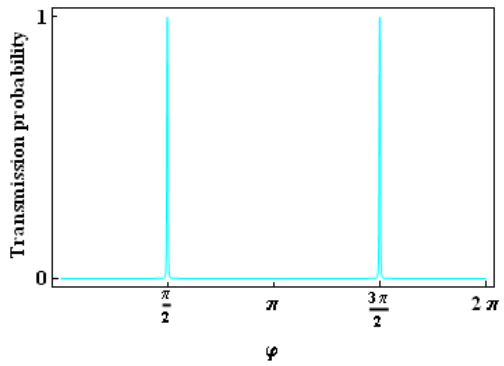

Figure. 3: Transmission probability of the twisted bilayer for $\alpha L_x = \pi$ and $k_y L_x = 0$ (Fabry-Pérot resonance) as a function of the misorientation angle φ. The doping of the reservoirs is taken such that $k_F L_x = 200$.

4. CONCLUSION:

As a conclusion, we have investigated the zero-energy transmission resonances across twisted bilayer graphene. We have reported an unusual Fabry-Pérot transmission resonances that does not exist neither for the case of the single neither for the bi-layer graphene occurring for a specific twist parameter and at normal incidence. This kind resonance exhibits a strong dependence on the misorientation of the interfaces and symmetry lattice axis of the twisted bilayer strip. The present work provides a way to monitor the electron transmission through such device.

5. REFERENCES

[1] Novoselov, K. S. *et al.*, Nature Phys. **2**, 177 (2006).

[2] Katsnelson, M. I. , Novoselov, K. S., and Geim, A. K. , Nature Phys. **2**, 620 (2006).

[3] Lopes dos Santos, J. M. B. , Peres, N. M. R. and Castro Neto, A. H., Phys. Rev. Lett. **99**, 256802 (2007).

[4] de Gail, R. , Goerbig, M. O. Guinea, F. ,Montambaux, G., and Castro Neto, A. H. , Phys. Rev. B **84**, 045436 (2011).

[5] de Gail, R. , Goerbig, F. ,Montambaux, G., Phys. Rev. B **86**, 045407 (2012).

[6] Shallcross, S. , Sharma, S. , Kandelaki, E., and Pankratov, O. A.,Phys. Rev. B **81**, 165105 (2010).

[7] Daboussi, A. , Mandhour, L. , Fuchs, J.N., and Jaziri, S. , Phys. Rev. B **89**, 085426 (2014)

[8] Katsnelson, M. I. , Eur. Phys. J. B **51**, 157 (2006).

[9] Tworzydło, J. , Trauzettel, B. , Titov, M., Rycerz, A. and Beenakker, C. W. J., Phys. Rev. Lett. **96**, 246802 (2006).

[10] Allain, P. E., and Fuchs, J. N., Eur. Phys. J. B **83**, 301 (2011).

[11] Katsnelson, M. I. , Eur. Phys. J. B **52**, 151 (2006).

[12] Snyman , I. ,and Beenakker, C. W. J. ,Phys. Rev. B **75**, 045322 (2007).

SCATTERING
BY Single Wall CARBON NANOTUBES USING WCIP METHOD

J. Selmi [1], R. Bedira [1], A.Gharsallah[1]

[1]Laboratoire de physique de la Matière Molle et Modelisation Electromagnetique, Faculté des Sciences de Tunis, 2092 ElManar, Tunisia

Selmi_jamila@yahoo.com,Rachida.Bedira@fst.rnu.tn,ali.gharsallah@gmail.com

ABSTRACT

The problem of scattering of an incident plane wave by carbon nanotubes has attracted considerable attention of scientific community, certainly for their remarquable physics proprieties. In this work, the Wave Concept Iterative Process (WCIP) has been applied to analyses the electromagnetic scattering problems of single wall carbon nanotubes in free space, showing its accuracy and fast convergence. Numerical results illustrate the scattering current density and Radar Cross Section (RCS) for single wall carbon nanotubes.

Keywords

Wave Concept Iterative Process (WCIP), Electromagnetic scattering, Carbon Nanotubes, Single Wall CNT (SWCNT), Radar Cross Section (RCS).

1. INTRODUCTION

Using the Wave Concept Iterative Process (WCIP) to resolved a problem of scattering wave by Carbon NanoTubes CNTs [1], is regarded as a challenge, because since its discovery WCIP is used to analyses microwaves circuits [2], [3], [4], and applied to reach scattering problems by conductors bodies [5] , [6].This paper presents the Wave Concept Iterative method in order to analyse the electromagnetic scattering by a carbon nanotubes. The current density of Single Wall Carbon NanoTubes is presented and compared with either method [7]. Then, the Radar Cross Section (RCS) is reached and compared with analytic method.

In this work single wall CNT (SWCNT) is studied, because the material has many unique proprieties.

2. Electromagnetic scattering by single wall carbon nanotubes using WCIP method

2.1. The Wave Concept Iterative Process (WCIP)

2.1.1 Concept of Waves

Consider an arbitrary shaped object bounded by surface S, and let $\vec{\mathbf{n}}$ denote the normal vector to the surface in each point as presented in Figure1.

The principle of the WCIP is the expressions of boundary and closing conditions in terms of waves, incident $\vec{\mathbf{A}}$ and reflected $\vec{\mathbf{B}}$, a system of equations relates both the incident and reflected waves is deduced from these conditions. This system is resolved by an iterative process. The resolution is achieved when a good precision is reached on the required value.

$$\vec{\mathbf{A}} = \frac{1}{2\sqrt{\mathbf{Z}_0}}\left(\vec{\mathbf{E}} + \mathbf{Z}_0\left(\vec{\mathbf{H}} \wedge \vec{\mathbf{n}}\right)\right) \qquad (1a)$$

$$\vec{B} = \frac{1}{2\sqrt{Z_0}}\left(\vec{E} - Z_0\left(\vec{H} \wedge \vec{n}\right)\right) \qquad (1b)$$

With $\mathbf{Z}_0$ is an arbitrary impedance parameter, chosen as the free space impedance.

$$\mathbf{Z}_0 = \sqrt{\frac{\mu_0}{\varepsilon_0}} = 120\pi\Omega \qquad (2)$$

$\vec{\mathbf{E}}$ and $\vec{\mathbf{H}}$ are the tangential components of electric and magnetic fields, respectively, where $\vec{n}$ denoted the normal vector to the surface S defined in each cells.

2.1.2. The Iterative process

The primary electromagnetic fields $(\vec{E}_0, \vec{H}_0)$ are introduced in the spatial domain with the adjunction of $\vec{A}_0$, the relationship between the incident and reflected fields is expressed by the following equations:

$$\vec{A} = \hat{\Gamma}\vec{B} \quad (3)$$

$$\vec{B} = R\vec{A} + \vec{B}_o \quad (4)$$

Where:

- $\hat{\Gamma}$ Designates the scattering operator described in the spectral domain [8].
- R is a reflected coefficient defined on the surface in the special domain [9].

2.2. Carbon nanotubes structure

The carbon nanotube CNT is formed by rolling up the honeycomb lattice structure of grapheme such that the circumference of the tube coincides with the chiral vector c = ma_1+ na_2 [10], here m and n are two integers that completely determine the structure and the properties of the carbon nanotube CNT (Figure1).

2.2.1. Single Wall CNT (SWCNT)

Single Wall CNT (SWCNT) is the result of the structure if one layer is used to form a tube (Figure2). if the tube consists of several co- centric cylinders, we call it multi-wall CNT (MWCNT).

CNTs with the structure (n, 0) are called zig-zag CNT because the pattern created along the circumference of the tube resembles a zig-zag motion. The structure (n, n) is called armchair. Tubes that have n # m are called chiral. The radius of the CNT is given by[11].

$$r = \frac{b_0}{2\pi}\sqrt{n^2 + mn + m^2}$$

$$b_0 = |a_1| = |a_2| \quad (5)$$

2.3. Electromagnetic scattering by SWCNT

The general theory can be used to construct the response of the CNT to any kind of source excitation. Therefore, the electromagnetic field impinging on the CNT takes the simple form of plane wave.

A carbon nanotube of chirality (n, m) will be metal if (2n + m) is a multiple of 3. If not, it will be semiconductor. Thus a carbon chair nanotube will be always metal (because there is 2m+m) while a nanotube zigzag or chiral will be either metal, or semiconductor [12].

The fields in outer region and inner one are given by[8]:

$$\begin{pmatrix} E_{2Z} \\ H_{2z} \end{pmatrix} = J_n(k_\rho\rho)F_n(z)\,a_2 + H_n^{(2)}(k_\rho\rho)F_n(z)\overline{R}_{12}\,.\,a_2 \quad (6)$$

$$\begin{pmatrix} E_{1Z} \\ H_{1z} \end{pmatrix} = J_n(k_\rho\rho)F_n(z)\,\overline{T}_{12}\,.\,a_2 \quad (7)$$

Where R_{21} and T_{21} are the reflection and transmission matrices respectively

Applying the previous equations we deduce incident and reflect wave's inner and outer carbon nanotubes.

$$\vec{A}_1 = \frac{1}{2\sqrt{Z_0}}\left(\vec{E}_{T1} + Z_0\left(\vec{H}_{T1} \wedge \vec{n}\right)\right) \quad (8)$$

$$\vec{A}_2 = \frac{1}{2\sqrt{Z_0}}\left(\vec{E}_{T2} + Z_0\left(\vec{H}_{T2} \wedge \vec{n}\right)\right) \quad (9)$$

$$\vec{B}_1 = \frac{1}{2\sqrt{Z_0}}\left(\vec{E}_{T1} - Z_0\left(\vec{H}_{T1} \wedge \vec{n}\right)\right) \quad (10)$$

$$\vec{B}_2 = \frac{1}{2\sqrt{Z_0}}\left(\vec{E}_{T2} - Z_0\left(\vec{H}_{T2} \wedge \vec{n}\right)\right) \quad (11)$$

3. RESULTS and discussions:

Figure.1 shows the honeycomb lattice structure of grapheme

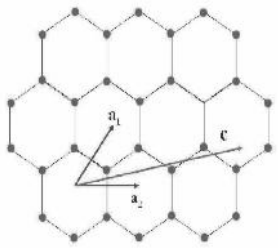

Figure.2 shows how to obtain the different kinds of single wall carbon nanotubes.

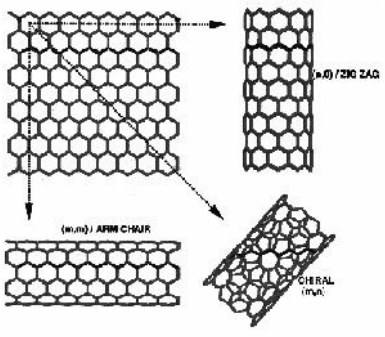

Figure.3 shows the single wall carbon nanotube and multiple wall carbon nanotubes

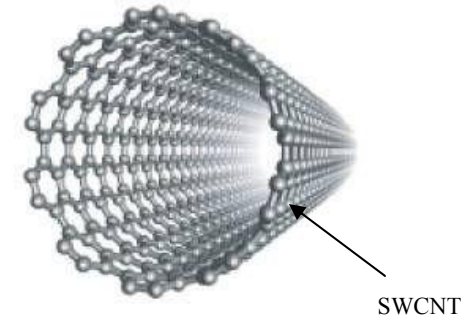

We represented the current on the surface of the structure the results are in agreement with calculates analytical

Figure 4 shows the current on the surface of the structure

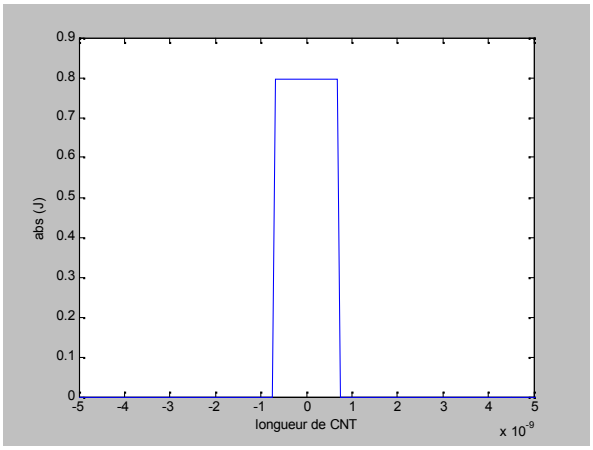

In figure 5 the Radar Cross Section is considered, a check with the analytic solution is included, a high degree of accuracy is obtained. The calculated numerical results are given about 40s. it is clear that the present (WCIP) method is not time consuming.

Figure 9 shows the Radar Cross Section

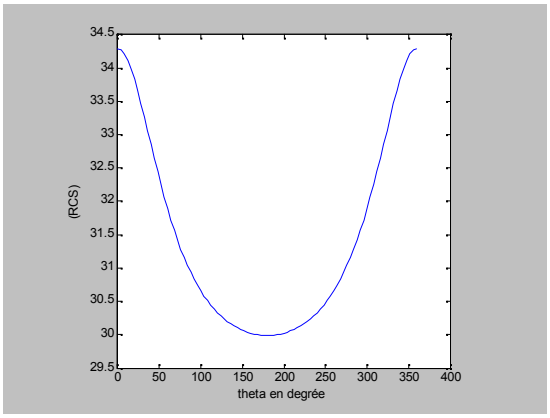

4. REFERENCES

[1] Iijima, I, 1991Nature London 354, 56.

[2] A. Gharsallah, A.Gharbi and H. Baudrand,. , 2001.Efficient analysis of multiport passive circuits using the iterative technique. Electromagnetics, 73-84.

[3] R.S. N'Gongo and H. Baudrand. 1999. Application of Wave Concept Iterative Procedure in Planar Circuits. Recent Res. Devel. Microwave Theory and Technique, 185-197.

[4] N. Raveu, O. Pigaglio, G.Prigent and H. Baudrand. 2007. Improvement in the Wave Concept Iterative procedure Through Spectral Connection. IEEE EuMW, Munich.

[5] R.Bedira, A.Gharsallah, A.Gharbi and H.Baudrand,. 2002. An Iterative Process Based on the Concept of Waves for Electromagnetic Scattering Problems. Electromagnetic, 129-140.

[6] J.Selmi, R.Bedira, A.Ghasallah, A.Gharbi and H.Baudrand.2010. Iterative Solution of electromagnetic scattering by arbitrary shaped cylinders.The Applied Computational Electromagnetic Society.

[7] Miano, G., Forestiere, C., Maffucci, A., Maksimenko, S.A., Slepyan, G.Y. (2011), "Signal propagation in carbon nanotubes of arbitrary chirality", *IEEE Transactions on Nanotechnology*, Vol. 10 pp.135-149.

[8] Mikki, S.,M, Kishk, . A . 2007, of optical scattering by carbon nanotubes. Microwave & Optical Technology Letters, Vol. 49, No. 10, 2360–2364, October.

[9] R. Ruppin,. 2006. Scattering of electromagnetic Radiation by a Perfect Electromagnetic conductor cylinder, Journal of Electromagnetic Waves and Applications, vol. 20, N° 13, 1853-1860,

[10] Xiang An and Zhi-Qing Lü. , 2006.,A.Fast Algorithm Based on Practical Basic SolutionVectors Domain Decomposition Methode for Scattering Analysis of Electriclly Large Cylinders", Journal of omputational Physics, 219. 930-942

[11] Smalley, R. E., M. S. Dresselhaus, G. Dresselhaus, and P. Avouri. 2001., Carbon Nanotubes: Synthesis, Structure, Properties and Applications, Springer.

[12] Miyamoto, Y., Louie, S.G., Cohen, M.L. 1996. Chiral conductivities of nanotubes. *Physical Review Letters*, Vol. 76 pp.2121-212

Development of Enzyme-Based Biosensor for Environmental Monitoring

Leboukh, S[1, 2]., Gouzi, H[2*]., Harek, Y[3]

[1]Centre Nationale de recherche en Soudage et Contrôle C.S.C, Route de Dély-Ibrahim, B.P 64, Alger, Algérie.
[2]Université Amar Telidji, Faculté des Sciences, Département de Biologie, Route de Ghardaïa, B.P 37G, Laghoaut 03000, Algérie.
[3]Laboratoire d'Electrochimie et Chimie Analytique, Département de Chimie, Faculté des Sciences, Université Abou Bekr Belkaid, Tlemcen 13000, Algérie.

[*]Author to whom correspondence should be addressed:
Hicham Gouzi
Université Amar Telidji, Faculté des Sciences, Département de Biologie, Route de Ghardaïa, B.P 37G, Laghoaut 03000, Algérie.
E-mail: h.gouzi@mail.univ-lagh.dz or hicham.gouzi@yahoo.fr; Tel: +213-551-22-77-53; Fax: +213 29 92 90 68

Abstract: Biosensors, combining a selective biological recognition element and a sensitive transducer, are versatile analytical tools applied more and more in different fields, such as medicine, food quality and safety control, and environment pollution monitoring. The intention of this article is to reflect the advances and describe the trends on biosensors for environmental applications. Biosensors are useful analytical tools for environmental monitoring, capable of providing results in real time, simple to use, portable and cost-effective. Biosensors, detecting and measuring specific compounds or compound classes such as pesticides, hazardous industrial chemicals, phenols and toxic metals.

Keywords: Enzyme; Biosensors; pollutants, Environmental monitoring

1 Introduction

There is a strong demand for environmental monitoring technologies today due to the ever increasing environmental pollutions [1]. Monitoring of contaminants in the air, water and soil is an instrumental component in understanding and managing risks to human health and the environment. Given this requirement as well as the time and cost involved in traditional analytical chemical analysis of environmental samples, there is an expanding need for simple, rapid, cost-effective and field portable screening methods.

Biosensors and bioanalytical methods appear well suited to complement standard analytical methods for a number of environmental monitoring applications [2].

Biosensors have replaced conventional methods, which are often complicated, less sensitive, time-consuming, expensive and not suitable for in situ monitoring [3]. Whereas stability and reproducibility have been sometimes problematic for biosensors due to the inherent instability of biomaterials used as sensing elements, several intelligent immobilization methods that help to overcome these difficulties emerged [1].

Enzyme sensors have been the target of intense research and development recently and have proven to be both rapid and highly selective. In this review, the author will emphasize the recent developments in the field of enzyme sensors and relevant technologies as applied to environmental monitoring.

2 Biosensor

A biosensor is an analytical device that consists of an immobilized biological material (e.g. enzyme) in intimate contact with a compatible transducer (e.g. electrode), which will convert the biochemical signal into a quantifiable electrical signal [4] (Fig. 1).

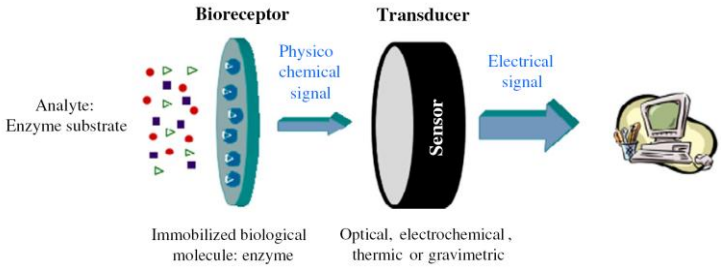

Figure 1 Scheme of biosensor [45].

The biomolecules are responsible for the specific recognition of the analyte whereas the physicochemical transducer supplies an electrical output signal which is amplified by the electronic component [5].

Biosensors are usually classified into various basic groups according either to the method of signal transduction or to the biorecognition principle [6]. Accordingly, biosensors can be categorized as electrochemical, optical, piezoelectric and thermal sensors on the basis of the transducing element, and as immunochemical, enzymatic, non-enzymatic receptor, whole-cell and DNA biosensors on the basis of the biorecognition principle.

In enzyme-based biosensors, the biological element is the enzyme which reacts selectively with its substrate [8]. The specificity of enzymes is the main reason for their use in biosensors [7]. Enzymes were historically the first molecular recognition elements included in biosensors and continue to be the basis for a significant number of publications reported for biosensors in general as well as biosensors for environmental applications. There are several advantages for enzyme biosensors. These include a stable source of material (primarily through biorenewable sources), the ability to modify the catalytic properties or substrate specificity by means of genetic engineering, and catalytic amplification of the biosensor response by modulation of the enzyme activity with respect to the target analyte [2].

Enzymatic biosensors have been developed using various electrochemical signal transducers, where enzyme is retained by immobilization, and various measuring methodologies. An important step is therefore the immobilization of the enzyme on the

device acting as transducer. Various immobilization methodologies as well as different materials have been used.

The altered catalytic and stability properties, most likely displayed by the immobilized enzyme after the immobilization process, have to be considered for evaluating the efficiency of the enzyme as biosensor. The principle behind the action of enzymatic biosensors is the inhibition with a consequent decrease of the catalytic activity of the immobilized enzyme in the presence of the polluting substance acting as the analyte utilized for quantification [50].

3 Immobilization of biomaterials

The development of biosensors based on immobilized enzymes came about to solve several problems such as loss of enzyme (especially if expensive), maintenance of enzyme stability and shelf life of the biosensor, and additionally to reduce the time of the enzymatic response and offer disposable devices which can be easily used in stationary or in flow systems. To do this, several immobilization techniques have been investigated. These techniques include physical entrapment, microencapsulation, adsorption, covalent binding and covalent cross-linking, and several different approaches to enzyme immobilization have been reported in the literature [9].

The first biosensor was an enzyme sensor (i.e. glucose) sensor reported by Clark in 1962 [10]. His biosensor measured the product of glucose oxidation by glucose oxidase using an electrode which was a remarkable achievement even though the enzyme was not immobilized on the electrode. Updark and Hicks have developed an improved enzyme sensor using enzyme immobilization. Their sensor combined the membrane-immobilized glucose oxidase with an oxygen electrode, and oxygen measurements were carried out before and after the enzyme reaction. Their report showed the importance of biomaterial immobilization to enhance the stability a biosensors. Typical immobilization carriers (e.g. beads or membranes) are made from glass, alginate or artificial resins.

Immobilization matrices which confer higher stability of biomaterials, and thus the sensor response, attracted greater attention and some interesting studies have been reported in the last few years [1].

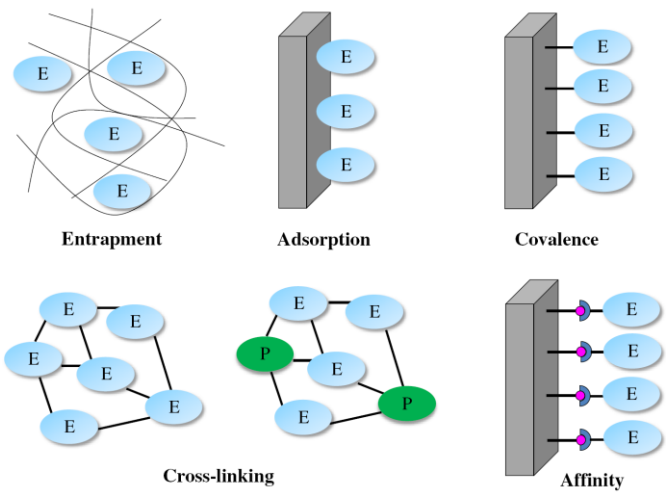

Figure 2 Shematic representation of the main different methods of enzyme immobilization. E: enzyme, P: inert protein [45].

4 Enzyme sensors for environmental analysis

Numerous enzyme sensors have been developed since the first enzyme sensor, and a considerable sum of these are used in environmental monitoring. The last few years have seen improvements in inorganic phosphate sensors using enzymes and it is expected that some of these sensors will be used in the field in the near future.

As a result of human and technological development, a wide range of man-made chemicals and by-products formed in industrial or combustion processes have been, and still are, released in the environment. Some of these substances, such as pesticides, heavy metals, phenols or polychlorinated biphenyls (PCBs), are well-recognized contaminants known to affect the quality of the environment. As a consequence, a variety of biosensors have already been developed and applied to their environmental determination [11].

4.1 Inorganic Phosphate

Inorganic phosphate in surface waters can be used as a measure of eutrophication status of different water bodies, such as surface and sea waters [12]. Various enzymatic biosensors for phosphate determination have appeared in the literature in recent years [13, 14].

Because the inorganic phosphate ion detection in aquatic environment demands measurement of concentrations as low as ppb (µM) levels, highly sensitive phosphate sensors have been developed, since the report by Guilbault et *al*. [15, 16]., which described the first phosphate sensor used two enzyme reactions catalyzed by alkaline phosphatase and glucose oxidase. The enzymes were mixed with gultaraldehyde and placed on a platinum electrode and the sensor detected the change in dissolved oxygen concentration before and after the enzyme reactions.

Guilbault and Cserfalvi [16] suggested that phosphate could be detected by using an enzyme reaction catalyzed by phosphorylase A, and Wollenberger and Scheller [16, 17] constructed a sensor based on the phosphorylase reaction that could measure mM concentrations of phosphate using an oxygen electrode. A combination of nucleoside phosphorylase and xanthine oxidase was found to be more suited for rapid detection than the phosphorylase based sensor. Amplification by orthophosphate recycling was achieved using an enzyme reaction catalyzed by alkaline phosphatase. Wollenberger et *al*. [14, 16] also constructed a sensor using these three enzymes i.e. phosphorylase, xanthine oxidase and alkaline phosphatase, which lowered the detection limit by 10-fold (10-2µM) compared to that without alkaline phosphatase (10-1 µM).

Parellada et *al*. [18] described a configuration based on the sequential action of three enzymes that opens up a way to construct reagentless enzymatic phosphate sensors.

4.2 Organophosphate

The enzymes acetylcholinesterase (AChE), butyrylcholinesterase (BuChE) and organophosphate hydrolase (OPH) have received much attention as alternatives for the detection of organophosphates (OPs) and have been demonstrated in a range of amperometric, potentiometric, conductometric and optical formats [19].

Organophosphorus pesticides are very potent irreversible inhibitors of cholinesterases. The inhibitory action of OPs is based on their ability to irreversibly modify the catalytic serine residue in acetylcholinesterases (AChE) [20]. There are several different methods of OP pesticide detection [21, 22, 23] and many of them are based on the cholinesterase inhibition test. The assay may be carried out in solution or the enzyme may be immobilized onto an electrochemical electrode [24].

Many biosensors, such as pesticides, have been developed to detect toxicants in environment [19, 25]. Organophosphates and carbamates used as insecticides e.g. paraoxon are quite toxic but are widely used in modern agriculture.

Jeanty and Marty [26], Villatte et *al*. [27]; Bernabei et *al*. [28] and Arduini et *al*. [29], reported both organophosphates and carbamate detection systems that were based on acetylcholinesterase AchE inhibition. AchE is an enzyme that catalyzes the hydrolysis reaction of acetylthiocholine to thiocholine which is inhibited by organophosphates or carbamates. The degree of inhibition correlates with the change in the concentration of organophosphates.

Liu et al. [19] reported paraoxon detection based on self-assembled AChE on a CNT-modified electrode. The LOD was 0.4 pM and the linearity was observed up to 1.6 mM.

Du et *al*. [36] developed an AChE biosensor in which AChE was immobilized onto a glassy-carbon electrode (GCE) surface modified with CdTe QDs/AuNPs. The inhibition of monocrotophos was proportional to its concentration in two ranges, 0.005–4.48 µM and from 0.009–0.067 µM, with an LOD of 1.34 nM.

Organophosphorous hydrolase (OPH), on the other hand, is able to hydrolyse a number of OP pesticides, such as paraoxon, parathion, coumaphos, methyl parathion, and chemical warfare agents such as sarin and soman. OPH enzyme reaction has been combined with a variety of transduction schemes to construct simple OPH biosensors for the direct quantification of these pesticides in the environment [52].

Hydrolysis of these OP pesticides generates p-nitrophenol, which is an electroactive and chromophoric product. Thus, OPH could be combined with an optical transducer to measure the absorbance of p-nitrophenol or with an amperometric transducer to monitor the oxidation or reduction current of this product [30].

A simple potentiometric enzyme electrode for the direct, sensitive, selective and rapid determination of organophosphate nerve agents, using organophosphorus hydrolase immobilized via crosslinking on the surface of a pH electrode that can potentially be used for on-line monitoring of detoxification processes [31].

Zhao et *al*. [57] developed an OPH biosensor for detection of methyl parathion, based on self-assembly of methyl parathion hydrolase (MPH) on the Fe_3O_4@Au nanocomposite. Under optimal conditions, the biosensor shows rapid response and high selectivity for the detection of methyl parathion, with a linear range of 0.5–1000 ng/mL and an LOD of 0.1 ng/mL.

OP pesticides and carbamates can be detected in not only single enzyme systems, but also bi-enzyme systems [49, 52]. Recently, a biosensor composed of bi-enzymes (AChE and ChO), CdTe QDs and ACh was developed to determine dichlorvos, with a linear range of 4.49–6780 nM and an LOD of 4.49 nM [36]. This biosensor has good performance in detecting residues of dichlorvos in real samples. A sensitive bi-enzymatic biosensor based on laccasse-tyrosinase-gold nanoparticles for carbamates (carbaryl, formetanate hydrochloride, propoxur and ziram) was prepared in a single step by electrodeposition of a chitosan hybrid film onto a graphene doped carbon paste electrode [49].

4.3 Phenols

Phenolic compounds, and especially chlorophenols, are significant environmental pollutants because of their high toxicity and possible accumulation in the environment [32]. Parellada et *al*. [19] developed an amperometric biosensor, with tyrosinase (a polyphenol oxidase with a relatively wide selectivity for phenolic compounds) immobilized in a higrogel on a graphite electrode, which correlated satisfactorily with the official method for the determination of the phenol index in environmental samples [18].

Laccase-based biosensors have interesting potential uses in the detection of phenolic compounds in the food industry and wastewaters as well as in biomedical and bioremediation applications. *Trametes versicolor* and *Aspergillus niger* laccases were entrapped in a polyaniline matrix for the determination of phenolic compounds. The linear detection ranges of this biosensor were between 0.4 and 6 μM for phenol, 0.2–1 μM for catechol and 0.2– 20 μM for L-DOPA in the case of *T. versicolor* laccase and 0.4–4 μM, 0.4–15 and 0.4–6 μM, respectively, for *A. niger* laccase [46].

Detection of phenolic compounds (including chlorophenols) was possible by using enzymatic biosensors loading oxidoreductive enzymes such as laccase, tyrosinase, horseradish peroxidase on various materials such as alcohol, Osmium complex, nafion/sol–gel silicate, chitosan, silica gel and using adsorption, covalent binding, entrapment, cross-linking as immobilization techniques [50].

T. versicolor laccase (Lac) was encapsulated by in situ electrospinning of a mixture of polyvinyl alcohol (PVA), Lac, PEO–PPO–PEO (polyethylene oxide–polyoxypropylene–polyethylene oxide, F108) and gold nanoparticles (Au NPs) (Liu et al., 2011). The obtained biosensor was able to detect chlorophenols with a sensitivity in the linear range following the sequence 2,4-dichlorophenol (2,4-DCP) > 2,4,6-trichlorophenol (2,4,6-TCP) > 4-chlorophenol (4- CP). The detection limits ranged between 0.04 μM for 2,4-DCP up to 12.10 μM for 4-CP. A high repeatability and an appreciable residual laccase activity (>60%) were observed after a 30-day storage period (Liu et al., 2011). The immobilization of tyrosinase in an electrochemically synthesized phosphate ion-doped polypyrrole film on a Pt disk electrode provided an amperometric biosensor with a sensitivity for the six phenols analyzed in the decreasing order catechol > phenol> 2-bromophenol > 2-chlorophenol > 2-iodophenol > 2-fluorophenol [47]. A good retention of the enzyme activity was assured by the polypyrrole thin film.

4.4 Bisphenol A

Scientific and public attention has been recently focused on a new class of environmental pollutants able to mimic or antagonize the effects of endogenous hormones. For this reason these chemicals have been called “endocrine disruptors” and their adverse effects on human and wildlife have been well documented. Bisphenol A (BPA) is a potent endocrine-disrupting compound and its toxicity is widely reported in literature [8].

Bisphenol A is a typical product of industrial societies produced in large quantities worldwide. Although only weakly estrogenic, the determination of bisphenol A in the environment is very important due to its extensive use and environmental ubiquity. BPA is one of the most important chemicals synthesized globally in high volumes and is in high demand [51].

Some amperometric enzymatic biosensors have been realised for the detection of BPA [34, 35, 36, 37]. However, the first biosensors focused on BPA determination have only recently appeared [38]. Based on a tyrosinase-carbon paste electrode, an optical biosensor for phenolic EDCs, including bisphenol A, nonylphenol and diethylstilbestrol, has also been reported [34].

Tyrosinase was used to fabricate an amperometric sensor involving a carbon nanotube modified glassy-carbon electrode for the detection of BPA. The authors observed a limit of detection of 20 nM of BPA with the biosensor developed [37].

4.5 Alkylphenol ethoxylates

Alkylphenol ethoxylates (APEs) belong to the group of non-ionic surfactants whose detection has become more important due to their endocrine-disrupting properties [6].
In wastewater treatment processes and in the environment, APEs degrade to alkylphenols (APs), which tend to be more toxic and show greater estrogenic activity. Rose et al. described the development of a capillary-based immunoassay (CIA) for APEs and APs, utilising glucose dehydrogenase (DH) as a label [39].

4.6 Heavy metals

Heavy metals are the cause of one of the most serious pollution problems of our time. Lead, chromium, cadmium, copper, zinc and mercury are among the most frequently observed metal contaminants.

The recognition of toxic effects from minute concentrations of heavy metals has resulted in regulations to reduce their presence in the environment to very low levels. There is a clear need for reliable, efficient and cost-effective wastewater treatment technologies and monitoring of the environment for the presence of heavy metals that adversely affect human health. Enzyme-based biosensors are now being utilized for monitoring heavy metal concentrations [38] ; Zhao and Jiang, 2010). A variety of enzymes have been used in the analysis of heavy metal ions based on activation or inhibition of their activities, and application of these phenomenons to the determination of these hazardous toxic elements offers several advantages, such as simplicity and sensitivity [9, 38]. Durrieu and Tran-Minh [40] described a biosensor for the determination of heavy metals based on inhibition of the alkaline phosphatase (AP) present on the external membrane of *Chlorella vulgaris* microalgae.

Biosensors based on urease inhibition are usually applied for the determination of mercury and have been reported for the determination of other heavy metals ions as well [41, 42, 43, 44]. In the biosensor proposed by Volotovsky et *al*. [42], a combination of specific additive sand-selective rewashing techniques allowed the urease-based biosensor to respond only to mercury ions. Berezhetskyy et al. [33] develop Alkaline phosphatase conductometric biosensors for measurement of heavy-metal ions in water.

A three-enzyme system (invertase, mutarotase, glucose oxidase) was immobilized on the surface of a conductometric transducer made by planar thin-film interdigitated electrodes, deposited on a ceramic pad [54]. The enzymatic system was sensitive to the presence of heavy metal ions such as Hg^{2+} and Ag^{+} acting as enzyme inhibitors. A possible reactivation of the biosensors was tested by EDTA (silver ions) or cysteine (mercury ions) solutions. Measurement of Hg+2 was also possible by an amperometric urease based-biosensor being the enzyme very sensitive to this ion [55]. Urease was also used for the development of a simple optical fiber biosensor for the determination of various heavy metal ions: Hg^{+2}, Ag^{+I}, Cu^{2+}, Ni^{2+}, Zn^{2+}, Co^{2+} and Pb^{2+} [56].

Moyo and Okonkwo [53] developed a horseradish peroxidase (HRP) biosensor in HRP was immobilized by physical adsorption onto a maize tassel (MT)-multiwalled carbon nanotube (MWCNT). The biosensing principle was based on the determination of the cathodic responses of the immobilized HRP to H_2O_2, before and after incubation in trace metal standard solutions. Using Cd^{2+} as a model metal ion, the inhibition rate of the trace metal was proportional to concentration in the range of 2–30 µg/l with a limit of detection of 0.51 µg/l. Recently, Cu^{2+}, Cd^{2+} and Pb^{2+} have been determined using horseradish peroxidase immobilized on platinum–polyaniline [32].

5. Conclusion

In recent years the research in the field of the biosensors was direct to the development of highly selective and sensitive devices, but it is our personal opinion that in the environmental analysis, as well as in food analysis, the use of biosensor is not going to be "exclusive" (like it may be for instance in the case of biocompatible implantable devices to be used in clinical chemistry).

The role of enzymatic biosensors in the determination of environmental pollutants is in our opinion not to completely replace the traditional, more sophisticated instrumental techniques, but to represent a valid complement to them, especially in all those situations where it is necessary to carry out measures "on the spot", reducing the overall times of analysis and minimizing the sample pretreatment process. In such situations a biosensor (or better an array of biosensors) would be the analytical tool supplying all the necessary information to monitor, in real time, the state of pollution of the matrix under investigation.

In the case of a positive response of one or more biosensors a "traditional" sampling procedure will be activated to carry out more specific assays aimed to confirm and quantify more precisely the extent of each case of environmental contamination. In general, biosensors for environmental analysis have several limitations: sensitivity, response time, and lifetime, which should be improved for them to become a competitive analytical tool. The areas of development that are expected to have an impact in biosensor technology are: immobilization techniques, nanotechnology, miniaturization, and multisensor array determinations.

Acknowledgements

We warmly thank Doctor Hicham GOUZI (University of Amar Telidji-Laghouat) for its contribution to the work presented here. We also thank the reviewers for their constructive comments. Authors declare that there are no conflicts of interests in this work.

References

1 Karube, I., Nomura, Y., (2000) 'Enzyme sensors for environmental analysis', *Journal of Molecular Catalysis B: Enzymatic*., Vol. 10, pp. 177–181.

2 Rogers, K.R., (2006) 'Recent advances in biosensor techniques for environmental monitoring', *Analytica Chimica Acta*., Vol. 568, pp. 222–231.

3 Fernández-Fernández, M., Sanromán., MÁ, Moldes, D., (2013) 'Recent developments and applications of immobilized laccase', *Biotechnology Advances*, Vol. 31, pp. 1808–1825.

4 Gronow, M., (1984) 'Biosensors', *Trends Biochem Sci*., Vol. 9, pp. 336–340.

5 Scheller, F., Schubert, F., (1992) 'Biosensors', New York: Elsevier Science Publishers.

6 Rodriguez-Mozaz, S., Marco, M-P., Lopez de Alda, M.J., Barceló, D., (2004) 'Biosensors for environmental applications: Future development trends', *Pure Appl. Chem*., Vol. 76, No. 4, pp. 723–752.

7 Verma, N., Singh M., (2005) 'Biosensors for heavy metals', *BioMetals*, Vol. 18, pp. 121–129.

8 Guilbault, G.G., Pravda, M., Kreuzer, M., (2004) 'Biosensors-42 years and counting', Anal. Lett, Vol. 37, pp. 14481–14496.

9 Amine, A., Mohammadi, H., Bourais, I., Palleschi, G., (2006) 'Enzyme inhibition-based biosensors for food safety and environmental monitoring', Biosensors and Bioelectronics, Vol. 21, pp. 1405–1423.

10 Buerk, D.G., (1993) 'Biosensors', Technomic Publishing, Pennsylvania, Chap. 4.

11 Rodriguez-Mozaz, S, López de Alda, M.J, Marco, M-P, Barcelo, D., (2005) 'Biosensors for environmental monitoring A global perspective', *Talanta*, Vol. 65, pp. 291–297.

12 Kroger, S., Law, R.J., (2005) 'Sensing the sea', *Trends Biotechnol*, Vol. 23, pp. 250–256.

13 Kulys, J., Higgins, I.J., Bannister J. V., (1992) 'Amperometric dertermination of phosphate ions by biosensor', *Biosens Bioelectron*, Vol. 7, No. 3, pp. 187–191.

14 Wollenberger, U., Schubert, F., Scheller, F.W., (1992) 'Biosensor for sensitive phosphate detection', *Sens Actuators.*, Vol. B 7, No. 1, pp. 412–415.

15 Guilbault, G.G., Nanjo, M., (1975) 'Phosphate Ion-Selective Electrode Using Immobilized Alkaline Phosphatase and Glucose Oxidase', *Anal. Chim. Acta*, Vol. 78, No. 69, pp. 69.

16 Engblom, S.O., (1998) 'The phosphate sensor', *Biosens. Bioelectron*, Vol. 13, No. 9, pp. 981-994.

17 Wollenberger, U., Schellar F.W., (1993) 'Enzyme activation for activator and enzyme activity measurement', *Biosens. Bioelectron*, Vol. 8, No. 6, pp. 291-297.

18 Parellada, J., Narvaez, A., Lopez, M.A., Dominguez, E., Fernandez, J.J., Pavlov, V., Katakis, I., (1998) 'Amperometric immunosensors and enzyme electrodes for environmental applications', *Anal Chim Acta*, Vol. 362, pp. 47–57.

19 Luckarift, H.R., Greenwald, R., Bergin, M.H, Spain, J.C., Johnson, G.R, (2007) 'Biosensor system for continuous monitoring of organophosphate aerosols', *Biosensors and Bioelectronics*, Vol. 23, pp. 400–406.

20 Massoulie, J., Pezzementi, L., Bon, S., Krejci, E., Vallette, F-M., (1993) 'Molecular and cellular biology of cholinesterases', Progress in Neurobiology, Vol. 41, pp. 31–91.

21 Mulchandani, A., Chen, W., Muchandani, P., Wang, J., Rogers, K.R., (2001) 'Biosensors for direct determination of organophosphate pesticides', *Biosensors & Bioelectronics.*, Vol. 16, pp. 225–230.

22 Velasco-Garcia, M.N., Mottram, T., (2003) 'Biosensor technology addressing agricultural problems'., *Biosystems Engineering*, Vol. 84, pp. 1–12.

23 Evtugyn, G.A., Budnikov, H.C., Nikolskaya, E.B., (1998) 'Sensitivity and selectivity of electrochemical enzyme sensors for inhibitor determination', *Talanta*, Vol. 46, pp. 465–484.

24 Hart, A.L., Collier, W.A., Janssen, D., (1997) 'The response of screen printed enzyme electrodes containing cholinesterases to organophosphates in solution and from commercial formulations', *Biosensors & Bioelectronics*, Vol. 12, pp. 645–654.

25 Vakurov, A., Simpson, C.E., Daly, C.L., Gibson, T.D., Millner, P.A., (2005) 'Acetylecholinesterase-based biosensor electrodes for organophosphate pesticide detection II. Immobilization and stabilization of acetylecholinesterase', *Biosensors and Bioelectronics*, Vol. 20, pp. 2324–2329.

26 Jeanty, G., Marty, J.L., (1998) 'Detection of paraoxon by continuous flow system based enzyme sensor', *Biosens. Bioelectron*, Vol. 13, No. 2, pp. 213-218.

27 Villatte, F., Maral, V., Mondace, S.E., Furinier, D., (1998) 'Engineering sensitive acetylcholinesterase for detection of organophosphate and carbamate insecticides', *Biosens. Bioelectron*, Vol. 13, pp. 157-164.

28 Bernabei, M., Chivarini, S., Cremisisni, C., Pallechi, G., (1993) 'Anticholinesterase activity measurement by a choline biosensor: application in water analysis', *Biosens. Bioelectron*, Vol. 8, No. 5, pp. 265.

29 Arduini, F., Ricci, F., Tuta, C.S., Moscone, D., Amine, A, Palleschi, G., (2006) 'Detection of carbamic and organophosphorous pesticides in water samples using a cholinesterase biosensor based on Prussian Blue-modified screen-printed electrode', *Analytica Chimica Acta*, Vol. 580, pp. 155–162.

30 Mulchandani, A., Chen, W., Mulchandani, P., Wang, J., Rogers, K.R., (2001) 'Biosensors for direct determination of organophosphate pesticides', *Biosens Bioelectron*, Vol. 16, No. 4-5, pp. 225–230.

31 Mulchandani, P., Mulchandani, A., Kaneva, I., Chen, W., (1999) 'Biosensor for direct determination of organophosphate nerve agents. 1. Potentiometric enzyme electrode', *Biosensors & Bioelectronics*, Vol. 14, pp. 77–85.

32 Degiuli, A., Blum, L.J., (2000) 'Flow injection chemiluminescence detection of chlorophenols with a fiber optic biosensor' *J Med Biochem*, Vol. 4, pp. 32–42.

33 Berezhetskyy, A.L., Sosovska, O.F., Durrieu, C., Chovelon, J-M., Dzyadevych, S.V., Tran-Minh, C., (2008) 'Alkaline phosphatase conductometric biosensor for heavy-metal ions determination', 'Biocapteur conductimétrique à alcaline phosphatase pour la détection de métaux lourds', *IRBM.*, Vol. 29, pp. 136–140.

34 Andreescu, S., Sadik, O.A., (2004) 'Correlation of Analyte Structures with Biosensor Responses using the Detection of Phenolic Estrogens as a Model Example', *Anal. Chem*, Vol. 76, No. 3, pp. 552–560.

35 Dempsey, E., Diamond, D., Collier, A., (2004) 'Development of a biosensor for endocrine disrupting compounds based on tyrosinase entrapped within a poly(thionine) film', Biosens. Bioelectron, Vol. 20, No. 2, pp. 367–377.

36 Notsu, H., Tatsuma, T., Fujishima, A., (2002) 'Tyrosinase-modified boron-doped diamond electrodes for the determination of phenol derivatives', *J. Electroanal. Chem*. Vol. 523, No. 1-2, pp. 86–92.

37 Mita, D.G., Attanasio, A., Arduini, F., Diano, N., Grano, V., Bencivenga, U., Rossi, S., Amine, A., Moscone, D., (2007) 'Enzymatic determination of BPA by means of tyrosinase immobilized on different carbon carriers', *Biosensors and Bioelectronics*, Vol. 23, pp. 60–65.

38 Rodriguez-Mozaz, S., Lopez de Alda, M.J., Barceló, D., (2006) 'Biosensors as useful tools for environmental analysis and monitoring', *Anal Bioanal Chem*, Vol. 386, pp. 1025–1041.

39 Rose, A., Nistor, C., Emneus, J., Pfeiffer, D., Wollenberger, U., (2002) 'GDH biosensor based off-line capillary immunoassay for alkylphenols and their ethoxylates', *Biosens Bioelectron*, Vol. 17, No. 11-12, pp. 1033–1043.

40 Durrieu, C., Tran-Minh, C., (2002) 'Optical Algal Biosensor using Alkaline Phosphatase for Determination of Heavy Metals', *Ecotoxicol Environ Saf*, Vol. 51, pp. 206–209.

41 Krawczynski vel Krawczyk, T., Moszczynska, M., Trojanowicz, M., (2000) 'Inhibitive determination of mercury and other metal ions by potentiometric urea biosensor', *Biosens Bioelectron*, Vol. 15, No. 11-12, pp. 681–691.

42 Volotovsky, V., Nam, Y.J., Kim, N., (1997) 'Urease-based biosensor for mercuric ions determination', *Sensors and Actuators B*, Vol. 42, pp. 233-237.

43 Mohammadi, H., Amine, A., Cosnier, S., Mousty, C., (2005) 'Mercury-enzyme inhibition assays with an amperometric sucrose biosensor based on a trienzymatic-clay matrix', *Analytica Chimica Acta*, Vol. 543, pp. 143–149.

44 Zhylyak, G.A., Dzyadevich, S.V., Korpan, Y.I., Soldatkin, A.P., El'skaya, A.V., (1995) 'Application of urease conductometric biosensor for heavy-metal ion determination', *Sensors and Actuators B*, Vol. 24-25, pp. 145-148.

45 Sassolas, A., Blum, LJ., Leca-Bouvier, BD., (2012) 'Immobilization strategies to develop enzymatic biosensors', *Biotechnology Advances*, Vol. 30, pp. 489–511.

46 Apetrei, C., Rodríguez-Méndez, M.L., De Saja, J.A., (2011) 'Amperometric tyrosinase based biosensor using an electropolymerized phosphate-doped polypyrrole film as an immobilization support. Application for detection of phenolic compounds', *Electrochim. Acta*, Vol. 56, pp. 8919–8925.

47 Liu, J., Niu, J., Yin, L., Jiang, F., (2011) 'In situ encapsulation of laccase in nanofibers by electrospinning for development of enzyme biosensors for chlorophenol monitoring', *Analyst* Vol. 136, pp. 4802–4808.

48 Oliveira, TM., Barroso, MF., Morais, S., Araújo M., Freire, C., de Lima-Neto, P., Correia, AN., Oliveira, MB., Delerue-Matos, C (2014) 'Sensitive bi-enzymatic biosensor based on polyphenoloxidases–gold nanoparticles–chitosan hybrid film–graphene doped carbon paste electrode for carbamates detection', *Bioelectrochemistry*, Vol. 98, pp. 20-29.

49 Rao, M.A., Scelza, R., Acevedo, F., Diez, M.C., Gianfreda, L., (2014) 'Enzymes as useful tools for environmental purposes', *Chemosphere*, In Press, Corrected Proof.

50 Ragavan, K.V., Rastogi Navin, K, Thakur, M.S., (2013) 'Sensors and biosensors for analysis of bisphenol-A', *Trends in Analytical Chemistry*, Vol. 52, pp. 248–260.

51 Zhang, W., Asiri, A.M., Liu, D., Du, D., Lin Y., (2014) 'Nanomaterial-based biosensors for environmental and biological monitoring of organophosphorus pesticides and nerve agents', Trends in Analytical Chemistry, Vol. 54, pp. 1–10.

52 Moyo, M., Okonkwo, JO., (2014) 'Horseradish peroxidase biosensor based on maize tassel–MWCNTscomposite for cadmium detection' *Sensors and Actuators B*, Vol. 193, pp. 515–521.

53 Soldatkin, O.O., Kucherenko, I.S., Pyeshkova, V.M., Kukla, A.L., Jaffrezic-Renault, N., El'skaya, A.V., Dzyadevych, S.V., Soldatkin, A.P., (2012) 'Novel conductometric biosensor based on three-enzyme system for selective determination of heavy metal ions', *Bioelectrochemistry*, Vol. 83, pp. 25–30.

54 Domínguez-Renedo, O., Alonso-Lomillo, M.A., Ferreira-Gonçalves, L., Arcos-Martínez, M.J., (2009) 'Development of urease bades amperometric biosensors for the inhibitive determination of Hg (II)', *Talanta*, Vol. 79, pp. 1306–1310.

55 Kuswandi, B., (2003) 'Simple optical fibre biosensor based on immobilised enzyme for monitoring of trace heavy metal ions', Anal. Bioanal. Chem. Vol. 376, pp. 1104–1110.

56 Zhao, Y., Zhang, W., Lin, Y., Du, D., (2013) 'The vital function of Fe3O4@Au nanocomposites for hydrolase biosensor design and its application in detection of methyl parathion', Nanoscale. Vol. 5, pp. 1121-1126.

Complex impedance diagram of Si by Electro-PyroElectric (E.P.E.) technique

N. Bennaji*, I. Mellouki and N. Yacoubi

* E-mail: bennajin@yahoo.fr

ABSTRACT

Abstract: A novel method for electrical impedance spectroscopy of semiconductors based on Electro-Pyroelectric (E.P.E.) technique, which integrated experimental and theoretical model, is reported in this paper. The amplitude and phase results of electrical impedance versus frequencies from 30Hz to about 100 kHz obtained by EPE method were in good agreement to those measured by using impedance analyzer. The method experimentally tested on Silicon (Si), was achieved in order to measure the corresponding complex impedance diagram and the electrical equivalent circuit. From the data acquired through this given experience, a thorough investigation of the dielectric loss tangent (tan(δ)), which is an important source of information in semiconductors, should be held since we could evaluate the relaxation time, AC and DC electrical conductivity.

Keywords: Electro-Pyroelectric, pyroelectric sensor, electrical heating, Electrical Impedance Spectroscopy.

I. INTRODUCTION

In a number of reports it has been shown that impedance spectroscopy is a useful tool to characterize the compactness of amphilic on solid state surfaces. It appears certain that impedance studies will become increasingly popular as more and more electrochemists and materials scientists indulge in these studies. In order to investigate electrical impedance of materials [1], the Electrical Impedance Spectroscopy (EIS) appears as a powerful, rapid and accurate non-destructive method. Therefore, it is destined to play an important role in fundamental and applied electrochemistry and materials science in the coming years. In a number of respects, it is the method of choice for characterizing the electrical behavior of systems in which the overall system behavior is determined by a number of strongly coupled processes, each proceeding at a different rate. Engineers understand the theoretical basis for impedance spectroscopy and gain skill only in the interpretation of impedance experimental data.

In this paper, we proposed electrical impedance experimental and theoretical model by Electro-Pyroelectric (EPE) technique using uniform electrical heating for performing high precision impedance bridges and automatic measuring equipment covering 30Hz to 100kHz frequency range [2,3]. The pyroelectric signals variations of amplitude and phase of sample are then obtained by fitting theory to experimental data of pyroelectric signal. Normalization procedure was used to eliminate number of media parameters of Electro-Pyroelectric cell that otherwise need to be known before one can determine the electrical impedance of the sample.

The electrical measurements of real and imaginary components of impedance parameters (Z' and Z'') permit to calculate dielectric loss tangent (tan(δ)), the relaxation time, AC and DC electrical conductivity.

Our method was experimentally tested on Si semiconductor layer. Excellent agreement of results obtained by (E.P.E) technique and those obtained by impedance analyzer.

2. E.P.E THEORETICAL MODEL

The expression of pyroelectric signal is obtained by resolution of heat equations in different media: air, sample, Mylar layer, PVDF film and backing. The theoretical model is detailed in references [2,3,4]. Instead, we consider uniform heating of the sample, the one-dimensional heat treatment is justified and spatial average pyroelectric voltage $\langle V_p(\omega)\rangle$ may be determined from relationship [2]:

$$\langle V_p(\omega)\rangle = h(\omega)\times Z_s(\omega) \quad (1)$$

Where Z_s is electrical impedance of sample and $H(\omega)$ expression is

$$h(\omega)=\frac{j2A_v S\Lambda I_\varepsilon^2(1-e^{-j\omega\tau})}{C_{th_s}C_{th_p}C_p(j\omega+\frac{1}{\tau_{th}})(j\omega+\frac{1}{\tau_e})\omega\ell_p\sigma_p}\times\frac{\left[(b_{bp}+1)(e^{\ell_p\sigma_p}-1)+(b_{bp}-1)(e^{-\ell_p\sigma_p}-1)\right]\times\left[2-\left((b_{sa}+1)e^{\ell_s\sigma_s}-(b_{sa}-1)e^{-\ell_s\sigma_s}\right)\right]}{(b_{sa}+1)\left[\begin{array}{l}(b_{gs}+1)\left[(b_{bp}+1)(b_{pg}+1)e^{\ell_p\sigma_p}+(b_{bp}-1)(b_{pg}-1)e^{-\ell_p\sigma_p}\right]e^{\ell_g\sigma_g}\\+(b_{gs}-1)\left[(b_{bp}+1)(b_{pg}-1)e^{\ell_p\sigma_p}+(b_{bp}-1)(b_{pg}+1)e^{-\ell_p\sigma_p}\right]e^{-\ell_g\sigma_g}\end{array}\right]e^{\ell_s\sigma_s}}$$
$$+(b_{sa}-1)\left[\begin{array}{l}(b_{gs}-1)\left[(b_{bp}+1)(b_{pg}+1)e^{\ell_p\sigma_p}+(b_{bp}-1)(b_{pg}-1)e^{-\ell_p\sigma_p}\right]e^{\ell_g\sigma_g}\\+(b_{gs}+1)\left[(b_{bp}+1)(b_{pg}-1)e^{\ell_p\sigma_p}+(b_{bp}-1)(b_{pg}+1)e^{-\ell_p\sigma_p}\right]e^{-\ell_g\sigma_g}\end{array}\right]e^{-\ell_s\sigma_s}$$

(2)

However, a number of pertinent values for air, sample, Mylar layer, PVDF film and backing need not to be used by normalizing the pyroelectric voltage of the test sample to that the sensor alone [5].

The spatial average pyroelectric voltage $\langle V_p'(\omega)\rangle$ is obtained by replacing sample by Mylar layer (or index s by g) in Eq. (1). Therefore finally thickness of Mylar layer becomes $2l_g$, to be replaced by only l_g in pyroelectric voltage following expression:

$$\langle V_p'(\omega)\rangle = h'(\omega)\times Z_g(\omega) \quad (3)$$

Where:

$$h'(\omega)=\frac{jA_s S\Lambda l_s^2(1-e^{-j\omega\tau})}{C_p C_{th_g} C_{th_p}\omega\ell_p\sigma_p(j\omega+\frac{1}{\tau_{th}})(j\omega+\frac{1}{\tau_e})}\times\frac{\left|(b_{hp}+1)(e^{\ell_p\sigma_p\tau_p}-1)+(b_{hp}-1)(e^{-\ell_p\sigma_p\tau_p}-1)\right|\times\left|2-\left((b_{ga}+1)e^{\ell_g\sigma_g\tau_g}-(b_{ga}-1)e^{-\ell_g\sigma_g\tau_g}\right)\right|}{\begin{matrix}(b_{ga}+1)\left[(b_{hp}+1)(b_{hg}+1)e^{\ell_p\sigma_p\tau_p}+(b_{hp}-1)(b_{hg}-1)e^{-\ell_p\sigma_p\tau_p}\right]e^{\ell_g\sigma_g\tau_g}\\+(b_{ga}-1)\left[(b_{hp}+1)(b_{hg}-1)e^{\ell_p\sigma_p\tau_p}+(b_{hp}-1)(b_{hg}+1)e^{-\ell_p\sigma_p\tau_p}\right]e^{-\ell_g\sigma_g\tau_g}\end{matrix}} \tag{4}$$

Where Z_g is the electrical impedance of sensor and C_{th_g} is specific heat capacity of sensor.

The impedance electrical of sample is obtained by a similar normalization procedure, in which the measured EPE signal was normalized to the one obtained with the sensor alone. This

$$\frac{\langle V_p(\omega)\rangle}{\langle V_p'(\omega)\rangle}=\frac{h(\omega)}{h'(\omega)}\times\frac{Z_s(\omega)}{Z_g(\omega)} \tag{5}$$

simplifies Eq. (1) to:

Therefore, in this section, we are considering a special condition imposed by the experience, according to thermally thin pyroelectric and thermally thin Mylar layer, under this condition: $\mu_s >> \ell_s$ and $\mu_g >> \ell_g$, upon setting $\exp(\pm\sigma_s\ell_s)\cong 1\pm\sigma_s\ell_s$

$$\frac{\langle V_p(\omega)\rangle}{\langle V_p'(\omega)\rangle}=cons\tan te\times\frac{Z_s(\omega)}{Z_g(\omega)} \tag{6}$$

In general, electrical impedance is a complex number that may be and $\exp(\pm\sigma_g\ell_g)\cong 1\pm\sigma_g\ell_g$. Thus, Eq. (5) became:

$$\begin{cases} Z_s(\omega)=|Z_s(\omega)|\exp(j\varphi_{Z_s}(\omega)) \\ Z_g(\omega)=|Z_g(\omega)|\exp(j\varphi_{Z_g}(\omega)) \end{cases} \tag{7}$$

Where $|Z_s(\omega)|$ and $|Z_g(\omega)|$ are respectively the amplitude of electrical impedance of sample and sensor and $\varphi_{Z_s}(\omega)$ and $\varphi_{Z_g}(\omega)$ are respectively the phase of electrical impedance of sample and sensor.

To further simplify Eq. (6), electrical impedance phase of sample can be written as:

$$\varphi_{Z_s}=\varphi_{V_p}-\varphi_{V_p'}+\varphi_{Z_g} \tag{8}$$

And the expression of amplitude of electrical impedance of sample is:

$$|Z_s(\omega)|=cte\times\frac{|\langle V_p(\omega)\rangle|}{|\langle V_p(\omega)\rangle'|}\times|Z_g(\omega)| \tag{9}$$

3 EXPERIMENTAL SET-UP

3.1 Electrical-PyroElectric experimental system

The bloc diagram of Electrical-PyroElectric system used to carry out the AC impedance spectroscopy of semiconductors is described in [2,3]. The measurement consisted of heating uniformly samples by sine-wave generator adjusted at electrical pulse duration of $\tau=1\mu s$ and modulated at frequency *f*. The output pyroelectric detector is fed into a lock-in amplifier (model SR-530) that operated at frequencies range form few Hertz to 100kHz.

3.2 Impedance analyzer

The principle of measure is the following; an AC stimulus signal is applied to samples under test, the AC voltage and current are both measured, then impedance of samples is obtained. A PC is used to control the instrumentation and collect impedance results for storage on disk and for display in graphical form. Impedance measurements are carried out using the four-electrode technique, two electrodes for current and two electrodes for voltage. The impedance analysis was performed using a frequency response analyzer [6] (LF impedance analyzer model 4192A). All data were obtained with 10V amplitude of sinusoidal voltage signal and modulation frequency in range 30 Hz–100 kHz.

4. EXPERIMENTAL RESULTS AND DISCUSSION

The normalized experimental curves of pyroelectric sensor signal given amplitude and phase of AC impedance versus frequencies from 30Hz to about 100 kHz. In figure 1 is represented experimental amplitude and phase of Si electrical impedance variations obtained by EPE method and impedance analyzer method. We noted from these results the good agreement between the curves of electrical impedance obtained by two techniques.

Their (E.P.E) complex impedance diagram (Z''=*f*(Z')) of Si is displayed in Figure 2. The impedance diagram reveals that the semicircle is slightly depressed and their center is shifted down to the real axis. In addition, depressed arc is typical for a dipolar system involving multi relaxation processes [7-9]. However, a single semicircular arc appears, that can be attributed to a contribution from the gain properties of the material. This arc arising as a result of a parallel RC equivalent circuit in the frequency range analyzed (Figure 2), where R represents the grain resistance, C the grain or geometric capacitance of the samples [10].

The values of real and imaginary components for such a circuit are given by:

$$\begin{cases} Z=\dfrac{R}{1+jRC\omega}=Z'-jZ'' \\ Z'=\dfrac{R}{1+(RC\omega)^2} \\ Z''=\dfrac{RC\omega}{1+(RC\omega)^2} \end{cases} \tag{10}$$

It is clear that Z′ depends on the applied frequency and its value is equal to R at zero frequency. On the other hand, Z″ exhibits a maximum peak at angular frequency equal to 1/RC. Figure 3a and b depicts the real and imaginary parts of impedance Z′ and Z″ as a function of frequency. The real and imaginary parts of the

complex impedance decreases especially for high frequency. The study of dielectric loss tangent (tan(δ)) is an important source of information in a thin film; since we can determine the electrical and dipolar relaxation time and its activation energy. It is expressed as [11]:

$$\tan(\delta) = \frac{Z''}{Z'} \qquad (11)$$

In addition loss tangent Eq. (11) is a parameter of a dielectric material that quantifies the dissipation of electric energy in the material. Figure 4 shows the frequency dependence of dielectric loss tangent (tan(δ)). There are no appreciable relaxation peaks in the frequency range employed in this study. However, it has been verified that in the absence of a well-defined tan(δ) peak, the relaxation time can be obtained from the complex impedance (Z'') diagram. It is also known that at the peaks corresponding to Z'' the relaxation time τ can be deduced from the following equation:

$$\omega_m \tau = 1 \qquad (12)$$

where ω_m is the angular frequency at Z'' peaks.
The AC conductivity was calculated from the following equation:

$$\sigma_{AC} = \frac{L}{Z' A} \qquad (13)$$

Where L is distance between electrodes and A is the cross-sectional area. The thickness of Si thin films is around 10 mm. Finally, the DC conductivity was obtained by extrapolation at zero frequency from AC measurements. Figure 5 shows the Frequency dependence of AC conductivity σ_{AC}.

Figure 1 **Figure 2**

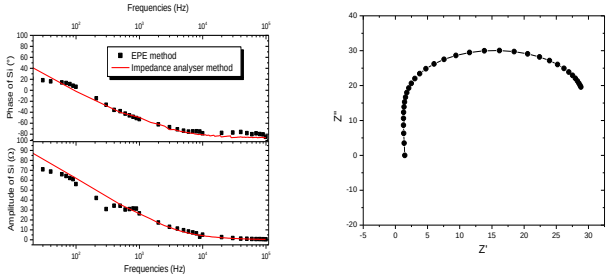

Figure 3 (a) frequency dependence of Z', (b) frequency dependence of Z''

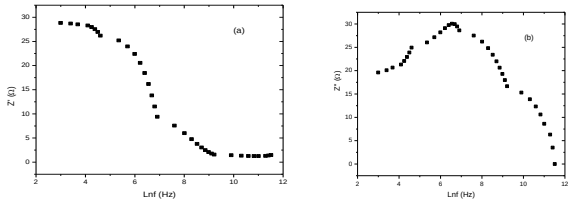

Figure 4 Variation of tanδ **Figure 5** Frequency dependence of AC conductivity $\sigma_{AC}(\omega)$

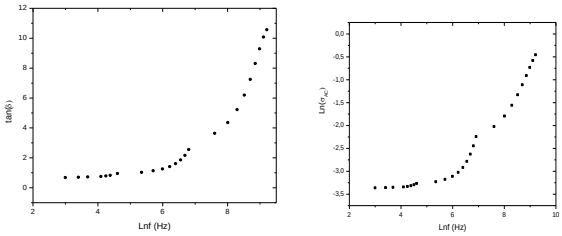

5. CONCLUSION

Electro-Pyroelectric (EPE) technique is shown to be sensitive and reliable tool for studying AC electrical impedance of semiconductors, dielectric loss tangent (tan(δ)), the relaxation time, AC and DC electrical conductivity. As a result of measurements the following conclusions have been made: Major advantages of this technique are the high measurement precision of electrical proprieties, simplicity, non destructive and uniform heating. A normalization procedure was used as a convenient way to eliminate the effect of a number of unknown parameters in other media of EPE cell. The variations of amplitude and phase of electrical impedance for Si obtained by EPE method were in good agreement with the curves obtained by impedance analyzer.

Finally, with improved EPE technique, it was good prospects in developing new theoretical model of semiconductor films electrical impedance that explain electrical behavior according frequencies and witch may exhibit characteristic of electrical equivalent circuits. In the future, we will work in order to explore frequencies range by improving look-in amplifier covering the frequency range 30 Hz-100 kHz.

6. REFERENCES

[1] Hamdy, A. S., Int. J. Electrochem. Sci. 1, 171-180, 2006.
[2] Bennaji, N., Mellouki I. and Yacoubi, N., 'Thermal properties of metals using photopyroelectric technique: Electrical heating', Sensor Letters 7, pp.716-720, 2009.
[3] Bennaji, N. *et al.*, 'Thermal properties of metals alloy by electrical pyroelectric method (EPE)', J. Phys.: Conf. Ser. 214, 012138, 2010.
[4] Mandelis, A., Zver, M.M., J. Appl. Phys. 57 (9), 4421, 1985.
[5] Azmi, B.Z., *et al.*, 'Normalisation procedure in thermal wave approach of thermal diffusivity measurement of solids using pyroelectric sensor', Infrared Physics & Technology, 45, pp.315-321, 2004.
[6] Ben Saad, K., Saadoun, M., Hamzaoui, H., and Bessaïs, B., 'AC impedance spectroscopy of porous silicon thin films containing metallic cations', Materials Science and Engineering C 28, pp.623-627, 2008.
[7] Goyal, N., Pramana J. Phys. 40 97, 1993.
[8] Shukla, R., *et al.*, J. Mater Sci. Mat. Electr. (3) 132, 1992.
[9] Vohra, A., Srivastva, K.K., Philos. Mag. (61) 201, 1990.
[10] Ouni, B., *et al*, jounal of Non-Crystalline Solids (367), pp.1-7, 2013.
[11] Cao, W., Gerhardt, R., Solid State Ionics (42) 213, 1990.

Chemical Vapor Deposition Synthesis of Individual Single Walled Carbon Nanotubes Aligned on an ST-cut Quartz Substrate and Measurement of their Electrical Transport Properties

El-Hadi Sadki [1], Tohru Watanabe [2], Takahide Yamaguchi [2], and Yoshihiko Takano [2]

[1] Physics Department, United Arab Emirates University, PO. Box 17551, Al Ain, United Arab Emirates
[2] National Institute for Materials Science (NIMS), 1-2-1 Sengen, Tsukuba, Ibaraki 305-0047, Japan

ABSTRACT
In this proceeding, we introduce a technique for synthesizing an individual single walled carbon nanotube (SWNT) aligned on an ST-cut quartz single-crystal substrate, and demonstrate the measurement of its electrical transport characteristics. The SWNT is CVD synthesized from an optimized catalyst's size that yields just one individual SWNT suitable for electrical transport measurements. The temperature dependence of its electrical resistance is measured from room temperature down to few Kelvins.

Keywords
Single walled carbon nanotubes, ST-cut quartz, CVD

1. INTRODUCTION
Single walled carbon nanotubes (SWNTs) are promising materials to replace silicon for future electronic circuits and devices because of their unique electrical transport properties [1]. However, the main obstacle for this realization is the lack of control on the properties of the synthesized SWNTs and their exact positioning on substrates to make reliable and reproducible devices.

Recently, it has demonstrated that by using single-crystal ST-cut quartz as substrates to synthesize SWNTs on them by chemical vapor deposition (CVD) leads to highly aligned and long SWNTs that are very suitable for electronic device fabrication [2]. However, so far no electrical transport measurements have been conducted on an individual SWNT on these substrates because they are usually synthesized as arrays, and, hence, it is difficult to isolate just one SWNT for these measurements (See figure 1).

In this work, we introduce a technique for synthesizing an individual single walled carbon nanotube (SWNT) aligned on an ST-cut quartz single-crystal substrate, and demonstrate the measurement of its electrical transport characteristics. The SWNT is CVD synthesized from an optimized catalyst's size that yields just one individual SWNT suitable for electrical transport measurements. The temperature dependence of its electrical resistance is measured from room temperature down to few Kelvins and briefly discussed.

2. EXPERIMENTAL
The fabrication process for the synthesis of an individual SWNT, and the deposition of the electrical terminals on top of it, is summarized as follows. A patterned metallic foil is used as a shadow mask for the evaporation of the cobalt catalyst pads needed for the CVD growth of the SWNTs. The cobalt catalyst, with a thickness of 2 nm, is evaporated through the mask's pattern by an electron beam (EB) evaporator. The area of the Co-catalyst pad is optimized to yield to the growth of one individual long and aligned SWNT suitable for electrical transport measurements. After catalyst deposition, the SWNT is synthesized by thermal CVD method using a tube furnace. ST-cut quartz substrates (Hoffman Materials, Inc) are placed at the center of the downstream side of the furnace. A typical CVD process is as follows: Substrate is heated in a 200 sccm O_2 flow from room temperature to 900 ^oC for 30 minutes and let to settle for 5 minutes. Next, the O_2 flow is stopped and replaced by 300 sccm Ar flow for 10 mins. Then, a 200 sccm H_2 gas is flown for 10 mins. Finally, the H_2 gas is co-flown with 300 sccm CH_4 gas for 15 mins, which leads to a SWNT synthesis. Finally, the sample is left to cool-down to room temperature in a continuous H_2 flow.

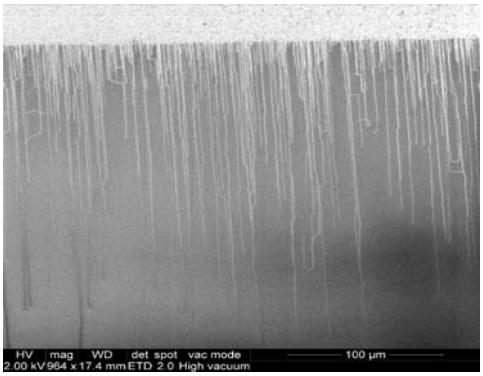

Figure 1. Scanning electron micrsocope (SEM) image of highly aligned single walled carbon nanotubes (SWNTs) on an ST-cut quartz substrate.

Electrodes on the SWNT are also fabricated using shadow mask evaporation technique. The metal masks are prepared by the same method as of that used for catalyst pattern. Palladium (Pd) is selected as the material of the electrodes because of its low contact resistance to SWNTs [3]. The Pd electrodes, with a thickness of 50 nm, are EB evaporated in a four-terminal configuration, with a typical distance of 4.0 μm between adjacent electrodes. The electrical properties of the SWNT are measured from room temperature down to 2 K, using a physical properties measurement system (PPMS: Quantum Design Inc.) for the

temperature control. Voltages of ~ ±1 V are applied by a voltage source through a 10 MΩ resistance connected in series with the sample, and the voltage is measured across the inner-electrodes on the sample by a voltmeter.

3. RESULTS AND DISCUSSION

Figure 2 (a) shows an SEM image of SWNTs synthesized from a catalyst pad of 100 x 10 μm in area. A lot of SWNTs are obtained in this case, with average lengths of more than 100 μm. On the other hand, as shown in Figure 2 (b), if a catalyst pad of 10 x 2 μm is used, only one or a few SWNTs are obtained, with typically the emergence of an individual SWNT of more than 100 μm in length. Figure 2 (c) shows deposited electrodes on another SWNT synthesized from the same pad's dimensions of 10 x 2 μm.

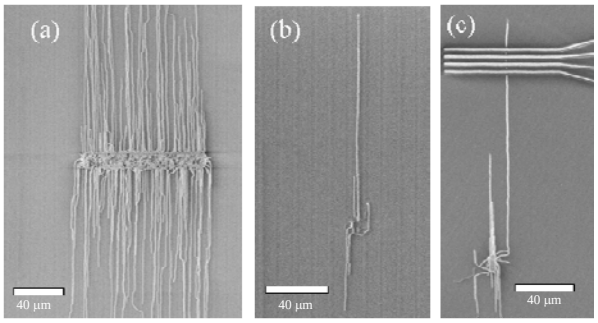

Figure 2. SEM images of SWNTs synthesized from different catalyst pads. Size of catalyst pad is 100 x 10 μm in (a), 10 x 2 μm in (b), and 10 x 2 μm in (c) with deposited metallic electrodes.

Figure 3 shows the result of the temperature dependence of the electrical resistance (normalized to its value at 300 K) of a SWNT measured with an electrical current of 10 nA. The nanotube has a diameter of 0.9 nm as measured by AFM.

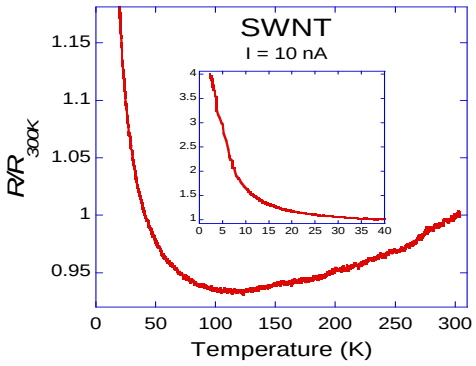

Figure 3. Temperature dependence of the electrical resistance of the nanotube (normalized to its value at 300 K). Inset shows the resistance in the low temperatures range. The electrical current is 10 nA in all measurements.

The SWNT's resistance decreases with decreasing temperature from room temperature down to about 120 K, and then it increases by decreasing temperature down to 2 K. At the lowest temperature of 2K, the resistance reaches about 4 times its room temperature value of 181 kΩ. The decrease in the resistance of the nanotube with decreasing temperature from room temperature down to about 120 K is attributed to its metallic nature [4]. To explain the "semiconducting-like" behavior of the resistance versus temperature below 120 K, it is noted that even "metallic" SWNTs can exhibit a "semiconducting" energy gap due their intrinsic curvature [5] and substrate effects [6]. Further studies are underway to investigate these properties of more individual SWNTs in this special configuration.

4. CONCLUSION

In conclusion, we have presented a technique for synthesizing an individual single walled carbon nanotube (SWNT) aligned on an ST-cut quartz single crystal substrate, and demonstrate the measurement of its electrical transport characteristics. The temperature dependence of its electrical resistance is measured from room temperature down to few Kelvins, and showed a decrease with decreasing temperature from room temperature down to about 120 K, and then an increase by decreasing temperature down to 2 K. Further studies are in progress to explain these properties.

5. ACKNOWLEDGMENTS

This study was supported by Nano-Integration Foundry (NIMS) in "Nanotechnology Platform Project" operated by the Ministry of Education, Culture, Sports, Science and Technology (MEXT), Japan. ESS would like to acknowledge the support from NIMS during his visit as a Guest Researcher.

6. REFERENCES

[1] Cao, Q. and Han, S.J. 2013. Single-walled carbon nanotubes for high-performance electronics. *Nanoscale*. 5, 19, 8852–8863. DOI= http://dx.doi.org/10.1039/C3NR02966B.

[2] Kang, S.J., Kocabas, C., Ozel, T., Shim, M., Pimparkar, N., Alam, M.A., Rotkin, S.V. and Rogers, J.A. 2007. High-performance electronics using dense, perfectly aligned arrays of single-walled carbon nanotubes. *Nat. Nanotechnol*. 2, 4, 230–236. DOI= http://dx.doi.org/10.1038/nnano.2007.77.

[3] Javey, A., Guo, J., Wang, Q., Lundstrom, M. and Dai, H.J. 2003. Ballistic carbon nanotube field-effect transistors. *Nature*, 424, 6949, 654–657. DOI= http://dx.doi.org/10.1038/nature01797.

[4] 26 Kane, C.L., Mele, E.J., Lee, R.S., Fischer, J.E., Petit, P., Dai, H., Thess, A., Smalley, R.E., Verschueren, A.R.M., Tans, S.J. and Dekker, C. 1999. Temperature-dependent resistivity of single-wall carbon nanotubes. *Europhys. Lett*, 41, 6, 683–688. DOI= http://dx.doi.org/10.1209/epl/i1998-00214-6.

[5] Kleiner, A. and Eggert, S. 2001. Band gaps of primary metallic carbon nanotubes. *Phys. Rev. B*, 63, 7, 073408 DOI= http://link.aps.org/doi/10.1103/PhysRevB.63.073408.

[6] Soares, J.S. and Jorio, A. 2012. Study of Carbon Nanotube-Substrate Interaction. *Journal of Nanotechnology*, 2012, 1-10. DOI= http://dx.doi.org/10.1155/2012/51273.

Different kinds of Carbon Nanotubes With Their Methods of Synthesis

Oudjertli S[1], Bensalem R [1], Alleg S[2]

[1]Laboratoire des Nanomateriaux-Corrosion et Traitements de Surfaces, Département de Physique university badji mokhtar b.p. 12, 23 000 Annaba

[2]Laboratoire de Magnétisme et Spectroscopie des Solides, Département de Physique university badji mokhtar b.p. 12, 23 000 Annaba

ABSTRACT

Carbon nanotubes have revolutionized the world of science by their unmatched properties and their various applications, Theoretical calculations predicted that carbon nanotubes were present metallic behavior or semiconducting depending on their diameter and chirality. These conduction properties are inherited from the particular structure of the graphite band. The winding of a graphene sheet on itself creates periodic boundary conditions perpendicular to the axis of the nanotube. Therefore a limited number of wave vectors is allowed in this direction. It depends on the diameter and winding the graphene sheet on itself.

Potential applications of these properties are in the field of nanoelectronics, not only the use of the nanotube as a molecular thread, but also as an active electronic component.

Keywords

Carbon Nanotubes-1, **chirality-2**

1. INTRODUCTION

Discovered by Professor IIJIMA [1] in 1991 the NEC laboratories using advanced electron microscopy technique , nanotubes have been constantly subject to search around the world saw their properties unmatched , the carbon nanotubes have a specific crystal structure , tubular , hollow and close , comprising atoms arranged in a regular pentagon , hexagon and / or heptagons , the diameter of these nano- structures and is a length of the order micrometer [2]. These nanotubes are

obtained from certain materials , particularly carbon and boron nitride. [3] regarding the classification of carbon nanotubes exist two types of carbon nanotubes , they have Single Wall Carbon Nanotubes (SWNT) , and Multi Wall Carbon Nanotubes (MWNT) .Each tube may be designated by two integers (n, m). The winding consists of superimposing two hexagons of graphene sheet . It is the choice of these two hexagons that will determine the diameter of the nanotube and its helicity (θ) . To set this helicity , we take a reference direction parallel to a side of a hexagon and the helicity is measured as the angle between the axis of the cylinder formed and this reference direction . the angle θ varies from 0 to 30 ° due to the symmetry of the lattice hexagonal. are several application domain for carbon nanotubes, such as applications in microelectronics (- Connectors, Diodes , Transistor single electron field effect transistor, logic gates etc..) , also other applications as (Issuance of individual nanotubes, luminescent elements , Flat Screen, X-ray tubes etc..).

2 STRUCTURE

Exist two types of carbon nanotubes:

Single Wall Carbon Nanotubes (SWNT) and Multi Wall Carbon Nanotubes (MWNT)

2.1 Single-Walled Carbon Nanotubes (SWNTs)

The single-walled nanotubes (single-walled nanotubes) are constituted by a single wall (Figure. 1 and 2).

In this case, the nanotube has a helicity (depending on how the two edges of the graphene sheet will overlap). Each tube may be designated by two integers (n, m) values in the unit vectors of the graphene network, the components of a vector connecting the same point along the circumference.

The winding consists of superimposing two hexagons of graphene sheet. It is the choice of these two hexagons that will determine the diameter of the nanotube and its helicity (θ) (Figure. 3).

To set this helicity, we take a reference direction parallel to a side of a hexagon and the helicity is measured as the angle between the axis of the cylinder formed and this reference direction.

Therefore, the angle θ varies from 0 to 30 ° in view of the symmetry of the hexagonal lattice. This angle allows to classify carbon nanotubes into different families according to their helicity. Chiral nanotubes [5]and non chiral nanotubes: two major families of nanotubes was obtained. Non-chiral nanotubes are those in which the hexagons of the upper part of the cylinder has the same orientation as those of the lower part. In this case when θ is 30 °, so it is a tube called "chair" and when θ is 0 ° is a tube called "zigzag", with (m = 0).

2.2 Multi Wall Carbon Nanotubes (MWNT)

Multi Wall Carbones Nanotubes are composed of several spaced walls of 0.340 nm. Two different configurations (Fig. 4), based on either an interlocking of said concentric tubes "Russian doll", either on winding a single spiral graphitic sheet, possible to consider this type of structure [6].

3 SYNTHESIS

Two types of synthesis are available depending on the temperature .

3.1 Average Temperature Synthesis

This pathway is an adaptation of the catalytic and pyrolytic methods. The principle is to decompose a hydrocarbon vapor to the surface of particles of a metal catalyst in an oven heated to an average temperature. Condensation of this vapor provides nanotubes

3.2 High-Temperature Synthesis

This pathway involves spraying the graphite carbon and condensing the steam in an enclosure where there is a strong temperature gradient in an atmosphere of inert gas (Helium, Argon).

4 RESULTS and discussions:

-Next its helicity , a nanotube is semiconducting or metallic superconductors.

- The nanotubes are extremely strong , a hundred times more than steel and weighs six times less (equivalent to section). Nanotubes , while being rigid , keep good flexibility .

- They have a better reactivity than graphites.Les carbon nanotubes are insoluble in water.

- Solubility is controlled by changing their size and end .

- Thermal stability up to 3000 ° C.

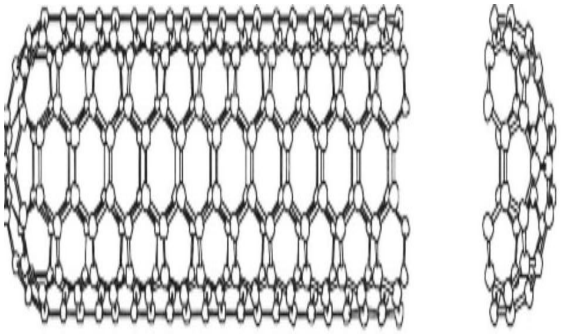

Figure. 1 Carbon Nanotubes (SWNT) [4]

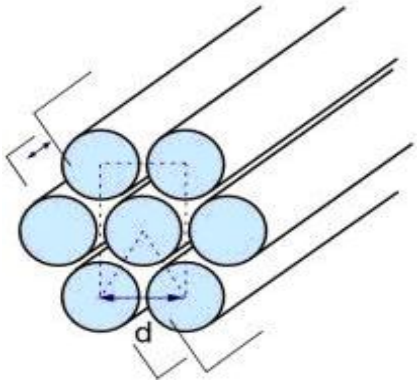

Figure. 2 A transverse cutting of SWNT

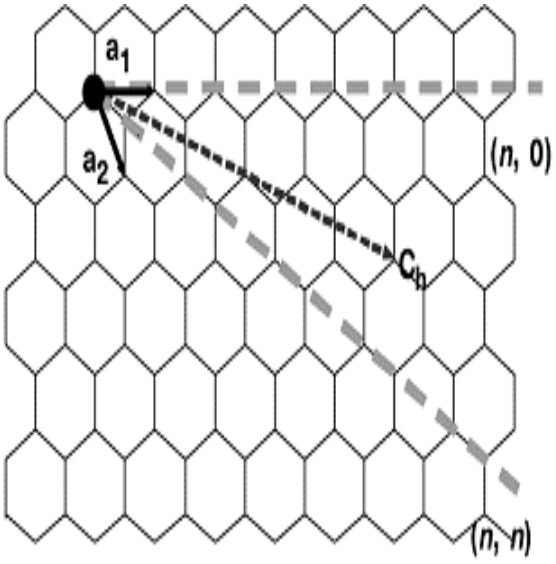

Figure. 3 Showing the possibilities of winding a graphitic sheet.

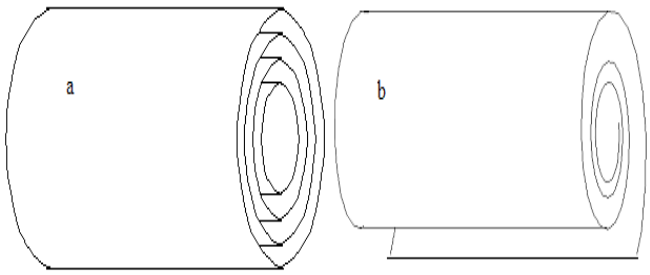

Figure. 4 Multi Wall Carbones Nanotubes
a) formed of concentric tubes b) Spirally wound

5 Conclusion

If carbon nanotubes are so successful is because they have properties unmatched in several areas, such as electrical, mechanical , chemical, thermal , electronic etc..

REFERENCES

[1]-D.S. Bethune *et autres.* (1993), *croissance Cobalt-catalysée des nanotubes de carbone avec des murs de simple-atomique-couche*, nature 363, 605 – 607- Sumio Iijama 1993, *nanotubes de carbone de Simple-coquille de 1 diamètre de nanomètre*, nature 363, 603 – 605- http://66.249.91.104/translate_c?hl=fr&u=http://www.almaden.ibm.com/st/nanoscale_science/past/nanotubes/&prev=/search%3Fq%3DHTTP%253B//%2Bnanotube.%26start%3D10%26hl%3Dfr%26sa%3DN

[2]-http://carbon.phys.msu.ru/publications/1952-radushkevich-lukyanovich.pdf

[3]-A. Oberlin, M. Endo, et T. Koyama, J. Cryst. Growth, 1976, 32, 335.

[4]- S. J. Tans, M. H. Devoret, H. Dai, A. Thess, R. E. Smalley, L. J. Georliga, and C. Dekker, “Individual single-wall carbon nanotubes as quantum wires,” Nature, vol. 386, pp. 474-7, 1997.

[5]-Izvestiya Akademii Nauk SSSR, métaux. 1982, #3, p.12-17 [dans le Russe]

[6]http://66.249.91.104/translate_c?hl=fr&u=http://www.freepatentsonline.com/4663230.html&prev=/search%3Fq%3DHTTP%253B//%2Bnanotube.%26start%3D10%26hl%3Dfr%26sa%3DN Carbon, 38, 1691–1697, 2000. 40

OPTIMAL DESIGN AND MANAGEMENT OF THERMAL STORAGE TANKS FOR MULTI-ENERGY DISTRICT BOILERS

Mouchira Labidi [1,2,3], Julien Eynard [2,3], Olivier Faugeroux [2,3], Stéphane Grieu [2,3]

[1] Cylergie, research center of Cofely GDF-Suez
18 Avenue Tony Garnier, 69007 Lyon, France

[2] PROMES-CNRS
Tecnosud, Rambla de la Thermodynamique, 66100 Perpignan, France

[3] University of Perpignan Via Domitia
52 Avenue Paul Alduy, 66860 Perpignan, France

ABSTRACT
As part of the second phase of the OptiEnR research project, the present work deals with improving multi-energy district boilers operation, by adding optimally sized and controlled thermal storage tanks to the plants. Previous studies focused on both a sizing approach based on a parametric analysis and an operation strategy. The aim of the present work is to improve the design of the tanks, in particular by evaluating the thermal losses and finding the adequate insulating materials. We focused on the stratification phenomenon and highlighted that the effectiveness of a thermal storage tank is related to the time during which the stored energy can be kept without considerable degradation. A case study allows the impact of thermal energy storage to be quantified.

Keywords
Multi-energy district boiler, thermal energy storage, stratification phenomenon, thermal losses, optimal design, management strategy.

1. INTRODUCTION
Nowadays, the storage of energy in suitable forms is a scientific and technical challenge. A number of approaches have been investigated over the years to store thermal energy, including rock storage and phase change materials, but the most pragmatic solution is using water. Indeed, water is an excellent storage medium for low-to-medium temperature applications because of a high volumetric heat capacity, a low cost, very good security properties and widespread availability. Consequently, hot water tanks (for stratified thermal energy storage) are considered as an attracting technology and used in several industrial applications [1,2]. It should be noted that thermal stratification has a major influence on performance. Stratification can be impacted by turbulence inside the tank as well as thermal losses [3].

First, using discretization of time and space, a stratified tank has been modeled. The resolution of the resulting model allows the water temperature for each of the tank layers to be accurately estimated. Next, a design methodology based on a complete parametric analysis is proposed in order to optimize the tank shape and find the adequate insulating material. Then, we used the proposed methodology in order to design a 200 m^3 hot water storage tank that will be installed at a Cofely GDF-Suez multi-energy district boiler located in Northeast France (Alsace region). We carried out simulations in order to highlight the impact of the geometrical characteristics of the tank, its insulation and the weather conditions on the thermal losses. As a result, we found that heat losses have to be considered as a key factor when designing thermal storage tanks. Indeed, the efficiency of such systems is mainly related to its design and insulation.

2. MODELING OF THE TANK
In order to investigate the main factors leading to thermal losses, a model describing the thermal stratification phenomenon in the hot water tank has been developed. Unlike simplistic models in which temperature is supposed to be uniform throughout the volume of the tank, the proposed discrete space model, adapted from the "turbulent mixing model" [4], takes into account the existing temperature gradient. The tank is divided into *N* equal volume layers. When energy is stored, hot water is allowed to enter by the top of the tank and is assumed to mix with the *m* first top layers. In discharging (release) mode, the process described above is reversed. So, cold water is allowed to enter by the bottom of the tank and is assumed to mix with the *m* first bottom layers. Heat loss by conduction through the walls and by convection with the ambient air, conduction between layers as well as inlet and outlet thermal mixing are taken into account. The resolution allows the water temperature for each layer of the tank to be calculated.

3. DESIGN OF THE TANK
As previously mentioned in the paper, the optimal volume of the thermal storage system can be defined on the basis of economic and energy criteria. However, a key point in the project is to design the tank by defining adequate geometrical characteristics as well as finding the insulating material allowing the thermal losses to be limited. To carry out this study, we used the model of the stratified water tank described in the previous section of the paper.

3.1 Case study
We selected as a case study a multi-energy district boiler managed by Cofely GDF-Suez. The plant, located in Northeast France (Alsace region), is connected to a heat network and equipped with a 4 200 kW biomass (wood) boiler and two gas boilers of 7 000 kW. A preliminary study, based on economic and energy criteria, has shown that 200 m^3 is the optimal size of the tank [5].

Geometrical characteristics. In order to define the adequate geometrical characteristics of the thermal storage tank, we evaluated in static mode (no water is passing through the tank) the impact of the ratio of Height to Diameter (H/D) on the thermal losses. We supposed that the 200 m^3 thermal storage tank is not insulated at all and initially filled with hot water at a temperature of 105 °C. The tank is not used during 24 hours. Outdoor temperature is supposed to be equal to 0 °C and unchanged through the day. Figure 1 highlights the way the ratio H/D impacts on the thermal losses. As it can be noted, by choosing for the tank a height equal to its diameter (H/D = 1), the average water temperature is decreased by 44 °C at the end of the day. Thus, such a temperature is 16 °C higher than when considering a ratio H/D equal to 5. So, we designed the tank as follows: V_{tot} = 200 m^3, H = D = 6.33 m.

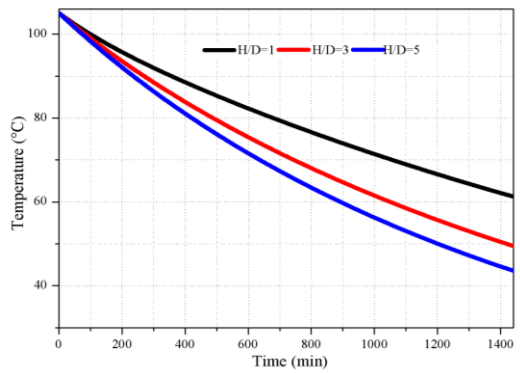

Figure 1. Impact of the ratio of Height to Diameter (H/D) on the thermal losses (static mode, non-insulated tank).

Insulation. The insulating material used and its thickness play an important role in the minimization of the thermal losses and, as a result, in saving energy. Figure 2 shows the impact of both the material used and its thickness on the thermal losses. If the objective is to lose no more than 1°C per day, the possible choices are: a 100 mm layer of Rockwool, a 50 mm layer of rigid polyurethane foam or a 150 mm layer of foam glass granulate. A definitive choice based on market price can then be made.

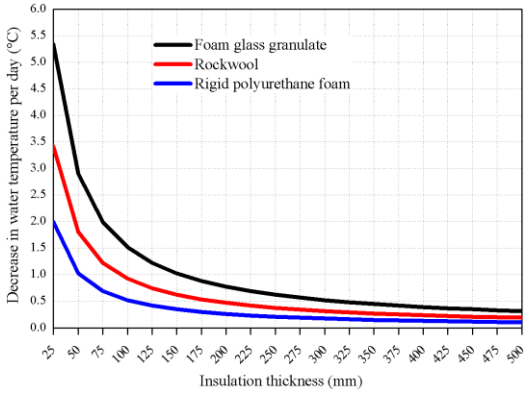

Figure 2. Impact of the insulating material used.

Weather conditions. Thermal losses are also influenced by the weather conditions, in particular outdoor temperature and wind speed. We carried out a parametric analysis in order to outline both the impact of the weather conditions on the tank operation during the cooling down phase and the way an appropriate insulation (e.g. a 100 mm thick layer of rock wool) can cope with unfavorable conditions. From Figures 3 and 4, we can easily notice that for a given ambient temperature, the impact of wind, implicitly considered through the heat transfer coefficient of air (h_{out}), can be limited if the tank is well isolated. In addition, to limit the effect of forced convection created by the wind and prevent the tank to be subjected to very low ambient temperatures during cold days, it must be located in a place well sheltered from both the wind and cold (e.g. a place where it can be buried).

4. RESULTS AND DISCUSSION

Table 1 summarizes the characteristics of the designed thermal storage tank. Adding an appropriately shaped and correctly insulated storage tank to the plant can have economic and energy benefits. Insulation allows the thermal losses to be minimized, in particular when the tank is not used (static mode).

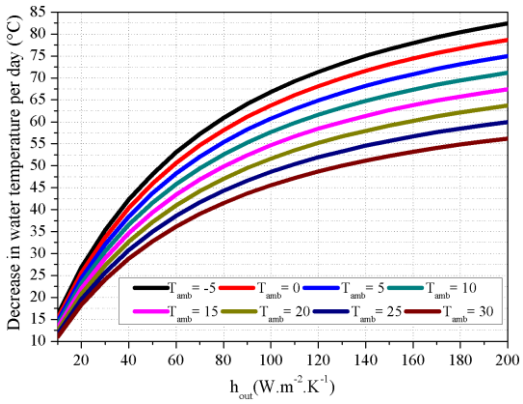

Figure 3. Impact of the weather conditions in case of a non-insulated tank.

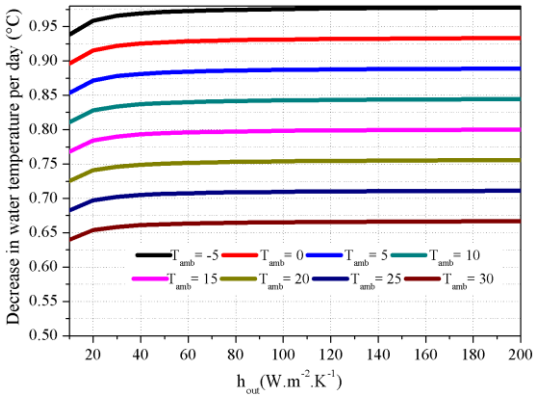

Figure 4. Impact of the weather conditions in case of an insulated tank.

Volume	Height	Diameter	Insulating material	Thickness of insulating material
200 m^3	6.33 m	6.33 m	Rockwool	100 mm

Table 1. Characteristics of the thermal storage tank.

5. REFERENCES

[1] Dehghan A. A. and Barzegar. A. 2011. Thermal performance behavior of a domestic hot water solar storage tank during consumption operation. *Energy Conversion and Management*, 52, 1 (January 2011), 468-476.

[2] Han Y. M., Wang R. Z., and Dai Y. J. 2009. Thermal stratification within the water tank. *Renewable and Sustainable Energy Reviews*, 13, 5 (June 2009), 1014-1026.

[3] Kaloudis E., Grigoriadis D.G.E., Papanicolaou E. and Panidis T. 2013. Large eddy simulations of turbulent mixed convection in the charging of a rectangular thermal storage tank. *International Journal of Heat and Fluid Flow*, 44 (December 2013), 776-791.

[4] Al-Najem N. M. and El-Refaee M. M. 1997. A numerical study for the prediction of turbulent mixing factor in thermal storage tanks. *Applied Thermal Engineering*, 17, 12 (December 1997), 1173-1181.

[5] Labidi M., Eynard J., Faugeroux O., Grieu S. 2013. Optimal design of thermal storage tanks for multi-energy district boilers. In *Proceedings of the 4th Inverse Problems, Design and Optimization Symposium* (Albi, France, June 26 - 28, 2013). IPDO 2013.

Thermo-electrical properties of polymers for Electro-Pyroelectric Technique (EPE)

A. Mami • I. Mellouki • N. Yacoubi

ABSTRACT

In this paper, we investigate thermally performance of polymers by both photothermal methods:
photo-thermal deflection and photo- pyroelectric technique (PPE) in back configuration .In addition to this, the electrical conductivity have been described using an impedance analyzer. The comparative study was performed on Sil-pad 900S layer, Sil-pad K10 layer and Mylar layer in order to involve it in the new so-called electro-pyroelectric (EPE) technique, as good thermal conductor and an electrical insulator.

Keywords

thermally performance, polymers, photothermal deflection ,photo-pyroelectric method (PPE), electro-pyroelectric (EPE) technique.

1. INTRODUCTION

The electro-pyroelectric (EPE) technique **[1]** showed recently an increased interest especially due to its simplicity, non destructive character and its high sensitivity.

In this paper, we proposed an experimental model of the electro-pyroelectric (EPE) technique as a reliable tool for the measurement of the thermal properties of condensed matter samples. The main idea behind this method is the use of a uniform electrical heating flowing through the serpentine at the metal contact etched in semi conductor sample deposit in good thermal contact with a polymer layer on one side of the pyroelectric (PE) sensor , tacking into regard that the polymer have to be a good thermal conductor and an electrical insulator for not having a short circuit. The generated thermal wave will propagate in each region of PPE cell and induce a temperature gradient producing on his turn a pyroelectric current.A comparative study was performed on Sil-pad 900S layer, Sil-pad K10 layer and Mylar layer in order to involve it in the new so-called electro-pyroelectric (EPE) technique.

This paper is organized as follows. In the next section the basics behind the EPE method and the essence of the problem to be solved will be described. In section 3 electrical proprieties are presented. In section 4 we show and compared thermally performance of polymers used photo-thermal deflection and photo pyroelectric technique (PPE) in back configuration before we draw our conclusions in the last section.

2. THERMAL CHARACTERIZATION OF POLYMERS

2.1 Theoretical considerations

2.1.1 Photopyroelectric method (PPE)

General theory of PPE signal has been already detailed elsewhere [**2**]. We give here only main results corresponding to use standard back configuration.

In one-dimensional heat approximation, PPE normalized voltage signal is a complex function contains all sample related parameters and it can be expressed when substrate (b) is thermally thick (thickness is larger than the thermal diffusion length), then in particular case where polymer sample (s) and pyroelectric sensor (p) are thermally thick , as: $\ln\left(\frac{|V_{Norm}|}{2}\right) = \lambda \cdot \sqrt{f} + \beta$ (1).

Finally thermal conductivity K_s and volume heat capacity C_s could be obtained from following equations $c_s = \frac{e_s}{\sqrt{D_s}}$ (2)

and $K_s = e_s \cdot \sqrt{D_s}$ (3).

2.1.2 The photothermal deflection technique 'Mirage effect' (PTD)

Photothermal deflection technique consists on generating thermal wave in the sample using a modulated halogen lamp come then fluid (air in our case) inducing in the surrounding a refractive index gradient. A laser probe beam "fixed" perpendicularly, skimming the sample surface undergoes a beam deflection**.**
The used samples material should be covered with a thin graphite layer that will absorb the incident light and therefore playing the role of a heat source. In the case of a uniform heating of the samples, a one-dimensional treatment of the thermal wave is sufficient.

The theoretical model is built on the resolution of heat equation in the different media, fluid, graphite layer, sample and backing.
In these conditions the sample surface's elevation temperature T_0 and the deflection of the probe laser beam are shown in the reference [**3**].

2.2 Experimental configuration and results:

Three commercial polymer samples [**4-5**] were used in this work: silpad 900S of 229 µm thick, , silpad K10 of 152µm thick and Mylar layer of 125 µm thick. Thermal conductivity values as provided by manufacturer are respectively 1.6 W m^{-1} K^{-1} , 1.3 W m^{-1} $K^{-1}$and 0.14 W m^{-1} K^{-1}.

2.2.1 Photopyroelectric method:

The photo pyroelectric (PPE) experiment was a standard one for back detection configuration **[6] .**

The intensity-modulated light was He-Ne laser operated at wavelength 632 nm and powered at 20 mW. Mechanically chopped light at frequency f, was incident on sample in thermal contact with polyvinylidene fluoride (PVDF) metalized film of 28µm-thick. His bottom surface was thermally attached to metal copper backing of about 6-mm-thick. The PPE signal data (amplitude and phase) was measured by Standford SR 530 lock-in amplifier in the frequency range 30–150Hz and computer controlled via an RS 232 interfaceThe thermal parameters of PVDF was e_p = 559.4309 ($J.K^{-1}.m^{-2}.s^{-1/2}$) and D_p= $5.4.10^{-8}$ $m^2.s^{-1}$, by extrapolation of literature data [**7**]. Since pyroelectric sensor has thermally thin/thick limit (defined by equation L_p/μ_p=1) at about 21.92 Hz, square root of frequency range used in experiment is about 5.47 $Hz^{1/2}$ to achieve thermally thick limit, until 12.24 $Hz^{1/2}$ where the degradation of the signal/ noise ratio is significant.

Figure.1 2 and 3 represented experimental and fit linear variations of pyroelectric logarithm signal as a function of frequency square root of silpad 900S , silpad K10 andMylar.

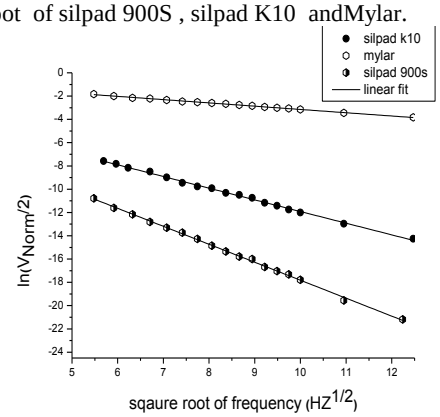

Figure. 1 Photopyroelectric amplitude variations according to the square root frequency of Silpad 900S,Silpad K10 and Mylar layer

As expected from equation (1), the curves 'logarithm of normalized amplitude of a PPE signal vs. square root of frequency is linear in the thermally thick regime, a linear fit allowing to calculate both the thermal effusivity and diffusivity .Then, we relies on equations (2) and (3) to finish remaining thermal parameters as shown Table 1.

To reassure the values obtained previously, we had recourse to efficient and well known technique called the photo-thermal deflection PTD.

2.2.2 Photothermal deflection technique

The samples are heated by a lamp light of Power 100W modulated by a mechanical chopper at a variable frequency. A He-Ne laser probe beam of wavelength 632.8 nm, skimming the sample surface at a distance x_0 of average 70µm, is deflected.

This deflection can be detected by a four quadrant photo-detector and converted to an electrical signal which is measured by a lock-in amplifier (EG & G5210). In Figures 2, 3 and 4 are represented the experimental and the corresponding theoretical curves of respectively the logarithm of the amplitude and the phase versus square root modulation frequency for the thermal conductivities values of each sample as provided by manufacturer.

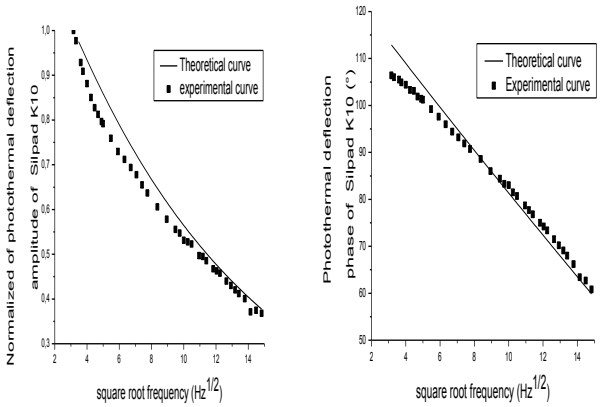

Figure. 2 Experimental curves and corresponding theoretical ones giving the Variations of the amplitude and the phase of photothermal signal according to the square root of the modulation frequency, for silpad K 10

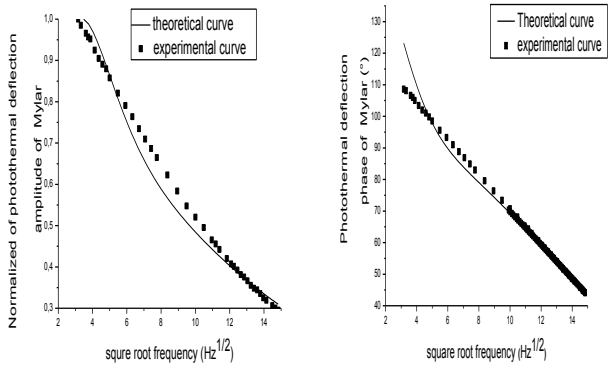

Figure. 3 Experimental curves and corresponding theoretical ones giving the variations of the logarithm of the amplitude (a) and phase (b) of photothermal signal according to the square root of the modulation frequency, for mylar sample

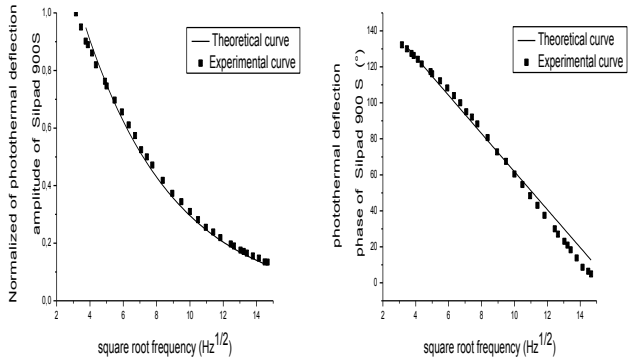

Figure. 4 Experimental curves and corresponding theoretical ones giving variations of the amplitude and the phase of photothermal signal according to the square root of the modulation frequency, for silpad 900S .

Therefore, If we compare the experimental curves to the theoretical ones obtained for different values on thermal diffusivity Dc we notice that the best coincidence is obtained for value of the thermal diffusivity Ds =7.5×10-8 m2.s-1, 7×10-8 m2.s-1 and Ds =6.7×10-7 m2.s-1 for respectively silpad K10, silpad 900S and Mylar 1which is in good agreement with that found in the photopyroelectric method.

The three samples thermal parameters so deduced are reported in Table 1.

	PPE method	**Mirage effect method**
Mylar		
Ks (W m^{-1} K^{-1})	0,17	0.14
Ds 10^{-7} (m^2 s^{-1})	6,20	6.7
Cs 10^5 (J K^{-1} m^{-3})	2.81	2.15
es (J K^{-1} m^{-2} $s^{-1/2}$)	221,52	183.75
Silpad K10		
Ks (W m^{-1} K^{-1})	0,99	1.3
Ds 10^{-8} (m^2 s^{-1})	7,40	7.5
Cs 10^7 (J K^{-1} m^{-3})	1.33	1.42
es (J K^{-1} m^{-2} $s^{-1/2}$)	3641,29	4629.10
Silpad 900S		
Ks (W m^{-1} K^{-1})	1.62	1.6
Ds 10^{-8} (m^2 s^{-1})	7.04	7
Cs 10^7 (J K^{-1} m^{-3})	2.30	2.28
es (J K^{-1} m^{-2} $s^{-1/2}$)	6 105.604	6 047. 431

Table.1: Thermal properties of the studied sample

3. ELECTRICAL CHARACTERIZATION OF POLYMERS

The direct measurement of the electrical conductivity was done using an impedance meter HP 4192A. Both floating and grounded devices can be tested.
In Figure.5 The electrical conductivity σ as a function of frequency of Silpad 900S Silpad K10 and Mylar is plotted.

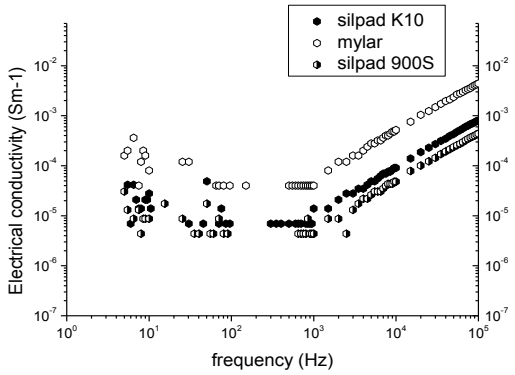

Figure. 5 Variation of electrical conductivity σ as a function of frequency of Silpad 900S Silpad K10 and Mylar.

So, Silpad 900S is the suitable material for our study because it has the least free charges is in spite that his electrical insulator up to only 3000 Hz .

4. CONCLUSION

In conclusion, silpad 900S has not only the highest thermal conductivity volume and heat capacity values and also the least free charge. So, it's the most suitable polymer sample to involve it in the new so-called electro-pyroelectric.
In the future, the Electro pyroelectric technique will be applied to semiconductor samples in order to obtain their thermal and electrical properties in spite that is limited in frequency.

5. REFERENCES

[1] Ivanov, R.**,** Marin, E., Moreno I and Araujo C 2010. Electropyroelectric technique for measurement of the thermal effusivity of liquids. *J. Phys. D: Appl. Phys*. 43, 225501

[2] Delenclos, S., Chirtoc, M., Sahraoui, A.H. , Kolinsky, C., Buisine, J.M. 2002.Assessment of calibration procedures for accurate determination of thermal parameters of liquids and their temperature dependence using the photopyroelectric method. *Rev. Sci. Instrum.* 73, 2773.

[3] Gaied, I., Amara, A., Yacoubi, N., and T. Ghrib, *Applied Optics.* 47, 1054-1062

[4]http://www.goodfellow.com/F/Polyethylene-terephthalate.html

[5]http://www.bergquistcompany.com/thermal_materials/sil-pad.html

[6] Abdellaziz, I., Mellouki, I.,and Yacoubi, N., 2009.Investigation of Thermal Properties of Bulk Zn Doped GaSb and Silicon by Photopyroelectric Technique. *Sensor Lett.* 7 ,656–660 .

[7] C Wang, A Mandelis. 1999. *Rev. Sci. Instrum*.70,2372. .

Syntehisis and Characterization of PAN-co-polymers as Carbon Nano Fiber Precursor

E. Ismar, A.S. Sarac

ABSTRACT

In this study, synthesis a co-polymer of polyacrylonitrile (PAN) and, producing a carbon nanofiber out of homo-polymer PAN and co-polymer of PAN and compression between these products was examined. In this perspective, acrylic acid (AA), itaconic acid (IA) and acrylonitrile (AN) were used as a precursor for polymerization reactions and copolymers were synthesized by using ammonium persulfate (APS) as an oxidant. Polymerization medium was water and dimethylformamide (DMF) mixture. Synthesized co-polymers were investigated by Fourier Transform Infrared Spectroscopy-Attenuated Total Reflection (FTIR-ATR) spectroscopy and characteristic peaks for acrylonitrile unit, acrylic acid and itaconic acid was seen. Thermal behavior was examined by using Differential Scanning Calorimeter (DSC) and Thermal Gravimetric Analyzer (TGA) and results showed that addition of monomers to acrylonitrile unit was reduced the Tg value of co-polymer PAN.

Keywords

Carbon nanofibre, PAN, AA, IA

1. INTRODUCTION

Carbon nanofibers have a great interest due to their high aspect ratio and a mechanical property even with it is a time and energy consuming process. Carbon nanofibers mainly, can be pitch based or polyacrylonitrile (PAN) based (Edie, 1998). In this study, different co-polymers of acrylonitrile were aimed to synthesis. In this perspective; acrylic acid and itaconic acid monomers were used. Instead of using homo polymer PAN, co-polymer of polyacrylonitrile have a positive effect to decrease cyclization reaction duration and temperature during oxidative stabilization process (Devasia, Nair, Sivadasan, Katherine, & Ninan, 2003). Acrylic acid (AA), itaconic acid (IA) and acrylonitrile (AN) were used as a precursor for polymerization reactions and copolymers were synthesized by using ammonium persulfate (APS) as an oxidacnt. Polymerization medium was water and dimethylformamide (DMF) mixture. Using a water:DMF mixture has a positive effect on the polymerization reaction (Bajaj, Paliwal, & Gupta, 1993; Ouyang, Cheng, Wang, & Li, 2008). Polyacrylonitrile-co-acrylic acid and Polyacrylonitrile-co-itaconic acid polymers were successfully synthesized with different feeding ratios. Synthesized co-polymers were investigated by Fourier Transform Infrared Spectroscopy-Attenuated Total Reflection (FTIR-ATR) spectroscopy and characteristic peaks for acrylonitrile unit, acrylic acid and itaconic acid units were seen. As indicated in the Figure 1, changing feeding ratios of acrylic acid unit has a linear relationship between CN/C=O peaks absorbance ratio. Thermal behavior was examined by using Differential Scanning Calorimeter (DSC) and Thermal Gravimetric Analyzer (TGA) and results showed that addition of monomers to acrylonitrile unit was reduced the Tg value of co-polymer PAN. Morphological behavior of carbon nanofibers was investigated by scanning electron microscope (SEM). Carbon nanofibers can be used in a various engineering fields.

2. EXPERIMENTAL

2.1 Materials & Methods

2.1.1 Materials

Polyacrylonitrile was purchased from Sigma Aldrich standard Mw 150,000 g/mol and was used as received. Dimethylformamide (DMF) was purchased from Sigma Aldrich and was used without any further purification. Acrylonitrile (AN), (99.5> %) and Ammonium persulfate (APS), (99.5> %) were obtained the Aksa Acrylic Chemistry Company and were used as received. Itaconic acid (99.5> %) and Acrylic acid was purchased from Sigma Aldrich. Ethanol and Methanol were all Merck reagents and were used without any purification.

2.1.2 Synthesis of Copolymers

Copolymerization of acrylonitrile with acrylic acid and itaconic acid carried in aqueous solution. Reaction medium contains deionized water and DMF. All polymerization experiments were carried out in 3 necked flask and bath temperature was set to 60 ^{o}C ± 2 ^{o}C. The poly (acrylonitrile-co-acrylic acid) and poly(acrylonitrile-co-itaconic acid) were synthesized by free radical polymerization and APS was used as an initiator in the aqueous medium. First solvent mixture was stirred at 60 ^{0}C during 30min, DMF:water mixture volume ratio was 50:50 and kept constant for all reactions. Distilled water was used for the reaction. Then, monomers (AN/AA or AN/IA) were added by dropwise and were stirred during 30 minutes.

2.1.3 FTIR-ATR

Frourier Transform Infrared Spectroscopy instrument is widely used to analyze the structure of organic materials. Main principle of infrared spectroscopy is, measure the infrared absorption by molecular vibrations, result of the molecular vibration infrared spectroscopy shows the wavelength values and generally, wavelength varies between 200 to 4000 cm^{-1} also crystalline solids make a lattice vibrations which is presented in the range of 20 to 300 cm^{-1} (Leng, 2010, pp. 235–297). In this study, FTIR-ATR was used to examine the functional groups of co-polymers.

2.1.3.1 Differential Scanning Calorimetry

The Modulated Temperature Differential Scanning Calorimetry (MTDSC) measurements were performed using a Q2920 from TA

instruments. DSC is the most well known thermal analysis for measuring the thermal properties of the sample such as; solid phase transformation, glass transition, crystallization, melting, and these measurements based on the difference between the sample material and the reference material (Leng, 2010, p. 305). DSC was used for examining the nanofiber webs behaviors under known temperature and examine the duration of the oxidation time for that temperatures. Thermal behavior comparisons between the commercial PAN polymer and synthesized PAN co-polymers was made using DSC and it was used under nitrogen and air environments.

3. RESULTS and DISCUSSIONS:

Addition of monomers to acrylonitrile structure helps to decrease the Tg value as seen in the figure, which provides lower energy requirements during the cyclization reactions. As seen from the DSC results co-polymers have a positive effect to shift to peak point to the lower temperature level, compared to homo polymer PAN.

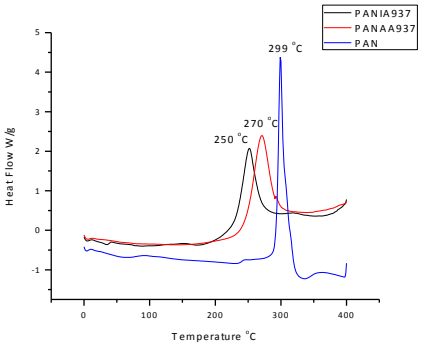

Figure 1: DSC curves for P(AN-IA), P(AN-AA) co-polymers and homo-polymer PAN.

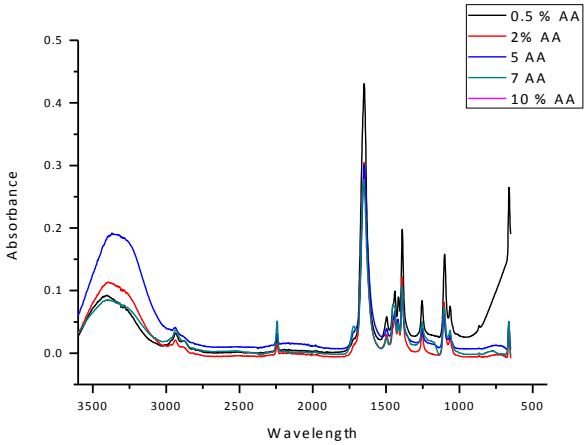

Figure 2: FTIR-ATR spectra of P(AN-AA) co-polymer for different feeding of wt% of AA and Correlation between FTIR-ATR absorbance ratio(CN/C=O peaks) with feeding wt% of AA

In **Error! Reference source not found.**Figure 2. the characteristic peak of C≡N stretching of AN repeating unit is observed as a strong absorption peak at around 2244 cm-1. The peak at about 1735 and 1628 cm^{-1} are related to the carbonyl stretching vibration of the carboxylic acid. The peak of carbonyl stretching in copolymers is shifted from 1737 to 1732 cm^{-1}, corresponding to increase in AA content. The characteristic peak of aliphatic -CH_2- stretching is at 2940 cm-1. There is also a strong band at 1454 related to bending vibration of -CH in -CH_2. The band at 1076 cm-1 is ascribed to the -CH bending mode in CH and also characteristic peak C=O which was observed due to addition of the monomer units, was observed between 1735-1710 cm^{-1}. These results are in agreement with (Bhanu ve diğerleri, 2002; Devasia ve diğerleri, 2003; Moghadam & Bahrami, 2005; Wangxi, Jie, & Gang, 2003)

4. REFERENCES

Bajaj, P., Paliwal, D. K., & Gupta, A. K. (1993). Acrylonitrile–acrylic acids copolymers. I. Synthesis and characterization. *Journal of Applied Polymer Science*, *49*(5), 823–833.

Devasia, R., Nair, C. P. R., Sivadasan, P., Katherine, B. K., & Ninan, K. N. (2003). Cyclization reaction in poly(acrylonitrile/itaconic acid) copolymer: An isothermal differential scanning calorimetry kinetic study. *Journal of Applied Polymer Science*, *88*(4), 915–920.

Edie, D. D. (1998). The effect of processing on the structure and properties of carbon fibers. *Carbon*, *36*(4), 345–362. d

Leng, Y. (2010). *Materials Characterization: Introduction to Microscopic and Spectroscopic Methods*.

Ouyang, Q., Cheng, L., Wang, H., & Li, K. (2008). Mechanism and kinetics of the stabilization reactions of itaconic acid-modified polyacrylonitrile. *Polymer Degradation and Stability*, *93*(8), 1415–1421.